Title: Engineering Design of Advanced H_2 – CO_2 Pd and Pd/Alloy Composite Membrane Separations and Process Intensification

Type of Report: Final Technical Report

Project Period Covered: 07/01/2012 –03/31/2016

Date Report was issued: May 2016

DOE Award Number: DE-FE0004895

Author: Dr. Yi Hua Ma

Name and Address of Submitting Organization:

Worcester Polytechnic Institute
100 Institute Road
Worcester, Massachusetts

DISCLAIMER

ABSTRACT

The integrated gasification combined cycle (IGCC) process is a way to co-produce synthesis gas, electricity, hydrogen, fuels and chemicals from coal and coal/biomass-mix in an environmentally responsible manner. The production of hydrogen via the water-gas shift (WGS) reaction is a key part of this process. Pd and Pd/Alloy-based catalytic membrane reactors used in the WGS process could significantly improve the efficiency of the IGCC process with a great potential for process intensification. Membrane reactors enable reaction, separation and product concentration to take place in a single unit operation, leading to conversion levels beyond thermodynamic equilibrium due to the continuous removal of H_2. Worcester Polytechnic Institute (WPI) has developed composite Pd and Pd/alloy composite hydrogen separation membranes with high H_2 flux, excellent selectivity and long-term durability for this membrane reactor process. WPI membranes used in a natural gas reforming operation were stable for over 6,000 hours (>8 months) at 500°C and 40 bar. Under the DOE Hydrogen Pathway Program (DE-FC-26-07NT43058) Pd membranes prepared by WPI exceed the DOE 2015 targets for H_2 flux, selectivity and stability. Furthermore, the scalability of the WPI technology has been shown to be relatively easy, and composite Pd/Cu and Pd/Au alloy membranes have been shown to be sulfur resistant and permeance recoverable.

In the present two-phase program, it was envisioned to take this technology from the laboratory to construction and testing of industrial-scale membrane modules and generation of a detailed engineering design of a large scale (WGS) membrane reactor. The specific objectives included (1) develop an integrated, cost-effective, H_2 production/separation process using WPI Pd membrane technology, (2) perform research, technology development and demonstration with the construction of a minimum of 2 lb H_2 per day at the pre-engineering/pilot scale membrane-based process, and develop strategies which effectively separate hydrogen from coal-based syngas with performance meeting the DOE 2015 flux, selectivity, cost as well as chemical and mechanical robustness targets, (3) design and construct a membrane separation module with the capacity of 100 lb per day of H_2, followed by validation and assessment of the design, membrane production and separation performance, (4) pursue technology scale-up and demonstration at a commercial sized facility resulting in a Full Engineering Design of a unit capable of producing a minimum of four tons per day of H_2, and finally (5) develop a comprehensive process intensification framework followed by process economic analysis.

During Phases I and II of this project, several Pd and Pd/alloy membranes were produced by WPI's patented technology and examined at the National Carbon Capture Center (NCCC) in coal-derived syngas and industrial conditions. At first, thirteen single-tube membranes were tested for a cumulative time of > 4,000 hours. These membranes showed high permeance and selectivity values and outstanding long-term performances under actual coal derived syngas never reported before. The membranes showed good stability in syngas although exhibiting an initial drop in permeance when compared to that under pure hydrogen; nonetheless, a flux > 2 lb H_2 per day was successfully achieved. The membrane permeation study in actual coal derived syngas performed at NCCC, demonstrated the high robustness and excellent physical integrity of composite Pd membranes, and more importantly elucidated the feasibility and reliability of the use of this technology under adverse industrial applications such as medium-high temperatures, high contaminants concentrations and large fluctuations in operating parameters typically observed in industrial processes. After successfully demonstrating the robustness of this technology at the pre-engineering/pilot scale, a multitube membrane module using seven membranes was designed, constructed and tested at NCCC. The module consisted of seven membranes and its total surface area was 5.25 times bigger than the single tube membranes. The replicability of this technology was demonstrated by the synthesis of all membranes with identical thickness and only deviating by > 1%. The multitube membrane module was tested for more than 800 hours at producing 6 lb/day of H_2 with a purity of 99.87 % throughout the test. A high H_2 recovery was achieved by this module, hindering its full performance; nonetheless, it estimated that the membrane module could produce more than 11 lb/day of H_2. The scale up process was successfully carried out, demonstrating that this technology is a viable option for industrial applications. Once more, the membranes demonstrated high robustness and excellent physical integrity.

Meanwhile at WPI, preliminary tests for process intensification were conducted, along with the development and validation of computational fluid dynamic (CFD) models for process optimization, and a thorough economic evaluation of the proposed technology. In terms of process intensification, Pd and Pd/alloy membranes were incorporated to a large-scale catalytic membrane reactor (CMR) rig built at WPI. Different reactions were conducted such as water-gas-shift, ethanol steam reforming, and an integrated methane steam reforming and water-gas-shift process. In all cases, the presence of the membranes enhanced the performance of the reactions, clearly demonstrating the effect of process intensification in CMRs. In specific, the CMR tested for WGS was capable of achieving a CO conversion of > 98% and producing H_2 at a rate of 1.2 lb/day with conditions analogous to those present in the gasification unit at NCCC. The CFD models predicted the performance of the CMRs and the multitube membrane module and therefore used for the optimization and tuning of the modules' design and operating conditions. Finally, an economic analysis was developed to estimate the economic performance of the Pd membranes when integrated to different processes such as in integrated gasification combined cycle (IGCC) power plants and hydrogen production plants based on coal and natural gas. The uncertainty of critical inputs (economic and financial assumptions, assignments of contingencies, different types of costs as well as the opportunity cost of capital) in the proposed process economic analysis framework were captured by Monte Carlo probabilistic methods to generate net present value (NPV) distributions as the basis of the economic viability assessment. The analysis conducted suggested that in the absence of any regulatory action on CO_2 emissions CMR technology could not be perceived as an economically viable option. However, better prospects arise if future regulatory action on carbon emissions is introduced, and therefore, initiatives to stimulate the realization of demonstration projects of this innovative technology at the commercial scale might be warranted.

In summary, this report presents detailed information on the synthesis of the membranes, testing methodology and protocol of characterization, simulation development and features of the economic analysis, along with a thorough description of the results obtained and conclusions.

TABLE OF CONTENTS

1. INTRODUCTION

The production of hydrogen from alternative methods has been gaining considerable interest in the last decades due to the need of responding to increasing H_2 demand for a fuel cell based transportation system as part of the developing H_2 economy. The Water Gas Shit (WGS) and the Methane Steam Reforming (MSR) reactions conducted in Catalytic Membrane Reactors (CMRs) may represent sound economically viable routes to satisfy such a large hydrogen demand. In industry, the WGS reaction, performed after the MSR of hydrocarbons to remove CO, is carried out in two stages: a first stage at high temperatures (310-450°C) to insure high throughput and a second stage at low temperatures (210-250°C) for high conversion. The produced hydrogen by the MSR and WGS processes is then purified by Pressure Swing Adsorption (PSA) to reach the high purity levels required by the ammonia production industry. All steps (MSR, high temperature shifter, low temperature shifter and purification) can be combined into a MSR-CMR or into a WGS-CMR based on hydrogen permeable membranes working at 400-550°C. The continuous removal of hydrogen as either reaction occurs, allows for higher CH_4 or CO conversion, the production of high purity hydrogen suitable for fuel cell applications, a high pressure (> 40-50 bar) reject stream rich in CO_2 readily to be captured at lower costs, and significant energy savings. Dense metallic Pd-based membranes have been studied mostly for the production of hydrogen in CMRs [1,2,3,4] due to their theoretical infinite selectivity towards H_2 and their high stability in steam at high temperatures of 400-500°C. A few studies on relatively large hydrogen production pilot plants (20-40 Nm^3/h) MSR-CMRs have already been performed by De Falco et al. [5] and Shirasaki et al. [6] with very promising results. All these studies on CMRs used a blended Syngas from pure industrial high pressure cylinders or locally available natural gas previously desulfurized. However, no studies have been performed in CMRs in actual Syngas from a coal gasification unit.

Indeed, the effect of contaminants on the hydrogen permeance of Pd-based membranes has extensively been studied for H_2S [7,8,9], CO [10,11,12], Cl [13], NH_3 [14] and for certain hydrocarbons [13] separately. Inert gases such as CO_2, Ar, N_2 and He are not thought to have a poisoning effect yet their presence in mixtures containing hydrogen may lead to a decrease in H_2 flux due to mass transfer resistance in the gas phase. H_2O is believed to adsorb on the palladium surface in the 250-450°C temperature range leading to some decrease in the hydrogen flux, however, its effect appeared to be totally reversible [15]. Industrial Syngas from a coal derived gasifier includes all contaminants mentioned above and a multitude more not quite known. Indeed, actual Syngas from coal may include: H_2S (0.2-1.3 vol%), COS (<0.1vol%), NH_3+HCN (<0.3vol%), C_2 hydrocarbons, PolyAromatics Hydrocarbons (PAHs), halides (such as CH_3F, CH_3Cl at around 2 ppmv), heavy metals (such as Hg, Cd, Pb), tellurides (arsenides, selenium , antimony), alkalis metals (Na, K, Ca), phosphorous and other compounds. The reactivity of the majority of these compounds with Pd and its alloys is not known and has not been characterized. Such a characterization in actual Syngas is essential for the development of a WGS-CMR based on Pd-based membranes.

No gas permeation study was conducted with composite Pd membranes exposed to actual coal derived syngas where the effect of known and unknown contaminants has never been addressed before. Indeed, the effect of contaminants on the H_2 permeance of Pd-based membranes has extensively been studied for H_2S, organic sulfur compounds, CO, Cl, NH_3, H_2O, and for certain hydrocarbons. Inert gases such as Ar, N_2, and He are thought to have negligible poisoning effects, yet their presence in mixtures containing H_2 may lead to a decrease in H_2 flux due to mass transfer resistance in the gas phase. The actual syngas from coal includes the contaminants above mentioned but also: H_2S (0.2-1.3 %), COS (<0.1 %), NH_3+HCN (<0.3 %), C_2 hydrocarbons, poly aromatic hydrocarbons (PAHs), halides (such as CH3F, CH_3Cl at around 2 ppmv), heavy metals (such as Hg, Cd, Pb), tellurides (arsenides, selenium, antimony), alkalis metals (Na, K, Ca), phosphorous, and other unknown compounds. It is therefore essential to carry out permeation studies of composite Pd membranes in actual coal derived syngas.

Furthermore, large scale gas separation membrane modules under industrial conditions have not been reported in the literature. Large-scale membrane-based separation processes require high available surface area to achieve the desired fluxes. In order to reduce costs in membrane technology while maximizing the permeate flux, it is necessary to increase the surface area of the membranes to volume of the module holding them. Therefore, a multitube membrane unit maximizes the amount of membrane surface area that can be accommodated in a given volume such as in the case of hollow fiber membrane modules [16]. It is important to mention that a very limited number of tests have been demonstrated under realistic conditions and few multitube membrane modules have been presented in the literature for H_2 purification. For instance, Tosti et al [17] showed the design of a finger-like permeator tube reactor useful for ethanol reforming. The module was capable of producing 6 L min^{-1} of H_2 utilizing 19 Pd-Ag membranes with a thickness of 50-60 µm and a total surface area of 1490 cm^2. Diniz da Costa et al. [18] reported a Cobalt based-silica multitube membrane reactor. The module was used for the water-gas-shift reaction producing a H_2 purity of 98%. Notice that the produced H_2 flux and a total surface area of the module were not reported in the study. Parsley et al. [19] showed the evaluation of a carbon molecular sieve multitube membrane module for the separation of H_2 from actual coal derived syngas in water-gas-shift reaction. The module consisted of 86 tubes with a surface area of 7600 cm^2 and was capable of producing H_2 with 90% purity. Consequently, it is necessary to carry out the development of a multitube membrane module based on Pd and Pd-Alloy operated under actual industrial settings.

Worcester Polytechnic Institute (WPI) has developed during the last 20 years composite Pd and Pd/alloy H_2 separation membranes with high H_2 flux, excellent selectivity and long-term durability for membrane separation and reaction applications. The WPI membranes used in a natural gas reforming reactor were stable for over 6,000 hours (>8 months) at 500°C and 40 bar. Under the DOE H_2 Pathway Program (DE-FC-26-07NT43058), Pd membranes prepared by WPI exceeded the DOE 2015 targets for H_2 flux, selectivity and stability. Furthermore, the scalability of the WPI technology has been shown to be relatively easy and composite Pd/Cu, Pd/Au and Pd/Au/Pt alloy membranes have been shown to be sulfur resistant and permeance recoverable up to 100%. Furthermore, during Phase I of the project presented in this document, WPI optimized the fabrication of Pd and Pd/Au membranes and quantified their flux, selectivity stability, resistance to sulfur impurities and their characteristics in desulfurized syngas atmospheres from an actual coal gasifier at National Carbon Capture Center (NCCC) in Wilsonville, AL. During Phase II of this program, a multitube membrane module was tested under the same conditions as the single tube membranes in Phase I to produce large quantities of H_2. Furthermore, a numerical simulation was developed to optimize the performance of multitube membrane modules at large scale. Other studies of Phase II included testing the membranes developed at WPI under different reactions, and a comprehensive economical evaluation of Pd-based membrane technology under the presence of uncertainty.

2. OBJECTIVES

The objectives of the Phase I study were: (1) to assess for the first time the mechanical stability of 200 cm^2 highly structured composite Pd and Pd-Au membranes in an industrial environment with possible upset conditions due to system trips, rapid variations in feed flow, temperature and pressure, (2) to study hydrogen flux and hydrogen purity of Pd-based composite membranes in actual coal derived syngas and, (3) to assess the eventual poisoning and the recoverability of composite Pd membranes. Hence, six composite Pd-based membranes were prepared in facilities of WPI. Among the six prepared membranes, three composite Pd membranes were tested at the Center for Inorganic Membranes Studies (CIMS) (Worcester Polytechnic Institute, Worcester, MA) under pure H_2 atmosphere and also tested at the National Carbon Capture Center (NCCC) (Wilsonville, Al) in an actual coal derived syngas atmosphere. Upon testing, the three membranes were sent back to CIMS facilities and tested in pure H_2 for recoverability tests.

The specific objectives of the Phase II program were: (1) to design and construct a membrane separation module with the capacity of producing 15 - 20 lb per day of H_2, followed by validation and assessment of the design, membrane production methods and separation performance, (2) Installation of the H_2 separation membrane module at NCCC to conduct long term parametric testing, (3) Optimization of H_2 flux and recovery, (4) Development of a computational fluid dynamics (CFD) model and its experimental validation, (5) Measurements and improvement of membrane life, contaminant resistance, durability during system upsets, and operational limits including temperature, pressure difference across membrane, etc., and (6) Economic analysis based on test results by the end of Phase II and an estimate of costs for commercial equipment and membranes according to information provided in Attachment 2 of the solicitation. Hence, a seven tube membrane module was designed and tested at NCCC under similar conditions for the single tube module. A CFD model of the multitube module was developed to analyze and optimize the performance of the system. Additionally, the membranes developed were tested in different reacting conditions such as methane steam reforming, water gas shift and ethanol reforming. Finally, an economic performance assessment of Pd-based membrane technology embedded in different plants was studied under the presence of uncertainty inputs.

The groups involved in the project included:

Worcester Polytechnic Institute (WPI): Dr. Yi Hua Ma, Dr. Nikolaos K. Kazantzis, Dr. Anthony G. Dixon, Dr. Ivan P. Mardilovich, Dr. Bernardo Castro-Dominguez, Mr. Liang-Chih Ma (PhD Student), Ms. Rui Ma (PhD Student)

Membrane Technology and Research, INC. (MTR): Dr. Richard Baker, Dr. Jay Kniep

T3 Scientific LCC (T3): Dr. Chung-Yi A. Tsai, Dr. Siu-Yue Tam

Johnson Matthey Inc. (JM, UK): Hugh Hamilton, Suzanne Ellis, Xavier Quek

3. LITERATURE REVIEW

3.1. Hydrogen Transport Properties of Palladium

The permeation of hydrogen (H_2) through transition metals, known as platinum metals, was first observed with the experiment on homogeneous plates of platinum (Pt) and iron (Fe) by Deville and Troost in 1863 [20]. Three years later, Graham (1866) discovered the phenomenon of diffusion of H_2 through palladium (Pd) at elevated temperatures [21]. In light of his report, Pd could absorb up to 935 times its own volume of H_2 when it was cooled down from red heat. Since then, there has been a substantial expansion of research activity in the fields of Pd-H systems and Pd-based membranes for H_2 separation.

Diffusion of H_2 into Pd lattices can form an alloy of Pd with metallic H_2, usually called Pd hydrides. According to the Hume-Rothery rules, since the atomic radius of H (1.558 Å) and the atomic radius of Pd (1.375 Å) are very close, they are considered to form a solid solution [22]. In addition, atomic H is small enough to fit into interstitial positions of Pd, so that the Pd hydride is recognized as a kind of interstitial solid solution. To understand characteristics of the Pd-H system, studying the Pd-H phase diagram is a good way to illustrate them. Figure 3.1 shows the equilibrium solubility isotherms of PdH_n for the Pd-H system [23]. The original data was adapted from the research studies by Wicke and Nernst (1964) [24] and Frieske and Wicke (1973) [25] in which the molar H/Pd ratio (n) at different H_2 partial pressures of different isotherms were determined by means of magnetic susceptibility.

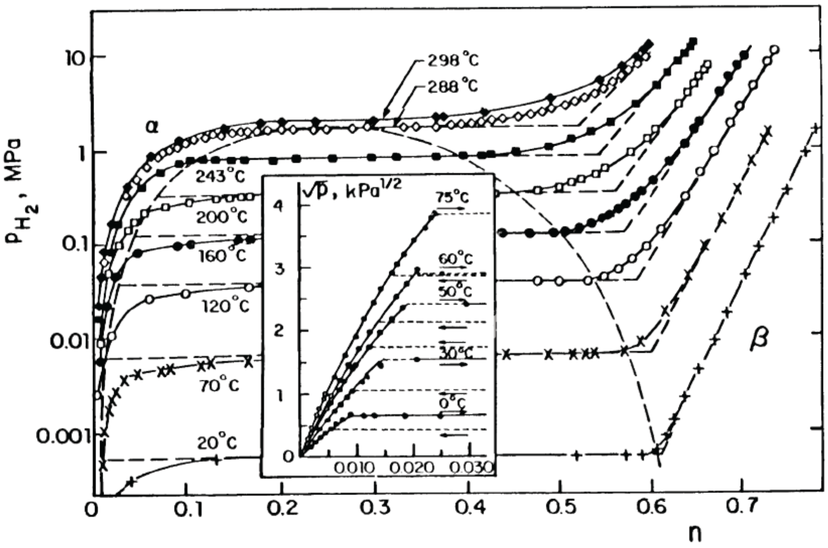

Figure 3.1. P-n-T phase diagram for the Pd-H system

The H_2 solubility, n (=H/Pd), is defined as the ratio of H atoms absorbed per Pd atom and is given as a function of H_2 partial pressure and temperature, shown in Figure 3.1. Normally, Pd hydrides containing less H with a smaller lattice parameter is called α phase, while Pd hydrides possessing more H with a larger lattice parameter is called β phase. Both phases have a face centered cubic (FCC) crystalline structure. Gillespie and Galstaun (1936) [26] found that there is a critical H_2 partial pressure (19.87 atm) and temperature (295.3°C) and corresponding n value (0.270) in the Pd-H phase diagram. Below the critical conditions, the Pd-H system exhibits a miscibility gap region where the two phases, α and β, would coexist with each other. In the miscibility gap region, H_2 solubility of each isotherm is independent of H_2 partial pressure, but dependent on the ratio of β phase to α phase, and as the H_2 solubility is given, the proportion of α phase or β phase can be determined by the level rule. In addition, several phase transformations between α and β in the immiscibility gap region would lead to severe deformation of Pd that is known as "H_2 embrittlement" [27]. The mechanism of H_2 embrittlement can be explained by lattice deformation after cycles of α and β phase transformation since the nucleation of the β phase with the larger lattice parameter from the α phase would induce lattice expansion and thereby impose strain in the lattice. Although the lattice of Pd would also expand beyond the miscibility gap region when loading H atoms, the change in lattice is gradual, rather than the abrupt change of phase transformation.

For the Pd membrane separation system, H_2 embrittlement would create microcracks on the membrane surface to lower the separation performance. Therefore, care is necessarily taken not to exceed the maximum H_2 partial pressure (P_{max}) of α phase at each given operating temperature in the miscibility gap region, above which the phase transformation would occur due to nucleation of β phase. The P_{max} of α phase depends on operating temperature, which can be described by Equation (3.1) [26]

$$\log(P_{\text{max}}) = 4.6018 - \frac{1877.82}{T} \tag{3.1}$$

Where P is in atm and T is in K. Alternatively, alloying Pd with other metals, such as Ag and Au, can reduce the critical temperature to diminish the area of the miscibility gap region due to higher H_2 solubility of Pd alloy, thereby reducing the probability of H_2 embrittlement.

The permeation behavior of H_2 through Pd membranes has been intensively investigated for many years, and it follows the multistep process called the "solution-diffusion mechanism." The solution-diffusion mechanism involved in H_2 transport from the high H_2 partial pressure side to the low H_2 partial pressure side is summarized in the following seven steps [28] and shown schematically in Figure 3.2:

(1) H_2 transport from the bulk gas to the gas layer nearby the membrane surface,
(2) reversible dissociative chemisorption of H_2 onto the membrane surface,
(3) reversible dissolution of atomic H from the surface into the bulk membrane,
(4) diffusion of atomic H through the bulk membrane,
(5) transition of atomic H from the bulk membrane to the surface on the low H_2 partial pressure side,
(6) recombinative desorption from the membrane surface,
(7) H_2 transport away from the membrane surface to the bulk gas.

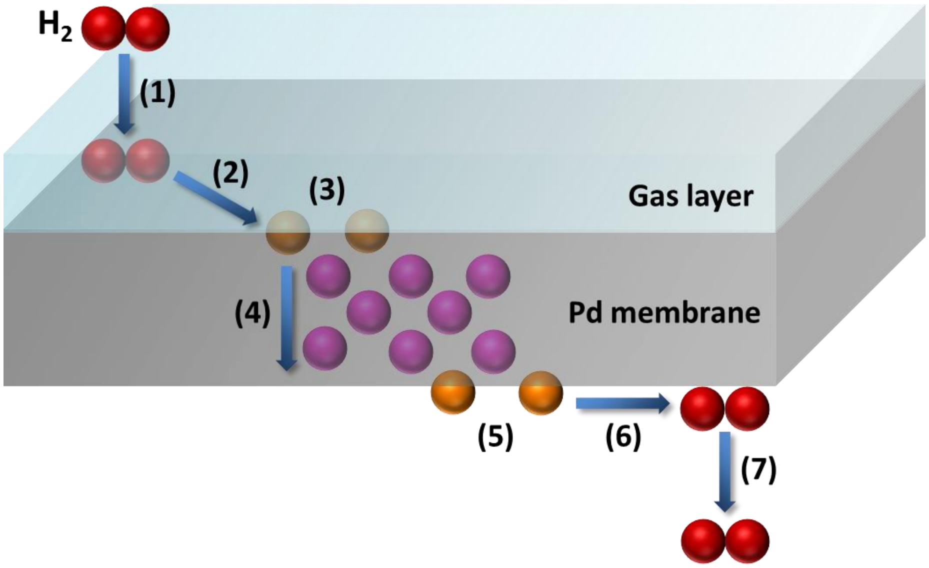

Figure 3.2. Schematic of H_2 permeation steps through as Pd membrane

It is well known that Sieverts' Law describes the solubility of a diatomic gas in metals which is proportional to the square root of the partial pressure of the gas in a thermodynamic equilibrium. Based on Sieverts' Law, the H_2 flux through the solution-diffusion mechanism can also be derived as a function of the difference of square roots of the H_2 partial pressure (Sieverts' equation), which is very significant for the prediction of the H_2 flux in practical applications. Therefore, to better understand the permeation behavior of H_2 through Pd membranes, studying the derivation of the Sieverts' equation may be a good way to illustrate it. First, regarding the H_2 flux through the Pd membrane governed by a dynamic equilibrium between desorption and adsorption, it can be expressed as the difference between the adsorption rate and the desorption rate, as shown in Equation 3.2:

$$J_{H_2} = k_d \cdot \theta^2 - k_a \cdot P_{H_2} \cdot (1-\theta)^2 \qquad (3.2)$$

where J_{H_2} stands for H_2 flux at the exit of diffusing H_2 with units of $m^3/(m^2\text{-h})$, P_{H_2} is the H_2 partial pressure with units of atm, and θ is the surface H_2 coverage. k_d and k_a are the rate constants of desorption and adsorption with units of $m^3/(m^2\text{-h-atm})$ and $m^3/(m^2\text{-h})$, respectively. In the adsorption-desorption process, due to the dissociative chemisorption of H_2, step (2), which enables only H_2 to be adsorbed onto the membrane surface and then to be dissociated into H atoms, Pd membranes have potentially infinite selectivity to H_2. Likewise, in the dissolution and transition processes, the H_2 flux through the Pd membrane at a dynamic equilibrium can also be expressed as the difference between the dissolution rate and the transition rate, as described in Equation 3.3:

$$J_{H_2} = k_o \cdot n_{H/pd} \cdot (1-\theta) - k_i \cdot (1 - n_{H/Pd}) \cdot \theta \qquad (3.3)$$

where k_o and k_i are the rate constants for the dissolution into membrane and the transition out of the membrane, respectively, in $m^3/(m^2\text{-h})$, and $n_{H/Pd}$ is the atomic H/Pd ratio expressed as the solubility of Pd. With regards to the diffusion of H atoms in the bulk membrane, the permeation flux at steady state can be depicted by Fick's Law as seen in Equation 3.4:

$$J_{H_2} = \frac{D}{\delta} \cdot (C_{ret} - C_{per}) \qquad (3.4)$$

where D is the H_2 diffusivity in m^2/s, δ is the thickness of Pd membrane in m, and C_{ret} and C_{per} are the H_2 concentration in the Pd sub-layers adjacent to the membrane surface at the retentate side and permeate side, respectively, in mol/m^3. Diffusion can be described by the "jump model" which states that H atoms jump between octahedral interstitial sites in the FCC Pd lattice [29]. The predictions of the jump model have been verified by quasielastic neutron scattering, and found that the average jump distance is a/√2 where a is the lattice parameter. In Equation 3.3, the concentration of H_2 can be expressed as the product of the atomic H/Pd ratio and the H_2 solubility coefficient, κ, with the unit of mol/m^3, as described in Equation 3.5.

$$\mathrm{C} = \kappa \cdot \mathrm{n_{H/Pd}} \tag{3.5}$$

The physical meaning behind the κ is the H_2 concentration in the Pd sub-layers at $\mathrm{n_{H/Pd}}$ value equal to 1, and is not to be confused with the H concentration. After substitution of Equation 3.5 into Equation 3.4, Equation 3.6 can be obtained in the following:

$$\mathrm{J_{H_2}} = \frac{\mathrm{D} \cdot \kappa}{\delta} \cdot (\mathrm{n_{H/Pd,ret}} - \mathrm{n_{H/Pd,per}}) \tag{3.6}$$

Considering the rate-limiting step, Ward and Dao (1999) [28] observed that the diffusion-limited permeation is expected for clean Pd membranes with the thickness of 1 μm or greater in the absence of external mass transfer resistance at above approximately 300°C. Under these conditions, the Pd structure is in α phase, so that the H/Pd ratio can be assumed to be very small ($\mathrm{n_{H/Pd}} \ll 1$), and the term $(1 - \mathrm{n_{H/Pd}})$ in Equation 3.3 can be neglected. Since diffusion is rate-limiting, both the adsorption-desorption process and the dissolution-transition process are at an equilibrium state; thereby the overall rates of adsorption and dissolution (Equation 3.2 and 3.3) are approaching zero, as depicted in Equation 3.7:

$$\mathrm{J_{H_2}} = \mathrm{k_d} \cdot \theta^2 - \mathrm{k_a} \cdot \mathrm{P_{H_2}} \cdot (1-\theta)^2 = \mathrm{k_o} \cdot \mathrm{n_{H/Pd}} \cdot (1-\theta) - \mathrm{k_i} \cdot \theta = 0 \tag{3.7}$$

After transposition of the formula, the ratio between θ and $(1-\theta)$ can be expressed by Equation 3.8:

$$\frac{\theta}{(1-\theta)} = \sqrt{\frac{\mathrm{k_a} \cdot \mathrm{P_{H_2}}}{\mathrm{k_d}}} = \frac{\mathrm{k_o} \cdot \mathrm{n_{H/Pd}}}{\mathrm{k_i}} \tag{3.8}$$

Solving Equation 3.8 for $\mathrm{n_{H/Pd}}$, the mathematical relationship between the H/Pd ratio and the H_2 partial pressure can be obtained in Equation 3.9, where $\mathrm{n_{H/Pd}}$ is proportional to the square root of the H_2 partial pressure as shown graphically in the α region of Figure 3.1. It can also be found that Equation 3.9 is equivalent to Henry's Law and is therefore only valid for the low atomic H/Pd ratio domain.

$$\mathrm{n_{H/Pd}} = \frac{\mathrm{k_i} \cdot \mathrm{k_a}^{0.5}}{\mathrm{k_o} \cdot \mathrm{k_d}^{0.5}} \mathrm{P_{H_2}^{0.5}} \tag{3.9}$$

Additionally, Equation 3.9 also indicates that the Sieverts' constant, $\mathrm{K_s}$, is actually the equilibrium constant for the adsorption-desorption process and the dissolution-transition process, as depicted in Equation 3.10:

$$\mathrm{K_s} = \frac{\mathrm{k_o} \cdot \mathrm{k_d}^{0.5}}{\mathrm{k_i} \cdot \mathrm{k_a}^{0.5}} \tag{3.10}$$

where $\mathrm{K_s}$ has the unit of atm$^{0.5}$, and the value of $\mathrm{K_s}$ for various temperatures can be determined by calculating slopes of isotherms in the low atomic H/Pd ratio domain of Figure 3.1.

From the thermodynamics point of view, the Sieverts' constant is dependent on temperature and can be expressed as a function of temperature in the Arrhenius relation:

$$K_s = \exp\left(\frac{\Delta S_{H_2}}{2R}\right)\exp\left(-\frac{\Delta H_{H_2}}{2RT}\right) \tag{3.11}$$

In Equation 3.11, $\Delta H_{H_2}$is the heat of desorption in J/gmol and $\Delta S_{H_2}$is the entropy of desorption in J/gmol-K. Note that both are based on H_2. Therefore, the standard values of ΔH_{H_2} and ΔS_{H_2}can be determined from Equation 3.11. By the substitution of Equation 3.9 and 3.10 into Equation 3.6, the Sieverts' equation is derived as shown in Equation 3.12, which indicates that the permeation flux of H_2 is linearly dependent on the difference of square roots of the H_2 partial pressure at a given temperature.

$$J_{H_2} = \frac{D \cdot \kappa}{K_s \cdot \delta} \cdot (P_{H_2,ret}^{0.5} - P_{H_2,per}^{0.5}) \tag{3.12}$$

According to assumptions made before, it should be noted that the Sieverts' equation is only valid at low H concentration in the bulk Pd and when diffusion is the rate-limiting step in the whole permeation process. In Equation 3.12, the H_2 solubility (S) is defined as the ratio of the solubility coefficient to the Sieverts' constant (κ/K_s) with units of mol/(m^3-atm$^{0.5}$). Both D and S are dependent on temperature, and they can be expressed as Arrhenius equations, as seen in Equation 3.13 and 3.14:

$$D = D_0 \cdot \exp\left(\frac{-E_D}{R \cdot T}\right) \tag{3.13}$$

$$S = S_0 \cdot \exp\left(\frac{\Delta H_s}{R \cdot T}\right) \tag{3.14}$$

Here E_D is the activation energy for H_2 diffusion in J/gmol, and ΔH_s is the enthalpy of H_2 dissolution in J/gmol. R and T stand for gas constant in J/(gmol-K) and temperature in K, respectively. D_0 and S_0 are constants for the H_2 solubility and the H_2 diffusivity, respectively. Furthermore, since the H_2 permeability, Q, is defined as the product of D and S, a similar temperature dependent expression for Q can be derived in Equation 3.15:

$$Q = D \cdot S = Q_0 \cdot \exp\left(\frac{-E_Q}{R \cdot T}\right) \tag{3.15}$$

where Q_0, the product of D_0 and S_0, stands for the permeability constant, and E_Q, the sum of E_D and ΔH_s, stands for the activation energy for H_2 permeability in J/gmol, After substitution of Equation 3.15 into Equation 3.12, the expression for J_{H_2} in terms of Q can be yielded:

$$J_{H_2} = \frac{Q}{\delta} \cdot (P_{H_2,ret}^{0.5} - P_{H_2,per}^{0.5}) \tag{3.16}$$

From Equation 3.16, the H_2 flux is proportional to the reciprocal of membrane thickness. However, due to non-uniformity of support surface and membrane deposits, it is very hard to measure and get the accurate value of membrane thickness. Therefore, for the convenience to describe the permeation behavior of Pd membranes, the H_2 permeance, F, defined as Equation 3.17, is used in most practical cases.

$$F = \frac{Q}{\delta} = \frac{J_{H_2}}{(P_{H_2,ret}^{0.5} - P_{H_2,per}^{0.5})} \tag{3.17}$$

Through H_2 permeation experiments with Pd membranes, it has been found that the H_2 pressure exponent (generally referred to as the n-value) in Equation 3.6 may deviate from 0.5, since the Sieverts' equation becomes invalid [30,31,32,33]. Based on assumptions made before for the derivation of Sieverts' equation (Equation 3.16), this correlation is only valid at low H_2 partial pressure conditions and when H_2 diffusion in Pd membranes is rate-limiting; otherwise, the term $(1 - n_{H/Pd})$ cannot be neglected in Equation 3.3, and both the adsorption-desorption process and the dissolution-transition process will not reach an equilibrium state to make Equation 3.7 valid, thereby causing an n-value deviating from 0.5.

Collins and Way [31] observed that the n-value would deviate from 0.5 and decrease from 0.602 to 0.566 with higher temperatures (550 to 600°C) for the pure Pd film on the ceramic support characterized at the pressure difference of 15 bar. It was supposed that H_2 diffusion may not be the rate-limiting step since surface contaminants initially present on the membrane surface may affect H_2 solubility of the membrane surface. Additionally, both H_2 solubility and H_2 diffusivity are dependent on temperature and influence n-values, so that n-values may depend on temperature. In addition, Morreale et al. [32] found that the n-value of the Pd membrane characterized at the high pressure (27.6 bar) would deviate from 0.5. They suggested that the H_2 diffusivity may be enhanced by high pressures, and the Sieverts' constant would also have been influenced by high pressure since a non-ideal solution would be formed by an increased concentration of H atoms within Pd lattice, in which attractive forces may be exhibited between dissolved H atoms. Thus, H_2 diffusion may not be the rate-limiting step to affect the n-value.

Another circumstance that prevents H_2 diffusion from being rate-limiting occurs when the thickness of Pd membranes is extremely thin, since H_2 diffusivity may approach or exceed the adsorption rate or absorption rate. Thereby the adsorption or the absorption becomes the rate-limiting step. According to the H_2 permeation mechanism proposed by Ward and Dao (1999) to determine the minimum thickness of Pd membranes at which the n-value would deviate from 0.5, it was found that when the thickness of Pd membranes was below 1 µm, the H_2 adsorption would become the rate-limiting step and dominate the whole permeation process to cause the deviation of the n-value from 0.5. Zhao et al. [34] observed that for the Pd membrane with the thickness below 1 µm, the H_2 flux was a function of transmembrane H_2 partial pressure but not the square root of transmembrane H_2 partial pressure, which is consistent with the calculation results by Ward and Dao [28]. Wu et al. [35] also reported that the n-value of extra-thin membrane (0.3-0.4 µm) would approach 1 since the H_2 permeation was mainly controlled by the surface process instead of the H_2 diffusion. On the other hand, when the Pd membrane contains pinholes or cracks, the solution diffusion mechanism is no longer the only possible way for H_2 permeation through the membrane, since H_2 would also pass through the membrane by these pinholes or cracks. The H_2 transport behavior through pinholes or cracks incorporates the Knudsen diffusion and the viscous flow, and can be described by the dusty-gas model, as seen in Equation 3.18 [36]:

$$J = \left(\alpha + \beta \cdot P_{avg}\right) \cdot \Delta P = \left\{\frac{2}{3} \cdot \sqrt{\frac{8}{\pi}} \cdot \frac{\varepsilon \mu_k d}{\delta \sqrt{RTM}} + \frac{1}{8} \cdot \frac{\varepsilon \mu_v d^2}{\delta \eta RT} \cdot P_{avg}\right\} \cdot \Delta P \tag{3.18}$$

where $\alpha \cdot \Delta P$ is the Knudsen diffusion, $\beta \cdot P_{avg} \cdot \Delta P$ is the viscous flow, μ_k and μ_v are the Knudsen and the viscous geometric factor coefficients, respectively, P_{avg} is the average pressure of the retentate side pressure and the permeate side pressure in bar, ε is the porosity, d is the pore diameter in m, M is the gas molecular weight in g/mol, and η is the gas viscosity in Pa·s. More detailed information about the dusty-gas model was presented by Mason et al. [37].

According to Equation 3.18, when the Pd membrane is characterized under the pure H_2 atmosphere and the Knudsen diffusion or the viscous flow dominates the H_2 permeation process, the H_2 flux would depend on the pressure difference rather than the difference of square roots of the pressure. Guazzone et al. [33] investigated the relationship between the n-value and the H_2/He selectivity of the Pd membrane and found that the n-value declines with increasing the H_2/He selectivity, and the n-value would approach 0.5 when selectivity is higher than 400, as shown in Figure 3.3. The effect of selectivity on the n-value was evidenced by their experimental results that the n-value was as high as 0.75 at 500°C for the Pd membrane with the selectivity much lower than 400.

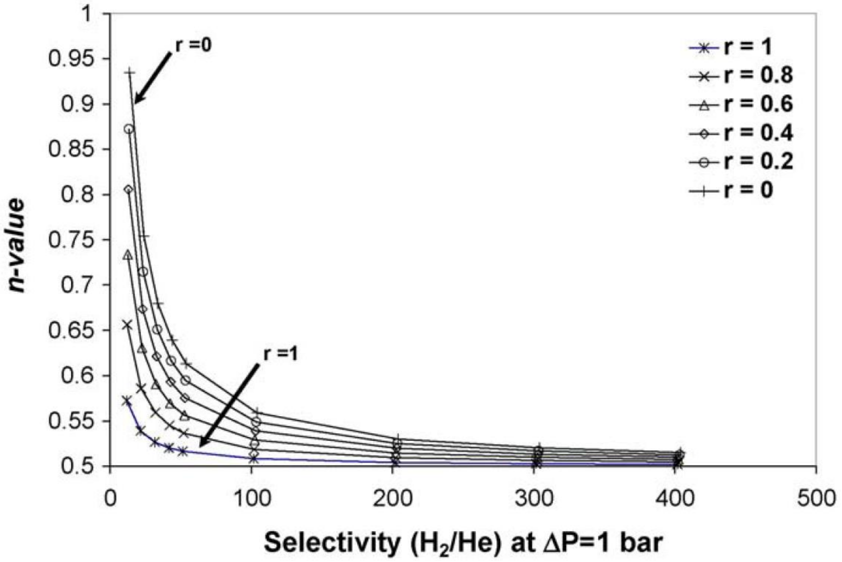

Figure 3.3. The n-value as a function of selectivity for various values of r (ratio of the contribution of the Knudsen diffusion to the overall leak). The figure was taken from Guazzone et al. [33].

In the case of composite Pd membranes, the significant mass transfer resistance of the support may also influence the H_2 permeation, causing the deviation of the n-values. The reason can be explained by the concept of mass transfer resistances (R) in series in the composite Pd membrane described by Equation 3.19 [38]:

$$R_{total} = \frac{1}{F_{overall}} = \frac{\delta_{overall}}{Q_{overall}} = R_1 + R_2 + R_3 + \cdots \approx \frac{\delta_1}{Q_1} + \frac{\delta_2}{Q_2} + \frac{\delta_3}{Q_3} + \cdots \tag{3.19}$$

It should be noted that subscripts 1, 2, and 3 refer to respective layers in the composite membrane. From Equation 3.19, it is clear that the overall mass transfer resistance for H_2 permeation is the sum of the resistance of each layer in the composite membrane. According to Equation 3.19, the mass transfer resistance contributed by the layer with an extremely small thickness or an exceedingly high permeability, in relation to other layers, can be neglected when added to the overall mass transfer resistance. Typically, even though the thickness of the Pd membrane is much smaller than that of the porous support, the mass transport resistance of porous support is often negligible since the permeability of porous support is extremely high compared to that of the Pd membrane. However, in some cases, the significant support resistance by lower permeability may have contributed to the overall mass transfer resistance to affect the H_2 permeation behavior. As the result, the Sieverts' equation becomes invalid and the n-value deviates from 0.5. It is evidenced by Guazzone et al. [33] that the n-value higher than 0.5 was found for the composite Pd membrane with the low-permeability support. In addition, the activation energy of the overall H_2 permeability is also a useful indication to describe the support resistance. Collins and Way [31] reported that the deviation of the n-value from 0.5 to 0.573 may be attributed to the higher activation energy for H_2 permeation through the composite Pd membrane, compared to pure Pd membranes, implying that the significant support resistance existing in the composite membrane would lead to the deviation of the n-value.

3.2. Palladium Alloys

Alloying of Pd with other metals provides a promising way to modify its physical and chemical properties and reduce membrane cost for different demands. To minimize the probability of H_2 embrittlement, Hunter [39] found that Pd/Ag alloys containing 20 wt% Ag or more can prevent H_2 embrittlement after 30 cycles of heating and cooling in H_2 atmosphere. The superior mechanical stability of Pd/Ag alloys to withstand temperature cycling can be contributed to suppression of the α to β phase transformation [40]. Pd/Ag alloys with higher H_2 solubility can reduce the critical temperature and pressure for phase transformation and, thereby, inhibit the α to β phase transformation during the heating and cooling. The lower critical temperature and pressure of Pd/Ag alloys can be illustrated by the equilibrium solubility isotherms in the Pd/Ag alloy system [41]. Thus, alloying of Pd with Ag is an effective way to protect the membranes from H_2 embrittlement. Another aspect of Pd membranes that can be improved by alloying Pd is H_2 permeability. The relative H_2 permeability of Pd alloys to Pd at 350°C and 500°C is shown in Figure 3.4 [12,42]. Based on the H_2 transport mechanism, the H_2 permeability, Q, is the product of the H_2 diffusivity, D, and the H_2 solubility, S. Both D and S are dependent on temperature and can be expressed by the Arrhenius equation.

In the Pd/Ag alloy system, the D decreases with increasing the Ag content [43,44]. However, the S of Pd alloys is enhanced by the Ag addition, and the peak of S occurs as the Ag content is about 30 wt% Ag. As a consequence, the Q, which is product of D and S, is largely enhanced by alloying with Ag due to the S of Pd/Ag alloys, and the highest Q of the Pd/Ag alloy foil is measured with a composition of 27 wt% Ag [43]. Similar to Pd/Ag alloys, Pd/Au alloys with higher H_2 permeability can also be explained by the higher S resulting from alloying with Au. Contrary to Pd/Ag and Pd/Au alloys, both the D and the S in the Pd/Cu system are reduced to a low value on alloying with Cu; however, it is found that H_2 permeability would pass through a peak as the Cu content is near 40 wt% Cu [45]. This peak in H_2 permeability is associated with the ordered body centered cubic (BCC) β phase in Pd/Cu alloys. When the composition of Pd/Cu alloys contains about 40 wt% Cu, the disordered FCC α phase would be changed to form the ordered BCC β phase with the higher D, and, thereby, H_2 permeability would be raised by the increase in the DS product. Consequently, it is considered that phase transformation to improve D through alloying Pd with Cu is another effective way to enhance H_2 permeability.

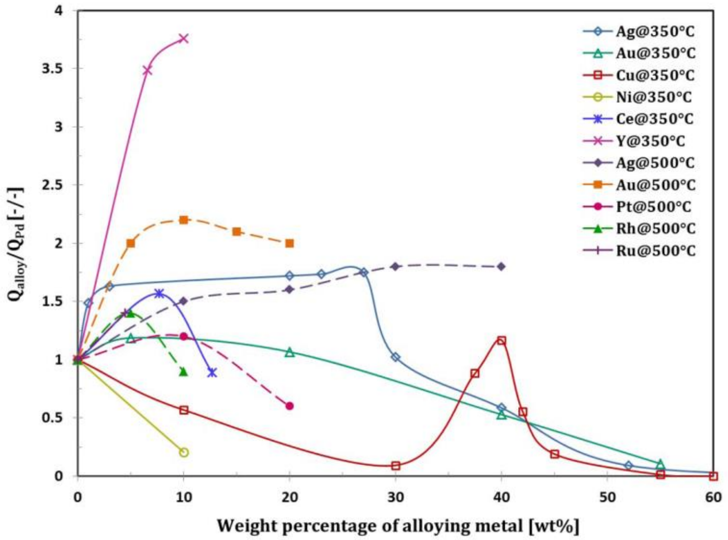

Figure 3.4. Relative permeability between Pd alloy and Pd with various alloying metal contents.

Beyond the H_2 embrittlement and H_2 permeability, mechanical strength of Pd-based membranes is also significant when they are applied in the H_2 separation apparatus. Pd-based membranes with higher mechanical strength would possess better durability under elevated temperature and pressure conditions, which can not only raise the efficiency of separation performance but also extend the membrane lifetime to reduce cost. Thus, the attempt to improve mechanical strength of membranes is justified. In the Pt/Pd alloy system, it has been shown that the ultimate tensile strength is enhanced with increasing the content of Pt [46]. Berseneva et al. [46] observed that the ultimate tensile strength of Pt/Pd alloys is proportional to the dissolution content of H atoms; however, for $Pd_{95}Pt_5$ and $Pd_{85}Pt_{15}$ alloys, there is drop in the ultimate tensile strength when the dissolution content of H_2 exceeds a certain value. This is due to the fact that the α phase of Pt/Pd alloys has been completely transformed to the β phase with the higher lattice constant when Pt/Pd alloys dissolve enough H atoms, and, thereby, the large increase in the lattice constant would cause the drop in the ultimate tensile strength. Therefore, in order to take advantage of strengthening in the ultimate tensile strength by alloying Pt to Pd, an appropriate operation condition should be considered.

Pd alloys have received significant attention due to, not only their outstanding H_2 permeability and mechanical strength, but also their superior chemical stability to resist sulfur poisoning when used in natural gas reforming processes. Morreale et al. [47] showed that only Pd/Cu alloys with FCC crystalline phase have the capability to resist H_2S poisoning in the H_2 atmosphere with the presence of 1000 ppm H_2S. They found that FCC $Pd_{70}Cu_{30}$ membranes exhibited 0-10% declines in the H_2 permeance under different temperature conditions, from 623K to 1000K, while BCC $Pd_{60}Cu_{40}$ membranes show a steep drop in the H_2 permeance. It was suggested that surface structure or surface chemistry of FCC crystalline phase is responsible for the H_2S poisoning resistance. . To understand H_2 permeance behavior of BCC Pd/Cu alloys under the same H_2S condition, Pd/Au alloys also have been extensively studied for H_2S poisoning resistance. McKinley and Nitro [7] observed that a Pd/Au alloy membrane containing 40 wt% Au just has a 21% decline in H_2 permeance when exposed to 4 ppm H_2S in H_2 atmosphere in 6 days, while a pure Pd membrane has 71% decline in H_2 permeance. Way et al. [48] characterized a Pd/Au alloy membrane containing 15 wt% Au under the WGS syngas (51 mol% H_2, 26 mol% CO_2, 21 mol% H_2O, and 2 mol% CO) at 400°C, and observed that Pd/Au alloy membranes can sustain 65% H_2 permeability when exposed to 5 ppm H_2S in WGS syngas. Within the above context, Pd alloys have many advantages over pure Pd, including minimization of the probability of H_2 embrittlement, enhancement of H_2 permeability, improvement of mechanical strength, and exhibition of superior chemical stability to resist H_2S poisoning. Therefore, the method of alloying Pd with other metals indeed plays an indispensable role in the development of Pd-based membrane technology for H_2 separation.

3.3. Catalytic Membrane Reactors (CMRs)

Process intensification refers to how to enhance a reactant's conversion of reversible reactions to generate more products. It is a significant challenge due to the limitation imposed by the thermodynamic equilibrium. Generally, changing reaction conditions such as pressure and temperature is one possible way to achieve this goal. Alternatively, by changing the composition at the reaction zone, it is possible to operate beyond the conventional chemical equilibrium as supported by Le Chatelier's principle. The membrane reactor technology is a typical approach to improve reactant conversion by the removal of product. The application of membrane reactor technology for a shift of the chemical equilibrium towards the product of interest was first proposed by Gryaznov and his coworkers in 1970 [107]. They performed dehydrogenation reactions in Pd/alloy membrane reactors in order to improve the overall conversion of cyclohexane. In the past decade, there have been extensive studies on the Pd-based membrane reactor used for H_2 production since an increasing interest into H_2 as a clean energy carrier.

According to the International Union of Pure and Applied Chemistry (IUPAC) definition, a membrane reactor is a device which incorporates the membrane separation process and the chemical reaction step; thus, the separation and the chemical reaction can be carried out simultaneously in a single unit. Furthermore, based on the membrane function, membrane reactors can be classified into several categories [23,49,50]. Generally speaking, when the membrane reactor is used for performing a catalyst reaction, and the membrane act as a catalyst and a permselective barrier, this kind of reactor is referred to as the catalytic membrane reactor (CMR). If the membrane is only permselective to certain species without any catalyst function, it would be referred to as the inert catalytic membrane reactor (ICMR). On the contrary, when the membrane only acts as a catalyst without any permselectivity, it would be referred to as the non-permselective catalytic membrane reactor (NCMR). In addition, according to different types of catalyst bed, both CMR and ICMR can be further divided into the packed bed catalytic membrane reactor (PBCMR), the fluidized bed catalytic membrane reactor (FBCMR), the packed bed inert catalytic membrane reactor (PBICMR), and the fluidized bed inert catalytic membrane reactor (FBICMR).

Regarding the Pd-based membrane reactor used for H_2 production, the Pd-based membrane is incorporated with the packed bed reactor and only permselective to H_2, so that the membrane reactor can be referred to the PBICMR. In this study, in order to simplify the expression of the Pd-based PBICMR, the term "Pd-based CMR" is used. The principle of the Pd-based CMR used for H_2 production is illustrated in Figure 3.5, in which the Pd-based membrane extends along the reactor and is in contact with the reactants and the catalyst (MSR catalysts or WGS catalysts). The product H_2 is continuously removed from the retentate side by the Pd-based membranes, thereby overcoming the limitation imposed by the thermodynamic equilibrium to enhance the overall conversion.

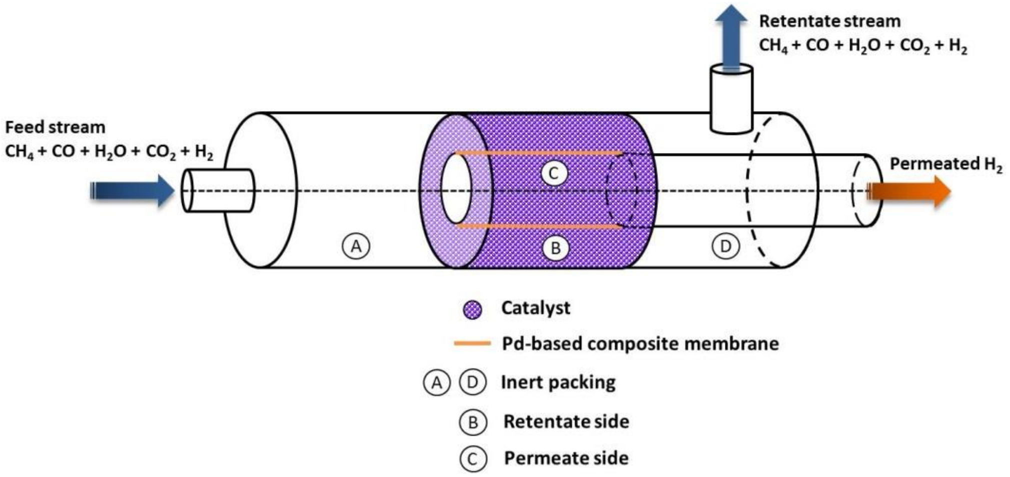

Figure 3.5. Schematic diagram of the Pd-based CMR used for H_2 production.

3.4.1 Application of CMRs in the Generation of H_2

a) Hydrogen from Natural Gas

Natural gas reforming also named methane steam reforming (MSR) is a well-established production method that currently generates 95% of hydrogen in the U.S. [51]. Conventionally, this reaction is carried out at high temperatures (700-1000°C) and mild pressures (3-25 bar) which results in the production of CO and H_2 with little CO_2 as byproduct. Carbon monoxide is reacted downstream in two, high- and low-temperature, water-gas-shift (WGS) reactors to further generate H_2 and CO_2. Equations 3.20-3.22 show both chemical reactions where MSR is highly endothermic while WGS is exothermic. After reaction, the purification of H_2 is traditionally carried out in a pressure swing adsorption (PSA) unit. Notice that in the conventional process, both MSR and WGS reactions are limited by their thermodynamic equilibrium when carried out in customary packed bed reactors (PBRs).

MSR $$CH_4 + H_2O \leftrightarrow CO + 3H_2 \tag{3.20}$$

WGS $$CO + H_2O \leftrightarrow CO_2 + H_2 \tag{3.21}$$

MSR $$CH_4 + 2H_2O \leftrightarrow CO_2 + 4H_2 \tag{3.22}$$

The application of membrane technology is economically attractive since it helps to reduce the number and size of equipment units needed, while simultaneously enhancing chemical conversions. Palladium-based membranes have shown to be the best candidates for their implementation in these processes since they can isolate hydrogen from gas mixtures at large quantities and high purities while maintaining high stability and robustness. In the case of CMR technology, the literature has shown membrane application up to a pilot-scale magnitude [50], as shown in Table 3.1. Palladium membranes are capable of operating at temperatures between 300-600°C, matching the temperatures of high-temperature-WGS catalysts (310-450°C). A low-temperature-WGS unit is no longer needed, since high CO conversions can be achieved through a single CMR unit. Furthermore, the effect of process intensification in MSR, allows operating this process at mild temperatures (Table 3.1) while maintaining high conversions, preventing coking and reducing the CO yield. The experimental tests shown in the literature demonstrate the effect of process intensification; nevertheless, the scale of operation is irrelevant for the industrial deployment of this technology. Patrascu et al. [52] showed the performance of methane steam reforming (MSR) in a large scale CMR achieving a permeate flux of 1.6 NL/min at a temperature of 525°C and a pressure of 10 bar and utilizing membrane with a surface area of the 175 cm^2. Furthermore, economically, CMR technology has shown success while integrated in power and hydrogen production plants. Kazantzis et al. reported the specific market and regulatory conditions under which Pd-based CMRs can be successfully integrated in the pertinent energy systems [53,54].

Regarding factors that affect the CH_4 conversion in the Pd-based CMR, Kikuchi [55] observed that the CH_4 conversion strongly depends on the H_2 permeance of Pd-based membranes. In other words, the higher the value of H_2 permeance, the higher the level of CH_4 conversion. Thus, reducing the membrane thickness and improving the permeability of membranes by alloying Pd with other metals or increasing operating temperatures are two possible ways to further enhance the CH_4 conversion in the Pd-based CMR. Another factor that affects the performance of CMRs is the presence of sweep gas. There are two primary effects of the sweep gas on CH_4 conversion in the Pd-based CMR. The first is that the higher flow rate of the seep gas would lead to the higher CH_4 conversion by increasing the driving force for H_2 permeation; the other is that the degree of the CH_4 conversion is also dependent on the type of sweep gas. Gallucci et al. (2004) reported that the highest CH_4 conversion is obtained when O_2 is used as sweep gas. This is because H_2 would be consumed at the permeate side by the chemical reaction with O_2, thereby increasing the driving force for H_2 permeation. However, from an industrial point of view, the use of steam as the sweep gas is better than that of O_2 when considering H_2 consumption by the chemical reaction with O_2 as well as H_2 separation from the H_2/H_2O mixture.

The feed composition and the feed flow rate also impose great influence on the CH_4 conversion. Nam et al. [56] showed that CH_4 conversion declines with increasing the feed flow rate, and especially increasing the feed flow rate in the presence of sweep gas, the degree of reduction in the CH_4 conversion is more apparent. This is due to the decrease in the magnitude of the equilibrium shift by reducing the fraction of H_2 removed from the retentate side via permeation at the same membrane capacity. Tong et al. [57] observed that CH_4 conversion would monotonically increase with the value of H_2O/CH_4 ratio in the traditional MSR reactor, in agreement with thermodynamic equilibrium calculation. For Pd-based CMR, the same monotonic increase in CH_4 conversion is also found. However, an excess of steam would dilute the H_2 concentration in the rententate side to lower the driving force for H_2 permeation. On the contrary, carbon may be formed in the system to reduce the reforming efficiency and the separation performance when the amount of steam in feed is insufficient. According to the report of Laegsgaard Jorgensen et al. [58], a H_2O/CH_4 ratio higher than 2.5 is enough to prevent carbon formation on the Ni-based catalyst and the Pd-based membrane surface.

b) Hydrogen from Coal

Coal gasification is another major method for H_2 production, contributing approximately to one-fifth of global H_2, as indicated in Figure 3.6. In the H_2 production process based on coal gasification, CO in syngas generated from the coal gasifier, reacts with steam in shift reactors to produce H_2 by the water gas shift (WGS) reaction. Due to the low CO conversion and severe operation conditions required in the conventional shift reactor, Pd-based CMR has received great interest for application in the coal gasification system for H_2 production. Today, many beneficial advantages exhibited by the application of the Pd-based CMR, compared to the conventional shift reactor, for the WGS reaction process can be found in different papers in the literature.

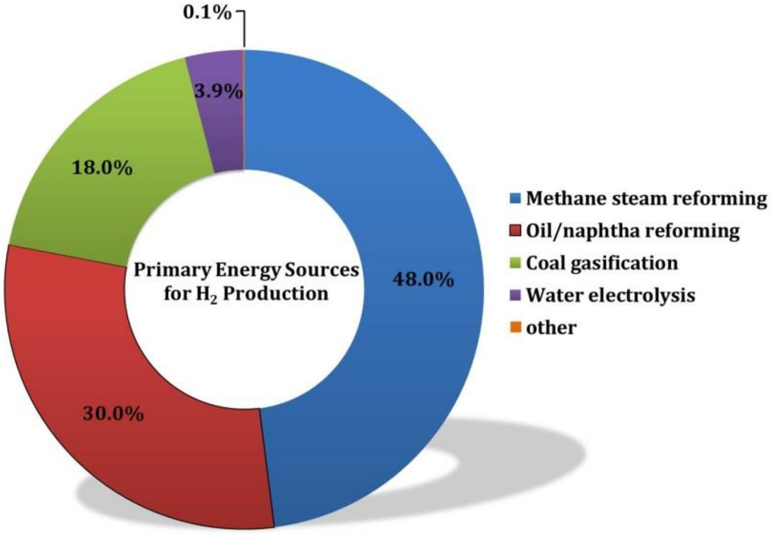

Figure 3.6. Share of primary energy sources for H_2 production.

Kikuchi et al. and Uemiya et al. [55] performed WGS experiments using Fe_2O_3/Cr_2O_3 as a catalyst in Pd-based CMR technology. The Pd membrane (20 μm thick) used in their studies was deposited on the porous glass tube by the electroless plating method. According to the Kikuchi et al. [55], 98% CO conversion, against 78% equilibrium conversion for the closed system, can be achieved by the use of Pd-based CMRs under optimal operating conditions: 400°C system temperature, 5 atm reaction pressure, equimolar ratio of H_2O and CO in the feed, 50 ml/min feed flow rate of H_2O/CO mixture, 400 ml/min sweep Ar flow rate, and 1 atm permeate pressure. In addition, they observed that the CO conversion increases with increasing value of the time factor (W/F), which was defined by the weight of catalyst (W) and the feed flow rate of CO (F). This is due to the higher H_2 permeation rate attained at higher values of W/F by increased contact between H_2 and the Pd membrane. Enhancing the driving force for the H_2 permeation rate by increasing the pressure difference between the retentate and the permeate side would improve the CO conversion.

In the study by Uemiya et al. [70], it was observed that higher H_2O/CO molar ratios would result in higher CO conversion in the Pd-based CMR, similar to a conventional shift reactor. However, the Pd-based CMR gave the same level of CO conversion at a H_2O/CO molar ratio of 1, which was obtained at a H_2O/CO molar ratio of 2 in a conventional shift reactor. From an economics viewpoint, the less steam required in the Pd-based CMR to achieve reasonable conversion levels would lead to lower costs of H_2 production. Additionally, based on the one-dimensional steady state model developed by Uemiya et al [70], both lowering the thickness of Pd membranes and increasing the sweep Ar flow rate in the permeate side would further enhance the CO conversion by increasing the H_2 permeation. Basile et al. [59] performed WGS experiments over a Cu-based catalyst in the Pd-based CMR using 0.2 μm thick Pd membrane that was deposited on the porous ceramic tube (γ-Al_2O_3/α-Al_2O_3) by the co-condensation method. They experimentally demonstrated that a maximum CO conversion of 98.89% can be achieved under 322°C and 1.12 bar using a counter-current sweep N_2 at a flow rate of 28.2 ml/min and a H_2O/CO molar ratio of 3.86 in the feed H_2O/CO mixture. They pointed out that their operation condition is milder than that in the report by Uemiya et al. [70], to obtain the same level CO conversion in the WGS reaction, showing considerable improvements achieved by the use of ultrathin Pd membrane. Besides, they found that there is an optimum operating temperature for the maximum CO conversion at specific experimental conditions. The maximum value of CO conversion can be considered as a compromise between the thermodynamic considerations for the exothermic WGS reaction (which is favored at low temperature) and the kinetic rate of the reaction (which increases with increasing temperature). On the other hand, they also studied the effect of feed composition on the CO conversion in the Pd-based CMR. It was shown that other gases, including H_2, CO_2 and N_2, appearing in the feed would lower the H_2 partial pressure in the retentate side to reduce the driving force for H_2 permeation, resulting in lower CO conversion in the Pd-based CMR. Moreover, the CO partial pressure decreased by other gases in the feed stream would give a lower kinetic rate for the WGS reaction, thereby reducing the CO conversion.

Criscuoli et al. [60] used a pure Pd membrane with a thickness of 70-75 μm in the Pd-based CMR to carry out WGS experiments over a Cu-based catalyst for three different feed mixtures. According to their report, the CO conversion strongly depends on the feed composition. It was experimentally demonstrated that the highest conversion is obtained when the feed composition approaches to the thermodynamically more favorable one. In comparison with a conventional fixed bed reactor and a mesoporous membrane reactor (in which membranes have pores distributions from 0.2 to 12 μm), only the CO conversion obtained in the Pd-based CMR is higher than the equilibrium conversion, showing the excellent performance of the Pd-based CMR used for the WGS reaction process.

Regarding the study of the Pd-based CMR using Pd alloy membranes for carrying out the WGS reaction, Basile et al. [60] experiments with cold rolled Pd membranes (70 μm) and the cold rolled Pd/Ag alloy membranes (50 μm) supported on porous ceramic tubes. In this study, the Cu-based catalyst was employed for the WGS experiment. They found that the CO conversion obtained in the Pd-based CMR using the Pd/Ag alloy membrane is higher than that using pure Pd membrane under same experimental conditions. It may be attributed to the higher H_2 permeability of Pd/Ag alloy membranes that removes more H_2 from the retentate side to thereby give higher CO conversion. In addition, it was pointed out that if the H_2 permeation rate is lower than the reverse WGS reaction rate, H_2 will be consumed rapidly and the CO conversion will drop suddenly, which is evidenced in the report. The same research team experimented with 50 μm cold rolled Pd/Ag alloy membranes supported on porous ceramic tubes. They presented the excellent CO conversion of 98.9% obtained in the Pd-based CMR at 325°C, 1 atma, a H_2O/CO molar ratio of 1.5 with 1.95×10^{-5} mol/s CO feed flow rate.

Iyoha et al. [61,62] studied the WGS experiment using 125 μm thick Pd and Pd/Cu alloy (20 wt% Cu) tubes at 900°C in the absence of additional heterogeneous catalysts. According to their reports, it was demonstrated that the operating temperature of 900°C would allow for the WGS reaction to proceed without any catalyst. In addition, both two Pd-based CMRs (Pd and Pd/Cu alloy) can give the CO conversion higher than the equilibrium value using the simulated syngas (53% CO, 35% H_2 and 12% CO_2 with 1650 ml/min Ar sweep gas at 900°C, retentate pressure ranged from 1.98 to 4.83 bar), and a H_2O/CO molar ratio of 1.5. However, the CO conversion and the H_2 recovery achieved by the use of Pd/Cu alloy tubes are lower than that by the use of Pd tubes, mainly due to the lower H_2 permeability of Pd/Cu alloy relative to Pd at 900°C. Furthermore, with increasing residence time, the CO conversion obtained in both Pd-based CMRs would increase apparently, while there is no obvious change in the CO conversion obtained in both the stainless steel reactor and the quartz-lined reactor. They supposed that surfaces of Pd and Pd/Cu alloy are catalytically active for the WGS reaction.

Studies of the Pd-based CMR working at high operating pressures (> 14 bar) have been also reported in the literature. At WPI, Augustine et al. [3] conducted WGS experiments over a Fe_2O_3/Cr_2O_3 catalyst in the Pd-based CMR using Pd membranes supported on porous Inconel tubes at 14.4 bar, 350, 400, and 450°C without any sweep gas in the permeate side. The best result obtained in their report is 98.2% CO conversion and 81.2% H_2 recovery at 450°C and a H_2O/CO molar ratio of 2.6. It was clearly shown that under high operating pressure conditions, even without the aid of sweep gas in the permeate side, an excellent CO conversion higher than 98% can be achieved due to the high H_2 permeation rate resulting from the great driving force for H_2 permeation.

Regarding the CO_2 capture by using the Pd-based CMR, since extremely high CO conversion can be achieved in the Pd-based CMR and H_2 in the syngas would permeate through the Pd-based membrane, a CO_2-rich stream can be obtained and sequestrated, resulting in CO_2 capture. Chiesa et al. [63] (2007) compared the CO_2 removal efficiency by using the Pd-based CMR to that by using the conventional CO_2 absorber in the coal fired integrated gasification combined cycle (IGCC) system. All calculated values in their study are based on experimental data collected in the literature. In light of their report, a higher CO_2 removal efficiency is obtained when coal fired IGCC integrates with the Pd-based CMR, exhibiting an appealing performance of the Pd-based CMR technology in CO_2 capture. In summary, the Pd-based CMR technology applied in the WGS process, not only exhibits the outstanding performance for process intensification, but also makes it possible to purify H_2 and CO_2 capture in one single step, making it a promising technology option.

Table 3.1. Palladium-based catalytic membrane reactors used for Methane Steam Reforming and Water Gas Shift reactions.

Membrane type	Thickness (um)	Membrane area (cm^2)	Reaction	Pressure (bar)	Steam/carbon ratio	Temperature (^oC)	Reference
Pd/Ag	50	5.3	MSR	1.22	3-9	300-500	[64]
Pd/Ag/PSS	10.3	10.7	MSR	1.36	3	400-550	[65]
Pd/PSS	20	60	MSR	9-20	3	400-500	[66]
Pd	4.5 - 22.5	6.3	MSR	1	3	500	[67]
Pd	4-5	175	MSR	<10	2-4	525	[52]
Pd/Ag	200	46	MSR	1-4	2-5	300-400	[68]
Pd/Ag	1,000	18.5	MSR	6-10	2.9	500	[58]
Pd-Ru/YSZ	5	13.28	MSR	35	3	580	[69]
Pd	20	25	WGS	3	1-5	400	[70]
Pd	1.4	21.5	WGS	2	3	350	[1]
Pd- Pd/Ag	7 - 10.3	50	WGS	1-12	1.1-2.6	350-450	[3]
Pd/Ag	25-40	15.7	WGS	1-4	7.4	200-300	[71]
Pd	10	200	WGS	7-20	2.5-3.5	420-440	[72]
Pd/Ag	2.2	6.8	WGS	26	5	400-450	[73]
Pd/Ag/ alumina	4.5	17-35	WGS	2	NA	400	[74]

4. METHODOLOGY

Summary

The first subsection of this chapter contains the detailed procedures used for the synthesis of the membranes used in this project. This includes the features of the supports utilized, pre-treatment of the supports, grading of the pretreated supports, activation and deposition of Palladium via electroless plating and methods for the deposition of other metals such as gold and platinum. The following subsection presents the methodology and protocol used for the characterization of the membranes along with detailed descriptions of equipment used in this project. The last subsection presents the details of the equipment used for testing the membranes in the gasification unit at the National Carbon Capture Center (NCCC) in Alabama.

4.1. Development of Pd and Pd-Alloy Composite Membranes

4.1.1 Porous Metallic Supports

The membranes synthesized in this project were based on porous stainless steel 316L support tubes with different dimensions. All membranes synthesized are listed in Appendix B. The supports 1”OD were purchased from two suppliers Chand Eisenmann Metallurgical (CEM) and Mott Corporation (Mott). CEM supports were characterized by a He permeance of 187 ± 31 $m^3/(m^2$ hr bar). However, the surface of the CEM support was very rough. Mott supports were characterized by an average He permeance of 160 ±12 $m^3/(m^2$ hr bar) and the surface was very smooth. Figure 4.1 shows the surface microstructure of the two different supports used for the preparation of Pd composite membranes. Mott supports show a relatively smoother surface.

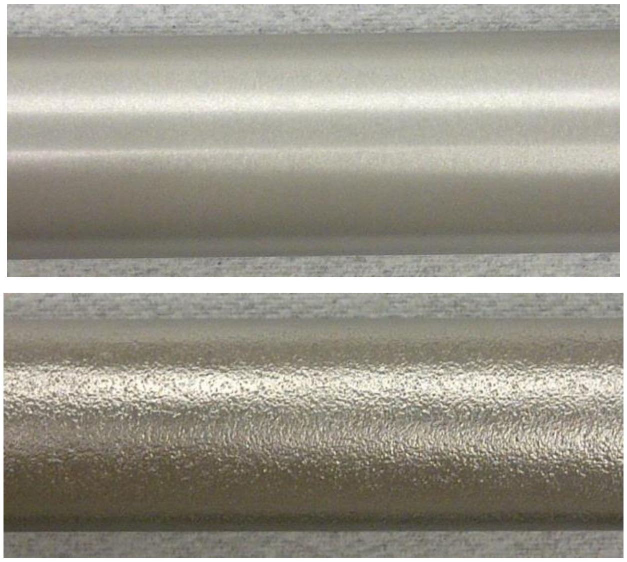

Figure 4.1. Upper: surface of Mott supports. Lower: Surface of CEM supports.

4.1.2 Pre-treatment of Porous Metallic Supports

Before starting the fabrication of Pd membranes, the porous supports are cleaned with an alkaline cleaning solution in order to remove contaminants on the support surface, such as oil, grease, and dirt; otherwise, these contaminants will result in low adhesive bond strength, causing the grading layer to flake from the metallic support later. In the cleaning procedure, porous metal supports are immersed into the alkaline cleaning solution for at least 30 minutes. Following alkaline solution cleaning, porous metal supports are thoroughly rinsed with deionized (DI) water to remove the residual alkaline solution trapped in the pores of supports until the support surface is pH neutral (pH = 7). To check the pH value of the support surface, a strip of a pH paper was used by touching the support surface during the rinsing process. After pH neutral of support surface is reached, the supports are immersed into isopropanol (IPA) solution for 5 minutes to hasten the drying of porous metal supports in later. Note that all the cleaning steps are performed in an ultrasonic bath at 60°C. When the cleaning procedure is finished, the porous metal supports are dried in an oven at 140°C overnight.

The next step is to carry out the controlled in-situ oxidation of the supports to form an oxide layer on the support surface using a Lindberg (Blue M732) oven with a heating or cooling rate of 10°C per minute. An oxide layer could act as an intermetallic diffusion barrier layer to effectively prevent intermetallic diffusion between the support metals (i.e. Fe, Cr, Ni) and Pd, which deteriorates the H_2 permeability of Pd membranes, at high temperature conditions [75]. However, initial permeance of supports would be significantly affected by the oxidation process since oxidation occurs in whole supports. Depending on media grades of the porous supports, different oxidation temperatures were used.

3.1.3 Grading of Supports

The grading of the support surface is the most important step for the fabrication of composite membranes. The purpose of the grading layer is not only to further improve the properties of the intermetallic diffusion barrier, but also to reduce the maximum pore size and narrow the pore size distribution. Mardilovich et al. [76] measured the actual pore size for PSS supports with various media grade using the mercury intrusion technique. They found that the pore sizes of PSS supports are significant larger than PSS supports media grade. For example, a PSS support with 0.5 µm media grade has an average pore size of 4-4 µm and a maximum pore size of 10-11 µm, respectively. In addition, the actual thickness of Pd film on the PSS support, without any surface modification by grading, is approximately 3 times the maximum pore size due to the Pd deposition inside the pores, evidenced that thickness of Pd films strongly depends on the surface pore size. Thus, in order to deposit thin Pd film on the PSS support, the grading step prior to the plating step is necessary for avoiding Pd to be deposited too deep into the pore structure of the support.

Consequently, all supports were graded in order to smooth out medium to small size pore mouths (~ 20-40 microns wide, 20 microns deep) by the use of alumina particles cemented with sol gel, activated alumina particles cemented with Pd and/or PdAg layer. Sols were prepared according to Yolda's method (Yolda 1974). Aluminum sec-butoxide ($Al[O(CH_3)CHC_2H_5]_3$, 95%. Alfa Aesar) was used as the aluminum precursor. The hydrolysis reaction was carried out at 75-95°C for 15 minutes. After hydrolysis, the peptization agent, HCl (10 M), was added (drop by drop). The initial milky sol was put to reflux for at least 6-8 hours. After reflux, the appearance of the sol changed from clear white to transparent with a blue tint Different size of alumina powders were used to grade supports. In general, the grading procedure consists of applying a layer with coarse particles (3-5 microns), a layer of medium size particles (1-3 microns) and a layer of fine particles (>0.3 microns). Each preparation for powder deposition may be a single powder or a mixture of powders within the dimensions cited above. Powders were deposited either by simple mechanical action (hand) from a concentrated slurry or by suction vacuum from a diluted slurry. Both deposition methods were used in the laboratory with similar results but suction vacuum from diluted slurry would be the most suitable for industrial processing.

Coarse, medium and fine particles were either used as received or activated with Pd nuclei depending on whether the cementing of the layer was performed with a sol gel layer or a short Pd plating ("Pd glue"). Pre-activated Al_2O_3 slurries are used as grading solutions in the grading procedure, and their compositions are summarized in Table 4.1. Every coarse, medium and fine layer was cemented by either dipping the support in an alumina sol gel for 10-30 seconds and let dry at room temperature or by plating Pd for a short period of time 15-20 minutes. Grading the support consisted of applying the coarse layer and cementing, applying the medium layer and cementing and applying the fine layer and cementing. When cementing with a sol gel a final calcination step at 500°C was required and when cementing with Pd a polishing step was required after drying to slightly smooth out the surface. Polishing the grading layer and PdAg with fine alumina sand paper was sometimes accomplished to decreased small surface defects.

Table 4.1. Compositions of pre-activated Al_2O_3 slurry

Component	Pd content	Slurry A	Slurry B	Slurry C	Provider
10 µm pre-activated Al_2O_3	2 wt.%	2 g/L			Johnson Matthey
3-4 µm pre-activated Al_2O_3	2 wt.%		2 g/L		Johnson Matthey
0.6 µm pre-activated Al_2O_3	2 wt.%			2 g/L	Johnson Matthey

4.1.4 Activation and Electroless Plating

For the purpose of initiation of autocatalytic electroless plating, seeding Pd nuclei on the support surface by the activation process is required. In the activation process, the formation of Pd nuclei can be described by Equation 4.1. The activation procedure in this project followed our previously reported methodology [77], and compositions of the activation solutions are summarized in Table 4.2.

$$\mathrm{Pd}^{2+} + \mathrm{Sn}^{2+} \longrightarrow \mathrm{Pd}^{0} + \mathrm{Sn}^{4+} \tag{4.1}$$

Table 4.2. Chemical compositions of Pd plating solution.

Component	Purity wt%	Quantity	Provider
$Pd(NH_3)4Cl_2$•H_2O	99	4 g/L	Alfa Aesar
Na2EDTA•$2H_2O$	99	40.1 g/L	Aldrich
NH_4OH	28	198 mL/L	Merck
H_2NNH_2	99	5.6 mL/L	Alfa Aesar

Prior to the activation process, the surface of graded supports were slightly polished with a sand paper (Norton 31550 Champagne A275 1500 grit) in order to smooth the supports surface for better Pd adhesion to supports surface in the later Pd plating process. Note that if the surface of a graded support is too smooth, the deposited Pd film would peel off easily from the surface. Hence, there is an optimum smoothness of graded support surface to achieve good Pd adhesion. The activation process included 3 loops of sequential immersion at room temperature, and every loop has 6 steps, described in the following:

1. To immerse PSS support into $SnCl_2$ solution for 5 minutes.
2. To immerse PSS support into DI water for 2 minutes.
3. To immerse PSS support into DI water for 3 minutes.
4. To immerse PSS support into $PdCl_2$ solution for 5 minutes.
5. To immerse PSS support into DI water for 2 minutes.
6. To immerse PSS support into HCl solution for 3 minutes.

Electroless Pd plating is an autocatalytic reaction for Pd deposition without any electric current passing through the plating solution. The rate of plating process strongly depends on the presence of a reducing agent. In this study, the Pd plating process used for Pd deposition follows the plating process. Chemical compositions of Pd plating solution and the autocatalytic reaction of electroless Pd plating are shown in Table 4.3 and Equation 4.2, respectively. In the plating process, Pd^{2+} ions provided by

$Pd(NH_3)_4Cl_2 \bullet H_2O$ are reduced by the reducing agent H_2NNH_2 while NH_4OH and $Na_2EDTA \bullet 2H_2O$ are used respectively as the complexant and the stabilizer during the process.

Table 4.3. Chemical compositions of Pd plating solution

Component	Purity	Used amount	Vendor
$Pd(NH_3)_4Cl_2 \bullet H_2O$	99 wt.%	4 g/L	Alfa Aesar
$Na_2EDTA \bullet 2H_2O$	99 wt%	40.1 g/L	Aldrich
NH_4OH	28 wt.%	198 ml/L	Merck
H_2NNH_2	99 wt.%	5.6 ml/L	Alfa Aesar

$$2Pd(NH_3)_4Cl_2 + H_2NNH_2 + 4NH_4OH \longrightarrow 2Pd + N_2 + 8NH_3 + 4NH_4Cl + 4H_2O$$

or (4.2)

$$2Pd^{2+} + H_2NNH_2 + 4OH^- \longrightarrow 2Pd^0 + N_2 + 4H_2O$$

Electroless Pd plating is carried out by immersing the activated support into the electroless Pd plating solution, applying vacuum in the tube side of the support by an aspirator. The temperature condition of the plating process is controlled at 60°C by a heated water bath. Typically, the hydrazine is added into the plating solution just before the immersion of the activated support, and one cycle of Pd plating has 90 minutes. The average thickness of Pd film is estimated by the gravimetric method, according to Equation 4.3:

$$\delta = \frac{\Delta m}{A \cdot \rho_{metal}} \cdot 10000 \qquad (4.3)$$

where δ is the film thickness in µm, Δm is the weight gain in g, A is the plated area in cm^2, and ρ_{metal} is the density of the plated metal in g/cm^3. Please note that all gravimetric measurements for thickness estimation are referred to Equation 4.3.

4.1.5 Pt Electroplating

For the purpose of strengthening the resistance to H_2S, an additional thin Pt layer on the top surface of Pd membranes is deposited by electroplating technique. The Pt plating bath, Platinum AP RTU, is purchased from Technic Incorporation, RI. In the plating process, a Pt clad Nb cylindrical mesh (with a diameter of 1.5 inch and a length of 12 inch) works as the anode, and the metal support works as the cathode. Both the cylindrical mesh and the metal support are connected with the DC power supply (Sorensen DCS8-125E). The plating process is conducted for 20 minutes with a voltage (ΔV) of 2.6 V and a current density ranging from 7.3 to 9.7 mA/cm^2. The temperature condition of the plating process is controlled by a heated water bath at 68°C. When the electroplating process is done, the Pd/Pt composite membrane is rinsed and immersed into DI water for at least 1 hour to ensure no residual plating solution left in the membrane, and then dried at 140°C in the oven overnight. The thickness of Pt film estimated through the gravimetric measurement is approximately 0.25 µm.

4.1.6 Au Electroplating

In order to protect the welds of cylindrical support, an extra thick Au layer is deposited on the welds through the electroplating method. The Au plating bath, TECHNI GOLD 25 ES RTU, is purchased from Technic Incorporation, RI. Similar to the Pt electroplating process, a Pt clad Nb cylindrical mesh (with a diameter of 1.5 inch and a length of 12 inch) works as the anode, and the metal support works as the cathode during the plating process. The DC power supply (Sorensen DCS8-125E), connecting the cylindrical mesh and the metal support, provides the voltage required for the Au electroplating process. A voltage (ΔV) of 0.55 V and a current density ranging from 0.5 to 3 mA/cm^2 are employed in the plating process. The plating process is carried out for 2 hours, and the operating temperature is 60°C controlled by a heated water bath. After finishing the plating process, the composite membrane is rinsed and immersed into DI water for at least 1 hour for the purpose of removing residual plating solution left in the membrane.

4.2. Membrane Characterization

4.2.1 He Leak Measurements

Part of the characterization procedure of the membranes consisted on measuring the Helium flux at different pressures throughout the synthesis of the membrane. Due to the He flux varying considerably (approximately 5 orders of magnitude difference) at different steps in the membrane fabrication process, three different flow meters are used to measure different ranges of He flux, as seen in Table 4.4.

Table 4.4. Three different gas flow meters and their measurement range.

Flow meter	Measurement range	Vendor
GCA Wet Test Flow Meter	> 300 ml/min	The Precisioni Scientific Company
4068 Digital Flow Meter	2 - 300 ml/min	All-Tech Incorporation
Bubble flow meter	< 2 ml/min	-

4.2.2 Permeation Tests

Permeation tests (including H_2 and He permeation testing) of Pd-based composite membranes were conducted at WPI in different apparatus, similar to the one described in Figure 4.2. The permeation module consists of a 316L SS tubular reactor, where the Pd-based composite membrane is inserted and sealed with stainless steel reducing units and a removable graphite ferrule. One end of the reactor is connected to a tube, allowing feed gas to flow into the retentate side (shell side), while the other end is connected to a tubing for gas exiting.

The permeation module was mounted either vertically or horizontally into a ceramic fiber heater, purchased from Watlow Electric Manufacturing Company, MO, and both ends of the module outside the heater are wrapped with insulation strips in order to prevent heat loss during the testing process. The module temperature was monitored by a K-type thermocouple located outside the reactor, and controlled via a Eurotherm 2116 temperature controller connected to the ceramic fiber heater. For the purpose of monitoring the operating temperature and purging permeate side with sweep gas, the open end of the PSS support was inserted with a J-type thermocouple, whose tip is located at the center of the membrane. Note that all the tubing and fittings were made of 316L SS, purchased from Swagelok Company, OH.

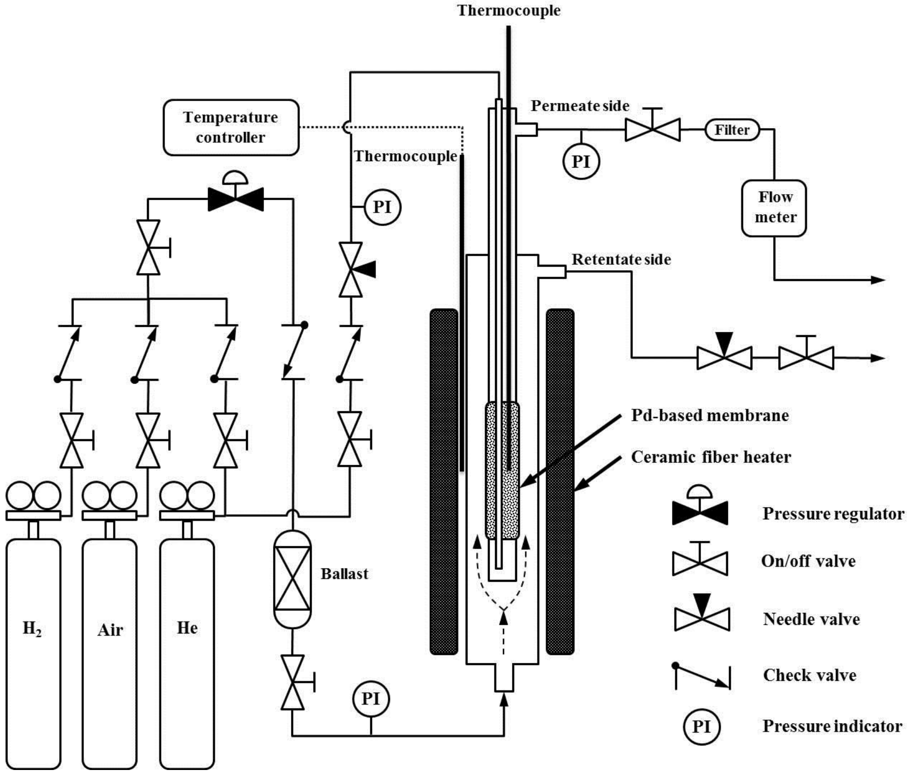

Figure 4.2. Schematic diagram of an experimental apparatus used for permeation tests at WPI.

The feed pressure was controlled by a pressure regulator (ranged from 0 to 20 barg), purchased from Swagelok Company, and measured by a pressure transducer (ranged from 0 to 500 psig), supplied by Transducer Direct Company, while the permeate side pressure is measured via a pressure transducer (ranged from 0 to 1000 torr), made by MKS Instrument Incorporation, MA. A ballast (1,000 ml), made by Swagelok Company, was installed before the permeation module, allowing the composition of gas to gradually change between H_2 and He. Regarding the measurement of the permeate flow rate, mass flow meters (M10MB type, made by MKS Instrument Incorporation) with different flow ranges were used for specific gas species. H_2 mass flow meters with flow ranges of 500, 1000, and 5000 sccm were used to measure the permeate H_2 flow rate, while a He mass flow meter with a flow range of 10 sccm was used for measurement of permeate He flow rate. During the entire course of testing, all measurement data of operating temperature, feed pressure, permeate side pressure, and permeate flow rate are transferred to a personal computer (PC) using a data acquisition breakout boards (SCB-68 type, supplied by National Instruments), and recorded continuously using LabView 7.1 software.

4.2.3 Characterization Protocol

After the membrane was installed in the permeance apparatus, the retentate and permeate of the system was purged using He at room temperature for at least 1 hour to remove air and moisture in the system. During the purge process, the feed pressure of He is controlled at 2 bara, while the permeate side pressure of He is controlled at 1 bara. The purpose of purge was to prevent Pd-based membranes from being oxidized in the heating process. After purge, the system is heated up to 350°C at a ramp rate of 5°C/min. Once the operating temperature reaches 350°C, sweep He is turned off, allowing the permeate side pressure to be ambient pressure of approximately 1 bar, and He leak measurement is performed under different feed pressure conditions (from 1.2 to 5 bara). Following the He leak measurement, He feed was switched to H_2 feed in a smooth transition with the aid of the ballast for gradual change of gas composition. When H_2 flux became stable (after approximately 24 hours), the H_2 flux is measured at different feed pressures (from 1.2 to 5 bara) for H_2 permeance calculation, and a linear regression of H_2 permeance was performed to confirm the Sieverts' correlation.

When H_2 permeance measurement is finished, both retentate and permeate sides were purged with feed He and sweep He for 30 minutes, then He leak of the Pd-based membrane is measured again by turning off sweep He in order to calculate H_2/He selectivity, which is the ratio of H_2 flux to He flux under the pressure difference of 1 bar (feed pressure is 2 bar and permeate side pressure is 1 bar). The same procedure for H_2 permeance and He leak measurement was repeated at 400, 450, 400, and 350°C, respectively. Note that before changing the operating temperature, He purge was carried out on both retentate and permeate sides. The purpose of the characterization at first stage of 350, 400, and 450°C was to gradually anneal the Pd-based membrane, allowing grain growth and stress relaxation, and clean the membrane surface by burning carbonaceous materials left on the membrane surface. At second stage of 450, 400, 350°C, by the H_2 permeance measurement with different temperatures, activation energy can be determined through the Arrhenius relation.

4.2.4 Scanning Electron Microscope and Energy Dispersive X-ray Analysis

The membrane microstructure is characterized using an Amray 1610 Turbo scanning electron microscope (SEM). In addition, a Princeton Gamma-Tech (PGT) Avalon energy dispersive X-ray (EDX) light element detector and a Robinson Retractable backscattered electron detector (RBS-1610 5MC type) equipped on the SEM are utilized for qualitative and quantitative composition analysis. Both microstructure characterization and composition analysis are carried out with the Sprint software (supplied by PGT Corporation).

According to the Castainge's equations (Equation 4.4 and 4.5), the penetration depth (D) and the lateral extension (R) for EDX analysis of samples (primarily consisted of Pd and Pt) with an acceleration voltage of 20 keV are between 0.47 to 0.80 µm and between 0.79 to 1.24 µm, respectively (Notthoff et al., 2013).

$$\mathrm{D} = 33 \cdot (\mathrm{E}_0^{1.7} - \mathrm{E}_\mathrm{c}^{1.7}) \cdot \frac{\mathrm{m}}{\mathrm{Z} \cdot \rho \cdot 1000} \tag{4.4}$$

$$\mathrm{R} = \frac{0.4114 \cdot \mathrm{Z}^{2/3}}{1 + 0.187 \cdot \mathrm{Z}^{2/3}} \cdot \mathrm{D} \tag{4.5}$$

where E_0 is the acceleration voltage of the incident electron beam in keV, E_c is the minimum emission voltage in keV, ρ is the density of the sample in g/cm^3, m is the averaged atomic mass, and Z is the average atomic number.

4.3. Coal-derived Syngas and Membrane Tests

Syngas at NCCC was produced by an air blown transport reactor integrated gasification (TRIG) type gasifier fed with powder river basin (PRB) coal. At the exit of the transport gasifier, the syngas was cooled down to 400°C and sent to the particulate control device (PCD), which consisted of sintered metal tube filters, where the ash/carbon particles concentration was reduced from 10,000 to 0.1 ppmv. After particulate removal, a split fraction of the raw syngas was sent to the syngas conditioning unit (SCU) where the syngas could have been subjected to desulfurization, mercury removal, ammonia cracking and hydrocarbon reforming, water gas shift, and other processes depending on the experimentation's specific needs. For the particular testing of composite Pd membranes, only desulfurization was performed in the SCU. Indeed, as for the reasons previously stated, the H_2 permeance and selectivity stability of composite Pd membranes was studied in industrial coal derived syngas with all impurities except for sulfur compounds removed with the aid of ZnO absorber beds. Figure 4.3 shows the actual syngas cleaning line composed of a ZnO bed (A) for sulfur removal, and a COS hydrolyser (B) for COS removal, both installed within the NCCC scope boundary lines network. The raw syngas H_2S concentration, averaging 300 ppmv, was reduced to less than 1 ppmv after the 1st ZnO bed. The syngas was then forced through the COS hydrolyser in order to convert any COS into H_2S and CO_2, however, COS concentration was always below the detection limit of the GC (model: Agilent 5890, column: J&W GS-GasPro, detector: FPD) even after vessel A. The concentration of poly aromatic hydrocarbons (PAHs) and trace metals was not measured directly for the syngas fed to the membranes, but was measured for syngas delivered to other experimental set-ups during the run. For PAHs measurements, syngas samples were passed through impingers containing isopropyl alcohol in ice bath and sent to external laboratories for analysis. Total PAHs concentration ranged between 300 and 600 ppmv, yet one needs to keep in mind that PAHs may deposit on ZnO beds, the COS hydrolyser bed, and pipe walls leading to a decrease in the PAHs content in the syngas fed to the membrane. The Hg, Se, and As concentrations usually equaled 10, 30, and 1 mg/Nm^3 respectively (EPA method 29). After desulfurization, 10 $lbs.h^{-1}$ of the desulfurized syngas was split, enriched with industrial grade H_2 (from cylinders) up to 30-40% and directed to the WPI-MTR skid. The H_2 enrichment was necessary to increase the driving force for H_2 permeation since the H_2 concentration of the syngas produced at NCCC was only 10%. The H_2 enriched syngas first passed through an empty buffer volume (vessel C also shown in Figure 4.3 to allow for gradual changes between N_2 / N_2/H_2 mixtures, N_2/H_2 mixtures / enriched syngas atmospheres and vice versa, and then through a second polishing ZnO bed (vessel D). The typical temperatures and pressures through the cleaning line are also reported in Figure 4.3. Pd coupons, 100 OD by 100 wide ring shape pieces cut out from a composite Pd membrane with the same structure as the membranes tested at NCCC, were hung from hooks at the head of vessels A, B and D and kept in their initial position through the entire length of the gasifier run. The surface characterization of coupons was performed using an Amray 1610 Turbo Scanning Electron Microscope (SEM) coupled with Energy Dispersion X-Ray (EDX) (Princeton Gamma-Tech Instruments Inc., Rocky Hill, NJ). The EDX detector was equipped with a beryllium window allowing the detection of light elements. Atom and weight concentration profiles were determined with the Spirit software (Princeton Gamma-Tech Instruments Inc., Rocky Hill, NJ). Elemental composition (line-scans) was performed at an acceleration potential of 10, 15 or 20 kV, 39 mm working distance, 33 angle tilt and a 5-10 min dwell time.

The WPI-MTR skid for the testing in actual syngas conditions of composite Pd-based membranes is shown in Figure 4.4. The skid essentially consisted of the ballast volume vessel C, the ZnO bed absorber vessel D, and a custom built high temperature oven (Thermal Product Solutions; New Columbia, PA) designed to operate in a Class I, Division II, Groups B, C, and D environment. The oven was equipped with a rectangular heating volume of 122 cm x 63.5 cm x 63.5 cm shown in Figure 4.5. The membrane module (Figure 4.5), designed by Membrane Technology and Research Inc. (MTR; Menlo Park, CA) and fabricated at Johansing Iron Works (Oakland, CA), had a design temperature and pressure of 500°C and 23.8 bar (350 psi) respectively. It consisted of a flanged tube-in-shell reactor with an inner shell diameter of 54.8 mm (2.16 inch) leading to a Reynolds number of about 600 at the operating conditions at site. The entire skid was designed by MTR, partially assembled at Johansing Iron Works and finalized on site at NCCC facilities. Leak tests and heat tracing were performed at NCCC site.

The feed stream (H_2 enriched syngas) first passed through the ballast volume C and the 2nd ZnO bed as stated above. After passing through a particle filter, the syngas was heated from approximately

160-180°C (temperature of the heat tracing) to 450°C by a heating coil inside the oven as shown in Figure 4.5 and Figure 4.6. Upon separation by the Pd-based membrane, the permeate and the retentate were combined and sent to a thermal oxidizer. The feed, permeate and retentate lines included pressure and temperature gauges (see Figure 4.4) for monitoring all the parameters. The H_2 permeate flux was measured with a rotameter since the work area was classified as explosion risk and no digital mass flow meter could be used without proper explosion proof equipment. The H_2 permeate flux was measured and recorded every 4e5 h by venting the permeate flux to the atmosphere and allowing a sufficient time, 10-15 min, for the rotameter float to stabilize. All gas sample streams were chilled (Universal Analyzers, Model: 1090; Baldwin, Model: e5900XP), ensuring a dew point of 5°C, prior to GC composition analysis. The composition (H_2, CO, CO_2, CH_4, N_2) of the H_2 enriched syngas fed to the membrane was continuously monitored with a GC (model: Rosemount 700, columns: Haysep T and Haysep N for CO_2 and Haysep T and MS-5A for H_2, CO, O_2, CH_4, N_2, detectors: TCD). The average concentration of all measured components is listed in Table 4.5 along with the operating conditions. The concentration of sulfur compounds in the feed syngas (H_2S, COS and CS_2) was closely monitored and no sulfur was detected via GC (<1 ppm). The gas composition of the permeate and the retentate were measured by GC (model: Siemens Maxum II, columns: HysepN and 5A-MS for H_2, N_2, CO, N_2 and CH_4, HysepN and HysepQ for CO_2 and H_2S, detectors: TCD) once or twice per day. Since the concentration of the impurities in the permeate could be measured quite accurately, the purity of the H_2 permeate flux was determined by mass balance i.e. subtracting total amount of impurities (N_2, CO, CO_2, CH_4) from 100%. The H_2 purity was also determined through direct GC measurements with results similar to the results derived from the mass balance equation when H_2 purity was lower than 99%.

Table 4.5. Average composition of the H_2 enriched desulfurized syngas stream fed to the membrane modules and operating conditions at NCCC.

	Single tube	**Multitube**
H_2 (%)	32	34
N_2 (%)	46	55
CO_2 (%)	7	1
CO (%)	7	0.5
H_2O (%)	7	-
CH_4 (%)	1	0.32
H_2S (ppm)	<1	<1
Impurities	Traces	Traces
Temperature (°C)	450	450
Pressure (barg)	11-12	11-12
Feed flow rate (kg/h)	4.52	4.52

The testing procedure consisted of the heating up to 450°C, a dwelling testing time at 450°C, and cooling down to room temperature. Heating up to 450°C was performed in two steps: (1) heating up to 250°C in N_2 atmosphere from bottled N_2 and (2) heating up to 450°C in N_2 atmosphere with plant N_2. The use of bottle N_2 was needed since plant N_2 was only available at 200°C. During the heating step, a bypass from vessel C to the permeate side (see Figure 4.4) ensured the purging of the permeate line with N_2. Once the temperature reached 450°C, the H_2 enrichment (from industrial bottles) started and the permeance of the membrane was monitored for one day in a N_2/H_2 mixture. The actual desulfurized syngas was then sent to the skid, plant N_2 was switched off and the H_2 enrichment was finally adjusted to have an average H_2 feed concentration of 33%. After a testing time of approximately 200-250 h, during which feed, retentate, and permeate compositions were measured daily, a N_2/H_2 mixture was fed to the membrane followed by plant N_2. The membrane was further cooled down to 250°C, N_2 (cylinders) was fed to the membrane and finally the oven temperature was set to 25°C.

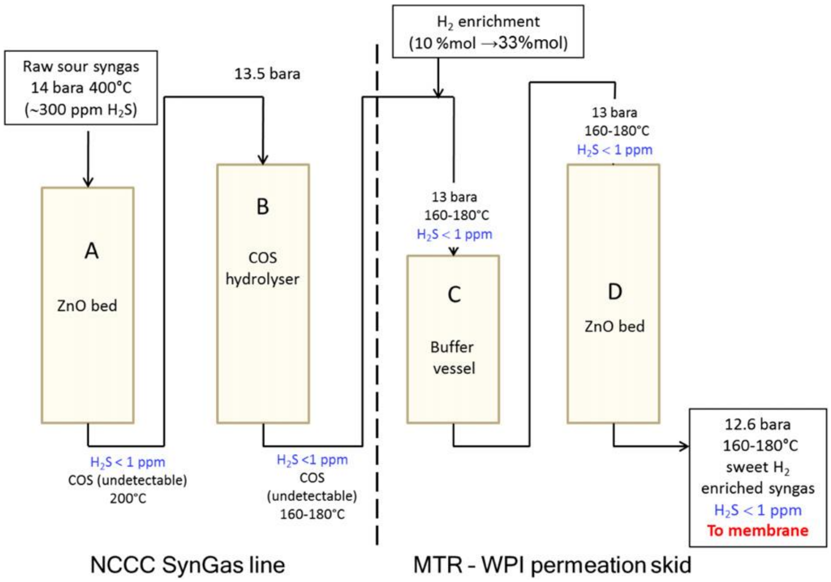

Figure 4.3. Syngas conditioning unit (SCU) (vessels A and B) and additional buffer vessel (C) and ZnO bed (D) on the WPI-MTR permeation skid.

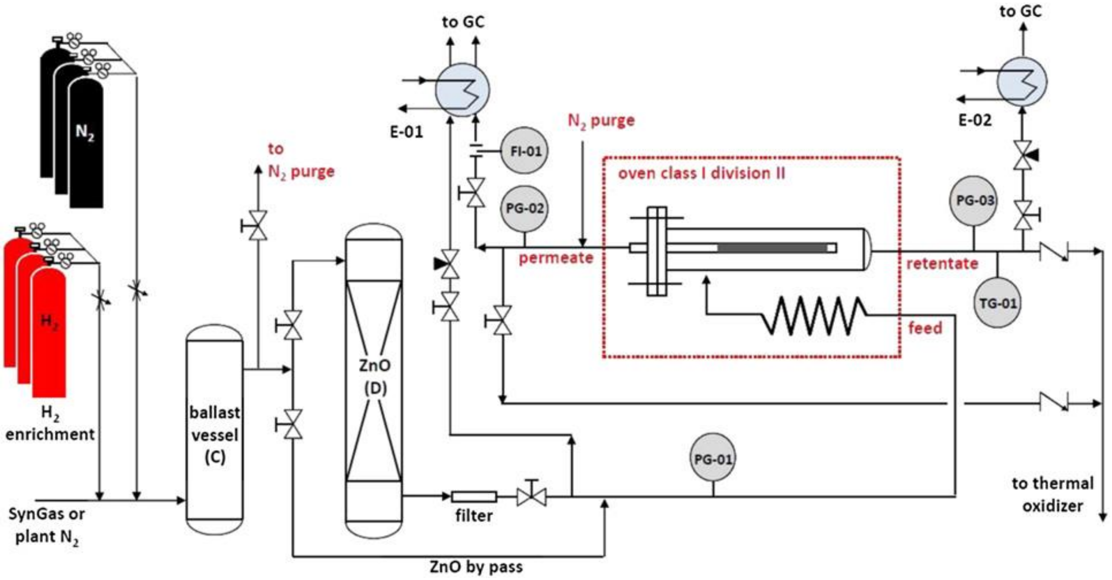

Figure 4.4. Flow diagram of the WPI-MTR permeation skid.

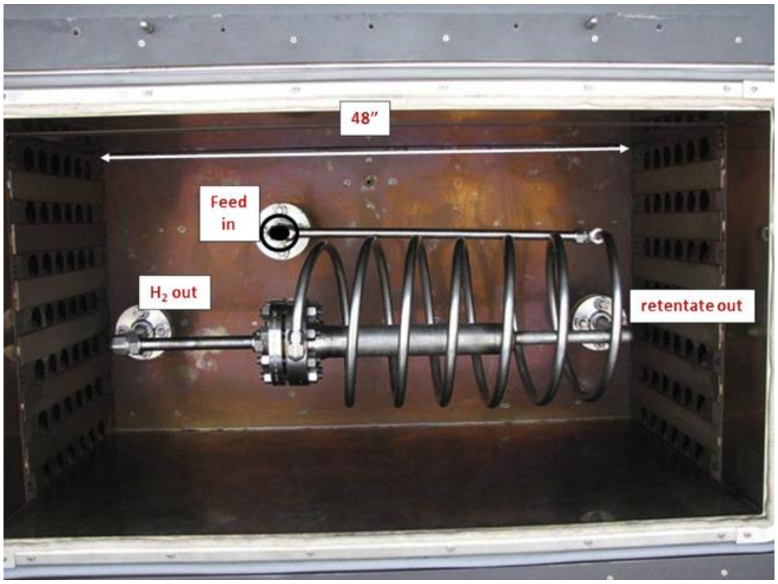

Figure 4.5. Photograph of the single tube membrane permeation module and the heating coil inside the oven heating.

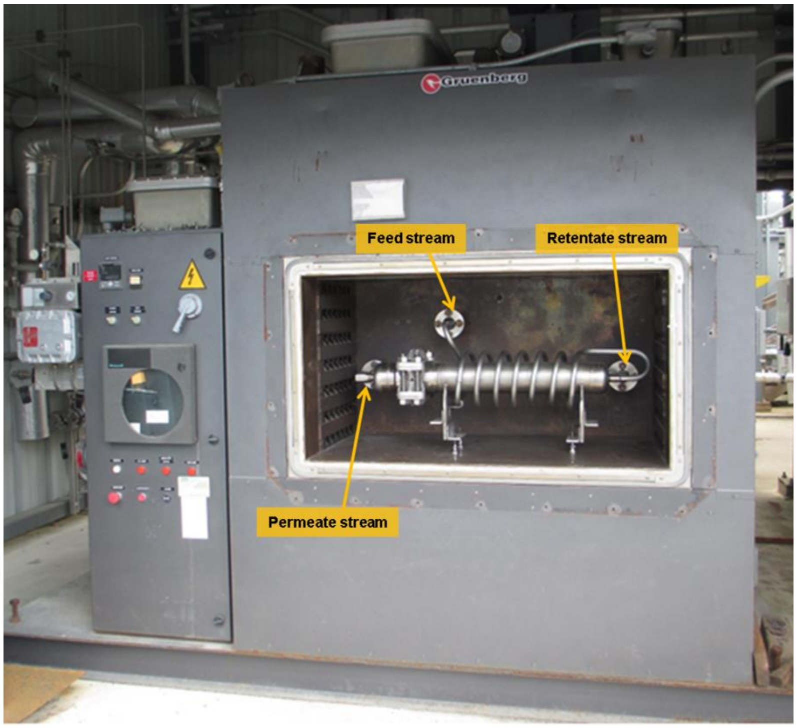

Figure 4.6. Photograph the setup for testing the multitube membrane module at NCCC (Notice that the door of the oven was removed for display).

5. SINGLE TUBE PALLADIUM- AND PALLADIUM-ALLOY MEMBRANE UNDER SYNGAS

Summary

Studying the hydrogen flux and hydrogen purity of Pd-based composite membranes in actual coal derived Syngas and assessing their eventual poisoning and recoverability of composite Pd membranes is one of the key objectives of Phase I and II of the project. Consequently, the present section encompasses the results of a comprehensive performance assessment of the different pilot-scale Pd/Alloy composite asymmetric membranes tested under long-term coal-derived syngas atmosphere testing. The membranes were developed and tested first at the CIMS-WPI laboratory under pure H_2 and later at the National Carbon Capture Center (NCCC) in Wilsonville, Al (NCCC) under a mixture of N_2/H_2 and H_2 enriched syngas coming from a TRIGTM gasification system. Thirteen membranes were examined for 4275 h and classified in four types: Pd, Pd/Au, Pd/Pt and Pd/Au/Pt membranes. Their respective H_2 permeance and purity profiles, permeance difference under pure hydrogen and syngas conditions as well as stability of operation were assessed. The membranes showed good stability in syngas although exhibiting an initial drop in permeance when compared to that under pure hydrogen. Pure Pd membranes displayed the highest permeability, but showed pinholes after being exposed to syngas. Pd/Pt membranes showed a reduced permeance drop under syngas conditions, indicating sulfur resistance properties. Furthermore, Pd/Au/Pt membranes, presented for the first time in the literature, displayed stable permeance and purity profile. The inhibition of the initial permeance drop and the long-term operation of these ternary membranes were demonstrated. Finally, Pd/Au membranes were shown to display the most stable permeance and purity characteristics. In this case, the initial permeance drop was significantly reduced, exhibiting the lowest decline amongst all cases considered. It is hypothesized that Au may act as a patch paste blocking defects on the Pd layer.

5.1. Scope of the Membranes Tested

Different Pd and Pd/Alloy membrane thicknesses were synthesized, tested and analyzed in order to study comprehensively the performance of each alloy under industrial conditions. In total, thirteen membranes were examined for 4275 h and classified in four types: Pd, Pd/Au, Pd/Pt and Pd/Au/Pt membranes. Their respective H_2 permeance and purity profiles, permeance difference under pure hydrogen and syngas conditions as well as stability of operation were assessed. It should be pointed out that these membranes were designed to produce H_2 with purity equal or higher than 99% and a permeance of 15 $Nm^3m^{-2}h^{-1}bar^{-0.5}$ under syngas conditions. Table 5.1 shows the summary of the principal characteristics of all the composite Pd and Pd/alloy membranes synthesized at the CIMS-WPI and the nomenclature used in this study. Thirteen Pd and Pd/alloy membranes were tested first at WPI under pure hydrogen for about 100 hours at 450^0C and afterwards were sent to the National Carbon Capture Center (NCCC) in Wilsonville, Al. to be tested under H_2/N_2 mixed gas and syngas conditions at 450^oC and 12.6 atm in the WPI-MTR Skid presented in section 3.2 of this document. The total effective testing time for all thirteen membranes was 4275 h. Two membranes, MA-127C*** and MA-131B***, were tested in our laboratory under a controlled mixture of CO, CO_2, H_2O and H_2. Moreover, temperatures ranging between 420-440^oC and a maximum pressure of 20 bar were used in this work. Notice also that these membranes were used for a catalytic membrane reactor test on a pilot-scale rig, presented in section 6 of this document) in order to better understand and assess the effect of these major syngas components on the membrane under consideration.

Table 5.1. Summary of the composite Pd and Pd/alloy membranes.

Membrane Nomenclature	Composition and thickness, µm	Testing time, h	Test Setting
MA-129b	14(Pd)+0.9(Au)	250	Industrial coal derived syngas and H_2 and N_2 mixture
MA-145B	8.5(Pd)+0.33(Au)+0.1(Pt)	650	
MA-138C	8.5(Pd)+0.35(Au)+0.06(Pt)	175	
MA-142	9.6(Pd)	225	
MA-150B	5(Pd)+0.8(Au)+0.9(Pd)	350	
MA-151B	4(Pd)+0.5(Pt)+0.9(Pd)	350	
MA-158	4.8(Pd)+0.45(Pt)	150	
MA-136B	10.3(Pd)+0.3(Au)+0.09(Pt)	725	
MA-126B*	8.2(Pd)+0.16(Au)	225	
MA-128*	10(Pd)+0.2(Au)	275	
MA-128b**	9.6(Pd)	175	
MA-129	13.1(Pd)	250	
MA-137B**	8.7(Pd)+0.5(Au)	475	
MA-127C***	7.4(Pd)	450	Mixture of CO, CO_2, H_2O and H_2
MA-131B***	8.3(Pd)	390	

5.2. Group 1. Pure Pd Membranes

Group 1 is comprised of pure Pd-based membranes. The characteristics of these membranes were used as the standard-basis in our comparative assessment of the performance of the Pd/Alloy membranes. Five Pd membranes were used for this study with different Pd thicknesses ranging from 7.4-13.1 µm (Table 5.2).

Table 5.2. Composition of the pure Pd membranes.

Membrane Nomenclature	Composition / µm
MA-127C***	7.4 (Pd)
MA-128b**	9.6 (Pd)
MA-129b*	13.1 (Pd)
MA-131B***	8.3 (Pd)
MA-142	9.6 (Pd)

The H_2 permeance of MA-129B* and MA-142 was tested initially under pure H_2 at WPI and later under H_2/N_2 gas mixture and syngas at NCCC. The respective profiles are shown in Figure 5.1. In this work, all the permeances shown as a single gray-labeled point represent the average permeance measured at WPI over 100 h. The H_2 permeance under H_2/N_2 atmosphere is shown with the series filled in white, while permeance under hydrogen enriched syngas is shown in solid-black series. Membranes MA-127C*** and MA-131B*** were used in CMRs to perform the WGS with only CO, CO_2, H_2 and H_2O present. Their H_2 permeance was measured before and after the reaction. It should be mentioned that MA-128b** was originally synthesized as a Pd/Au membrane (MA-128*). However, after testing, MA-128* was polished and replated with 2 µm of Pd. It was expected that the mechanical treatment removed the Au layer of the membrane. However, due to intermetallic diffusion, traces of Au might still be present in the membrane or in the support. Therefore, its characteristics were used only for comparison purposes and its permeance was not included in Figure 5.1.

MA-129B* showed an initial H_2 permeance of 23.2 $Nm^3m^{-2}h^{-1}bar^{-0.5}$ at WPI. At NCCC however, afterwards the flow rapidly declined to 11.6 $Nm^3m^{-2}h^{-1}bar^{-0.5}$ and further down to 8.1 $Nm^3m^{-2}h^{-1}bar^{-0.5}$ after 200 h. The hydrogen permeance experienced a drop of 55% compared to its initial value. After removal, the surface of the membrane was covered with a thick black layer.

The permeance of MA-142 at 450°C measured at WPI under pure H_2 was 29.2 $Nm^3m^{-2}h^{-1}bar^{-0.5}$ with a H_2/He selectivity >2500. At NCCC, MA-142 was tested for a total of 230 h under H_2/N_2 and syngas atmosphere. The membrane first dwelt under H_2/N_2 where the H_2 permeance declined compared to the value measured under pure H_2 at WPI. After 40 h under H_2/N_2, the average permeance decreased by 70%. Upon syngas introduction, no significant decrease of the H_2 permeance was observed indicating that H_2 permeance inhibition (mostly due to surface contamination) occurred in the H_2/N_2 mixture. The permeance of MA-142 membrane was 5.8 $Nm^3m^{-2}h^{-1}bar^{-0.5}$ and remained constant in syngas for 120 h (80% loss compared to the level observed at WPI). After this time, the flow started to increase abruptly indicating the opening of pinholes resulting in a loss in selectivity.

The WPI permeance of MA-128b** was 17.7 $Nm^3m^{-2}h^{-1}bar^{-0.5}$. The membrane showed a permeance drop to 11.1 $Nm^3m^{-2}h^{-1}bar^{-0.5}$ under syngas. The permeance drop corresponded to 37% of the original permeance. This reduction in permeance was significantly lower than that of MA-129B* and MA-142. It is important to notice that the membrane thickness of MA-128b** was the same as MA-142 but thinner than MA-129B*. This meant that the permeance drop observed in these membranes did not depend on the thickness of the Pd layer and was mainly due to surface contamination. The lower permeance drop in MA-128b** could be attributed to the presence of Au traces within the Pd structure and/or the support.

Before being tested as CMRs, MA-127C*** and MA-131B*** were tested at 420°C and displayed H_2 permeances of 21.7 and 21.9 $Nm^3m^{-2}h^{-1}bar^{-0.5}$. After the reaction, the membranes had H_2 permeances of

18.9 and 19.4 $Nm^3m^{-2}h^{-1}bar^{-0.5}$, respectively. This corresponded to a permeance drop of 13% and 11%, respectively. The permeance drop under syngas of MA-04* and MA-10 was significantly larger than that of MA-127C*** and MA-131B*** and this phenomenon occurred within a shorter period of time. This behavior suggested that the presence of CO, CO_2 and H_2O did not affect the stability of pure Pd membranes and that the permeance drop was caused by the presence of other contaminants.

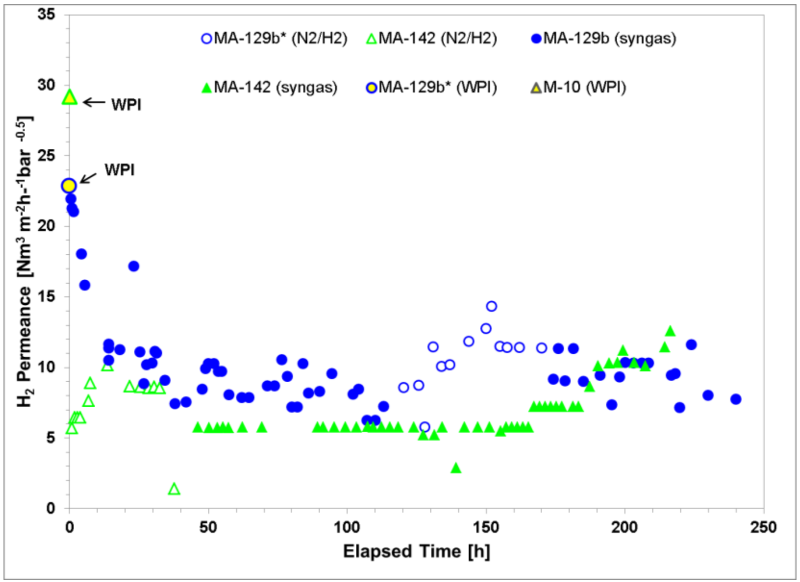

Figure 5.1. H_2 Permeance of pure Pd membranes as a function of time.

The H_2 purity profiles of pure MA-129B* and MA-142 are shown in Figure 5.2. The hydrogen purity of MA-142 under syngas was 99.7% that remained constant for 120 h; the purity decreased however to 77.9% after 227 h. The H_2 purity of MA-142 did not seem to depend on the gas composition. MA-129B* had a more stable purity profile throughout the test with an average value of ~98%. The H_2 purity was >99.2% at the beginning of the test and declined to 96.8% after 240 h. The purity of MA-129B* seemed to be lower under H_2/N_2 mixed gas than that under syngas conditions. MA-129B* was more robust and had longer stability under syngas conditions than MA-142. The permeance of MA-129B* decreased by 50% from its original value while MA-142 decreased by 75%. The reason was the thicker dense Pd film of MA-129B* (13.1 μm) when compared to that of MA-142 (9.6 μm). It is important to mention that although the permeance of these membranes dropped considerably, their performance was still competitive. According to Oyama et al. [78] membranes with permeances >6 $Nm^3m^{-2}h^{-1}bar^{-0.5}$ and with H_2/N_2 selectivities >1000 are within or above a Robeson upper boundary limit of Pd membranes.

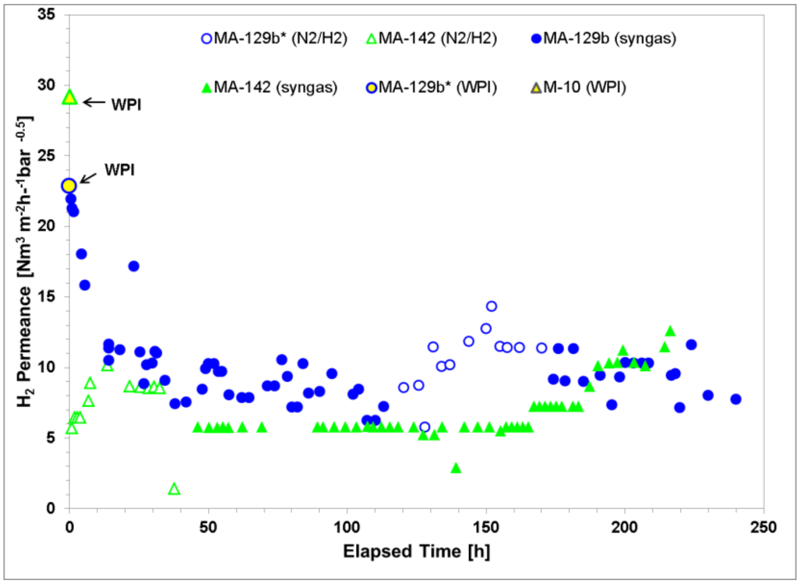

Figure 5.2. H_2 Purity produced by pure Pd membranes as a function of time.

Although, the previous Pd membranes showed an H_2 purity drop under syngas; MA-128b** had H_2 purities greater than 99.4% that remained constant for 175 h. The performance of MA-128b* is an exception of the already seen Pd membranes suggesting that the previously deposited Au still affected the performance of this membrane. Pure Pd membranes failed after ~200 h of operation under syngas conditions. The harsh environment reduced their stability causing the formation of pinholes on the surface of the membrane as shown in Figure 5.3. The SEM picture shows the surface morphology of MA-142 in the deteriorated area. The presence of a crack caused by the long-term exposure of syngas or H_2S could be clearly seen. These defects appeared to a lower extent in MA-129B* because of its thicker Pd layer. Studies on Pd membranes were usually conducted for short periods of time under clean gas conditions [79,80]. However, as demonstrated here, it was necessary to test the membranes for a minimum of 200 h under industrial conditions to ensure their stability. Ryi et al. [81] attempted to increase the stability of pure Pd membranes within this timeframe. They showed that pure Pd membranes tested under pure H_2 conditions tended to fail before 200 h. Furthermore, the H_2 purity produced by MA-131B*** was 99.97% at 15 bar, but declined when the pressure was increased to 20 bar. This suggested the existence of pinholes that allow more impurities to penetrate the Pd layer at higher pressures.

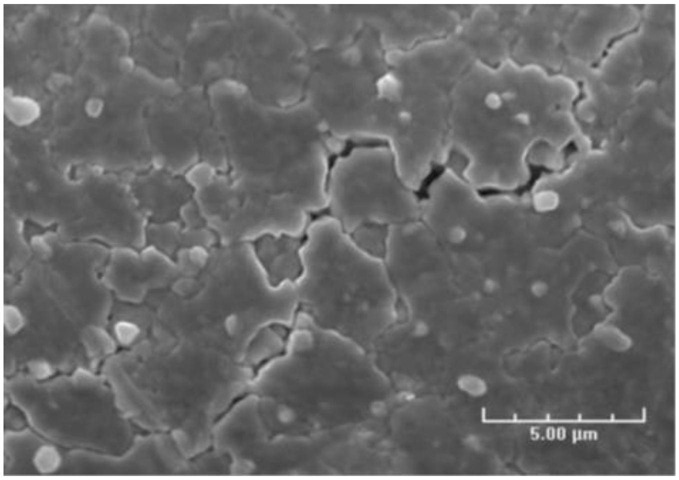

Figure 5.3. SEM image of a crack formed at the Pd surface layer of MA-142.

5.3. Group 2. Pd/Au Membranes

Group 2 is composed of asymmetric composite membranes formed by Pd and on top a layer of Au. Different thicknesses, shown in Table 5.3, were used for testing the features of these membranes. MA-126B* had a dense Pd layer of about 8.2 µm thickness with a topmost layer of Au with a thickness of 0.16 µm. MA-128* had a Pd thickness of 10 µm and 0.2 µm of Au. MA-137B** consisted of an 8.7 µm Pd layer and an 0.5 µm Au layer. Both MA-126B* and MA-137B** had a similar palladium thickness but different amounts of Au for comparison. Membrane MA-129Bb consisted of a dense 14 µm Pd layer and was additionally covered with an 0.9 µm Au layer. Notice that MA-129Bb was designated as MA-129B before Au was deposited and was tested as a pure Pd membrane in the previous section. MA-129Bb had a similar Au load as MA-137B** but twice as much Pd. Finally, MA-150B consisted of a dense Pd layer of only 5 µm covered with an 0.8 µm Au layer and an 0.9 µm Pd layer on top of the Au layer.

Table 5.3. Pd-Au asymmetric membrane composition.

Membrane Nomenclature	Composition / µm
MA-126B*	8.2(Pd) + 0.16(Au)
MA-128*	10(Pd) + 0.2(Au)
MA-137B**	8.7(Pd) + 0.5(Au)
MA-129Bb	14(Pd) + 0.9(Au)
MA-150B	5(Pd) + 0.8(Au) + 0.9(Pd)

The permeance of the Pd/Au membranes was tested under H_2/N_2 mixture and syngas atmospheres. Figure 5.4 shows the permeance of these membranes as a function of time. The permeance of the membranes under H_2/N_2 mixture and under syngas is shown for all membranes including the WPI permeance shown as a single gray-labeled point.

MA-126B* showed an initial permeance at WPI of 28.2 $Nm^3m^{-2}h^{-1}bar^{-0.5}$ and dropped to 21 $Nm^3m^{-2}h^{-1}bar^{-0.5}$ under H_2/N_2 and to 8.5 $Nm^3m^{-2}h^{-1}bar^{-0.5}$ under syngas. MA-137B** had a WPI permeance of 29.2 $Nm^3m^{-2}h^{-1}bar^{-0.5}$. Under H_2/N_2 atmosphere, the membrane showed a permeance of 9.5 $Nm^3m^{-2}h^{-1}bar^{-0.5}$. The permeance increased after switching to syngas, and then decreased to reach a steady average permeance of 13 $Nm^3m^{-2}h^{-1}bar^{-0.5}$. MA-137B** was tested for 470 h producing 0.63 kg of H_2 per day at the end of testing.

MA-129Bb had a WPI permeance of 11.4 $Nm^3m^{-2}h^{-1}bar^{-0.5}$ with a H_2/He selectivity >2700. This Pd/Au membrane was tested for 250 h under H_2/N_2 mixtures and syngas atmospheres. After 40 h in H_2/N_2 mixture, the permeance had a steady permeance which corresponded to a 25% decrease in permeance. Upon syngas introduction, the H_2 permeance decreased 37%.

MA-150B showed a WPI permeance of 22.7 $Nm^3m^{-2}h^{-1}bar^{-0.5}$ with a H_2/He selectivity >2207. MA-150B was tested for a total of 350 h. The H_2 permeance of MA-150B declined by 36% under an H_2/N_2 mixture and, upon the introduction of syngas, it gradually decreased further. MA-128* was not tested under pure H_2 at WPI therefore its permeance was not included in Figure 5.4. However, its permeance was the same under H_2/N_2 and syngas (17.6 $Nm^3m^{-2}h^{-1}bar^{-0.5}$) conditions. The membrane remained stable for 100 h, but an increase in H_2 flux occurred along with a large leak.

Similar to pure Pd membranes, Pd/Au membranes exhibited an initial drop in permeance as soon as they came in contact with the N_2/H_2 mixture. This phenomenon supported the fact that some contaminants were adsorbed on the piping walls and stripped out with the hot N_2/H_2 mixture. The Au content on the membranes reduced the H_2 permeance. For instance, MA-137B** with a thinner Au layer (0.5 µm) displayed a permeance 40% greater than MA-129Bb (0.9 µm). In the case of MA-129Bb and MA-150B, both membranes had a similar Au load; however, MA-150B had an upper Pd layer, which could have improved its permeance. Additionally, it is important to notice that MA-150B had a thinner Pd layer. MA-129Bb was subjected to syngas atmosphere and H_2S treatments after 120 h of testing. H_2S was introduced at a concentration of 10.6 ppm leading to a reduction of H_2 permeance to 3 $Nm^3m^{-2}h^{-1}bar^{-0.5}$. After 200 h, the H_2S input was stopped and the membrane recovered its initial H_2 permeance of 7.2 $Nm^3m^{-2}h^{-1}bar^{-0.5}$ in about 30 minutes.

The addition of Au did not seem to affect the initial WPI permeance when compared with pure Pd membranes. The reason was that the active sites of the Pd layer were available for H_2. Gold did not seem to block these sites, suggesting that intermetallic diffusion of Au into Pd occurred. In addition, it could be seen that Pd/Au membranes experienced a fast loss in permeance at first, most probably due to the adsorption of unknown contaminants on the surface and no further significant permeance loss occurred indicating a low or negligible bulk contamination. Surface poisoning affected the permeance of the membrane in two stages: surface and bulk sulfidation. First, the surface of the membrane was contaminated by H_2S, failing to separate H_2. This was evidenced by the initial decrease in permeance (from the permeance measured at WPI to the initial sulfur exposure). The second stage involved the bulk deterioration of the Pd film, which in the case of Pd/Au was not present causing no further permeance drop.

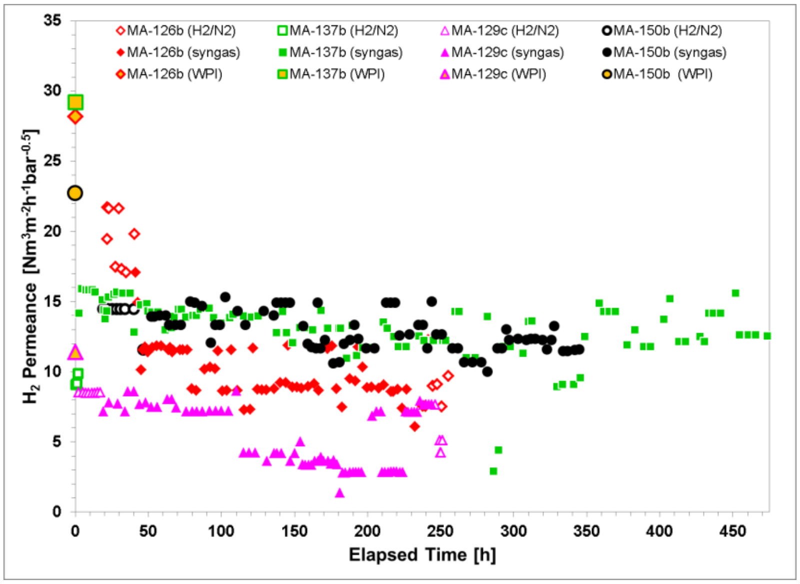

Figure 5.4. H_2 Permeance of Pd/Au membranes as a function of time.

The purity of the Pd/Au membranes was more stable throughout the test as shown in Figure 5.5. The H_2 permeance of the Pd/Au membranes did not depend on whether the feed gas was H_2/N_2 or syngas. The H_2 purity produced by the MA-126B* membrane stayed above 99.89% during the entire 220 h of testing. After removal from the test, no carbonaceous deposit was observed on the membrane surface. MA-137B** had a rather stable purity ~99.9% throughout the measurements. MA-129Bb showed that the introduction of H_2S between 120 h and 200 h had no effect on H_2 purity. The resulting H_2 purity under syngas during 250 h was >99.5%. MA-150B had a stable H_2 purity profile of 99.5%. These results showed that Pd/Au membranes were stable in a syngas atmosphere for over 200 h, in contrast with pure Pd membranes.

Under syngas, the H_2 purity produced by these membranes remained constant, but the permeance decreased. This suggested that the active sites of the surface became poisoned at first, decreasing the H_2 permeance. In the case of pure Pd membranes, the bulk Pd layer was further poisoned, damaging it and generating defects. However, for Pd/Au membranes, while the surface became contaminated, Au diffused towards the defects on the bulk preventing the development of pinholes. Indeed, Au seemed to fill and cover any pinholes or defects produced at the Pd layer, acting as a patch paste.

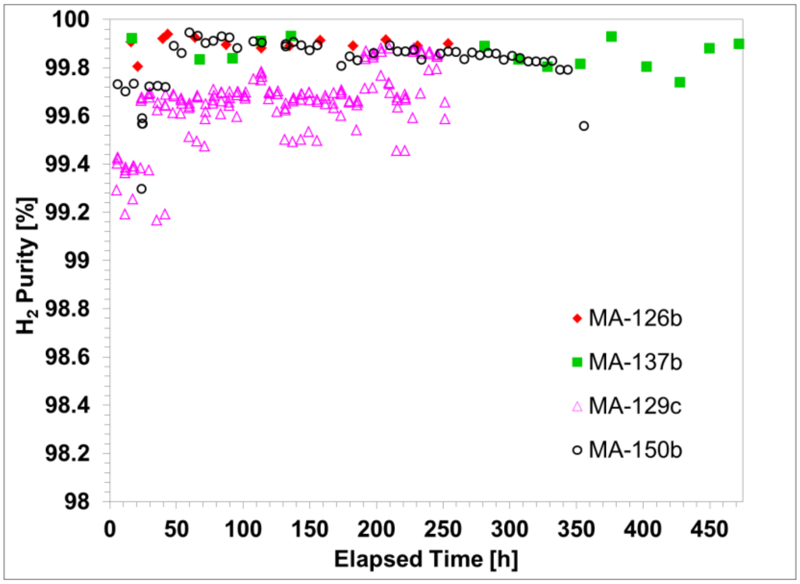

Figure 5.5. H_2 Purity produced by of Pd/Au membranes as a function of time.

5.4. Group 3. Pd/Pt Membranes

Group 3 is composed of asymmetric membranes formed by Pd with Pt on the top. Although few studies have been reported on Pd/Pt membranes; it is suggested that Pt has H_2S resistant properties that can be exploited to improve the resistance of Pd/Alloy membranes [46,82,83]. Kajiwara et al. showed a small change on the lattice structure of Pt (0.39 to 0.35 nm) after sulfidation compared to that of Pd (0.39 to 0.65 nm) [84]. The reported Pd/Pt membranes had cracks allowing the leak of other gases to pass through.

For the purposes of this investigation, two membranes were fabricated with compositions shown in Table 5.4. MA-151B consisted of a 3.9 µm thick dense Pd layer, which was additionally covered, with an 0.5 µm Pt layer and an 0.9 µm Pd layer on top of the Pt layer. MA-158 membrane was plated with 4.8 µm of Pd and 0.45 µm of Pt on top, to produce a Pd/Pt asymmetric membrane. Notice that this is the first time that the results of a performance assessment of Pd/Pt membranes are reported in the literature under actual coal derived syngas.

Table 5.4. Pd/Pt membrane composition.

Membrane Nomenclature	Composition / µm
MA-151B	4(Pd) + 0.5(Pt) + 0.9(Pd)
MA-158	4.8(Pd) + 0.45(Pt)

Figure 5.6 shows the H_2 permeances at WPI, under H_2/N_2 mixture and syngas of the Pd/Pt membranes as a function of time. The H_2 permeance of MA-151B (Pd/Pt/Pd) measured at WPI was 15.7 $Nm^3m^{-2}h^{-1}bar^{-0.5}$ with a H_2/He selectivity of 393. Although, MA-151B had a high platinum content close to its surface; it still displayed a high H_2 permeance. This Pd/Pt/Pd membrane was tested for a total of 350 h under H_2/N_2 and syngas atmospheres. The membrane first dwelt under H_2/N_2 where the permeance declined by 36%. Upon syngas introduction, a slight decrease in permeance was observed reaching a minimum of 8.4 $Nm^3m^{-2}h^{-1}bar^{-0.5}$. At 160 h, the flow started to increase abruptly indicating the opening of pinholes and a loss in selectivity. The feed gas was alternated between H_2/N_2 and syngas but the permeance kept increasing independently of the composition of the feed.

The H_2 permeance of MA-158 measured at WPI was 16.5 $Nm^3m^{-2}h^{-1}bar^{-0.5}$ with an ideal selectivity of 590. At NCCC, MA-158 was tested for a total of 150 h. The permeance of the membrane declined by 59% under H_2/N_2, as seen in previous membranes. The permeance of MA-158 also remained relatively constant in syngas after 150 h of testing. Unfortunately, the gasifier' operation stopped and further testing was not performed in order to observe whether this Pd/Pt membrane also failed at times >150 h. Since, MA-151B had a Pd layer on top of the Pt film; its H_2 permeance was slightly higher than MA-158.

The magnitude of the H_2 permeance of the Pd/Pt membranes was lower when tested at WPI than those composed of pure Pd. This was the result of covering the surface of the Pd layer, where the active sites were located with Pt. Once the membrane became poisoned pure Pd and Pd/Pt membranes showed permeances of the same magnitude. This indicated that while the active sites of the surface of pure Pd membranes became occupied by the contaminant; Pd/Pt membranes reduced the effect of the contaminant. Pt might have an effect on reducing poisoning, but further investigation is required.

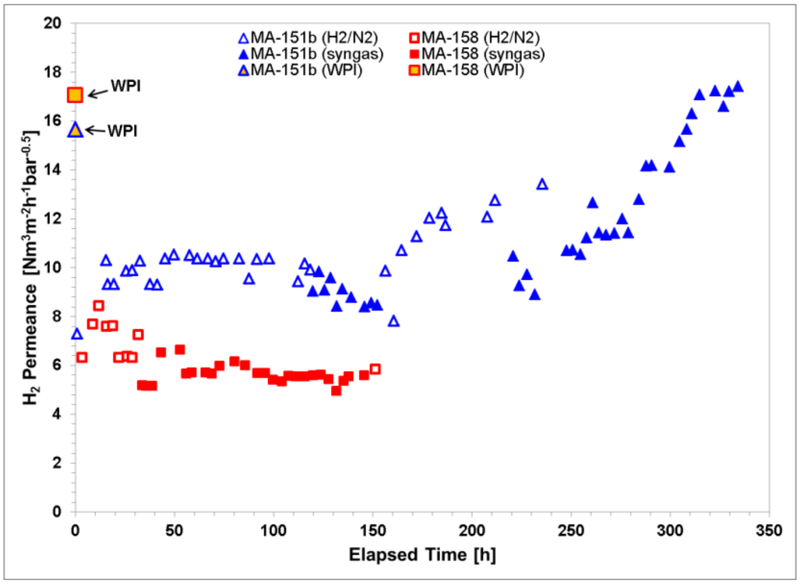

Figure 5.6. H_2 Permeance of Pd/Pt membranes as a function of time

Figure 5.7 shows the H_2 purity of the Pd/Pt membranes as a function of time. MA-151B showed an initial H_2 purity of 98% that remained stable for 100 h under H_2/N_2. After feeding syngas for about 50 h; the purity of the membrane increased to 99%. At this moment, the H_2/N_2 was introduced again, and the purity experienced a steady drop to 93%. The feed gas was changed again to syngas where the purity seemed to recover. However, the decline in purity continued until the end of the test. MA-158 was tested for a shorter time period. This membrane was more stable and produced a higher H_2 purity than that of MA-151B. Under H_2/N_2 atmosphere the membrane showed an H_2 purity of 99%, while under syngas, the membrane produced H_2 with a purity of >99.5%. Notice that the produced H_2 purity of MA-151B in Figure 5.7 was similar to MA-142 (pure Pd) in Figure 5.2. Both membranes remained stable for about 150 h and afterwards, a sudden loss of selectivity occurred. This suggested that Pt did not patch the defects in the Pd layer.

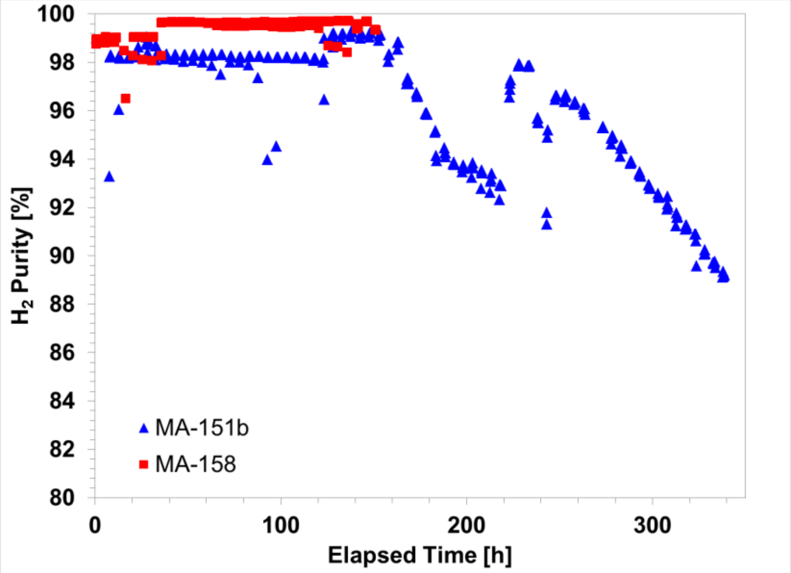

Figure 5.7. H_2 Purity produced by Pd/Pt membranes as a function of time.

5.5. Group 4. Pd/Au/Pt Membranes

Group 4 is comprised of membranes formed by Pd, Au and Pt. Ternary alloy membranes such as Pd/Cu/Ni [85], Pd/Ag/Cu [86] and Pd/Cu/Au [87] have been extensively reported. However, performance assessment results of Pd/Au/Pt membranes have never been reported in the pertinent literature. It was expected that the combination of these metals will highlight the properties of Au and Pt in their capacity to enhance the sulfur resistance of the membranes.

Different compositions were used for testing the characteristics of these metals as shown in Table 5.5. MA-145B and MA-138C had similar palladium and gold loads (close to ~8.5 µm of Pd and ~0.34 µm of Au), but a different platinum load with 0.1 µm and 0.06 µm, respectively. MA-136B membrane had a 10.3 µm of Pd, and 0.3 µm layer of Au on top and an 0.09 µm layer of Pt.

Table 5.5. Pd/Au/Pt membrane composition.

Membrane Nomenclature	Composition / µm
MA-145B	8.5(Pd) + 0.33(Au) + 0.1(Pt)
MA-138C	8.5(Pd) + 0.35(Au) + 0.06(Pt)
MA-136B	10.3(Pd) + 0.3(Au) + 0.09(Pt)

The H_2 permeances of the Pd/Au/Pt membranes are shown in Figure 5.8. The H_2 permeances measured at WPI are shown in a single- point format as previously indicated, and as a function of time under H_2/N_2 and syngas. MA-145B displayed a H_2 permeance at WPI of 17.4 $Nm^3m^{-2}h^{-1}bar^{-0.5}$ with a H_2/He selectivity >1000. At NCCC, MA-145B was tested for 460 h; under H_2/N_2, the permeance declined from its initial WPI value. The permeance partially recovered after 13 h of testing. Upon syngas introduction, the permeance first decreased but remained constant. A gasifier trip occurred and a H_2/N_2 mixture was introduced to preserve the membrane. Under H_2/N_2, the permeance recovered, showing a permeance close to the one measured at WPI. The recovery of the permeance might be the result of the Pt addition, yet this hypothesis needs further verification. Due to the long time needed to repair the gasifier, the membrane was cooled down to room temperature and remained at atmospheric temperature and pressure. After the gasifier was repaired, a second test was started. The membrane dwelt under an H_2/N_2 atmosphere and the permeance was similar as before the cooling down. The permeance under syngas was 11 $Nm^3m^{-2}h^{-1}bar^{-0.5}$ and remained stable. This permeance was similar to the one measured during the first 60 h in syngas. Unfortunately, a second gasifier trip occurred and the run was terminated.

The H_2 permeance of MA-138C at WPI was 28.4 $Nm^3m^{-2}h^{-1}bar^{-0.5}$ with a H_2/He selectivity >680. MA-138C was tested for a total time of 169 h. The membrane first dwelt under H_2/N_2 where the permeance declined compared with its initial WPI value. After 40 h under H_2/N_2 the average permeance decreased by 65%. The introduction of syngas had no significant effect on the permeance. The permeance of MA-138C was 9.5 $Nm^3m^{-2}h^{-1}bar^{-0.5}$ and remained constant after 123 h under syngas. The feed was switched back to H_2/N_2 where the membrane exhibited the same permeance as before feeding with syngas.

The WPI permeance of MA-136B was 22 $Nm^3m^{-2}h^{-1}bar^{-0.5}$ with an ideal selectivity of 732. At NCCC, MA-136B was tested for 718 h. The membrane first dwelt under H_2/N_2 where the permeance decreased compared to the levels previously measured at WPI. Under H_2/N_2, the average permeance had a permeance drop of 60%. Syngas was fed afterwards and maintained for 578 h. During the first 200 h the H_2 permeance increased slightly followed by a sustained average permeance of 10.5 $Nm^3m^{-2}h^{-1}bar^{-0.5}$until the end of the test.

Compared to pure Pd membranes, the ternary alloy displayed WPI permeances with a similar magnitude. Although, Pt slightly reduced the permeance of the Pd/Pt membranes; its effect was not evident in this group. The difference was due to the smaller amount of Pt deposited onto these ternary membranes. Au, on the other hand, did not seem to interfere with active sites of the Pd layer.

Furthermore, compared with pure Pd membranes, the permeance of Pd/Au/Pt membranes did not deteriorate with time. The effect could be attributed to the Au present in the membranes.

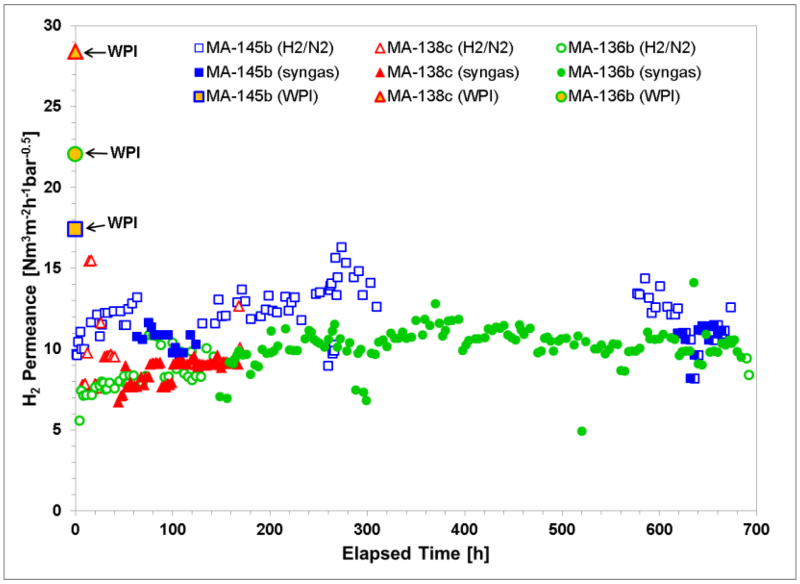

Figure 5.8. H_2 Permeance of Pd/Au/Pt membranes as a function of time.

.

The purity produced by the Pd/Au/Pt membranes is shown in Figure 5.9. MA-145B produced H_2 with a purity of >99.8% throughout the test. The H_2 purity produced by MA-138C was higher under syngas than the purity under H_2/N_2. For instance, the average purity of the H_2 produced under H_2/N_2 and syngas was 96.9 and 98.8%, respectively. MA-136B produced H_2 with purity >99% but had a slight but steady decline throughout the 700 h of operation. Notice that the statistical outliers present in the above figure can be attributed to inevitable errors on the experimental measurements involving a rather complex process system such as the one under consideration. However, the main/central trend depicted in the membrane's performance profile is clearly identifiable, thus reliably supporting the aforementioned conclusions.

Compared with pure Pd membranes, the ternary alloy showed superior stability for producing highly pure H_2. Although MA-138C did not reach a purity of 99%, it remained stable throughout the test. The cause of the lower selectivity of MA-138C could be a small defect present in the membrane. This defect did not grow since the H_2 purity did not decrease. This suggests that Au stabilized the pinhole and did not allow its deterioration. The effect of Pt on this pinhole stabilization could not be concluded since, leak growth was observed in one of the Pd/Pt membranes.

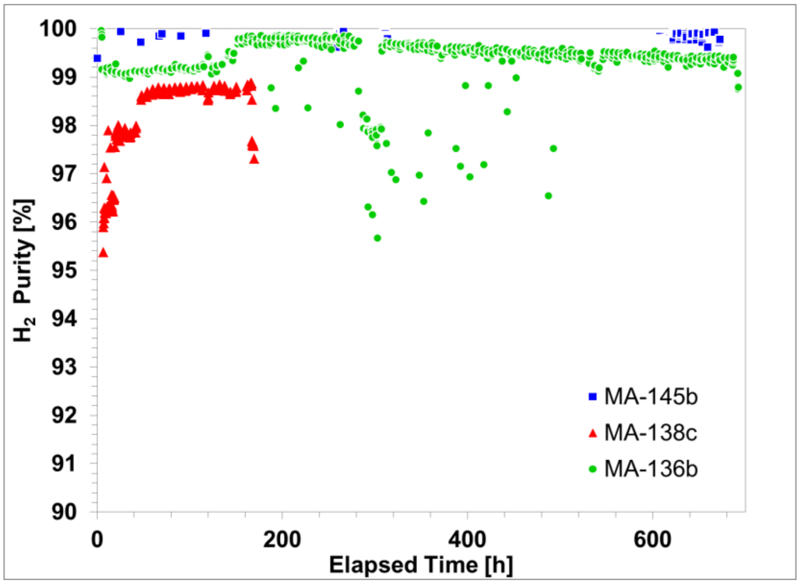

Figure 5.9. H_2 Purity produced by Pd/Au/Pt membranes as a function of time.

5.6. Overall Performance of the Pd and Pd/Alloy Membranes

The performance of the Pd, Pd/Au, Pd/Pt and Pd/Au/Pt composite asymmetric membranes under coal-derived syngas was evaluated in four categories: H_2 permeance, permeance drop compared to the value measured at WPI under pure H_2, quality of produced H_2, and stability of the membrane. Although, each membrane performed differently, the average value of the Pd and Pd/Alloy groups was used to evaluate their characteristics. Notice that Table 5.6 shows the characteristics of 11 membranes, which are the most representative for this study.

Permeability was used as a parameter for evaluation, since it provided a better understanding of the intrinsic properties of the material that allowed/promoted hydrogen permeation. Permeability excluded the resistance provided by the thickness of Table 5.6, had the following order Pd > Pd/Au/Pt ≥ Pd/Au > Pd/Pt. Pure palladium displayed the highest permeability, while all composite Pd/Alloy membranes showed a reduced permeability. This was reasonable since Pd was the active material that catalyzed the dissociation and thus the transport of H_2. The permeability of the Pd/Au membranes under syngas was 19% lower than that of pure Pd membranes. Platinum seemed to result in a deterioration of the membrane's permeance profile. For instance, the Pd/Pt membranes displayed the lowest permeability, 58% lower than pure Pd membranes. As explained before, Pt blocked the active sites of the Pd layer and therefore resulted in lower activity. For the case of the ternary composite membranes, their H_2 permeability decreased by only 11%. The drop in permeability was lower than Pd/Pt possibly because of the presence of Au and the smaller Pt load.

All Pd and Pd/Alloy membranes showed a permeance drop when in contact with the stream containing traces of different contaminants such Mg, Na, Hg, S, etc. These contaminants were previously investigated and were found to be desorbed at the equipment walls. The permeance drop was estimated from the initial permeance displayed at WPI and the average permeance shown at NCCC. The permeance drop due to mass transfer resistance of gas mixtures is negligible and was estimated to be in the range of 0.6-1.6%. The order of membranes, from the lowest permeance drop to the highest, is as follows: Pd/Au > Pd/Pt > Pd/Au/Pt > Pd. Pure Pd membranes showed the highest permeance drop. Pd/Au membranes showed the smallest drop followed by Pd/Pt and the ternary membranes. These results suggested that adding alloys helped to protect the active sites of the Pd layer from harsh environments. Alloys seemed to hinder some of the sites where the poison attacked the surface of the membrane.

The maximum H_2 purities produced under actual syngas conditions by the different membranes had the following order: Pd/Au > Pd/Au/Pt > Pd > Pd/Pt as shown in Table 5.6. The presence of Au improved the H_2 selectivity of the membrane by patching any defects or pinholes on the surface of the Pd layer. On the other hand, the Pd/Pt showed the lowest H_2 purity. The effect of Pt appeared to be harmful to the production of pure H_2. The purity displayed by the ternary composite membrane was similar to Pd/Au. It seemed that even in small amounts, Au had a positive effect on the membrane.

The stability of the membranes was estimated based on the maximum time where the membranes achieved a consistent purity >99% under syngas conditions. Notice that, as shown in Table 5.6, the time of stability does not necessarily represent the time when the membrane failed in achieving a purity of 99%. In some cases, this time represented the moment when the test was terminated. For instance, the two tested Pd membranes failed in achieving this purity at 49.5 and 182.9 h. Therefore, it was considered that pure Pd membranes failed at 182.9 h, which was the maximum time found in this work. Membranes composed of Pd/Au did not fail during testing. They always displayed purities >99%, so the sole limitation was the testing time. The longest testing time under syngas atmosphere of Pd/Au membranes was 471 h. In the case of Pd/Pt membranes, one membrane failed after only 29 h of testing. The other Pd/Pt membrane did not fail, but its testing stopped after 112 h in syngas. The ternary Pd/Au/Pt membrane showed one failed membrane. This membrane did not reach a purity of 99% from the beginning of the test. The maximum operating time of Pd/Au/Pt membrane was 535.5 h. Therefore, the stability of the tested composite membranes followed the order of Pd/Au > Pd/Au/Pt > Pd > Pd/Pt. This implied that Au, during intermetallic diffusion, patched the defects that appeared in the Pd layer. Platinum had the opposite effect; it opened cavities within the Pd structure.

Table 5.6. Characteristics of the different Pd and Pd/Alloy membranes under coal-derived syngas.

Type	Membrane	Permeability[a)], $Nm^3m^1m^{-2}h^{-1}bar^{-0.5}$	Maximum H_2 purity, %	Initial permeance drop, %[b)]	Time w/ purity >99%, h[c)]	Reason of termination
Pure Pd	MA-129B*	$2.21x10^{-4}$	99.26	55	49.5	Failed
	MA-142	$9.03x10^{-5}$	99.73	75	182.9	Failed
	Average	$1.56x10^{-4}$	99.5	65		
Pd/Au	MA-126B*	$1.15x10^{-4}$	99.94	33	198.5	Stopped
	MA-137B**	$1.67x10^{-4}$	99.93	68	471	Stopped
	MA-129Bb	$1.02x10^{-4}$	99.88	36	223	Stopped
	MA-150B	$1.19x10^{-4}$	99.95	38	293	Stopped
	Average	$1.29x10^{-4}$	99.93	44		
Pd/Pt	MA-151B	$8.89x10^{-5}$	99.69	34	29.3	Failed
	MA-158	$4.09x10^{-5}$	99.07	59	112	Stopped
	Average	$6.49x10^{-5}$	99.38	46		
Pd/Au/Pt	MA-145B	$1.53x10^{-4}$	99.91	28	64.8	Stopped
	MA-138C	$1.06x10^{-4}$	98.83	65	N/A	Failed
	MA-136B	$1.55x10^{-4}$	99.86	61	535.5	Stopped
	Average	$1.38x10^{-4}$	99.53	52		

a) Permeability was estimated based on the total metal thickness of the membranes and calculated from the permeance under syngas conditions. b) The initial permeance drop was calculated from the permeance displayed by the membranes under pure H_2 vs. the permeance under syngas or N_2/H_2 mixture. c) This is the period of time where the membrane displayed a purity >99% under syngas conditions.

5.7. Performance of Au and Pt as Membrane Composites

It is important to notice that these results represent the actual performance of the membranes under real industrial conditions and therefore the environment was not controlled as in the laboratory. Therefore, further research investigations are undoubtedly warranted in order to have a more conclusive and sound understanding on the characteristics of these membranes. However, based on the performance of the Pd/Au and Pd/Au/Pt membranes shown in this work, the role of Au appears to be 1) a patching paste that cures the defects present at the surface of the membrane, 2) a pinhole stabilizer and 3) an agent that hinders poisoning. Competition of active sites, the Tamman temperature of Au and the Kirkendall effect [88] could certainly contribute to an explanation of the manifested properties. The Tamman temperature of Au (395^{o}C) is significantly lower than Pd (641 ^{o}C). Therefore, operating at 450 ^{o}C, places Au into a state of higher molecular mobility than Pd. In asymmetric membranes, at the Au-Pd boundary, the Kirkendall effect takes place. Gold crosses the Au-Pd boundary and diffuses into the Pd layer; while Pd remains relatively motionless within its limits. This effect allows Au to fill in the voids or defects present in the Pd layer like a patching paste. If the defect is significantly big, Au cannot fix the pinhole. However, its deposition at the walls of the defect seems to stabilize it and prevent further growth.

The experiments suggested that Au hindered poisoning of the Pd surface. This could be explained by competition for active sites during adsorption. Some of the sites where sulfur adhered were already occupied by Au preventing a strong attachment to the Pd surface. This was supported by the permeance recovery that Pd/Au membranes showed when treated under pure H_2 at 450^{o}C.
Platinum also appeared to hinder poisoning in a similar way as Au did, but did not seem to cover the defects of the Pd surface. The Tamman temperature of Pt (747.4^{o}C) is higher than Pd (641^{o}C). Therefore, for the case of Pd/Pt membranes, Pt was in a state of lower molecular mobility than Pd and consequently at the Pt-Pd boundary, the Kirkendall effect took place. Pd crossed the Pt-Pd boundary and diffused into the Pt layer; while Pt remained relatively stationary. This effect seemed to generate defects on the Pd layer. In the case of Pd/Au/Pt, Au has the highest mobility and can diffuse towards the Au-Pd or Au-Pt. Nevertheless, since the Tamman temperature of Pd is lower than Pt, Au will have a tendency to diffuse towards Pd. That was the reason why the curing effects of Au were notable in the ternary alloy. The diffusion of Pd towards Pt was minimized due to the presence of Au between both metals.

5.8. Post-Characterization of the Membranes Tested at NCCC

5.8.1 Permeance Recovery of MA-128C and MA-137B

After the syngas test at NCCC, two membranes MA-128C and MA-137B were further tested at WPI in a pure H_2 atmosphere at 450 and 500°C in order to study the possible recovery prospects of the H_2 permeance. The recovery of MA-128C, shown in Figure 5.10a, was performed in pure H_2 at 450 °C and a ΔP of 1 bar. The initial H_2 permeance measured at WPI in a pure H_2 atmosphere was 11.5 $Nm^3m^{-2}\ h^{-1}\ bar^{-0.5}$ and thus in excellent agreement with the final NCCC permeance of 11.1 $Nm^3m^{-2}h^{-1}bar^{-0.5}$. After 150 h at 450 °C, 24 h at 500 °C, and an additional 120 h at 450 °C, the H_2 permeance at 450 °C was 13.8 $Nm^3m^{-2}h^{-1}bar^{-0.5}$; that is, 78% of the initial permeance (17.7 $Nm^3m^{-2}h^{-1}bar^{-0.5}$) was recovered. Figure 5.10a also shows that after 150 h at 450 °C, the H_2 permeance reached a steady value, indicating that the maximum recovery value was reached. Furthermore, it appeared that the treatment at 500 °C did not enhance the recovery value since the permeance at 450 °C remains the same before and after the treatment at 500 °C. Table 5.7 lists the H_2 permeance measured at every stage of testing (at WPI, NCCC, and recovery at WPI) for all membranes. This result confirms the fact that poisoned pure Pd surfaces in actual syngas derived from coal can only be partially recovered in H_2 atmospheres at 450−500 °C.

The H_2 recovery test of MA-137B, shown in Figure 5.10b, was performed in pure H_2 at a ΔP of 1 bar in two steps: (1) 66 h at 400 °C and (2) 167 h at 450 °C. It was not possible to compare the final NCCC permeance with the initial H_2 permeance at 450 °C during the recovery process since at 400 °C in pure H_2 the H_2 permeance partially recovered after 66 h. After a dwell time of 167 h at 450 °C, the H_2 permeance increased steadily to a value equal to 30 $Nm^3m^{-2}h^{-1}bar^{-0.5}$, that is, the H_2 permeance measured at WPI before the syngas test. Therefore, the permeance of Pd−Au alloy membranes prepared by the deposition of a 0.5 μm Au layer on top of Pd appeared to be close to 100% recoverable after exposure to desulfurized syngas from coal. Hence, we achieved 100% recoverability by increasing the Au top layer from 0.2 to 0.5 μm. However, it is unfortunate that such Au addition did not eventually mitigate the initial H_2 permeance loss.

5.8.2 Microstructure and Au Surface Concentration of MA-137B

Figure 5.11 shows the cross-section of membrane MA-137B. The dense layer of MA-137B was uniform with an average thickness of 5.5 μm. After the first H_2 test (data not included in this work), the Pd thickness determined by gravimetric measurements was estimated and found equal to approximately 4 μm. Since after the first test 2.1 μm of Pd and 0.5 μm of Au were plated, the approximate theoretical thickness of 6.6 μm was found to be in very good agreement with the 5.5 μm in thickness determined by SEM. Taking into consideration that the He permeance of the bare support after grading was 80 $Nm^3m^{-2}h^{-1}bar^{-0.5}$ and that during the first H_2 test the membrane was only 4-μm-thick, the H_2 permeance at 450 °C should have been equal to 68 $Nm^3m^{-2}h^{-1}bar^{-0.5}$ according to our mass transfer model. However, the permeance of MA-137B (PSS-316L/grading/3−4 μm Pd) during the first test was only 44 $Nm^3m^{-2}h^{-1}bar^{-0.5}$ at 450 °C, indicating that, in addition to mass transfer resistance in the porous support, other possible resistances seem to be playing a significant role in the H_2 permeation mechanism. As of today, efforts are being made in determining whether the polishing steps add significant resistance to the H_2 transport through the composite membrane. Indeed, the polishing step may contribute to the creation of an additional resistance since polishing may lead to a thin gap in between Pd layers. In the presence of such gaps, an increase in resistance for the H_2 permeation would be possible since H_2 has to reassociate, diffuse molecularly across the gap, and redissociate on the Pd to overcome the gap barrier. Such gaps between Pd layers have been observed in our laboratory but could not be associated with an increase in resistance for H_2 permeation at the moment. However, even if we assumed a H_2 permeance value of 68 $Nm^3m^{-2}h^{-1}bar^{-0.5}$ for MA-137B after the first test, that would only represent 60% of the permeance of a Pd foil with a similar thickness of 3−4 μm, indicating the presence of significant mass transfer resistance within the porous support.

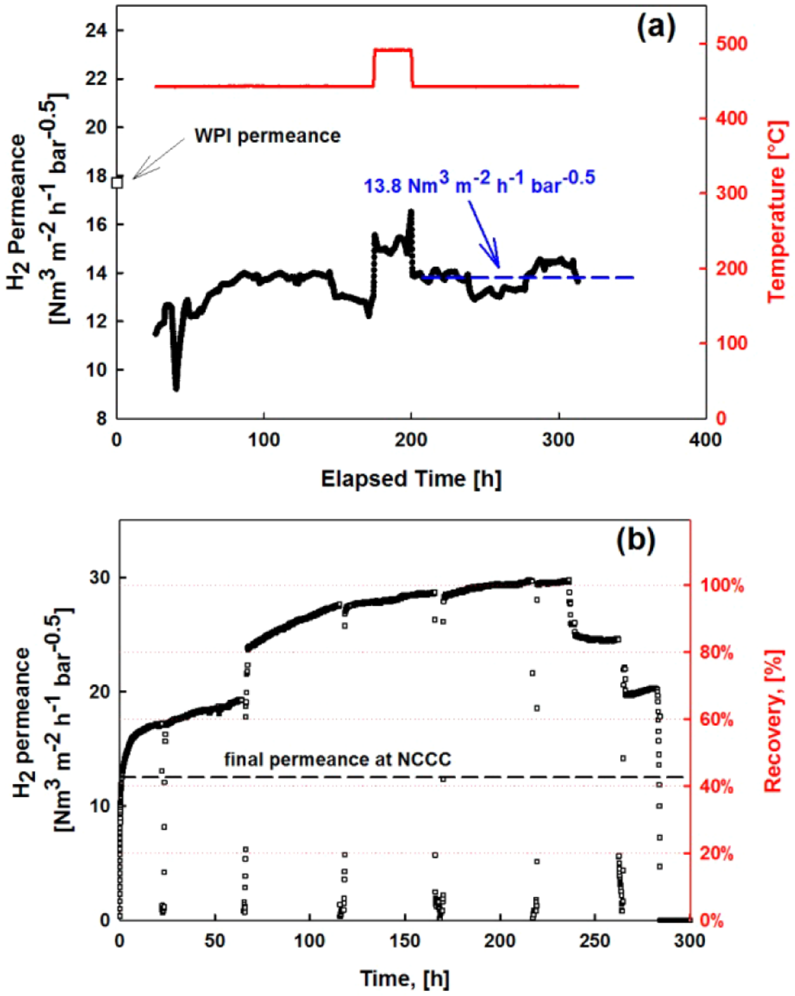

Figure 5.10. H_2 permeance as a function of time during a recovery test at WPI for (a) MA-128C and (b) MA-137B.

Table 5.7. Performance Assessment and Recovery for M-03b and M-07.

Membrane	WPI Permeance*	NCCC Permeance	Permeance ratio (NCCC/WPI)	Permeance after recovery	Permeance ratio (recovery/WPI)
MA-128C	17.1	11.1	63	13.8	78
MA-137B	29.2	14.4	49	30	100

* Notice that all permeances in the table have units of $Nm^3m^{-2}h^{-1}bar^{-0.5}$

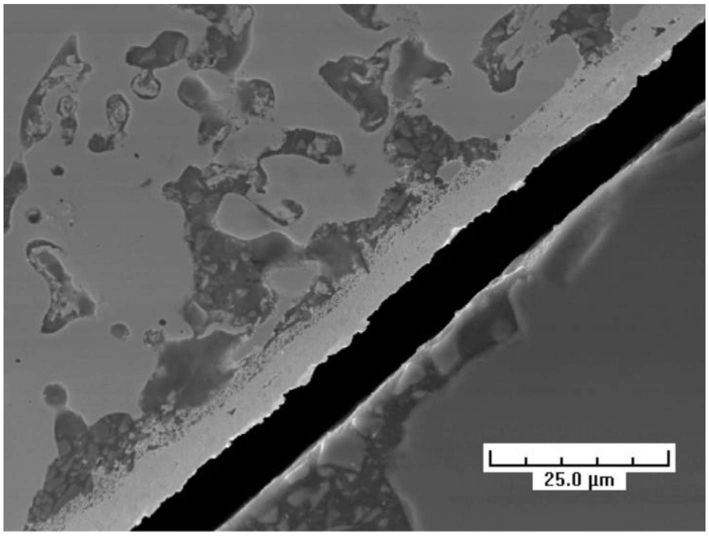

Figure 5.11. Cross section of MA-137B.

The Au content of the MA-137B membrane was determined with gravimetric methods and X-ray diffraction while EDX was used to measure the thickness of the Pd−Au alloy. Figure 5.12 shows a dense layer of MA-137B was uniform with an average thickness of 5.5 µm. After the first H_2 test (data not included in this work), the Pd thickness determined by gravimetric measurements was estimated and found equal to approximately 4 µm. Since after the first test 2.1 µm of Pd and 0.5 µm of Au were plated, the approximate theoretical thickness of 6.6 µm was found to be in very good agreement with the 5.5 µm in thickness determined by SEM. Taking into consideration that the He permeance of the bare support after grading was 80 $Nm^3m^{-2}h^{-1}bar^{-0.5}$ and that during the first H_2 test the membrane was only 4-µm-thick, the H_2 permeance at 450 °C should have been equal to 68 $Nm^3m^{-2}h^{-1}bar^{-0.5}$ according to our mass transfer model. However, the permeance of MA-137B (PSS-316L/grading/3−4 µm Pd) during the first test was only 44 $Nm^3m^{-2}h^{-1}bar^{-0.5}$ at 450 °C (as mentioned earlier), indicating that, in addition to mass transfer resistance in the porous support, other possible resistances seem to be playing a significant role in the H_2 permeation mechanism. As of today, efforts are being made in determining whether the polishing steps add significant resistance to the H_2 transport through the composite cross-section line scan analysis performed on MA-137B. While Figure 5.12a shows a cross-section with the line along which the line scan was performed, Figure 5.12b shows the Pd and Au composition along the arrow. Even though elemental compositions determined with EDX techniques cannot be trusted without the use of standards, the line scan still allows the determination of the thickness of the Pd−Au layer or the depth of Au diffusion into the Pd layer. In the case of MA-137B, the 0.5 µm of Au formed a 2.0−2.5-µm-thick Pd−Au layer with a linear decrease in Au concentration. Hence, the structure of MA-137B consisted of the porous support 316L, the grading layer, 3.0−4.0 µm of Pd, and approximately 2.0−2.5 µm of a Pd−Au alloy with a significant Au gradient.

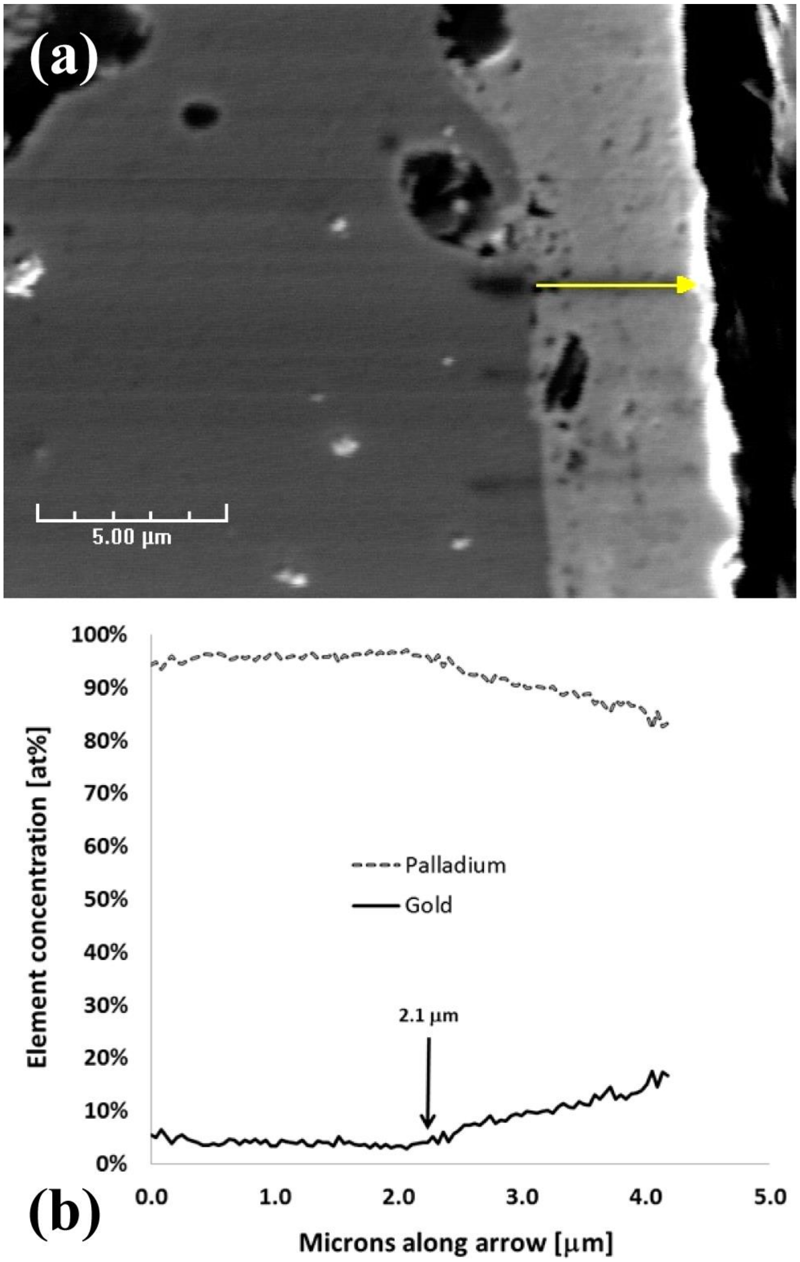

Figure 5.12. (a) Cross-section of MA-137B showing the arrow along which the line-scan was performed. (b) Elemental composition (atom %) as a function of distance along the line-scan arrow.

Knowing the microstructure of MA-137B, the average Au content of the Pd–Au alloy (2.0–2.5 µm in thickness) laying on top of the Pd layer (3.0–4.0 µm in thickness) could be determined gravimetrically. From the weight gain, it was determined that a 0.5 µm Au layer was plated. Taking 2.5 µm as the thickness of the Pd–Au layer, it is then reasonable to assume that 2.0 µm of Pd were needed to form the Pd–Au alloy layer. Hence, it was possible to calculate an average Au content of 19 atom % for the 2.5-µm-thick Pd–Au alloy on the outer surface of MA-137B. Assuming the gradient to be linear, as shown by EDX, the surface Au concentration could then be as high as 38 atom %. The average Au content of the Pd–Au layer was also determined by X-ray diffraction. Figure 5.13a shows the X-ray pattern of M-07, with the Au and Pd reference peaks overlaid, and Figure 5.13b shows the lattice cell parameter calculated at every reflection as a function of $\cos^2(\theta)$ for a more precise determination of the cell value. From Figure 5.13a, one can clearly see that all peaks of M-07 lie between the Au and the Pd standard peaks, yet the

Pd–Au alloy is richer in Pd since peaks are closer to the Pd lines. Calculating the lattice parameter for all scanned reflections and plotting them as a function of $\cos(\theta)^2$, an average lattice parameter of 3.934 nm was calculated for the Pd–Au alloy which corresponded to an average Au content of 23 atom % (Vegard's law in Okamoto and Massalki [89]). The XRD Au content was in good agreement with the average Au content determined from gravimetric methods, which was expected since the X-rays' penetration in metals falls within the 1.5–2.5 μm range. It is important to keep in mind that the Au surface concentration was higher than 23 atom %.

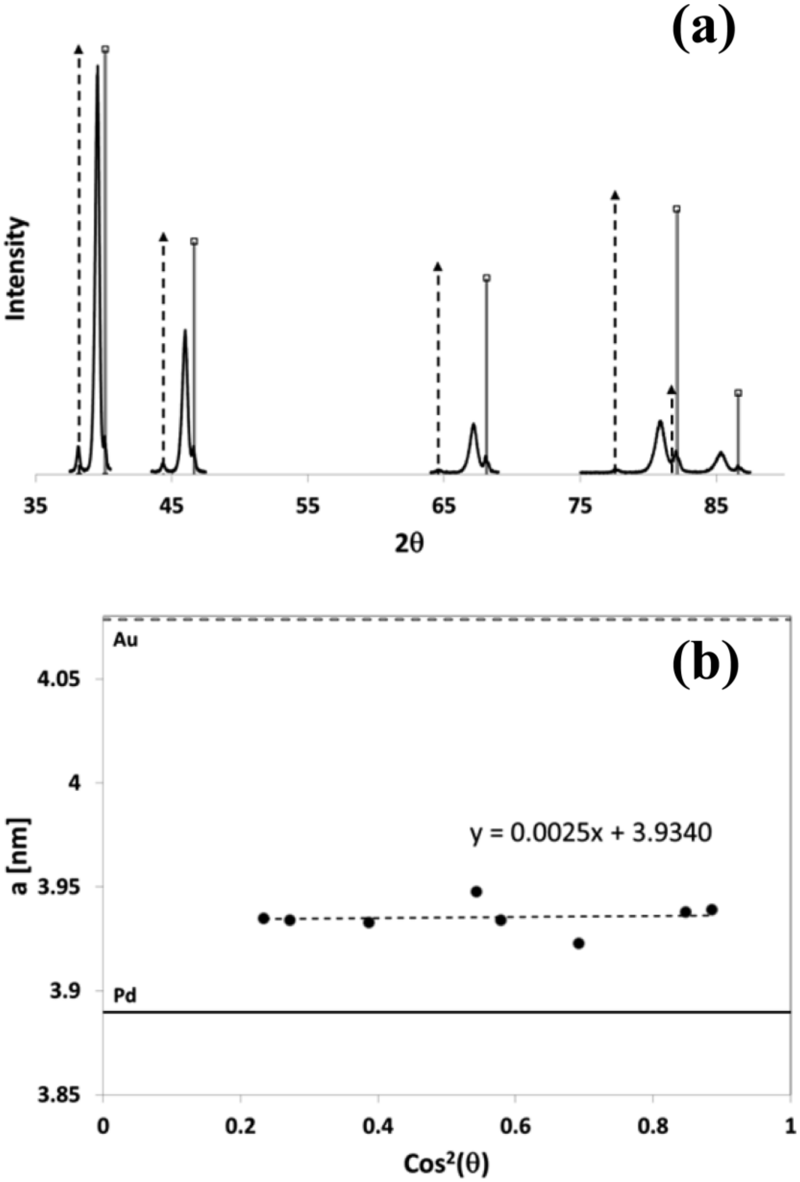

Figure 5.13. (a) X-ray pattern of M-07 with Au (dash) and Pd (full) lines overlaid. (b) Pd–Au alloy lattice parameter as a function of $\cos^2(\theta)$ for lattice parameter determination.

5.8.3 XPS Study of Pd Surfaces Exposed to Actual Desulfurized Syngas

The XPS analysis of the Pd surfaces exposed to actual coal derived syngas was performed. Efforts were made to understand the initial permeance decline occurring even in the presence of N_2–H_2

mixtures due to the carry-over of poisoning compounds. The XPS analysis of a 0.1 µm grade 1 cm^2 PSS 316L coupon plated with 2.0−4.0 µm of Pd and attached to membrane MA-128C was performed to determine the contaminants that would deposit on a pure Pd surface. Only the Pd coupon attached to MA-128C was analyzed, and Table 5.8 lists all the elements found on its surface. Among all contaminants that could be present in syngas only Mg, Na, O, Pd, C, S, F, As, Sb, Cd, Pb, Zn, V, Cl, B, P, Se, and Au were scanned and Na, Mg, O, S, Hg, and C were found. The depth profile of all elements, except sulfur, was performed and is shown in Figure 5.14. Counting for sulfur during depth profile analysis was unfortunately omitted, and new coupons exposed to syngas will be analyzed during the next round of campaigns to determine the sulfur depth profile concentration within the Pd bulk. Na and Mg did not pose real concerns since their presence could easily be attributed to ashes. Oxygen was also present but was not considered as a poisoning agent even though it may occupy H_2 adsorption sites. Furthermore, Na, Mg, and O were detected up to a depth of 30 nm only. Hg was detected up to 300 nm but at a very low level of 0.1 atom %. To the best of our knowledge, the poisoning effect of Hg on the hydrogen permeance of Pd and Pd−Au alloys has never been studied before; therefore it is quite difficult to relate the initial permeance decline to the Hg content. For the sake of the discussion in the context of this work, we assumed the effect of Hg to be negligible as a “first approximation.” The sulfur concentration at the Pd surface was 1 atom %, which was significantly lower than the S concentration found by Chen after exposing Pd coupons to even 0.2 ppm H_2S at 400 °C. Considering that the S atom blocks four active sites for the H_2 dissociation,53−56 only 8% of the Pd surface atoms are unavailable for H_2 dissociation. This number appears to be low in order to be responsible for the high permeance reduction of 37% observed in MA-128C. Indeed, considering the multistep model for the H_2 permeation a pure Pd membrane of 8 µm in thickness at 450 °C with a H_2 partial pressure of 4 bar should have a H_2 surface coverage of approximately 76%. Therefore, very little H_2 flux reduction would be expected when the atomic coverage of the poisoning component is below 24%. This finding is also substantiated by the calculations performed using a competitive adsorption model for H_2 permeation on the basis of which, and under the same operating conditions reported above, no appreciable flux reduction has been predicted.

Carbon was found at a concentration of 68.6 atom % at the surface, indicating the presence of a carbon overlayer on the very top of the sample. The carbon concentration decreased rapidly to approximately 40 atom % at 25 nm and then somewhat gradually to 16 atom % at 150 nm and finally down to 3−5 atom % at a depth of 1000 nm. It is interesting to highlight the fact that even though XPS showed the presence of a carbon overlayer, the Pd coupon (and also MA-128C after test) appeared shiny with the typical metallic luster of Pd metal. Therefore, it may be possible that the C present is due to the adsorption of a very thin film of hydrocarbon molecules on the Pd. The presence of C within the Pd bulk may be explained by disproportionation reactions as seen in carbon uptake studies already published.36,40 The high C concentrations found at the surface and even at a depth of 100 nm are significantly higher than the maximum C content in Pd, which is approximately 13−16 atom %.36,60 The carbon measured in this sample may not have come from the Pd bulk. It is commonly known that part of the C found on samples in XPS analysis may originate from atmospheric CO2 adsorption and/or handling as well as the considerable effect on XPS results of sample surface roughness. Indeed, the roughness of the coupon (a 0.1 µm grade PSS 316L plated with 2−4 µm of Pd) may be well above 1−2 µm, and since the irradiated surface area during XPS depth profile (1.1 µm deep) measurements was 200 µm in diameter, it may be that the high levels of C found on the surface were due to some C present in the valleys. However, if the sample roughness could explain the presence of C at a depth of 1.1 µm, the other contaminants, Na, Mg, O, and Hg, should also have been detected at deeper levels. A preliminary XRD analysis performed on a Pd layer deposited on a cold rolled W coupon (internal standard) and also exposed to the same syngas as MA-128C showed no presence of C within the Pd bulk. Future XRD and XPS analysis of nonporous Pd coated coupons will shed more light on the presence of C in Pd and Pd−Au layers exposed to coal derived syngas. As of today, it is very probable that the initial 51% decrease in permeance of MA-137B is related to the C adsorbed on its surface (46−69 atom % C present on the surface of the Pd coupon) blocking the sites for H_2 dissociation. Indeed, the 51% decline in the permeance was not expected of a Pd−Au alloy with at least 23 atom % of Au on its surface and 1−3 ppm levels of sulfur at 450 °C. It is therefore reasonable to assert that the initial decrease in the H_2 permeance can be attributed to the adsorption of unsaturated hydrocarbons on Pd followed by dehydrogenation reactions.

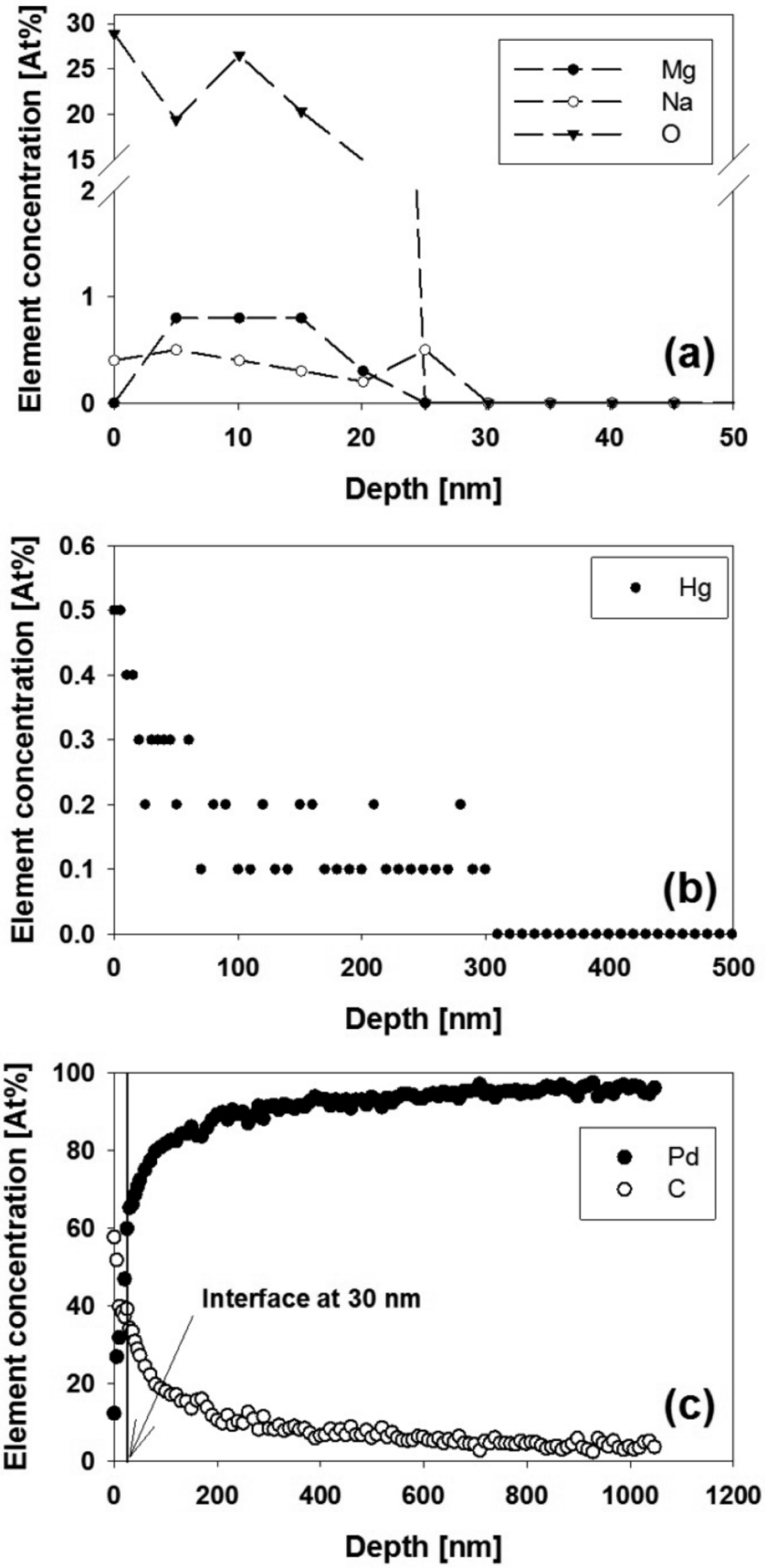

Figure 5.14. Element concentration as a function of depth of a Pd surface exposed to the same syngas as MA137b. (a) Na, Mg, and O; (b) Hg; and (c) Pd and C.

Table 5.8. Surface Composition of a Pd Film Exposed to Syngas during M-03b Testing.[a]

	Mg	Na	Pd	O	C	S	Hg
As received	ND	0.4	13.8	15.8	68.6	1	0.5
After 50 Å sputter	0.6	ND	41.6	11	45.8	0.7	0.3

[a] The atomic percents were calculated omitting H2 (not detectable by XPS) and were normalized to 100%. ND = None Detected. The element was not present or below the detection levels of the instrument. Composition values were accurate to within ±10 relative percent. The elements F, As, Sb, Au, Cd, Pb, Zn, V, Cl, B, P, Se, and Au were all scanned for but not detected.

6. MULTITUBE MEMBRANE MODULE AND MEMBRANE LIFETIME

Summary

The specific objectives of the Phase II program are: (1) Design and construction of a membrane separation module with high capacity of producing H_2, followed by validation and assessment of the design, membrane production methods and separation performance, (2) Installation of the H_2 separation membrane module at NCCC to conduct long term parametric testing of the module, (3) Optimization of H_2 flux and recovery, (4) Development of a computational fluid dynamics (CFD) model and its experimental validation, (5) Measurements and improvement of membrane life, contaminant resistance, durability during system upsets, and operational limits including temperature, pressure difference across membrane, etc. Consequently, this section shows the development of a multitube membrane module, its experimental testing and optimization of its parameters via the development of CFD models and a long-term test of membranes analog to those utilized in the multitube membrane module.

6.1. Long-Term Test of Coupon Pd/Au Membranes

Coupon membranes MA-159 and MA-160 were synthesized with similar conditions to the membranes used in a multitube membrane module. In specific MA-160 had the same support properties (0.5 µm media grade) as the membranes used in the multitube module than MA-159 (1.0 µm media grade). The purpose of this section is to analyze the lifetime, performance and restoration-properties of these membranes. These coupons were tested under pure H_2 at 350 and 450°C with sporadic He leak tests for a cumulative time of 14,000 hours or 1.6 years. MA-160 was stable for 10,700 hours of continuous test with 3 repair steps showing an overall H_2 reduction in permeance of 62%, but an excellent separation factor. MA-159 was tested for ~4000 hours and suffered 5 repairs. This membrane presented a high H_2 permeance, but its stability was lower than MA-160 (possibly due to the difference in media grade of the porous support.)

Description

MA-159

Membrane MA-159 was prepared on a 0.5”OD 316L PSS support with a media grade of 1 µm. MA-159 has a length of 6” and effective surface area 60 cm^2 that allows testing it in the single membrane module at WPI. The support was first covered with sol-gel and then calcined at 600°C for 12 hours. After calcination the support was graded following the regular procedure with the medium and fine powder from JM (UK) based on a 2 wt% Pd - Alumina catalyst without any additional activation or treatment. After grading a 5.0 µm Pd layer was deposited. Furthermore, a gold layer of 0.4 µm was deposited on top of the palladium membrane surface. MA-159 had a He leak after synthesis of 0.01 sccm/bar. This Au enriched membrane displayed an initial H_2 permeance of 7.4 $Nm^3m^{-2}h^{-1}bar^{-0.5}$ and a He leak of 0.42 sccm/bar at 350°C. The temperature was increased to 450°C and consequently the permeance increased gradually to 42 $Nm^3m^{-2}h^{-1}bar^{-0.5}$ after 137.5 h due to in-situ alloying. The permeance remained stable; however, the He leak increased considerably (~35 sccm/bar) and the experiment was stopped after 800 h of testing for further investigation and characterization of the leak location.

MA-159 was repaired and renamed as MA-159b. Gold rings were plated at both sides of the welding area, reducing the He leak to 0.3 sccm/bar at room temperature. The membrane was tested for 100 h at 450°C under pure H_2. The He leak increased again to 45 sccm/bar and the test was terminated. MA-159b was subjected to a mild polish treatment to remove any Pd peel off. Palladium rings were plated in the welding area close to the cap, twice. This treatment reduced the overall He leak of the membrane to

30 sccm/bar. Subsequently, the first half of MA-159b was plated once, reducing the leak even further to 18 sccm/bar. Finally, a complete Pd plating treatment was conducted along the whole membrane. Undetectable He leak was found at pressure differences of 2 bar. At this point MA-159b was renamed to MA-159c. MA-159c was tested for ~200 h showing a H_2 permeance of 25 and 35 $Nm^3m^{-2}h^{-1}bar^{-0.5}$ at 350 and 450°C, respectively. He leak increased gradually to 8.3 sccm/bar. The membrane was removed from the module and plated once more to increase the Pd layer thickness to 11 µm; this membrane was renamed to MA-159d. MA-159d was tested for 700 h showing a stable H_2 permeance of 35 $Nm^3m^{-2}h^{-1}bar^{-0.5}$, similar to the permeance displayed by MA-159c. Nevertheless, He leak appeared reaching 40 sccm/bar at room temperature. The membrane was replated to 12 µm, renamed as MA-159e and tested for 1000 h showing a He leak of 15 sccm/bar by the end of the test. The permeance of MA-159e, was stable with a value of 23 and 35 $Nm^3m^{-2}h^{-1}bar^{-0.5}$at 350 and 450°C, respectively. Notice that the membrane remained under pure He for 20 h, as indicated in Figure 6.1, due to a problem with the H_2 security system. Afterwards this period, the permeance of the membrane showed a steady decline at 350°C and stopped once the temperature was increased to 450 °C. After MA-159e failed, it was repaired once more and renamed as MA-159f. The membrane was tested for 1400 h showing a stable H_2 permeance of 32 $Nm^3m^{-2}h^{-1}bar^{-0.5}$at 450°C, while He leak increased gradually from >1 to 17 sccm/bar.

Notice that the cumulative test of MA-159 after ~4000 h of continuous test and 5 repair steps is shown in Figure 6.1. Overall, the membrane showed a stable permeance as shown in Table 6.1; however, it displayed a continuous He leak that seemed to decline after repair, but increase as the tests proceeded. It is important to mention that, for each test session, additional palladium was deposited to cover the defects of the membrane before the test was reinitiated; nevertheless, for MA-159b, only rings at the welding area were plated and consequently the increase in thickness was neglected. The He leak, shown in Table 6.1, represents the value obtained at 450 °C before the test was terminated; while the H_2 permeance was taken as the average value displayed throughout the test at 450 °C. Furthermore, it is important to mention that the media grade of the support influenced significantly the lifetime of the membranes. This is evidenced by the lower stability displayed by MA-159 where several repairs were needed.

Table 6.1. List of characteristics of MA-159.

Membrane	Testing time / h	Dense Pd thickness/ µm	Final He leak* /sccm.bar^{-1}	H_2 Permeance* / $Nm^3m^{-2}h^{-1}bar^{-0.5}$
MA-159	830	5	35	45
MA-159b	250	5 (rings)	45	40
MA-159c	210	8.5	8.3	36
MA-159d	700	11	20.5	34
MA-159e	1000	12	15	33
MA-159f	1350	15	17	31

* Hydrogen permeance and He leak at 450°C

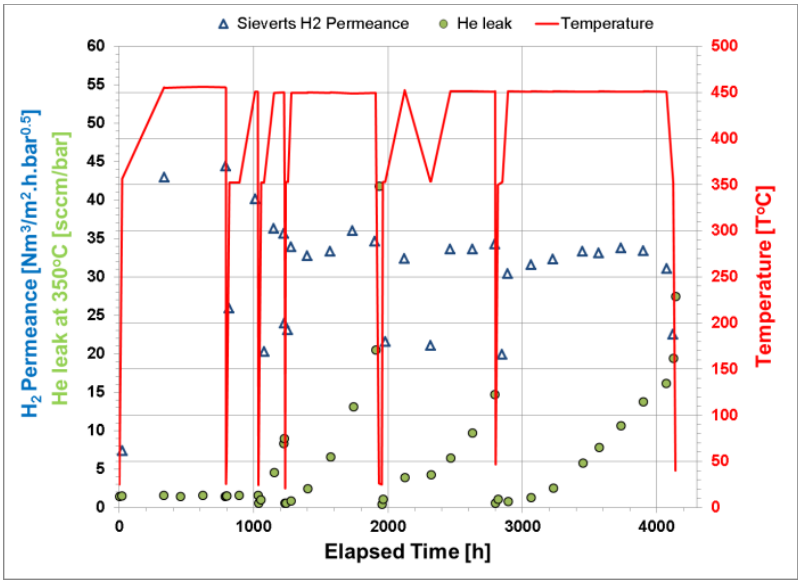

Figure 6.1. Hydrogen permeance and He leak tests of MA-159.

MA-160.

Membrane MA-160, like the above described membrane, was prepared on synthesized on 0.5”OD 316L PSS support, but with a media grade of 0.5 µm. MA-160 has a length of only 6” and effective surface area - 60 cm^2. Notice that this membrane is an exact replica of the seven membranes prepared for long term comparative testing in the multi- tube module. This membrane had a stable H_2 permeance of 50 Nm^{3}m^{-2}h^{-1}bar$^{-0.5}$ at 450^{o}C. Furthermore, the He leak after 1200 h; nevertheless, after 1480 h, the membrane was accidentally exposed to He for 62 h as indicated by the yellow lines in Figure 6.2. There was no immediate change to the membrane’s He leak; but, the performance deteriorated gradually after the He exposure, increasing its He leak to a maximum leak of 14.5 sccm/bar. The H_2 permeance dropped immediately by 12% to 44 Nm^{3}m^{-2}h^{-1}bar$^{-0.5}$ and remained constant until the end of this test; the total testing time was 2950 h. At this point the test was partially terminated to identify the location of the leak as well as repair the membrane. Gold rings were plated on both sides of the welding area, reducing the He leak to 0.5 sccm/bar. The membrane renamed as MA-160b and was tested for 1000 h. Notice that He leak increased to 45 sccm/bar by the end of the test and that due to technical problems, the membrane was oxidized with air for 10 h, after 400 h of this test or 3350 of cumulative testing time, causing a sudden He leak growth.

MA-160b was repaired by plating 5.8 µm of Pd and renamed as MA-160c. During this test, it can be observed that several oxidation stages due to a failure in the system. These oxidation stages occurred at the times where the temperature oscillated. These oxidations did not affect the permeance nor the He leak presented in the membrane. Subsequently, the temperature of the membrane was raised to 450^{o}C and its permeance was tested for ~600 h; the He leak remained stable throughout this test. Unfortunately, the system suffered another error and a third oxidation stage occurred. The membrane was then tested at 350^{o}C for 200 h followed by a continuous He test of 300 h. Afterwards, H_2 was fed once more; nevertheless, the membrane’s permeance reduced by ~50% while the He leak remained unchanged. The membrane test was reinitiated after 5760 h of test showing a stable permeance of 20 Nm^{3}m^{-2}h^{-1}bar$^{-0.5}$ and a He leak of 1.5 sccm/bar. It is important to mention, that at the beginning of the test, the membrane suffered from several cooling-heating cycles due to failures of the electric system; nevertheless, the He leak remained unaffected. The hydrogen permeance, on the other hand, reduced from 27 to 20 Nm^{3}m^{-2}h^{-1}bar$^{-0.5}$ after the temperature fluctuation occurred at 6,630 h. Afterwards, the permeance showed a steady decline reaching a steady state of 15 Nm^{3}m^{-2}h^{-1}bar$^{-0.5}$ at 8,000 h until 9,300 h. The test was terminated for maintenance of the system and reinitiated to test the membrane for another 1,000 hours.

The cumulative test of MA-160, shown in Figure 6.2, was 10,700 h of continuous test with 3 repair steps with as shown in Table 6.2 The membrane showed a reduction in permeance of 62% but an excellent separation performance. The physical integrity of MA-160 was clearly demonstrated after the cumulative test (Figure 6.3). Notice that MA-160 presented superior stability properties than MA-159, possibly due to the use of a reduced media grade of the support.

Table 6.2. List of characteristics of MA-160.

	Testing time / h	Dense Pd thickness/ µm	Final He leak* /sccm.bar^{-1}	H_2 Permeance*/ $Nm^3m^{-2}h^{-1}bar^{-0.5}$
MA-160	2950	4.6	14.5	45
MA-160b	1000	4.6 (rings)	45	43
MA-160c	6750	10.4	4.5	18

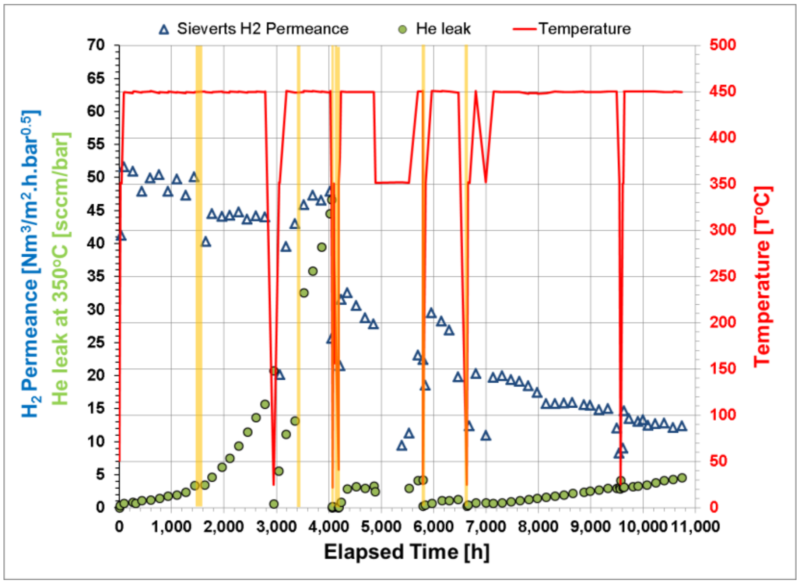

Figure 6.2. Hydrogen permeance and He leak tests of MA-160, and yellow lines indicating membrane oxidation stages.

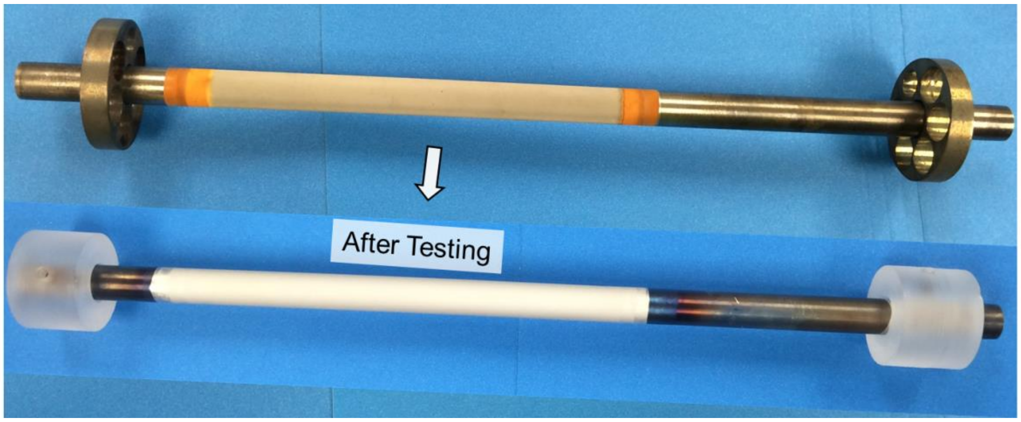

Figure 6.3. Photo of MA-160, before and after H_2 permeation test.

6.2. Multitube Membrane Module

Pilot-scale field tests generate information about the performance of energy systems and thus help in the deployment of a new technology. The purpose of this section is to demonstrate the application of palladium based membrane technology for the purification of H_2 at a pilot scale. A multitube membrane module with a total permeable area of 1050 cm^2 was tested under actual coal-derived syngas at the National Carbon Capture Center (NCCC) in Wilsonville Al. The module was composed of seven composite asymmetric membranes with a Pd/Au/Pd layered structure. The membranes were arranged with one membrane at the center of the module and six membranes equally distributed around it. The membranes had an average composition of 7 µm Pd and 0.4 µm Au and a cumulative He leak of < $0.01cm^3$/min/bar before initiating the test. The multitube module was operated at 450°C, 12.6 bar and 10 lb/h of desulfurized syngas provided by a gasification unit and enriched with H_2 to 34% The membrane module showed a stable H_2 permeance with an average value of 16.2 $Nm^3m^{-2}h^{-1}bar^{-0.5}$ throughout 840 hours of continuous testing. The purity of the produced H_2 was in the range of 99.87-98%. An H_2 production of 6 lb/day and a H_2 recovery of 64% were achieved representing a significant development in the field. The scalability and industrial applicability of this technology was successfully demonstrated.

Description

6.2.1. Membrane fabrication and initial characterization

Eight porous stainless steel (PSS) tubes purchased from Mott Metallurgical Corp. were used for the synthesis of the membranes. Each porous tube had a surface area of 150 cm^2 and dimensions of 15 in. in length and 0.5 in. OD. Each porous support had a Media Grade of 0.5 µm. The supports were subject to grading using two types of slurries composed of pre-activated alumina particles. The first grading step consisted of coarse particles with sizes in the range of 1-3 µm; while fine grading introduced particles of 0.6 µm. The grading layers were glued with palladium as previously described [77,90,91].The membranes were then activated and electroless plated to create a dense Pd layer of the graded supports; for further reference on this procedure please refer to the pertinent literature [77,92]. Afterwards, a gold layer was deposited on top of the palladium in order to improve the stability and recoverability of the membranes, as reported by Chen et al. [101]. After Au deposition, the membranes were stored at 40°C for 6 months under air. The He leak of the membranes after this period changed as shown in Figure 6.4. Notice that some membranes presented an increased He leak while others decreased. It is suspected that overall, all membranes had a He leak increase and that the membranes which showed a reduction in He permeation were mainly affected by moisture blocking the defects present on the surface of the membranes.

Due to the change in the He leak, a topmost layer was formed on top of the Pd before the module was assembled with seven of the eight membranes and subsequently shipped to the NCCC facilities. The thickness of the Pd and Au layers was estimated through gravimetric measurements and each step of the synthesis was characterized by a He leak test. Figure 6.5 shows the different thickness of the stages in the synthesis of the composite membranes; on average the membranes had a thickness layer of 5.4 µm Pd, 0.4 µm Au and 1.6 µm Pd, with an intermediate grading layer of 2.5 µm. Notice that the replicability of synthesizing these membranes is effectively demonstrated, having a standard deviation in the Pd layer thickness of 0.9 µm or about 10%.

Furthermore, Figure 6.6 shows the average He leak at each step of the synthesis. As purchased, each support had a He flux of 200 L/min at one bar ΔP and it was reduced to a cumulative (all seven membranes) He flux of < $0.01cm^3$/min. The supports showed half the He flux after oxidation and further reduction to 56 cm^3/min after grading. Grading is a critical step in the formation of a defect-free Pd membrane since it reduces the uneven pore size distribution of the support and smooths its surface, allowing the formation of an even Pd thickness after plating [90,92]. The total permeable surface area of the seven membranes is 1050 cm^2. The additional synthesized membrane was tested at WPI under controlled conditions with pure H_2 for comparison purposes.

The multitube membrane module was designed to hold seven Pd/Au/Pd membranes. The module had one membrane located at the center of the module and six equally spaced membranes surrounding it.

The surrounding membranes were kept at 1.31 in. from the central membrane and were distributed in a hexagonal arrangement; the membrane module was designed to have a length of 38 in., as shown in Figure 6.7. The axial positions of the membranes varied in order to allow Swagelok connections within the confinement of the 4.5 in. OD shell of the module. For instance, the connection of the central membrane was at a longer position than the surrounding ones; while the position of the remaining connections was alternated between shorter and medium lengths, as shown in Figure 6.7b. A holder was placed on the tip of the membranes to maintain the configuration of the membranes and potentially act as a baffle for better mixing of the gases. The multitube membrane module had a shell-and-tube configuration and was sealed utilizing an assembly consisting of flanges, studs and clamps (Grazyloc 4 in.) which can be seen in Figure 6.8.

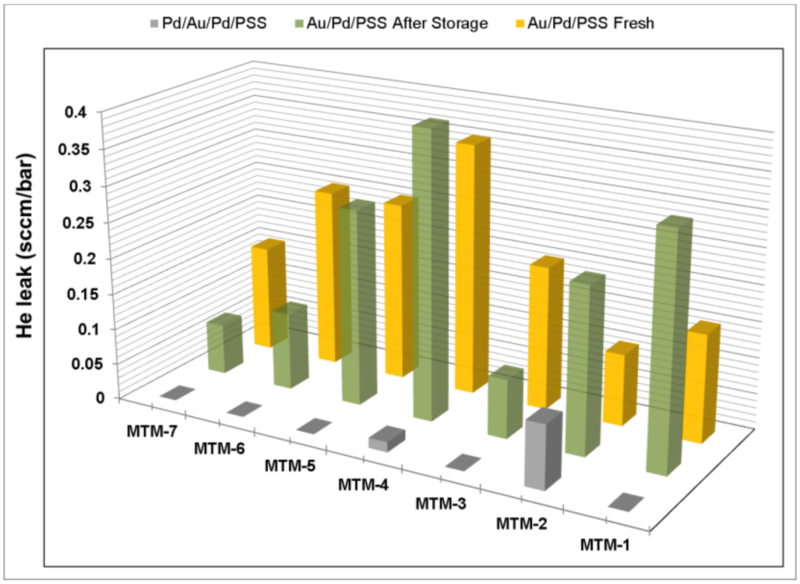

Figure 6.4. He leak of each membrane as fresh Pd/Au, after storage and final leak.

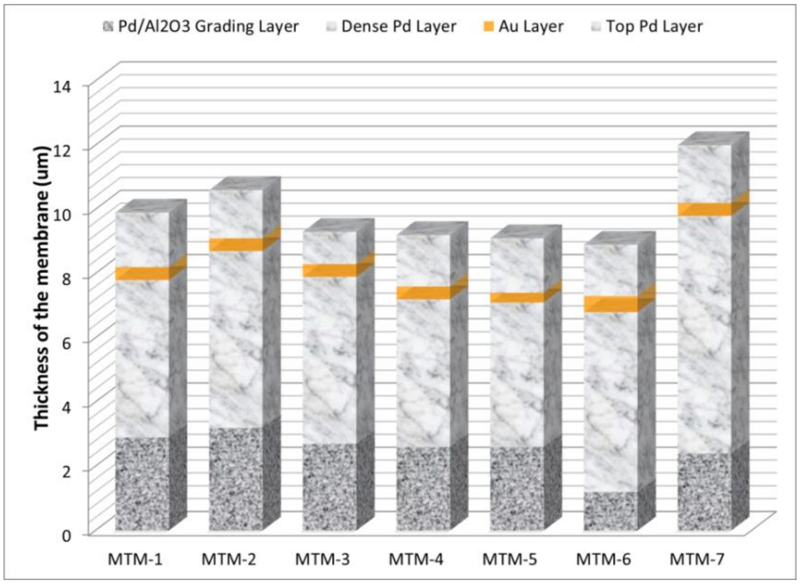

Figure 6.5. Composition of the multilayered composite membranes used in the present study.

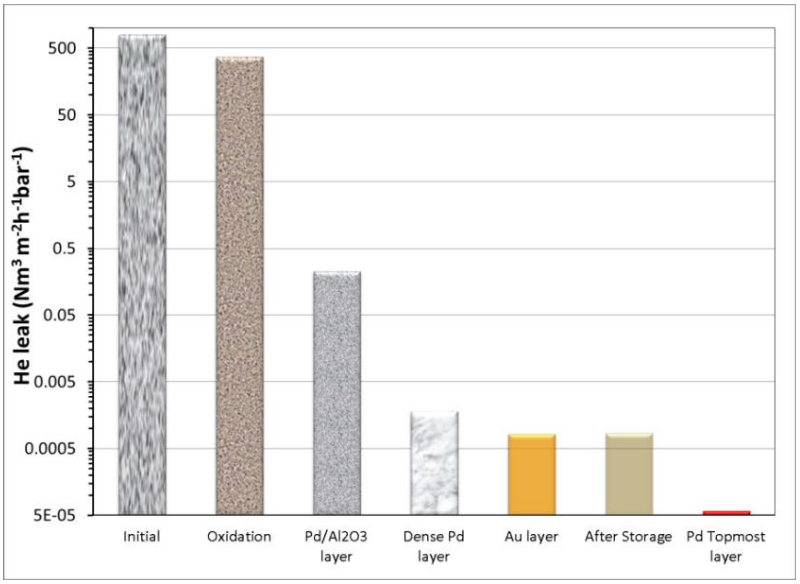

Figure 6.6. Average He leak through the Pd/Au/Pd membranes throughout each synthesis step.

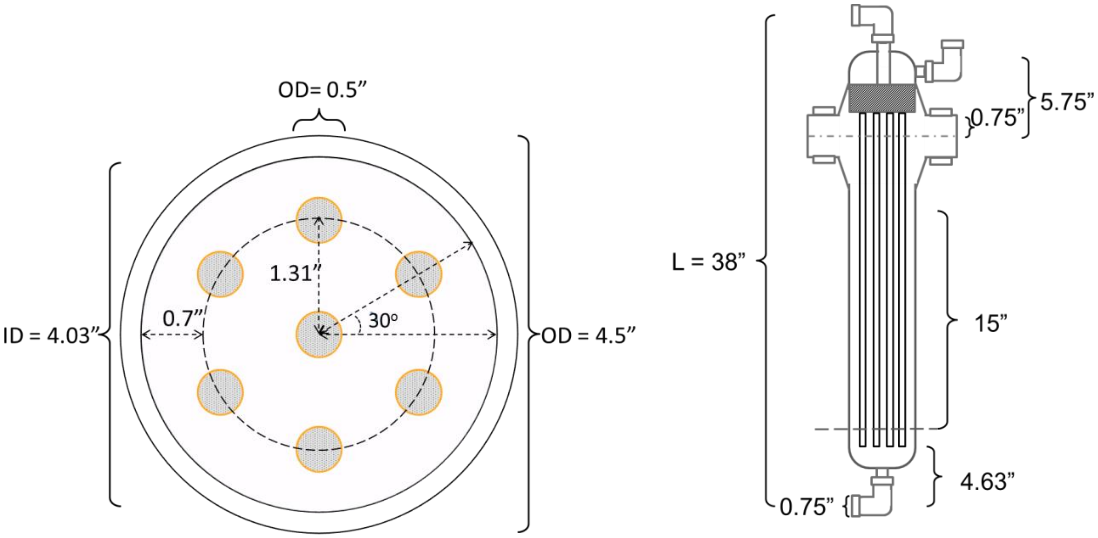

a)

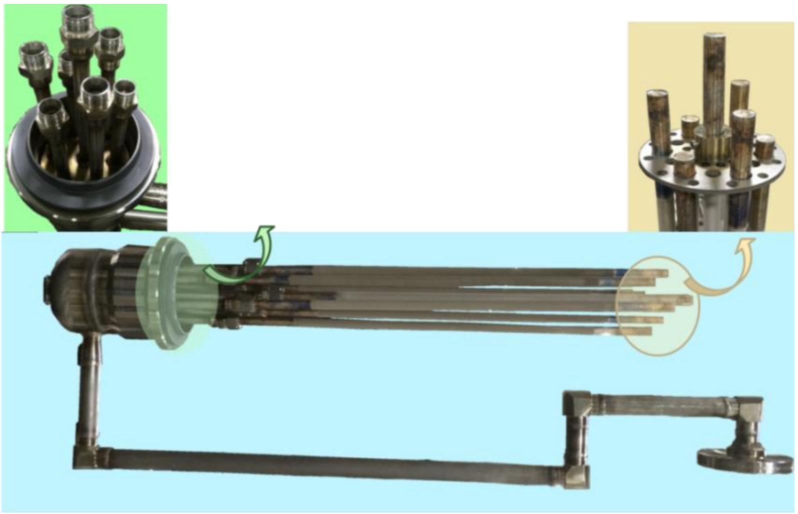

Figure 6.7. a) Schematic of the multitube membrane module design, b) photograph depicting the membranes' arrangement.

6.2.2. Field Tests of the Multitube Membrane Module

The multitube membrane module containing the seven Pd/Au/Pd membranes was installed in the WPI-MTR skid at the National Carbon Capture Center in Wilsonville, Al. [93] and it is shown in Figure 6.8. The module was purged with pure N_2 and its operating pressure was increased to > 12 bar and the temperature was increased to 450^{o}C. It is important to mention that the module showed no leak while testing the module seal. After reaching the operating temperature, a mixture of 35:65 H_2/N_2 was fed to the system, followed by the actual coal derived syngas. For further information about the configuration of the rig and the gasifier, please refer to previous sections of this document and/or literature references [93,94,95]

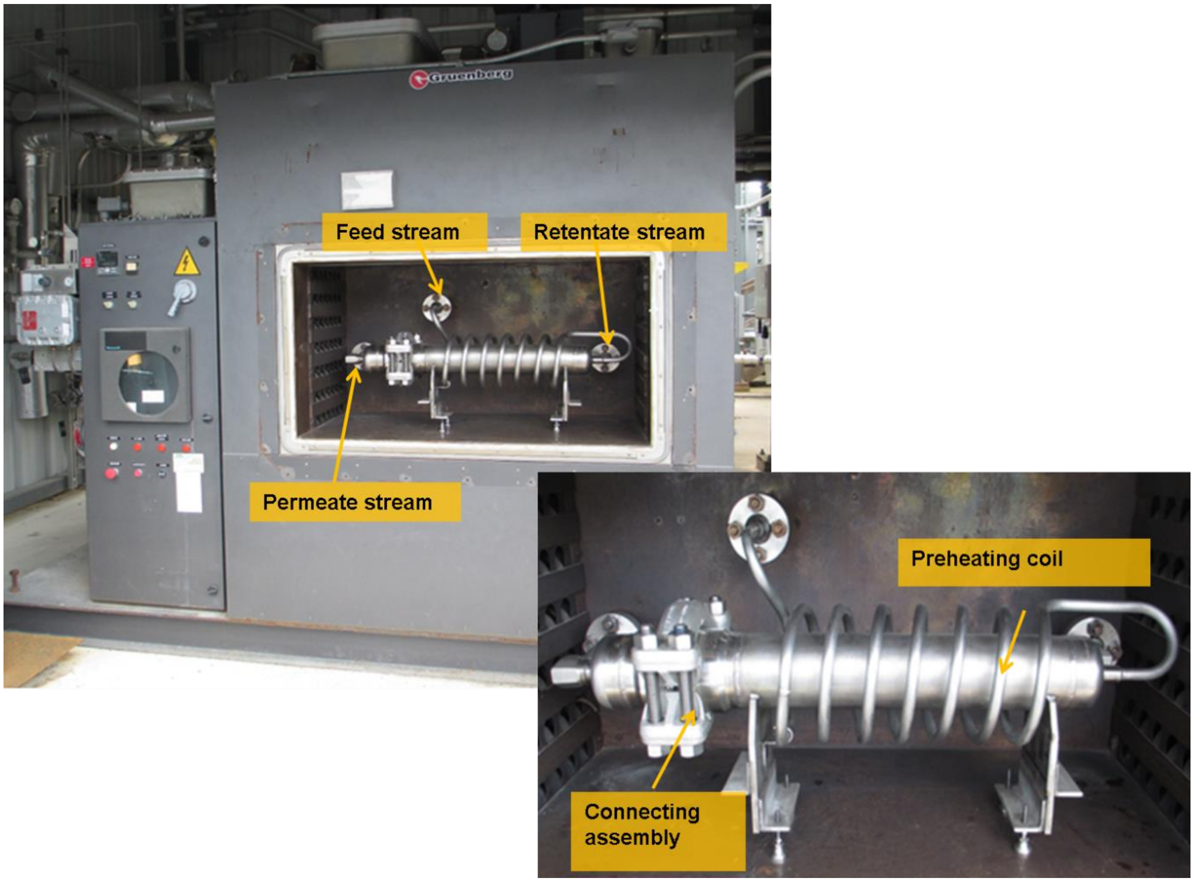

Figure 6.8. Photograph of the setup for testing the multitube membrane module at NCCC (Notice that the door of the oven was removed to facilitate display).

As in previously reported gasification runs at NCCC [94,95], approximately 10 lb/h of gas with a variable composition was fed to the module as shown in Figure 6.9. At first, the module was tested under a 35:65 H_2/N_2 mixture for 100 h followed by flowing coal-derived syngas which was composed mainly of H_2, CO_2, N_2 and CH_4 for ~700 h. The initial evaluation of the performance of the membrane module was based on its H_2 permeance ($\bar{P}_{H2}$), produced H_2 purity and H_2 recovery (R) as defined in Equations 6-1 to 6.3:

$$\bar{P}_{H2} = \frac{F_{H2,perm}^{out}}{A\left(\sqrt{p_{H2}^{ave}} - \sqrt{p_{H2}^{perm}}\right)} \tag{6.1}$$

$$Purity = \frac{F_{H2,perm}^{out}}{\sum F_{i,perm}^{out}} \cdot 100 \tag{6.2}$$

$$R = \frac{F_{H2,perm}^{out}}{F_{H2,feed}} \cdot 100 \tag{6.3}$$

Here $F_{H2,feed}$ and $F_{H2,perm}^{out}$ are the H_2 flow rates for the feed and the permeate outlet streams, respectively. A is the permeable surface area of the membranes, p_{H2}^{ave} and p_{H2}^{perm} are the H_2 partial pressures inside the module shell and in the permeate side, respectively. Given the number of data points, p_{H2}^{ave} was approximated as the average of the H_2 partial pressure of the feed ($p_{H2,feed}$) and the retentate ($p_{H2,ret}$).

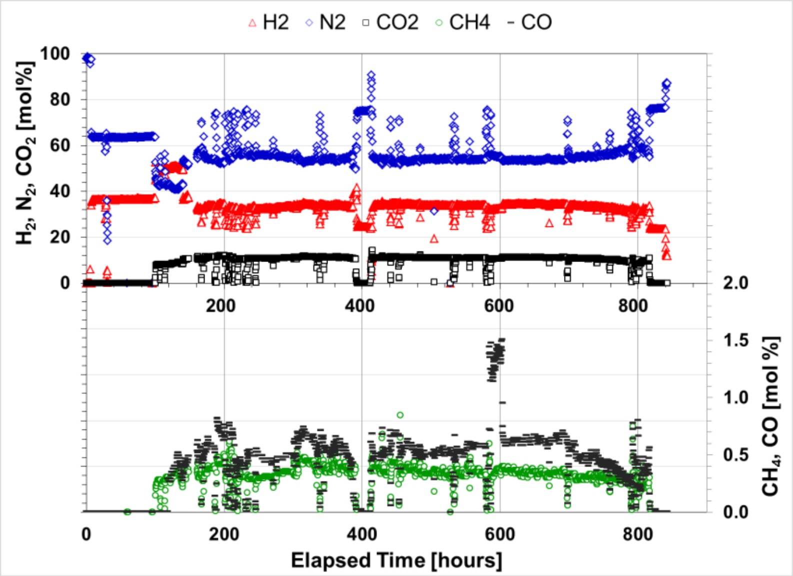

Figure 6.9. Composition of the gas mixture fed to the module as a function of time.

The H_2 permeance and purity of the module are displayed as a function of time as shown in Figure 6.10. At first, the membrane module showed a permeance in the range of 7-10 $Nm^3m^{-2}h^{-1}bar^{-0.5}$ when tested under H_2/N_2 mixture as depicted in Figure 6.10 in solid black data points. When syngas was fed into the module, a slight oscillation in permeance was observed during the first 100 h, followed by a steady performance. Notice that the average permeance under H_2/N_2 mixture and syngas were found to be of 8.8 and 8.2 $Nm^3m^{-2}h^{-1}bar^{-0.5}$, respectively indicating a 6% reduction in permeance under syngas conditions. The maximum flux achieved by these membranes was 6 lb/day of H_2. It is important to mention that the module displayed constant properties (Figure 6.10) even though the continuous changes in the feed stream were present.

Furthermore, the additional synthesized membrane MTM-8 with the same dimensions and characteristics was tested in the facilities of Worcester Polytechnic Institute under clean and pure H_2. The H_2 permeation test is shown at 350 and 450°C in Figure 6.11, displaying permeances of 75 and 80 $Nm^3m^{-2}h^{-1}bar^{-0.5}$, respectively. In terms of flux the membrane showed a maximum productivity of 1.03 lb/day at a pressure difference of 0.35 bar. Moreover, a hypothetical multitube model composed of pure Pd membranes with a thickness of 7.4 µm, and tested under pure H_2 at 450°C was calculated to generate a theoretical H_2 permeance of 63 $Nm^3m^{-2}h^{-1}bar^{-0.5}$. In addition, the single tube membranes previously tested under similar syngas conditions at NCCC [94], showed H_2 permeances between 5 - 15 $Nm^3m^{-2}h^{-1}bar^{-0.5}$ and under pure H_2 at WPI permeances between 10 - 29 $Nm^3m^{-2}h^{-1}bar^{-0.5}$.The reduction of the cumulative H_2 flux across this multitube membrane is attributed to i) the fast depletion of H_2 along the membrane module; ii) the mass transfer resistance caused by the boundary layer formed at the surface of the membrane; iii) the permeance inhibition caused by CO, CO_2 and steam [96]; and finally iv) the potential sulfur content on the feed lines of the system at NCCC as previously reported [95]. At these operating conditions, the module presented a depletion of H_2 along the membrane module hindering actual value of the permeance. For instance, the feed stream presented an average H_2 partial pressure of 4.3 bar and it was reduced to 2.5 bar at the retentate or by a factor of about 1.7. This reduction in driving force is not linear, as assumed in the present estimation of the permeance shown in Figure 6.11. Furthermore, radial mass transfer limitations cause concentration polarization which occurs when H_2 diffusion is slower than the permeation rate. Indeed, the presence of a H_2 depleted boundary layer can significantly reduce the displayed H_2 flux across the membranes [97].

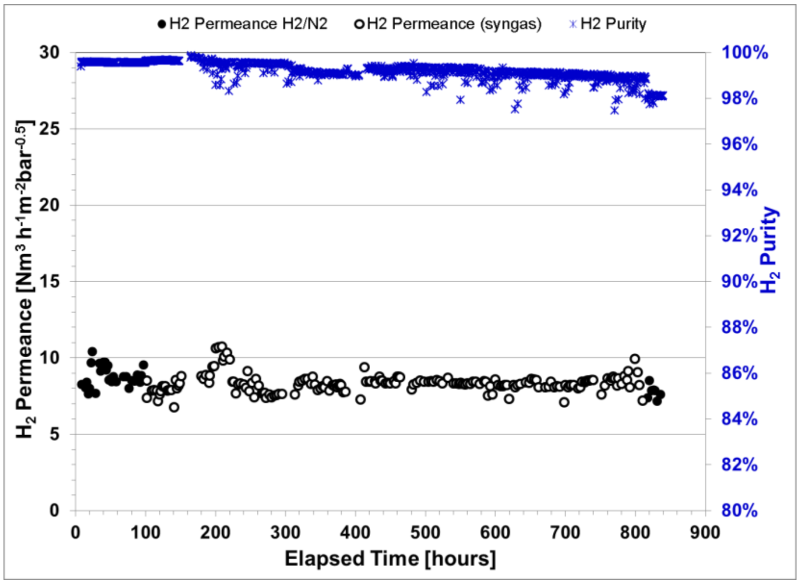

Figure 6.10. Hydrogen permeance and purity profiles of the multitube membrane module at NCCC.

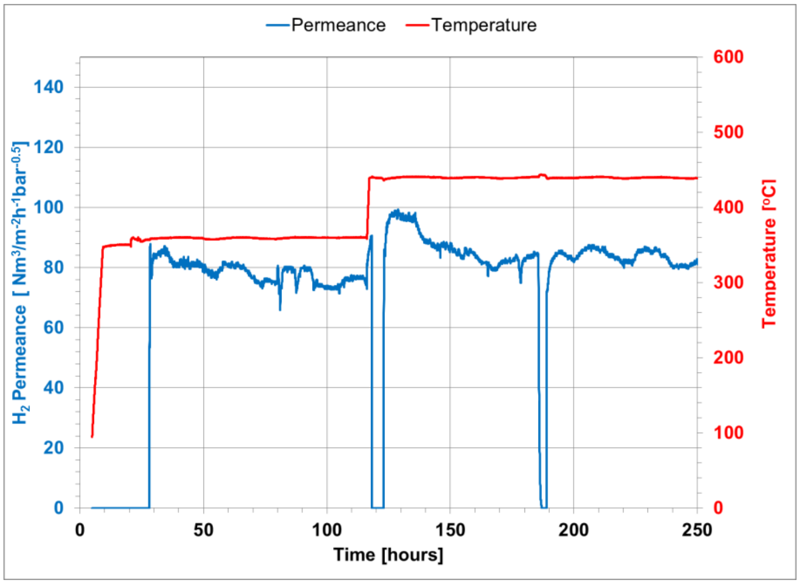

Figure 6.11. Hydrogen permeance of membrane MTM-8 at WPI.

A refined mathematical analysis was performed in order to approximate more accurately the permeance of this module. By neglecting the presence of uneven radial mass distribution and mass transfer resistances, but including the nonlinearity of the H_2 partial pressure within the module, the permeance of the membrane module was estimated by solving the differential equation shown in Equation 6.4. F_{H2} is the local H_2 flow rate across the membrane module, A the total surface area, and p_{H2} is the local H_2 partial pressure, which is defined as the product of the total operating pressure and the local H_2 mole fraction in the retentate (Equation 6.5). The initial conditions of this ODE were specified as the given average experimental values such as feed gas composition and flow rate.

The permeance was adjusted accordingly in order to match the displayed H_2 recovery, retentate composition and total H_2 flow rate at the outlet of the permeate stream. Notice that given the complexity of this calculation, the permeance estimate was shown only for the average properties rather than for every single point through time as the data shown in Figure 6.10. The H_2 permeance of the membrane module was estimated to be 16.2 $Nm^3m^{-2}h^{-1}bar^{-0.5}$, which is considered to be a more accurate value than that obtained using Equation 6.1, because p_{H2} on the retentate side was allowed to vary nonlinearly, as shown in Figure 6.12.

$$\frac{dF_{H2}}{dA} = \bar{P}_{H2} \cdot \left(\sqrt{p_{H2}} - \sqrt{p_{H2}^{perm}} \right) \tag{6.4}$$

$$p_{H2} = p_{total} \frac{F_{H2,ret}}{\sum F_{i,ret}} \tag{6.5}$$

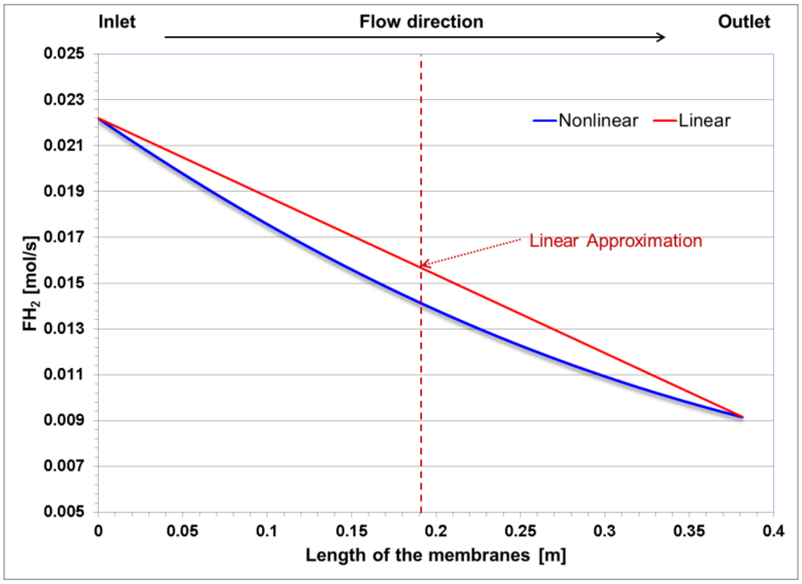

Figure 6.12. Axial distribution of the retentate H_2 flow rate, showing the difference between the linear and refined mathematical approximation.

The presence of CO is well known to affect the permeance of Pd membranes [96]. Competitive absorption of CO within the active sites available reduces the potential solution of more H_2 molecules and consequently inhibits their performance under ideal conditions. It is important to mention that other contaminants present in syngas such as sulfur have been shown to reduce the permeance of Pd membranes. In the single tube field tests from Phase I [94,95], it was found that even traces of sulfur can significantly reduce the H_2 permeance; nevertheless, the presence of the Au aids in the recovery of the lost permeance by exposing the membranes to pure H_2 at 450°C. Other contaminants such as Na, Mg, O, S, Hg and C were previously found on the surface of the Pd membranes tested under coal derived syngas [95].

The H_2 purity produced by these membranes began at 99.5% under H_2/N_2 and underwent a sudden increase to 99.63% when syngas was fed and up to 99.87% after being tested for 67 hours in syngas conditions. Afterwards, the purity of the module decreased steadily reaching a minimum purity of 98.84% after 670 hours under syngas conditions. Notice that at the end of the test, the H_2 purity was of 98.13% under a H_2/N_2 mixture. It is important to mention that the lifetime of these membranes is significantly improved compared to pure Pd membranes, whose life time is estimated at 200 h under industrial settings [81,94]. Additionally, the single tube membrane tests previously reported in Phase I and [94] showed Pd/Au composite membranes displaying H_2 purities in the range of 99.95-99.8% with a lifetime of 535 hours for a Pd/Au/Pt membrane. Furthermore, the H_2 purity profiles achieved by this technology throughout the testing time clearly outperform the ones exhibited by conventional technologies such as cryogenic distillation [98]. Additionally, assuming that the purity of the permeated H_2 decreases linearly with time, as shown by Figure 6.10, it is expected that this module will produce H_2 with a purity of 91% after a year of continuous operation. Furthermore, once the defects of the membranes become significant, they can be regenerated by surface cleaning and palladium replating, reducing the leak of the membranes and extending their total lifetime [91].

Figure 6.13 shows the H_2 recovery achieved under the aforementioned conditions as a function of time. Notice that when the membrane module was under H_2/N_2 at the beginning of the test, the average recovery was estimated to be 52%. Under syngas conditions, the average H_2 recovery increased to 64%. This effect can be explained by analyzing the H_2 flow rate of the feed stream. As mentioned before, 10 lb/h of gas was fed into the module, but the different compositions between the H_2/N_2 mixture and syngas provoked changes in the molar flow of H_2. For instance, 10 lb/h of gas feed is equivalent to 88 mol/h of H_2 fed for a (35/65) H_2/N_2 mixture, but it is 79 mol/h of H_2 fed for syngas enriched to 35%; there is a 10% difference in H_2 molar flow rate between the H_2/N_2 mixture and syngas. Furthermore, the space velocity of the gases is different for H_2/N_2 and for syngas. It is estimated that 5.5 m^3/h of H_2/N_2 was fed into the system at standard conditions, while syngas had a volumetric flow rate of 4.9 m^3/h.

Indeed, having a higher feed flow rate directly affects the recovery achieved (Figure 6.13) by the module since higher membrane surface area is needed to accomplish the transport of all H_2 molecules fed, even though the H_2 partial pressure is similar. Higher feed flow rate utilizes the available surface area of the membranes better, even though recovery is reduced. In other words, obtaining a low H_2 recovery directly implies that the membranes were occupied evenly and that the displayed permeance is closer to the permeance under pure H_2. High recoveries, such as those presented in this work, do not show the maximum H_2 flux that the module can achieve, since it is hindered by H_2 depletion within the unit. Figure 6.14 shows the module's H_2 recovery as a function of the H_2 feed flow rate. An exponential decay is observed and a plateau can be predicted at a recovery of ~40%.

Notice that the maximum theoretical H_2 recovery achievable by the module is < 90% which can be improved by the presence of sweep gas in the permeate side and/or by increasing the retentate pressure. Additionally, it is expected that the presence of baffles could improve mixing and avoid mass transfer resistances, improving further the H_2 recovery of the module [99].

The successful results obtained from the 7-membrane module tests reported here demonstrate that the good performance previously found [94,95] for a single membrane tube can be scaled up. These results are promising for the future development of palladium composite membrane modules with more tubes and hence greater permeation area.

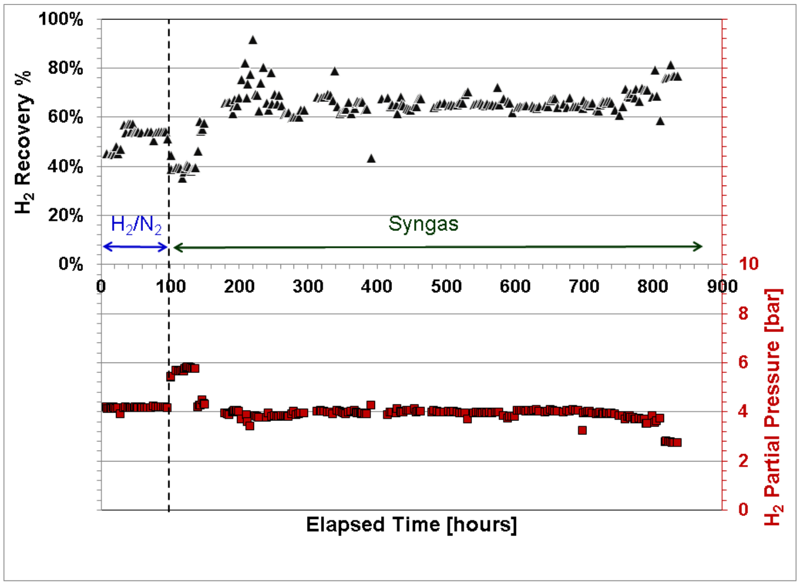

Figure 6.13. Hydrogen recovery and H_2 partial pressure of the multitube membrane module tested at NCCC.

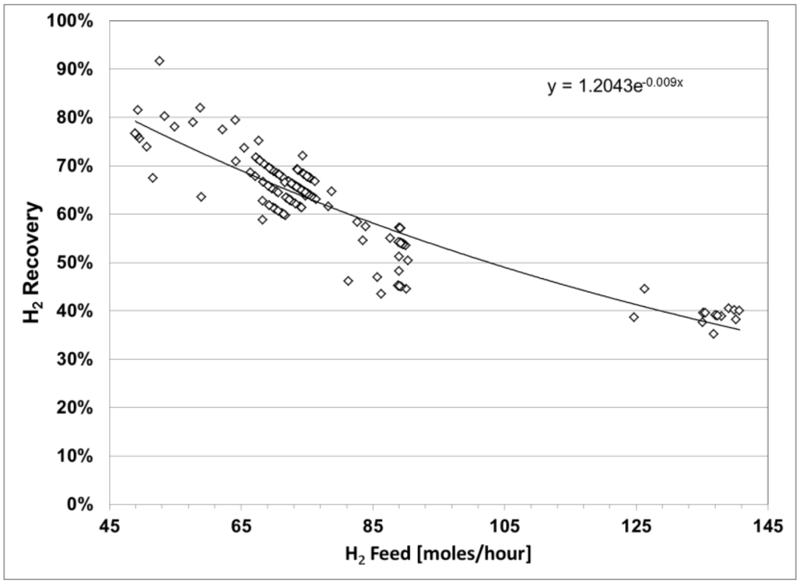

Figure 6.14. Hydrogen recovery as a function of the feed H_2 flow rate.

6.3. Numerical Model of the Multitube Membrane Module

A computational fluid dynamics (CFD) model for the multitube membrane model was developed, validated and used in order to predict and optimize the performance of the module under different conditions. The model consisted on a 3-D representative geometry subject to the continuity, Navier-Stokes and conservation of energy equations. COMSOL Multiphysics 5.0 was used to solve the equations within the proposed geometry. The performance of the multitube membrane system was analyzed based on the total H_2 recovered under the different operation conditions and compared to the experimental module. Axial H_2 concentration profiles were generated showing and improved H_2 recovery at low Re. Furthermore, it is shown that operating at high Re number or high Péclet numbers minimizes the effect of diffusion by markedly enhancing the convective forces. Although low feed flow rates lead to a high H_2 recovery, they diminished the usage of the membrane. Furthermore, temperature distribution profiles showed the influence of convective heat transfer of the gases to the membranes. Permeability distribution profiles along the membranes display the influence of temperature on H_2 permeance. Operating at higher feed temperatures, close to the membrane temperature, increases the H_2 recovery of the module; nevertheless lower temperatures display lower efficiencies due to the reduction of temperature at the surface of the membranes. Based on the results obtained, the optimum operating conditions maximize H_2 recovery; typically enhanced by low-moderate feed rates and high feed temperatures. This heat and mass transfer model was validated by comparing the results obtained in with the simulation model and those obtained from the actual multitube membrane device at the National Carbon Capture Center in Alabama.

Description

6.3.1. Isothermal model

A representative sketch of the actual multi-tube membrane module depicting the direction of the flow along with the outlet streams is shown in Figure 6.15. Table 6.3 contains a list of the parameters used in this simulation. The geometry used in the simulation framework (Figure 6.16) was simplified by neglecting any physics occurring at end of the membranes as shown in Figure 6.16

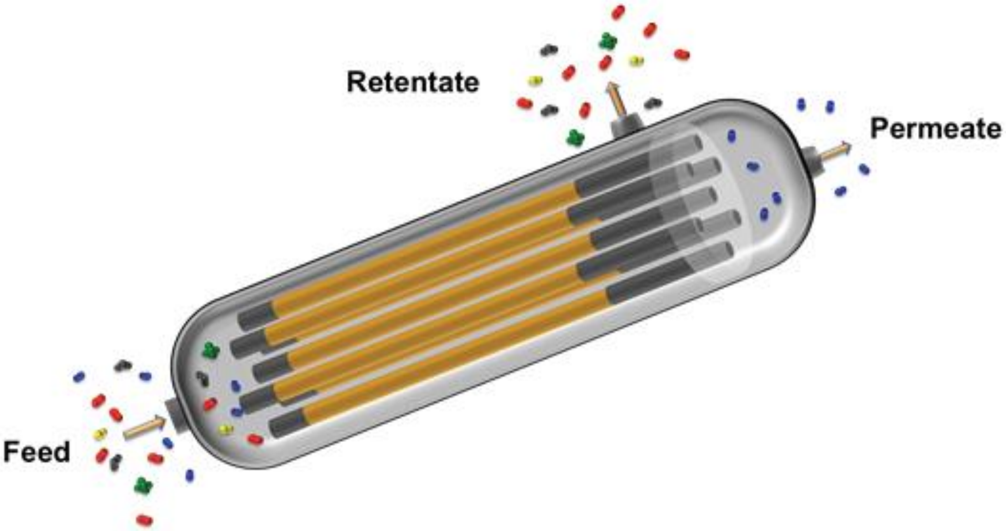

Figure 6.15 Representative sketch of the actual multi-tube membrane module.

Table 6.3. Operational settings for the module.

Shell Pressure/atm	12.6
Tube Pressure/atm	1
H_2 Permeance / mol $m^{-2}s^{-1}Pa^{-0.5}$	$7.7x10^{-4}$
Reynolds number	1-300
Initial gas composition /mole %	
H_2	43.0
N_2	50.0
CO	5.0
CO_2	1.5
CH_4	0.5

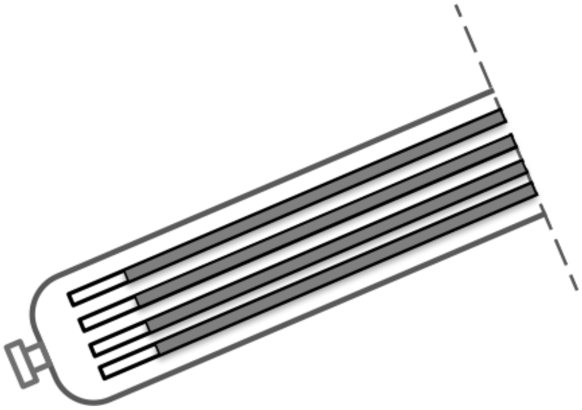

Figure 6.16. Simplified geometry of the multitube membrane module.

The isothermal model was generated with COMSOL Multiphysics 4.3b and "Reacting Flow" as the physics. This physics targets the removal of a specific species as reactants on the surface of a catalyst as specified by the species continuity equation in Equation 6.6:

$$\nabla \cdot \mathrm{j}_i + \rho(\mathrm{u} \cdot \nabla) w_i = \mathrm{R}_i \tag{6.6}$$

where $\nabla \cdot \mathrm{j_i}$ represents the diffusion of species i, $\rho(\mathrm{u} \cdot \nabla)\mathrm{w_i}$ advection and $\mathrm{R_i}$ the rate of reaction.

Diffusion of species i is assumed to be isothermal and was defined as (Equation 6.7):

$$\mathrm{j_i} = -\left(\rho D_i^m \nabla w_i + \rho w_i D_i^m \frac{\nabla M_n}{M_n}\right) \tag{6.7}$$

$$D_i^m = \frac{1 - w_i}{\sum_{k \neq i} \frac{x_k}{D_{ik}}} \tag{6.8}$$

$$M_n = \left(\sum_i \frac{w_i}{M_i}\right)^{-1} \tag{6.9}$$

The mass flux of the system was defined by Equation 6.10:

$$\mathrm{N}_i = \mathrm{j}_i + \rho \mathrm{u} w_i \tag{6.10}$$

The equation of motion (Equations 6.11-6.12) was used to describe the flow syngas inside the module:

$$\rho(\mathrm{u}\cdot\nabla)\mathrm{u} = \nabla\cdot\left(-p\mathrm{I} + \mu(\nabla\mathrm{u} + (\nabla\mathrm{u})^T) - \frac{2}{3}\mu(\nabla\cdot\mathrm{u})\mathrm{I}\right) \tag{6.11}$$

$$\nabla\cdot(\rho\mathrm{u}) = 0 \tag{6.12}$$

The change in density as a function of the mass fractions in the module was defined as:

$$\rho = \frac{p}{RT}\left(\sum_i \frac{w_i}{M_i}\right)^{-1} \tag{6.13}$$

In contrast with previous models which applied source and sink terms to simulate transport across the membrane, our model used a reacting boundary flux based on Sieverts' Law (Equation 6.14):

$$-\mathrm{n}\cdot\mathrm{N}_i = \overline{\mathrm{P}}_{\mathrm{H}_2}\left[\sqrt{\mathrm{p}_{\mathrm{H}_2}^{\mathrm{shell}}} - \sqrt{\mathrm{p}_{\mathrm{H}_2}^{\mathrm{tube}}}\right] \tag{6.14}$$

Where n · Ni represents the H_2 flux across the membrane, $\overline{\mathrm{P}_{\mathrm{H}_2}}$ the permeance of the membrane, and $\mathrm{p}_{\mathrm{H}_2}^{\mathrm{shell}}$ and $\mathrm{p}_{\mathrm{H}_2}^{\mathrm{tube}}$the H_2 partial pressure at the shell and at the tube, respectively. Partial pressure on the tube side was set to be at 1 atm.

The flow was assumed to be laminar in all cases. The inlet was specified to be a normal inlet flow. The outlet had a pressure of 12.6 bar with no viscous stress. The species transport had the initial mole fractions shown in Table 6.3. A Fine mesh was defined as shown in Figure 6.17 containing 3,181,368 degrees of freedom. A direct solver with two segregated groups was adopted for the calculation. A super computer with 130 GB RAM memory was used in this work.

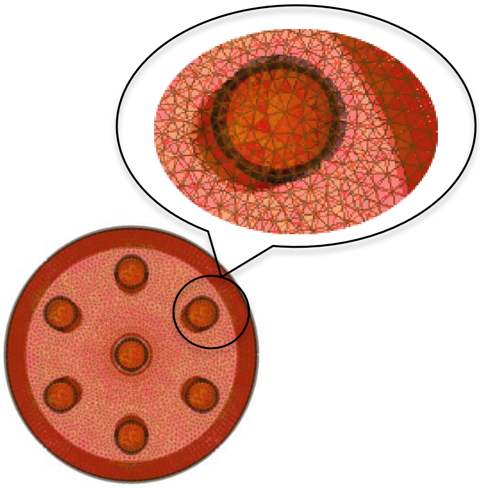

Figure 6.17. Cross-sectional view of developed mesh.

Additionally, the H_2 recovery was analyzed and defined as the percentage extracted from the module through the tubes:

$$R_{H_2}(\%) = \frac{F_{H_2}^{in} - F_{H_2}^{out}}{F_{H_2}^{in}} \cdot 100 \tag{6.15}$$

Where $F_{H_2}^{out}$ and $F_{H_2}^{in}$ are the amount of H_2 at the outlet and the feed of the module, respectively. The usage of the membrane $\varphi(\%)$was studied as well and defined as:

$$\varphi(\%) = \frac{\gamma}{\gamma_{max}} \cdot 100 \tag{6.16}$$

Where γ is the amount of H_2 removed and γ_{max} the maximum theoretical H_2 flux across the membrane.

The performance of the module was tested under different Reynolds (Re) numbers since advection forces affect the mass transport properties of the system. Different inlet velocities were used to modify the Re of the fluid flow. The velocity profiles, shown in Figure 6.18, depict that the velocity of the gas decreases after the expansion between the inlet and the membrane module. Velocity increases when the gases encounter the membranes; this is due to the reduction of available cross-sectional area.

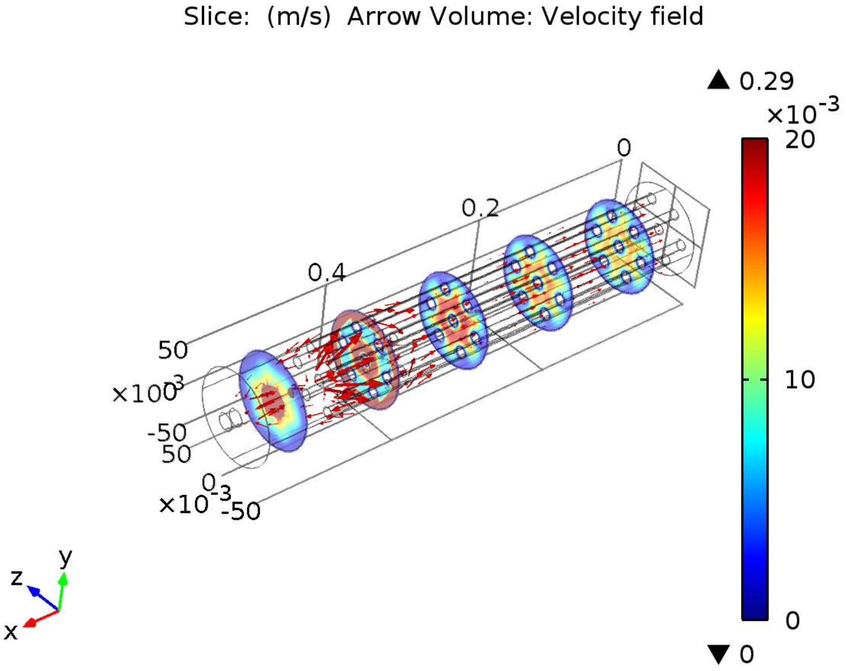

Figure 6.18. Velocity profile of syngas inside the membrane module at moderate Re numbers.

As shown in Figure 6.19 and Figure 6.20, different Re numbers displayed different H_2 mole fraction profiles within the membrane module. For instance, at low Re numbers, H_2 is totally removed from the module (Figure 6.19a). H_2 has enough time to diffuse radially towards the surface of the membranes, before it is ejected out of the module. The H_2 recovery at this point is at its maximum point, but the membrane usage capacity is not exploited.

As the Re numbers increase, H_2 molecules do not reach the surface of the membranes as fast as before. This allows for the membranes to be used further down axially (Figure 6.19b). This continues up to the point where H_2 is unable to diffuse totally towards the adjacent membrane. At this point recovery starts to decrease. High Re numbers supply enough syngas, allowing the membrane to be more uniformly used axially (Figure 6.19c). However, recovery is significantly reduced.

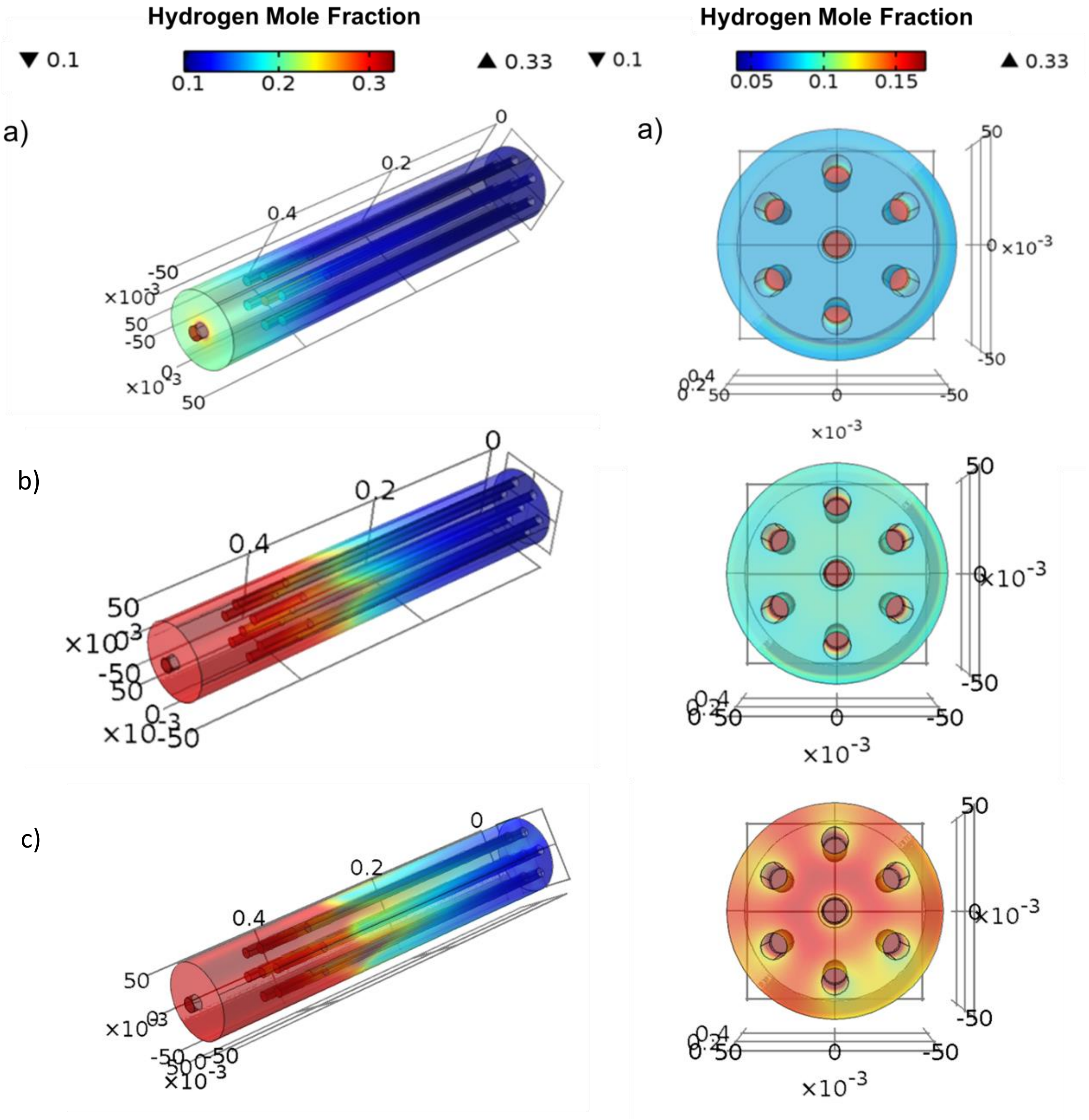

Figure 6.19. Cross-sectional view of the H_2 mole fraction distribution at different Re numbers: a) Low Re number, b) Medium Re, c) High Re

The module shows the formation of a H_2 depleted boundary layer adjacent to the surface of the membrane which is often called concentration polarization (Figure 6.19). This phenomenon is caused by the slow diffusion of H_2 molecules in the radial direction. Concentration polarization decreases the efficiency of the membrane since the driving force is dictated by the H_2 partial pressure difference between the H_2 molecules located next to the membranes surfaces at the retentate and the tube sides. At the tube side, it was assumed to be uniform since pure H_2 is present. However, at the retentate it changes according to the flow, gas composition and rate of removal. Concentration polarization can be clearly seen in Figure 6.19, where the bulk syngas located far from the surface of the membrane is not disturbed. The boundary layer of depleted H_2 becomes thicker as the flow moves along the axial direction. At high Re numbers, the boundary layer becomes thinner. This caused by the constant H_2 supply by the advective flow. Therefore, high Re numbers increase the efficiency of the membranes; nonetheless, the H_2 recovery of the process reduces. For the effective utilization of membrane technology, an optimization between recovery and membrane utilization needs to be performed. Figure 6.20 shows the Re number where the recovery and membrane utilization intersect, suggesting an optimal point for operating the module.

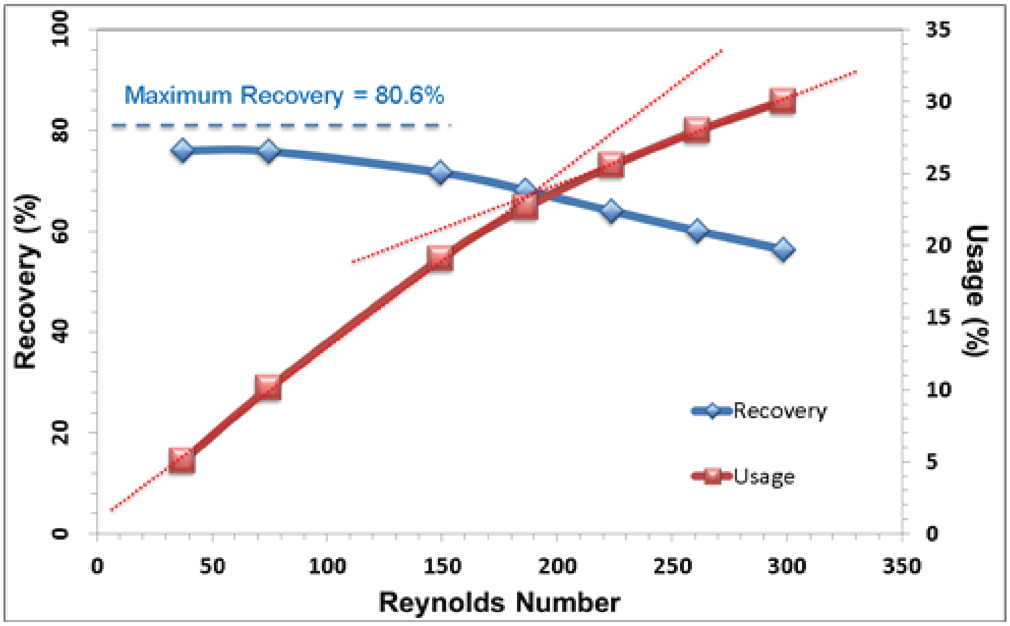

Figure 6.20. Recovery of H_2 and membrane utilization as a function of different Re numbers.

The maximum theoretical recovery, based on the operating conditions, was estimated to be 80.6%, which corresponds to a membrane usage of <5%. At the optimum point, the recovery reaches ~65%, but the usage of the membranes dramatically increased to 25%. After the optimum point, the effect of higher Re numbers keeps improving the usage of the membranes, but to a lower extent. The recovery of H_2 keeps deteriorating after reaching the optimized condition.

6.3.2. Non-isothermal model

To further improve the model's accuracy, heat transfer was added to the model to further explore the performance of a non-isothermal system. In the isothermal model discussed above, it was assumed that inlet feed temperature is the same as the shell temperature. However, in reality, due to the limitation of pre-heat length, feed temperature is always lower than what we expect. This caused a temperature distribution along the reactor. As previously studied by Mardilovich et al. [100], H_2 flux is positively influenced by temperature as shown in Figure 6.21 after high temperature treatment for 5hours. Notice that in the study, temperatures higher than 500°C were not taken into consideration since high temperatures induce intermetallic diffusion between the support and the Pd film, causing a drop in H_2 permeation.

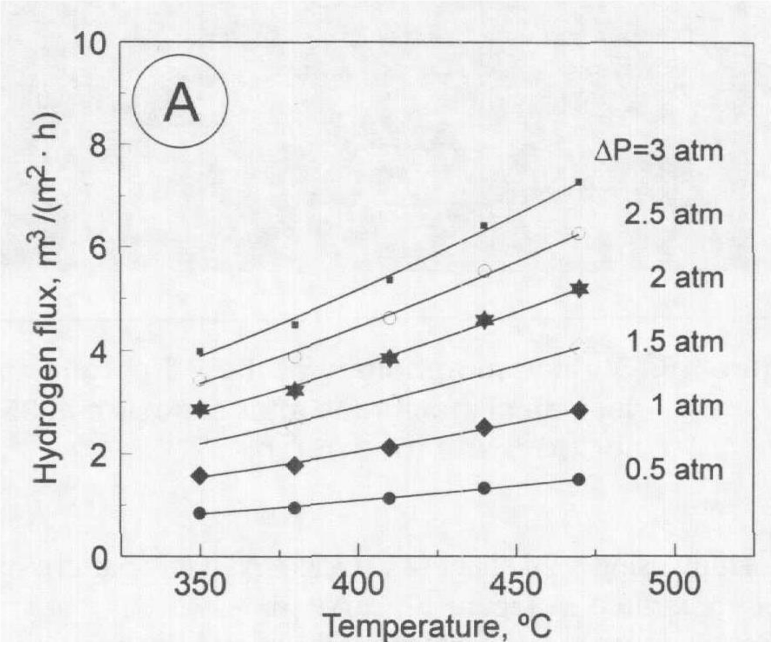

Figure 6.21. Influence of temperature on H_2 flux under different ΔP.

Furthermore, membrane permeability Q is influenced by temperature by Equation 6.17 presented by Koc et. al [53]:

$$Q = Q_0 e^{-E_p/(R \cdot T)} = 6322.7 e^{(-\frac{15630}{R \cdot T})} \tag{6.17}$$

Where E_p is activation energy [J], Q_0 is permeability constant [$m^3 \mu m/(m^2 hatm^{0.5})$]. Thus, it is important to include the energy transport to the previous isothermal model. In COMSOL Multiphysics 5.0, physics “Non-isothermal Flow” and “Transport of Diluted Species” are used to develop the non-isothermal model. The same geometry was used as shown in Figure 6.22.

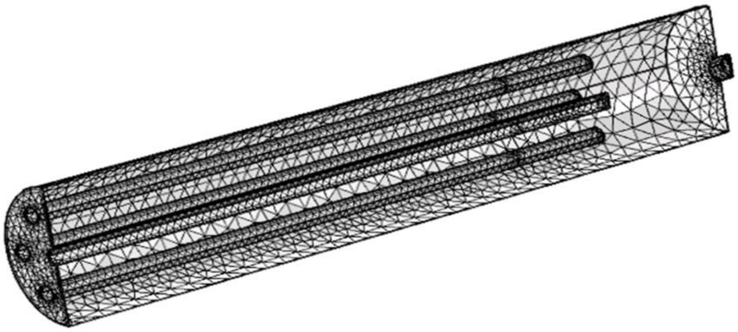

Figure 6.22. Geometry of the model and mesh.

The equation of motion and continuity were used in this model, but differently; the continuity equation was expressed on a mole concentration base instead of mass fraction as shown in Equation 6.18:

$$\nabla \cdot (-\mathrm{D_i} \nabla \mathrm{c_i}) + \mathrm{u} \cdot \nabla \mathrm{c_i} = \mathrm{R_i} \tag{6.18}$$

In the “Non-isothermal Flow” model, the conservation of energy is introduced as:

$$\rho \mathrm{C_p} \mathrm{u} \cdot \nabla \mathrm{T} = \nabla \cdot (\mathrm{k} \nabla \mathrm{T}) + Q \tag{6.19}$$

Considering the effect of temperature to membrane permeance, Sievert’s law now has the expression of:

$$\mathrm{J_{H_2}} = \frac{\mathrm{Q_0}}{\delta} \exp\left(\frac{-\mathrm{E_Q}}{\mathrm{RT}}\right)\left(\mathrm{P_{H_{2,ret}}^{0.5}} - \mathrm{P_{H_{2,per}}^{0.5}}\right) \tag{6.20}$$

“Normal” mesh was applied to the model, with 1,980,170 degrees of freedom. Applying the non-isothermal model, the influence of Reynolds number to H_2 recovery as well as concentration polarization displays a similar performance as the isothermal model. To further analyze the influence of temperature to the system, H_2 recovery was studied under different feed temperatures at a fixed feed flow rate.

As shown in Figure 6.23 and Figure 6.24, as the feed temperature increases, a lower H_2 concentration appears at retentate side, which suggests a stronger depletion of H_2 in the retentate and thus a higher recovery. This is caused by the positive influence of temperature to the membranes’ permeability. Notice that among the two main reasons for mass transfer resistance are: resistance of the membrane and concentration polarization; temperature significantly reduces the membranes’ resistance by enhancing the permeability, but it has a small influence on concentration polarization as diffusivity increases to a smaller magnitude. Another factor that is influenced by temperature is the gas density. Considering the temperature gradient along the membrane, gas density also changes along the membrane, which makes the non-isothermal model more accurate than the isothermal model.

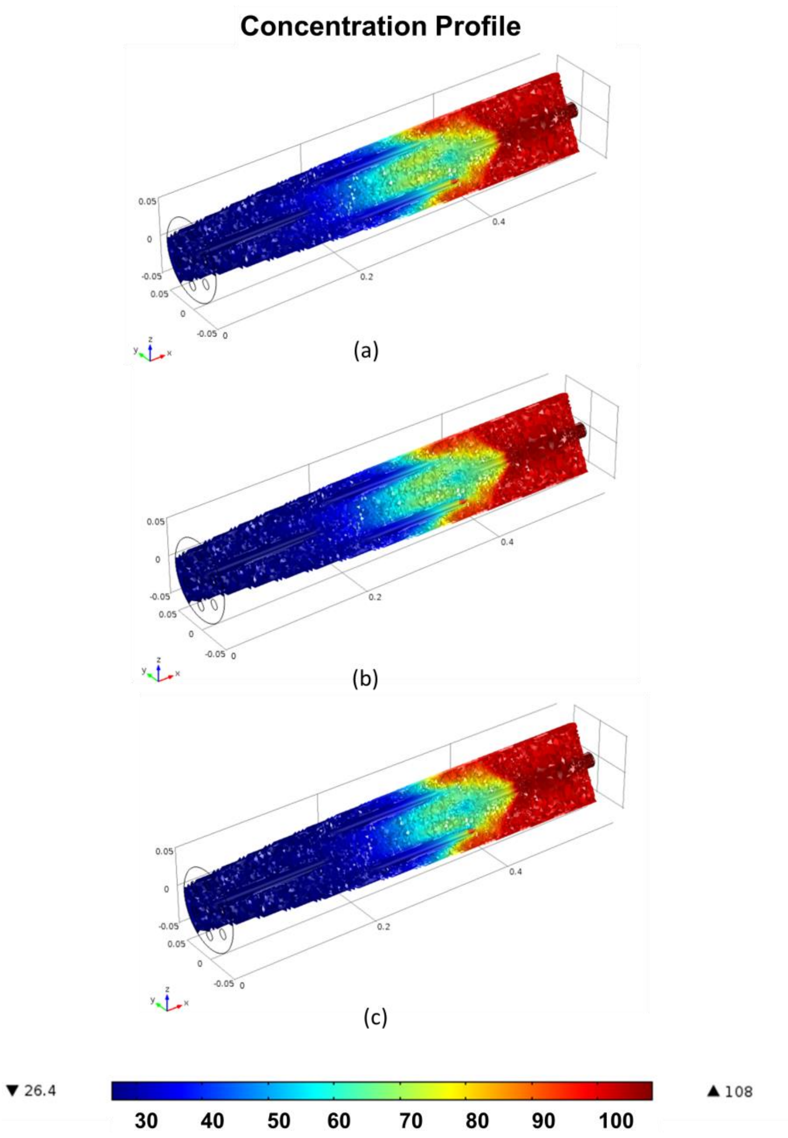

Figure 6.23. Concentration distribution of H_2 at a feed flow rate of 15 ft^3/h with inlet temperature of (a) 523K (b) 600K (c) 723K.

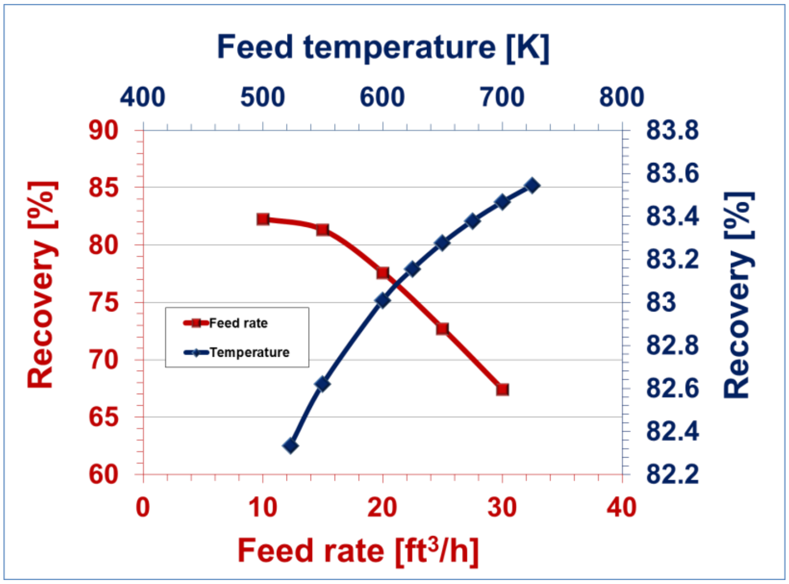

Figure 6.24. Recovery of H_2 as a function of the feed flow rate and feed temperature.

7. DEVELOPMENT OF CATALYTIC MEMBRANE REACTORS

Summary

The production of hydrogen from alternative methods has been gaining considerable interest in the last decades due to the need of responding to increasing H_2 demand for a fuel cell based transportation system as part of the developing H_2 economy. The Water Gas Shift (WGS), Methane Steam Reforming (MSR) and Ethanol Steam Reforming (ESR) reactions conducted in Catalytic Membrane Reactors (CMRs) may represent sound economically viable routes to satisfy such a large hydrogen demand. Consequently, a natural step in the development of this project is the application of membrane technology into catalytic membrane reactors (CMRs) which combine reaction and separation units in one single piece of equipment in order to enhance chemical conversions. This effect, called "process intensification", consists on improving chemical processes by redirecting traditional operational schemes into more precise and efficient operations. This section of the document describes the development of a catalytic membrane module unit used for WGS, MSR and ESR reactions in a pilot-scale rig built at WPI.

7.1. Pilot-scale Catalytic Membrane Reactor Rig

A catalytic membrane reactor (CMR) module was built in the facilities of WPI according to the objectives of Phase II of this project. The CMR rig was designed to embody up to 2.54 cm O.D., 25.4 cm length membranes. A schematic of the experimental setup is shown in Figure 7.1. The device can be divided into three main parts: a mixture preparation section, a preheater, and the reactor module.

• *Mixture preparation section:* The pure gases (H_2, CO, CO_2, and N_2) are supplied from the gas cylinders with the pressure regulators (PR-XX) to the mixture preparation section. Each gas feed line consists of a 7 µm porous stainless steel filter (Filter-XX, Swagelok), a mass flow controller (FC, Bronkhorst High Tech), and a check valve (0.68 barg). The feed line is then connected to a pressure indicator (PI-01, MKS instruments) and a 3.8 L ballast volume. This additional volume ensures an optimal mixing of the gases and eases the transition between the inert gas used in the start-up and the syngas mixture to be tested. A bypass line connected to the permeate that allows to purge the lumen of the membrane during the heating/cooling procedures is also present in the nitrogen stream, avoiding the presence of air or hydrogen. Finally, the dry feed stream is equipped with an additional bypass line connected with a needle valve (V-12) to a forward pressure regulator and then to the micoGC for frequent control of the feed composition. Steam and ethanol for the reactions are made by feeding water and/or ethanol to the preheater by means of a HPLC pump (Pump-01, Eldex); the complete vaporization of the water/ethanol in the preheater is promoted by feeding the liquid water in the tube side of a stainless steel tube-in-tube heat exchanger (E-01) that uses the hot retentate stream coming out from the reactor as the heating medium. From a process safety standpoint, the ballast volume is also connected to a vent line through a poppet check valve with an adjustable cracking pressure ranging from 23.2 to 40.4 barg (V-11, Swagelok). All the fittings, the tubing, and the body of valves (Swagelok) are 316 stainless steel.

• *Preheater:* The preheater consists of a 316 stainless steel tube (80 cm length, 5.08 cm of external diameter) filled with 1 cm quartz Raschig rings (SP Industries) and placed in an electrically heated furnace (Furnace-01, Watlow 1.6 kW); the temperature is controlled by a PID controller (Omega) governed by a 1.6 mm (1 /16 in.) o.d. thermocouple type K (Omega) placed in the external side of the SS tube. The temperature of the mixture exiting from the preheater is measured by means of an additional thermocouple type K (TI-01, Omega). The piping connecting the preheater and the reactor, and in the steam line between the heat-exchanger (E-01) and the preheater, is traced with flexible heating tapes (Omega) and thermally insulated to avoid steam condensing in cold spots of the system.

- *Reactor:* The test section consists of a 316 stainless steel reactor (100 cm length, 5.08 cm o.d. with wall thickness of 0.32 cm) placed in a furnace (Furnace-02, Watlow 1.6 kW) whose temperature is controlled through a PID controller (Omega). The annulus volume surrounding the membrane is filled with catalytic particles confined by stainless steel 316 L meshes. To monitor the axial temperature profiles in the catalytic bed, a 5-point thermocouple (TI-02, Omega) is placed at a distance of approximately 1 cm (3 /8 in.) from the membrane surface. A thermocouple (TI-03, Omega) with similar characteristics is also present in the membrane lumen. As mentioned before, an inert sweep gas (N_2 or He) is used in the permeate side to prevent the oxidation of the palladium coating during the start-up operations. The permeate stream leaving the reactor is fed to a pressure indicator (PI-03, MKS Instruments), to two adsorbent beds mounted in parallel, and then connected with a mass flow meter (FI-02, Bronkhorst High Tech), a back pressure regulator (PC-02, Bronkhorst High Tech), and through a multiport valve (Vico) to the GC (Agilent 490 MicroGC, dual channel equipped with 5MS and PPU columns). The permeate stream is also connected to a vent line through an adjustable cracking pressure valve (V-14, 3.510.4 barg) to avoid, in the event that the membrane breaks, the steam reaching the mass flow meter and GC. The retentate stream, which under normal operating conditions and in the presence of a membrane with a virtual infinite selectivity contains the totality of the unreacted water vapor, is connected to two heat-exchangers in series in order to condense all the water present. In particular, the cooling fluid in the first one (E-01) is the liquid water to be fed to the reactor, while the second (E-02) is chilled with a 50% aqueous mixture of ethylene glycol to ensure a dew point for the retentate stream of 4-5 ^{o}C. Before the first heat exchanger, an additional vent line equipped with an adjustable cracking pressure valve (V-15, 23.240.4 barg) is installed for safety reasons. The temperature of the retentate stream after leaving the first heat exchanger is further monitored by a thermocouple type K (TI-04, Omega). The condensate water is then led to a 3.8 L liquid reservoir, from which it is automatically removed by a zeroloss high pressure pneumatic drain valve (Robodrain RD750, eCompressedair). The retentate stream is also equipped with two adsorbent beds (Moisture filter 01 and 02), a mass flow meter (FI-02, Bronkhorst High Tech), a back pressure regulator (PC-02, Bronkhorst High Tech) and then sent through the multiport valve to microGC. Finally, an additional pressure indicator (PI-02, MKS Instruments) is placed after the reactor to monitor the pressure drop in the catalytic bed.

The thermocouple signals are acquired via a National Instruments acquisition card, while the other tunable parameters (pure liquid water and gases flow rates, permeate and retentate pressures) are checked, controlled, and saved in real time through RS232 Pc-ports and a custom-built Labview code. Finally, the stream compositions are measured via the Galaxie (version 1.10) factory software from Agilent Technologies. It is worth noticing that, for process safety reasons, the entire instrumented process system is fully automated, computer controlled, and can be operated remotely with the aid of a computer.

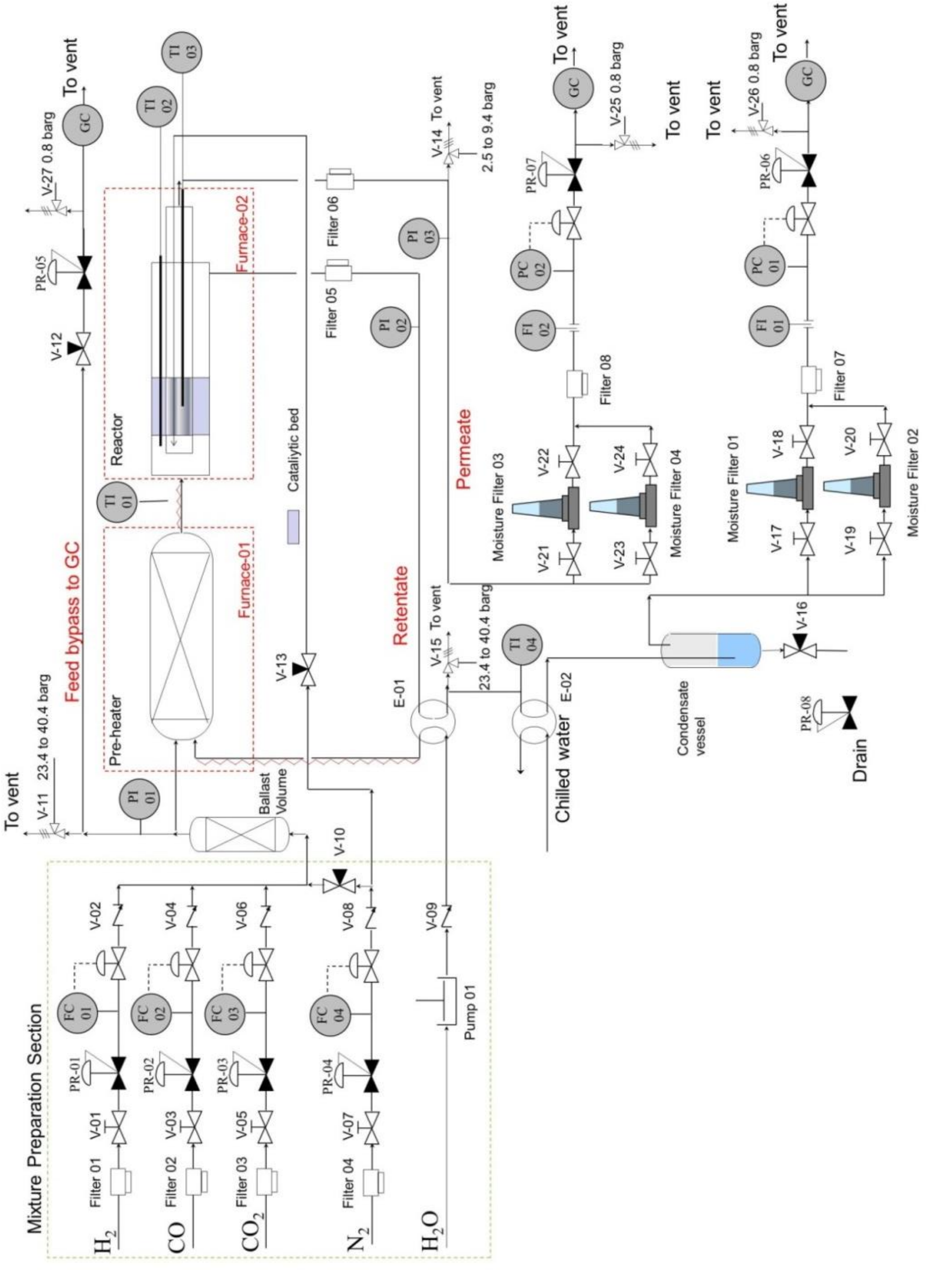

Figure 7.1. Schematic of the CMR apparatus constructed in WPI

7.2. Water-Gas-Shift Reaction

Composite palladium and Pd-based membranes represent an appealing technology option to increase the CO conversion and the H_2 recovery in the water-gas-shift (WGS) reactor as a result of the continuous removal of hydrogen over the course of the reaction. Even though many studies have been performed in this area, their outcome typically represents a proof-of-concept involving reactors with small membrane area. The present section therefore addresses the scaling up of the process to obtain high hydrogen production rates through the use of large surface area, ~0.02 m^2, composite Pd membranes. Two thin, $\delta < 10$ µm, defect-free composite membranes were prepared and tested under pure gases and water gas shift reaction conditions. Syngas similar to the actual gasifier (NCCC) reacting mixture (40% H_2, 42.2% CO, and 17.8% CO_2 and steam to carbon ratio varying between 2.5 and 3.5) was fed to the WGS catalytic membrane reactor (WGS-CMR) with a total flow rate up to 1.5 Nm^3h^{-1}, 20 bar maximum pressure, and temperatures ranging 420-440°C. In the presence of crushed catalyst, CO conversions higher than the equilibrium conversions were obtained within the entire gas hour space velocity (GHSV) range considered in the present study, for pressures between 7 and 20 bar. At a relatively low feed flow rate, GHSV = 1130 h^{-1}, a maximum CO conversion of 98.1% was achieved, with a hydrogen recovery of 81.5% at 440°C. On the other hand, at the highest GHSVs, the system appeared to be limited by the activity of the ferrochrome catalyst. At 20 bar of absolute pressure in the retentate side, 440°C, and GHSV = 5650 h^{-1}, the hydrogen production rate was found to be 5.6 Nm^3 day^{-1}. Remarkably high hydrogen purity, in excess of 99.97% and 99.2% for the two membranes, respectively, was achieved also in experiments performed with a retentate pressure of 20 bar.

Description

Membranes MA-127 and MA-131B were tested in pure hydrogen and nitrogen experiments before conducting the watergas shift tests. A summary of the history of the hydrogen permeance and H_2/inert ideal selectivity obtained for membranes MA-127C and MA-131B is depicted in Figure 7.2 as a function of the thickness of the metal layer. The two membranes showed very similar properties, having a H_2 permeance at 420°C of 21.8 $Nm^3m^{-2}h^{-1}$ $bar^{-0.5}$, H_2/N_2 selectivity at ΔP = 1 atm in excess of 12,000 and a thickness of 7.4 and 8.3 µm for membranes MA-127C and MA-131B, respectively. The WGS experiments were performed according to the following procedure: nitrogen stream with a flow rate of 1 NL min^{-1} was fed to the reactor until the test pressure was reached. The newly loaded catalyst was then allowed to be fully oxidized by mixing the nitrogen stream with 6.2 g min^{-1} of steam for at least 1 h or until no hydrogen produced by the oxidation reaction was detectable with the GC in the retentate stream. Then, the nitrogen stream was ceased, and in the normal operating conditions, a syngas stream (42.2% CO, 40% H_2, and 17.8% CO_2 on a dry basis) was fed to the preheater and mixed with the desired flow of water vapor to reach a steam to carbon ratio equal to or higher than 2.5 to avoid coke formation on the membrane surface. The WGS experiments were conducted for at least 4 h, until steady-state conditions were reached for the temperature profile on the catalytic bed and for the flow rates and compositions of the permeate, retentate, and feed streams. The results were then evaluated in terms of hydrogen purity, carbon monoxide conversion, and hydrogen recovery. In particular, the hydrogen purity was determined with the mass balance of the impurities (i.e. CO and CO_2) present in the permeate stream analyzed with the GC. For these gases, calibration curves in the low concentration region were developed ensuring a resolution of 100 ppm. As a consequence, it is believed that because the CO and CO_2 could be determined quite accurately, the balance used to obtain the hydrogen purity was more precise than the direct measurement of the H_2 concentration in the permeate stream. Finally, in all the experiments performed in this study, the methanation reaction, that is the main side reaction under WGS conditions, remained negligible and no CH_4 was observed in the GC analysis

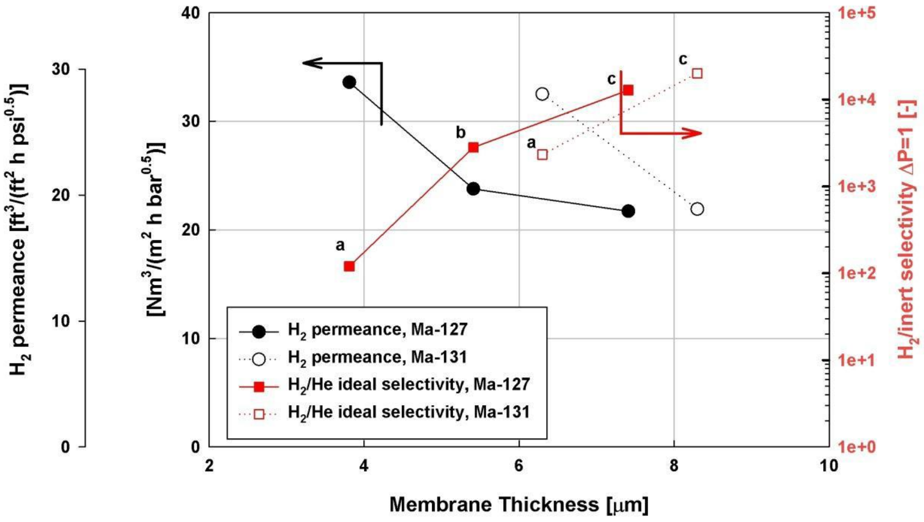

Figure 7.2. Comparative performance assessment of membranes MA-127C and MA-131B in terms of hydrogen permeance and H_2/inert ideal selectivity. (a) The first H_2 exposure, permeance, and H2/He selectivity were retrieved at 450 C; (b) and (c) tests performed in the WGS rig at 420 °C, the selectivity was calculated for the gas pair H_2/N_2.

7.2.1 Effect of the GHSV and Catalyst Particle Size.

Membranes MA-127C and MA-131B were tested with the syngas composition reported above and with a fixed steam to carbon ratio of 2.5. The experiments were carried out at high pressure in the retentate side, that is, 15 and 20 bar, to enhance the driving force for hydrogen permeation, while the permeate side was maintained close to the atmospheric pressure. In addition, relatively high wet feed flow rates were employed, ranging between 0.3 and 1.5 Nm^3h^{-1}, to reduce the influence of the concentration polarization phenomenon. The annulus volume surrounding the active surface of the palladium membranes, 265 cm^3 , was filled with 257 g of as-received iron-chrome catalyst in pellets, 5.4 x 3.6 mm, for the experiments performed with membrane MA-127C, while a catalyst load of 313 g was employed for membrane MA-131B after being crushed and sieved (16/+40 mesh). In Figure 7.3, the hydrogen permeate flow and hydrogen purity are reported as functions of the wet feed flow rate for membrane MA-127C. The experiments were performed at 420°C, as average temperature level in the catalytic bed. As clearly shown in Figure 7.3, the hydrogen permeate flow increased monotonically by increasing the feed flow rate, as well as the retentate pressure. Both these conditions indeed increased the average hydrogen partial pressure at the gas membrane interface. At high feed flow rates, the hydrogen content was depleted less drastically along the membrane length and the concentration polarization phenomenon was less severe due to a better gas transport in the catalytic bed, while an increase in the total pressure reflected directly in a higher hydrogen partial pressure at the metal surface. It is worth noticing that the hydrogen purity was also in excess of 99.97% in the experiments performed at 20 bar of absolute pressure in the retentate, indicating the presence of a very dense and selective palladium layer. In Figure 7.4, the same sets of data were reported in terms of CO conversion and hydrogen recovery versus the gas hour space velocity (GHSV) along with the X_{CO} at thermodynamic equilibrium conditions, representing the maximum conversion achievable with the traditional packed bed reactor under the same operating conditions.

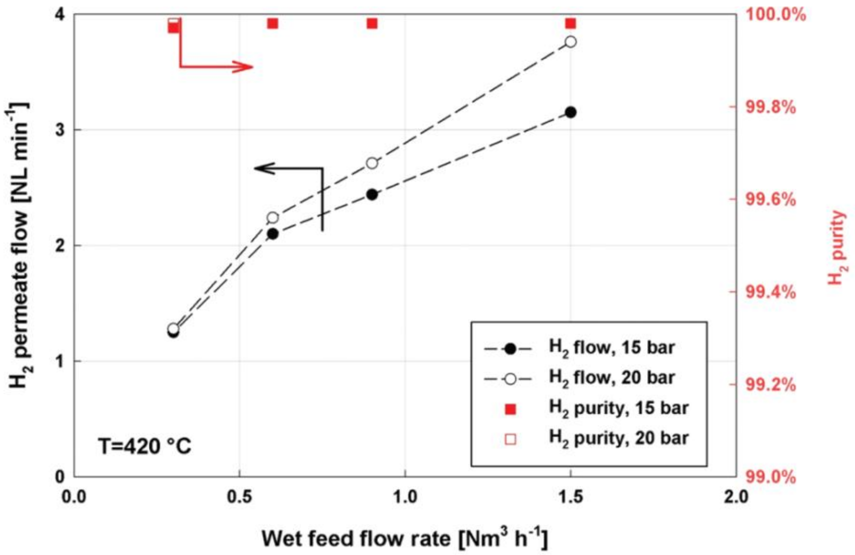

Figure 7.3. Hydrogen permeate flow and H_2 purity in WGS experiments performed on membrane MA-127C at 15 and 20 bar of retentate pressure. Syngas composition: 20.5% CO, 19.5% H_2, 8.6% CO_2, and 51.4% H_2O.

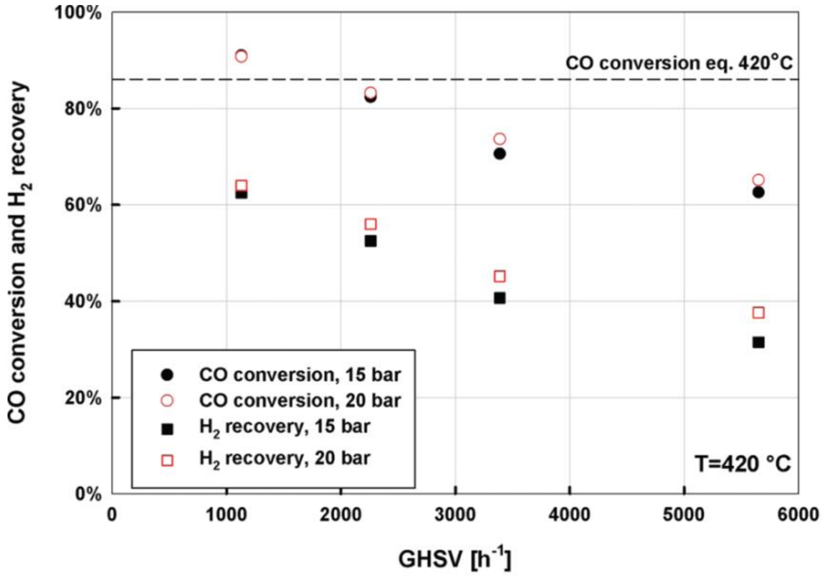

Figure 7.4. Carbon monoxide conversion and hydrogen recovery in WGS experiments performed on membrane MA-127C at 15 and 20 bar of retentate pressure.

The X_{CO} showed a decline with increasing the GHSV as a result of the shortening of the contact time of the syngas with the catalyst surface. On the other hand, a reduction in hydrogen recovery was also observed with increasing the feed flow rate: such a behavior is consistent with the idea that increasing the feed flow rate, the relative importance of the mass transfer resistance in the composite membrane itself became more and more relevant. In other words, the surface area of the membrane was not enough to allow the hydrogen partial pressure to approach the theoretical limit. The membrane reactor exhibited a higher conversion with respect to the thermodynamic equilibrium X_{CO} only at the lowest GHSV considered in this work: 1130 h^{-1}. For higher feed flow rates, the thermodynamic equilibrium was never reached at both pressures, indicating that an insufficient catalytic surface area was available for the reaction.

Additional experiments were performed mimicking a conventional reactor by closing the permeate side of the reactor and waiting until pseudo-steady state conditions were achieved (i.e. constant pressure on the lumen side of the membrane ((1% in 30 min)). This configuration has been chosen to maintain the same catalyst load as well as pallet configuration with respect to the WGSCMR experiments previously performed. The outcome represented the CO conversion in the limit in which the hydrogen recovery is approaching zero, which can be considered, at least in first approximation, as the value obtainable under packed-bed operating conditions. A CO conversion of 65.2% at GHSV = 2250 h^{-1} and at pressure ranging between 7 and 15 bar was measured and found well below the thermodynamic equilibrium X_{CO} at 420°C of 86.0%. This evidence confirmed the idea that the catalytic area available for the WGS reaction was not sufficient to obtain a complete CO conversion at the high feed flow rate considered in this work.

The tests on membrane MA-131B were therefore performed with the iron-chrome catalyst crushed and sieved 16/+40 mesh (corresponding to an average particle diameter of 710 μm) in order to increase the surface area available for the reaction. Syngas composition, steam to carbon ratio, pressure, and feed flow ranges were maintained unchanged with respect to the experiments performed on membrane MA-127C. The results in terms of hydrogen permeate flow, hydrogen purity, and CO conversion are reported in Figure 7.5 and Figure 7.6, respectively. As shown in Figure 7.5, the behavior for the hydrogen permeate flow versus the feed flow rate was similar to the one obtained for membrane MA-127C. In the case of membrane MA-131B at 1.5 Nm^3h^{-1} of wet feed flow rate, 20 bar of retentate pressure, a noticeably H_2 permeate flow of 5.6 Nm^3day^{-1} was achieved. The purity of the hydrogen produced with membrane MA-131B was high, 99.9799.98%, and comparable with the previous results for the WGS runs conducted at 15 bar, while at the highest pressure of 20 bar the purity slightly declined to 99.2%. The leak growth that the membrane MA-131B exhibited was higher than that of membrane MA-127C: this is compatible with the higher temperature at which this specific membrane was exposed in the watergas shift experiments. It is worth noticing indeed that even if the parameters for temperature control on the reactor furnace remained unchanged with respect to the ones used in the tests involving membrane MA-127C, the average temperature in the reactor increased up to 440°C; the higher catalytic surface area and, as a consequence, the higher CO conversion were responsible for such a higher steady-state temperature in the reactor due to the exothermic nature of the WGS reaction. The CO conversion and hydrogen recovery for experiments carried out with membrane MA-131B are reported in Figure 7.6 versus the GHSV; for comparison purposes, the results obtained with membrane MA-127C at 20 bar of retentate pressure are reported in the same figure. In the case of the WGS runs performed on membrane MA-131B, the carbon monoxide conversion exceeded the thermodynamic equilibrium X_{CO} in the entire feed flow rate range (GHSV values between 1130 and 5650 h^{-1}) and resulted in a conversion well above the one found in the membrane MA-127C case under the same conditions. In the limit of low feed flow rates, in which the system is mainly controlled by the resistance associated with the gas transport toward the catalytic bed, a CO conversion of 98.1% and a hydrogen recovery of 81.5% were achieved at 20 bar of total pressure in the retentate side. As shown in Figure 7.6, the CO conversion appeared to approach the equilibrium conversion at high feed flow rates even if a hydrogen recovery higher than 40% was attained. The presence of such a hydrogen permeate flux was expected to enhance noticeably the CO conversion, with respect to the thermodynamic equilibrium conversion. In this case, the shortening of the contact time in the WGS reactor, decreased from 24.8 s at GHSV = 1130 h^{-1} and 20 bar of pressure to 4.7 s at GHSV = 5650 h^{-1} and 20 bar of pressure, could be responsible for the reduction of the catalyst activity, indicating that at the highest feed flow rate considered in the present work the system was kinetically limited by the presence of the WGS catalyst. By increasing the GHSV, the X_{CO} dropped from 68.1% to 55.7% at GHSV between 4000 and 12,000 L $kg^{-1}h^{-1}$ at 350°C and remained below the thermodynamic equilibrium conversion within the entire GHSV range investigated.

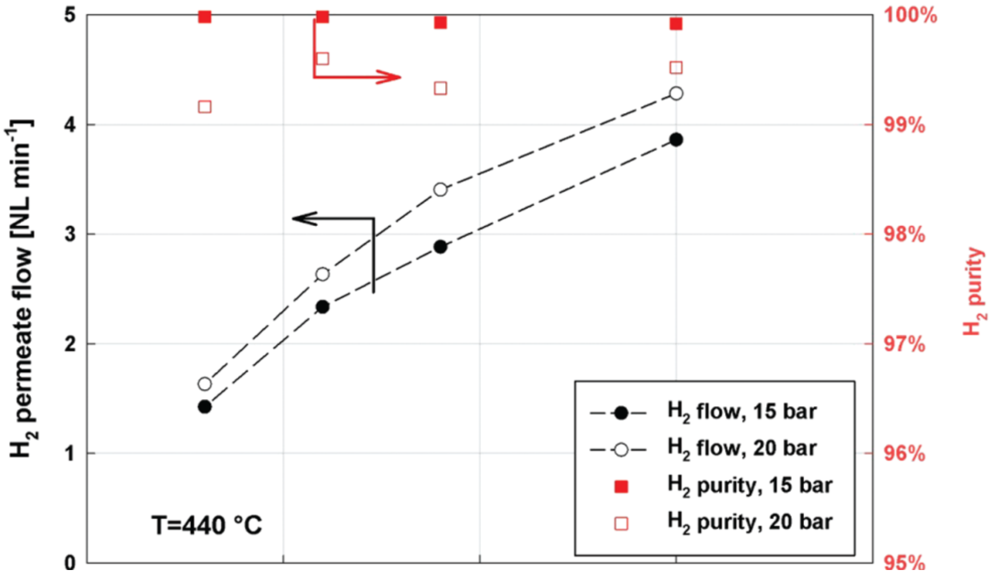

Figure 7.5. Hydrogen permeate flow and H_2 purity in WGS experiments performed on membrane MA-131B at 15 and 20 bar of retentate pressure. Syngas composition: 20.5% CO, 19.5% H_2, 8.6% CO_2, and 51.4% H_2O.

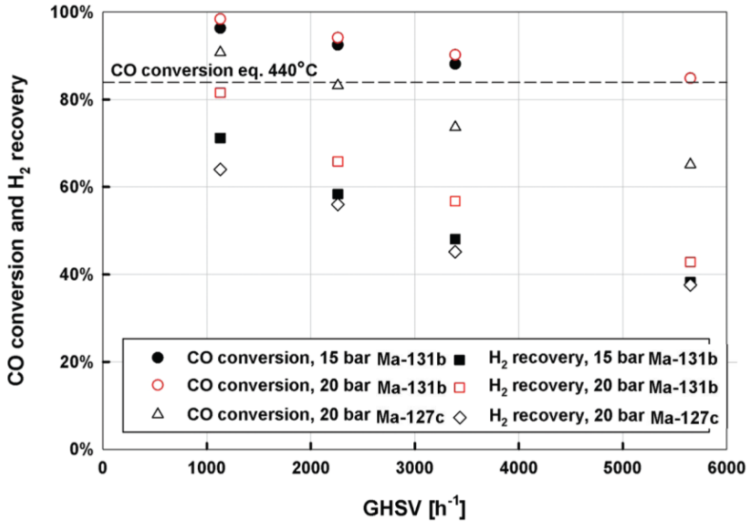

Figure 7.6. Carbon monoxide conversion and hydrogen recovery in WGS experiments performed on membrane MA-131B at 15 and 20 bar of retentate pressure and 440°C. Data obtained for membrane MA-127C at 20 bar and 420°C are reported for the sake of comparison.

7.2.2 Effect of Retentate Pressure and H_2O/CO Ratio.

Figure 7.7 shows the CO conversion and the hydrogen recovery obtained on the WGS-CMR equipped with membrane MA-131B as a function of the retentate pressure for experiments performed at 440°C, GHSV = 2260 h^{-1}, steam to carbon ratio of 2.5, and pressure ranging between 7 and 20 bar. The dashed line represents the equilibrium conversion calculated at the same inlet conditions. Because the WGS is an equimolar reaction, there should be no pressure influence on the equilibrium CO conversion. In the presence of a WGS-CMR, the high pressure improved the hydrogen permeation by increasing the driving force and enhancing noticeably the CO conversion. Also, the hydrogen recovery was highly influenced by increasing the pressure in the retentate side reaching at 20 bar the value of 65.8%. To clarify the hydrogen recovery behavior, in the same figure the trend of the maximum hydrogen recovery, achievable in the configuration used is also reported, that is, considering a minimum H_2 partial pressure at the retentate outlet equal to the hydrogen partial pressure in the permeate side.

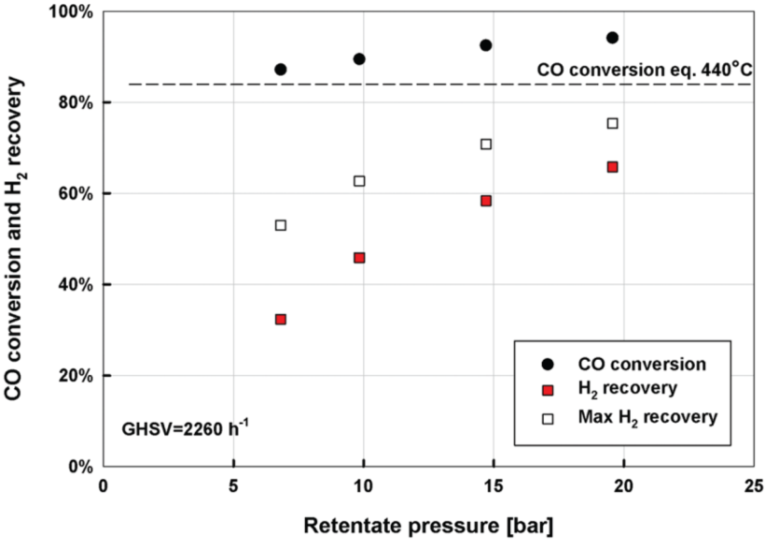

Figure 7.7. Carbon monoxide conversion and hydrogen recovery for membrane MA-131B as a function of the retentate pressure. Experiments performed at 440°C with a GHSV = 2260 h^{-1} (feed flow rate = 0.6 Nm^3h^{-1}).

7.2.3 Membrane Stability.

At the end of the WGS runs permeances and selectivities of the membranes were measured in pure hydrogen and nitrogen experiments at a temperature of 420°C and at pressures up to 5 bar: a summary of the characteristics of membranes MA-127C and MA-131B before and after the WGS are reported in Table 7.1. The H_2 permeance for membrane MA-127C after 450 h in syngas, hydrogen, or mixtures atmospheres declined by 12.7%; it should be emphasized that the nitrogen leak showed only a slight increase, 0.76 sccm bar^{-1}, giving a final H_2/N_2 ideal selectivity at ΔP = 1 atm of about 2490. Similar experiments were also performed on membrane MA-131B after 390 h of testing in pure hydrogen and syngas mixtures. MA-131B exhibited a leak growth higher than that of MA-127C, resulting in a final N_2 leak of 4.72 sccm bar^{-1} (H_2/N_2 ideal selectivity at ΔP =1 atm of about 550). A permeance loss of about 11.2% was found at the end of the testing period. As mentioned before, the more marked leak growth that the membrane MA-131B exhibited was in agreement with the higher temperature at which the membrane was operated and evaluated in the aforementioned WGS experiments.

The membrane MA-127C, after having been removed from the reactor, was cut and then analyzed by SEM. The cross section of MA-127C is depicted in Figure 7.8 and shows a relatively smooth and uniform Pd layer with a thickness of 6.7 μm, which is in good agreement with the measured gravimetric thickness value of 7.4 μm. Finally, the surface of membrane MA-127C was analyzed by SEM-EDX techniques. The Pd surface of MA-127C exhibited the typical annealed Pd clusters and only showed traces amount of iron. Furthermore, neither chrome nor copper was detected. In addition, no carbon was found on the surface. The absence of coke formation was indeed expected because of the high steam to carbon ratio employed in the WGS experiments.

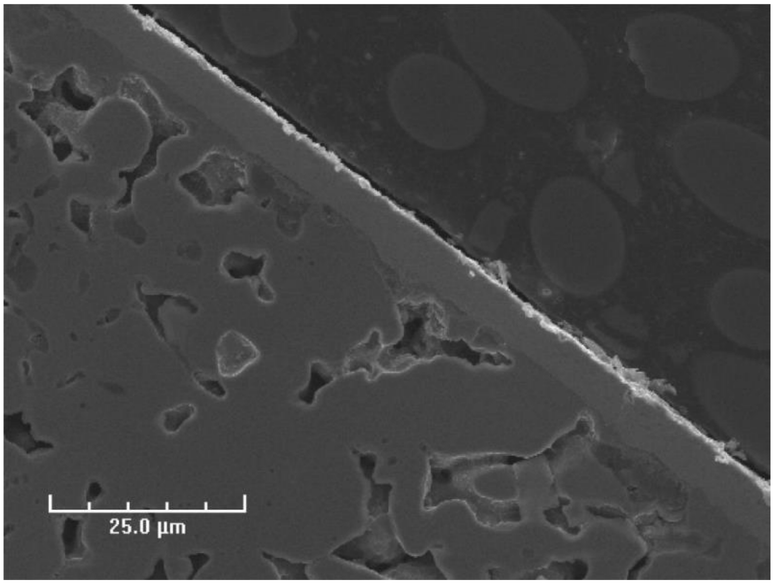

Figure 7.8. Cross section of membrane MA-127C; magnification = 1000X.

Table 7.1. Thickness, Selectivity, and H_2 Permeance of Membranes MA-127C and MA-131B, for the First H_2 Test before and after the Water-Gas-Shift Reaction.

Membrane	Condition	Pd thickness [µm]	Selectivity	H_2 Permeance [$Nm^3m^{-2}h^{-1}bar^{-0.5}$]	T [°C]
MA-127C	1st H_2 test	3.8	130	33.6	450
	before WGS reaction	7.4	12000	21.7	420
	after 450 h	7.4	2490	18.9	420
MA-131B	1st H_2 test	6.3	415	28.9	450
	before WGS reaction	8.3	20000	21.9	420
	after 390 h	8.3	500	19.4	420

7.3. Integration of Methane Steam Reforming and Water Gas Shift

Palladium-based CMRs, which have shown to be effective in methane steam reforming (MSR) and water-gas-shift reactions (WGS), efficiently remove H_2 to induce higher conversions. As a result, this section demonstrates the technical performance of a novel CMR which utilizes two catalysts in series rather than one. In the system, the first catalyst, confined on the shell side of the reactor, reforms methane with water yielding H_2, CO and CO_2. After reforming is completed, a second catalyst positioned in series, reacts with CO and water through the WGS reaction yielding pure H_2O, CO_2 and H_2. A tubular composite asymmetric Pd/Au/Pd membrane, presented for the first time in the literature, is situated throughout the reactor to continuously remove the produced H_2 and to induce higher methane and CO conversions yielding ultrapure H_2 and compressed CO_2 ready for dehydration. The experimental results in i) a conventional packed bed reactor packed (PBR) for MSR, ii) a PBR with two catalysts in series and iii) a CMR with two catalysts in series, are shown, compared and thoroughly described. Furthermore, a comprehensive 2-D computational fluid dynamics (CFD) model was developed to explore further the features of the proposed configuration. The reaction was studied at different conditions such as space velocities, temperatures, pressures and initial feed gas composition. The CMR module was operated for 600 hours displaying high a H_2 permeance and purity, higher CH_4 conversion and a reduced CO yield.

Description

7.3.1 Membrane fabrication

A composite Pd/Au/Pd membrane labelled as MA-170 was prepared on a 1.27 cm OD and 38.1 cm in length 316L PSS support with media grade of 0.5 µm. The total permeable area of the membrane was of 152 cm^2. One end of the membrane was welded to a 316L nonporous tube capped while the other end to a nonporous tube. The support showed an initial He flux of 200 L/min at a pressure difference of one bar. To synthesize the membrane, the support was first covered with sol-gel and then calcined at 600°C for 12 hours. After calcination, the supports were graded following a previously reported procedure with medium and fine pre-activated powder, provided by Johnson Matthey (UK), based on a 2 wt% Pd-Alumina catalyst without any additional activation or treatment. Notice that the grading procedure reduced the He flux across the membrane by >99.9% as shown in Table 7.2. After grading, the surface of the membrane was activated with $SnCl_2$-$PdCl_2$ and then electroless plating was used to deposit a dense Pd layer. A thin gold layer of 0.2 µm was deposited on top of the palladium surface via conventional electroplating. Notice that gold has shown to enhance the properties of Pd-based membranes such as: permeance, stability and contaminant-recoverability [101] and therefore was used in this work. Finally, to provide active sides on this asymmetric membrane and further reduce the He leak present, a pure Pd topmost layer was deposited. The thickness of the membrane was estimated by gravimetric methods. The final composition and leak of the membrane was 6.9 Pd/ 0.2 Au/ 3.2 Pd and <0.01 sccm/bar, respectively. The thicknesses and He leak at each step of the synthesis are shown in Table 7.2.

Table 7.2. Characteristics of the membrane at different phases of the synthesis.

Membrane synthesis step	Thickness / µm	He Leak (sccm/bar) @25°C
Initial support	NA	197,360
Oxidation and calcination	NA	91,830
Grading Pd(Al_2O_3)	2.8	66
Pd layer	6.9	3
Au deposition	0.2	1.39
Pd layer (final)	3.17	NA

7.3.2 Reaction tests and membrane characterization

The H_2 permeation tests and reactions were performed in the CMR rig previously described. The composition of the feed was controlled by mass flow controllers and premixed with steam generated in a preheater. The wet mixture was fed to the reactor which contains the membrane surrounded by the catalysts. The catalysts used for MSR and WGS were a Nickel-based catalyst (HiFUEL R110, Alfa-Aesar) and an Iron-chrome catalyst (HiFUEL W210, Alfa-Aesar), respectively; notice that these catalysts were crushed and sieved (16/+40 mesh) before usage. The water of the retentate was condensed, while the product and retentate flow rates were passed through water absorbent beds before the composition was measured by mass flow meters and a gas chromatograph. Three main experiments were conducted on the CMR-rig including: i) MSR in a conventional packed bed reactor (PBR), ii) MSR/WGS in a PBR, and iii) MSR/WGS in a CMR. It is important to notice that no sweep gas was utilized in any of the experiments presented in this work.

For the CMR reaction, a protective cage was designed in order to prevent any potential damage of the membrane caused by the friction of the catalyst particles and the wall of the membrane as previously reported in the literature. The cage was made out of stainless steel grids and it consists of a two concentric confines; one surrounds the membrane while the other is used to hold the catalyst in place, as shown in Figure 7.9b. Notice that the surface of the membrane is never in contact with the grid of the cage. The catalyst section of the cage has a volume was of 480 cm^3 and it was filled 120 g of MSR catalyst and 120 g of WGS catalyst. This membrane-catalyst cage system can be up-scaled in order to develop multitube CMR modules.

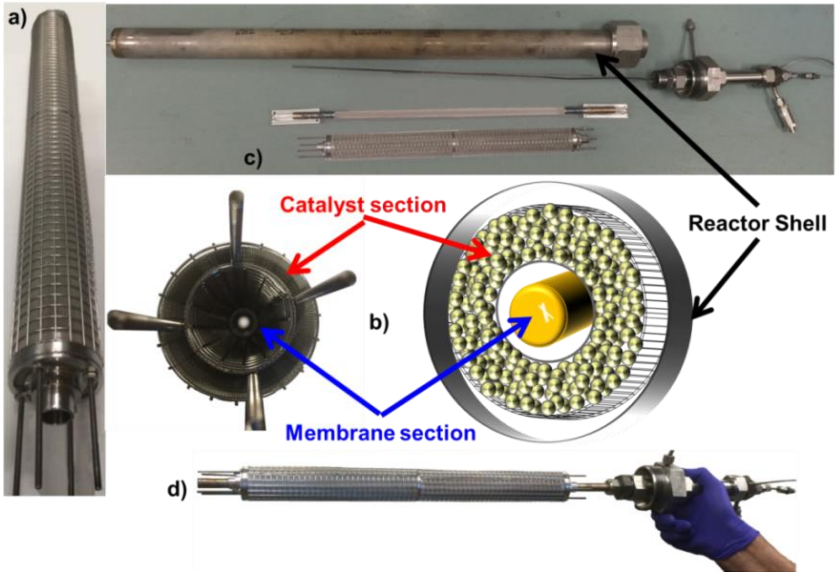

Figure 7.9. Cage, catalyst and membrane configurations used in this work: a) assembled protective cage without a membrane, b) cross-sectional view of the cage and its schematic representation, c) different components of the CMR module, d) integrated cage-catalyst-membrane.

7.3.3. Mathematical Model

Detailed modeling, helpful for the analysis of CMRs, has been used in the interpretation of data and accordingly, a 2-D computational fluid dynamics (CFD) model was developed in COMSOL

Multiphysics 4.3b in order to examine the properties of the module and comparing theoretical values with experimental results. A 2-D configuration of the model was chosen in order to include the non-ideal flow effects that occur in the reactor. The performance of the simulation was compared against the experimental values obtained in this work; and for MSR, the 1-D model presented by Ayturk et al. [102] were a 99.4% accuracy was found when compared to other literature sources including conventional PBRs and CMRs. Figure 7.10 shows the configuration of the 2-D simulation, where MSR catalytic section is located adjacent to the feed flow stream, followed by the WGS section upstream; the membrane was specified to be at the bottom, taking advantage of the symmetrical configuration of the module; additionally, it is shown the mathematical mesh used to solve the momentum and continuity equations. The physics used for the model was “reacting flow in porous media” and whose assumptions include:

1) Isothermal conditions
2) Steady state
3) Intrinsic kinetics for MSR and WGS reactions
4) Laminar flow
5) Non-slip boundary condition for the fluid flow
6) Negligible effect of the protective cage to the flow pattern

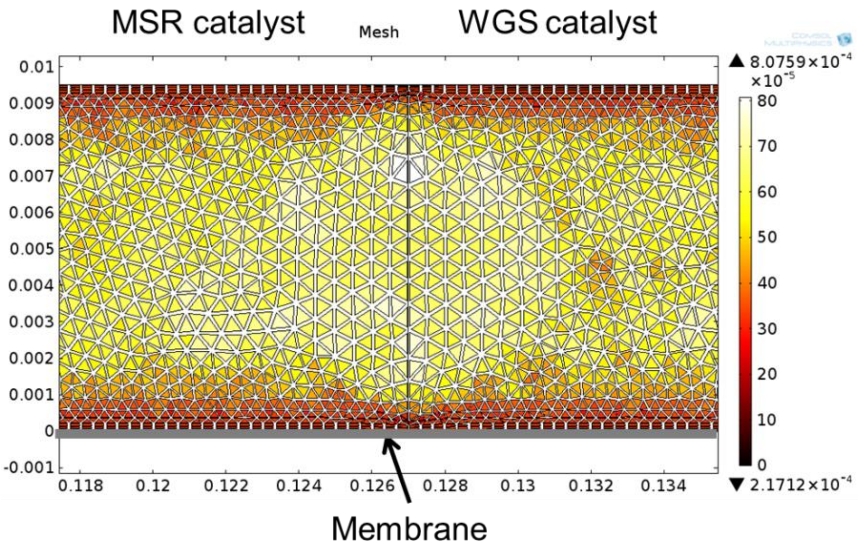

Figure 7.10. Configuration of the simulation depicting the two catalyst sections, the location of the membrane, and the size and geometry of the used mesh.

The reaction rates for MSR were specified as:

$$r1 = \frac{k1}{P_{H2}^{2.5}} \frac{P_{CH4}P_{H2O} - (P_{H2}^{3}P_{CO}/K1)}{DEN^{2}} \tag{4}$$

$$r2 = \frac{k2}{P_{H2}} \frac{P_{CO}P_{H2O} - (P_{H2}P_{CO2}/K2)}{DEN^{2}} \tag{5}$$

$$r3 = \frac{k3}{P_{H2}^{3.5}} \frac{P_{CH4}P_{H2O}^{2} - (P_{H2}^{4}P_{CO}/K3)}{DEN^{2}} \tag{6}$$

Where DEN is defined as:

$$DEN = 1 + K_{CO}P_{CO} + K_{H2}P_{H2} + K_{CH4}P_{CH4} + \frac{K_{H2O}P_{H2O}}{P_{H2}}$$

Please refer to the previously literature for kinetic constants [102]. Furthermore, the reaction rate used for the WGS reactor model was specified as [103]:

$$r4 = \ 10^{2.845} \cdot e^{\frac{-111}{Rg \cdot T}} \cdot P_{CO}P_{CO2}^{-0.36}P_{H2}^{1-0.09} \cdot \left[1 - \frac{P_{H2}P_{CO2}}{K\ P_{H2O}P_{CO}}\right] \tag{7}$$

Additionally, the flux across the membrane (N_i) was based on Sieverts' law as follows:

$$N_i = \ \overline{P_{H2}}\left(\sqrt{P_{H2}^{Shell}} - \sqrt{P_{H2}^{Tube}}\right) \tag{8}$$

Where $P_{H2}^{Shell}$and P_{H2}^{Tube}represent the hydrogen partial pressure at the retentate and the permeate, respectively and $\overline{P_{H2}}$ is the permeance of the membrane obtained experimentally. Furthermore, the calculation of binary diffusion coefficients (D_{AB}) were estimated according standard engineering procedures [104]:

$$D_{AB} = \ 0.0018583\sqrt{T^3\left(\frac{1}{M_A} + \frac{1}{M_B}\right)}\frac{1}{p\sigma_{AB}^2\varphi_{D,AB}} \tag{9}$$

Where $M_i$is the molecular weight of component *i*, p type pressure of the system, σ_{AB}^2 the parameters of the Lennard-Jones potential between molecules A and B, and $\varphi_{D,AB}$ the collation integral for diffusion. The conversion of methane was defined as:

$$X_{conversion} = \frac{F_{CH4,feed} - F_{CH4,ret}}{F_{CH4,feed}} \tag{10}$$

7.3.4 He leak tests and H_2 permeation tests

After the module was installed in the CMR rig, the temperature of the membrane module was increased from room temperature to 350°C under He gas at a rate of 1°C/min and a pressure of 2 bar. At this temperature, a helium leak test showed undetectable leak and H_2 was introduced to the module. Hydrogen permeance was measured as a function of time continuously every 30 seconds as shown in Figure 7.11. After 80 h, the temperature was increased to 450°C displaying a slight increase in H_2 permeance. The temperature was kept for 160 h and two helium leak tests were performed displaying undetectable He leak. Notice that on the first He leak test, steam was fed to the system along with He for one hour to fully oxidize the WGS catalyst. The membrane showed a H_2 permeance of 70 and 80 $Nm^3m^{-2}h^{-1}bar^{-0.5}$ at 350 and 450°C, respectively. After 290 hours of continuous testing, the module's temperature was increased to ~600 °C under pure H_2 stream for 3 h to activate the MSR catalyst. Notice that after activation, the membrane presented a He leak of 0.4 sccm/bar at 450 °C. MA-170 showed high H_2 flux and an ideal H_2/He selectivity of over 4,300 after the catalyst was activated. Even though, it has been shown that to improve the thermal stability of the membranes, porous Hastelloy and Inconel supports perform better than PSS at temperatures higher than 500°C [105]; the membrane showed a considerable high thermal stability.

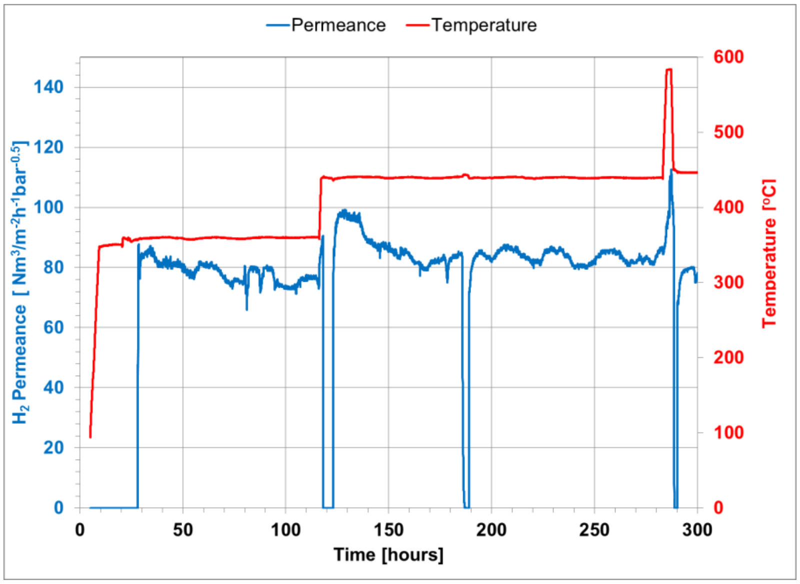

Figure 7.11. Hydrogen permeance, He leak tests at 350, 450 and activation at 585°C at different elapsed times.

Moreover, Gade et al. [106] showed that unannealed Pd-Au membranes require ~300 hours under typical operating conditions to fully annealed in-situ the Pd-Au surface of the membrane and consequently reach a steady H_2 flux. Nevertheless, as shown in Figure 7.11, after H_2 feed was introduced in to the system at 350°C, the H_2 flux across the membrane reached a steady state very fast. This effect could be the result of plating Pd on top of the Au surface which added active sites for the permeance to occur. Pure Pd membrane foils have shown a H_2 permeance that follows the Arrhenius correlation as shown in Eq 7.1, where *t* is the thickness of the membrane in μm, 15,630 is the activation energy in J/mol and 6,322.7 is the pre-exponential factor in $m^3\mu m.m^{-2}h^{-1}atm^{-0.5}$. Furthermore, considering that the presented Pd/Au/Pd membrane has a Pd layer of 10.1 μm, the expected permeance of its pure Pd foil analog is of 47 $Nm^3m^{-2}h^{-1}bar^{-0.5}$ at 450°C. It is important to mention that the hydrogen permeance of the presented Pd/Au/Pd membrane is superior by a factor of 1.7. This enhanced behavior of the membrane is due to the presence of gold, which as previously reported [42], it can raise the permeance up to 2 times higher due to an increase in diffusivity. Although, the amount of gold in the presented membrane is 2% which is below the optimum 5% [107], the membrane displayed an excellent and stable H_2 flux.

$$\overline{P_{H2}} = \left[6322.7\, e^{-\frac{15630}{RT}}\right] \Big/ t \qquad (7.1)$$

7.3.5. MSR in a conventional packed bed reactor (PBR)

Methane steam reforming was carried out in a conventional packed bed reactor (PBR) to experimentally demonstrate the effect of process intensification and the presence of the secondary catalyst. As mentioned before, the major advantage of the CMRs compared to a conventional PBR is the conversion enhancement of the equilibrium-limited MSR by removing in-situ the produced H_2. Therefore, in order to study the performance of a PBR, a solid stainless steel pipe was placed instead of the membrane in order to maintain identical geometric features of the CMR reactor. As shown in Figure 7.12, different space velocities, temperatures and steam-to-carbon ratios were used to investigate the performance of the PBR; all reaction conditions were set to a total pressure of 2 bar, since higher pressures did not show significant changes in the reaction performance. Notice that the catalyst loading was set around 5000 h^{-1} as specified by the provider of the catalyst. Furthermore, the experimental results were graphically depicted along with the computational simulation's outcomes as shown in Figure 7.12.

Let us examine the performance of the PBR by analyzing its methane conversion at 500°C and a steam-to-carbon of 3. It is observed, that at even small space velocities, methane conversion is below its chemical equilibrium (shown as a dotted line in Figure 7.12; this effect is caused by the reduction of the contact time of methane with the catalyst. Furthermore, the effect of temperature on the conversion of methane is clear; it increased from 40 to 60% when the temperature of the reactor was increased from 500 to 600°C. This is in agreement with the fact that MSR is an endothermic reaction which is highly favored by high temperatures.

Additionally, adding steam has a positive effect on the reaction, doubling the conversion when the steam-to-carbon ration is increased from 3 to 5. Furthermore, excess steam is generally present in MSR process since it, not only increases conversion but also, prevents coke formation. It is important to mention that the results presented in this work are similar to the results reported in the pertinent literature [64,102]. Additionally, the CFD simulation results, shown in Figure 7.12, match the experimental data with an average error of 7.8%. It is important to mention, that the experiments were carried out in a pilot-scale module and therefore this results are more susceptible to divergences from controlled settings.

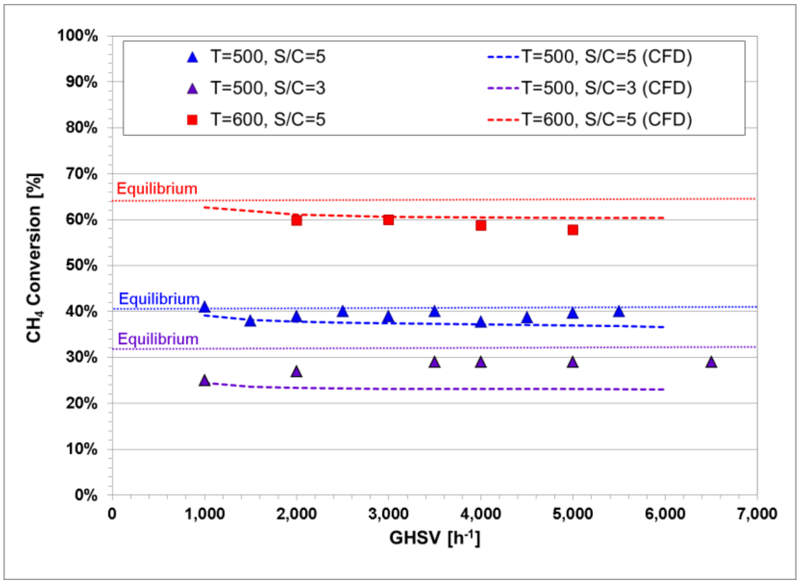

Figure 7.12. Experimental and computational simulation methane conversion in a PBR as a function of different space velocities and conditions at a total pressure of 2 bar.

7.3.6. MSR/WGS in a conventional packed bed reactor (PBR)

The reforming of methane and the water gas shift reactions were studied in a conventional packed bed reactor (PBR) to demonstrate the effect of the secondary catalyst and thus effectively demonstrate the presence of a membrane afterwards. The reactor was packed in stages while a solid stainless steel pipe was used instead of a membrane in order to maintain the geometry of the module as shown in Figure 7.13. The PBR was packed in series with a fresh Ni-based reforming catalyst and a Fe-Cr based WGS catalyst with an overall proportion of 20% and 80% for reforming and WGS, respectively. The configuration of the catalysts within the reactor, shown in Figure 7.13, was split as MSR-WGS-MSR-WGS-MSR. The MSR-WGS reactor was tested at 475°C since the Fe-Cr catalyst temperature limit is specified by the provider to be of 500°C. After packing the module, steam and He were fed to the system to oxidize the WGS catalyst until H_2 was not detectable by the GC; this process took around 1 hour. Afterwards, the temperature of the module was increased to ~600 °C under pure H_2 stream for 3 h to activate the MSR catalyst. After these procedures, the reaction tests were carried out.

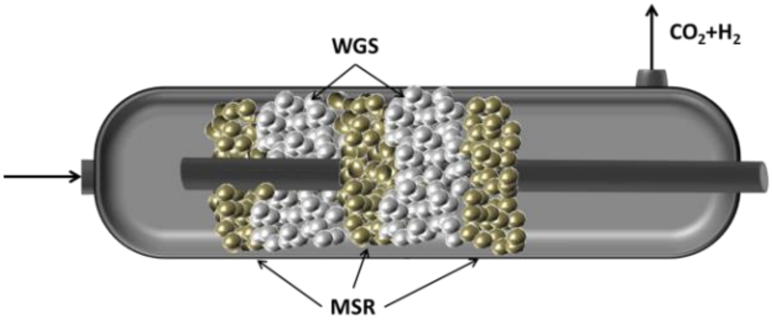

Figure 7.13. Schematic of the catalyst distribution throughout the PBR reactor.

The conversion of methane at 475°C, 2 bar and a GHSV of 3500 h^{-1} was found to be of 18% as shown in Figure 7.14; however, it decreased slightly as the pressure was increased. It is important to mention that the purpose of adding the WGS catalyst is to prevent or reduce the formation of CO in the module, which as shown by Figure 7.14, it is possible to observe that although in small quantities, CO is present in the product of the reaction. The amount of CO reduces as pressure increases; this indicates that the production of CO is hindered by pressure; or it could mean that the activity of the WGS catalyst is favored at higher pressures (Equation 3.21). Given the stoichiometry of MSR (Equations 3.20 and 3.22), it is expected a reduction on methane conversion and simultaneously CO generation as the pressure of the reactor increases; at the same time, as reported by Atwood et al. [108], the WGS reaction intensifies at higher pressures. These two mechanisms contribute to obtaining lower CO yields.

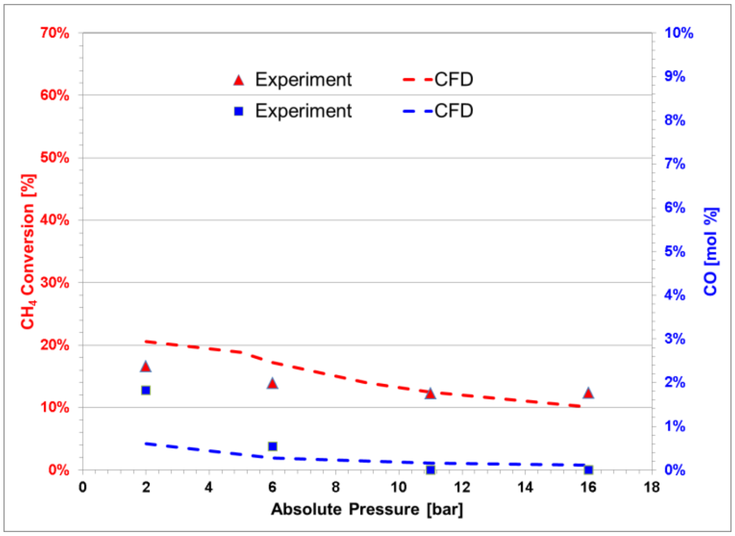

Figure 7.14. Experimental and computational simulation of two catalysts in a PBR as a function of different pressures at a GHSV of 3500 h^{-1}, a temperature of 475 °C and a S/C=5.

It is important to notice that in this dual-catalyst reactor, the WGS reaction occurs in the presence of a significant amount of H_2, which limits its performance. Figure 7.15 shows that even though lower theoretical CO is present in the dual-catalyst reactor; the experimental results of the pilot-scale bed appeared to be hindered by the intrinsic error in the measurements. Nevertheless, through the simulation, it is found that as the space velocity increases, the difference in CO production decreases further for the dual-catalyst bed. This effect can be attributed to two factors: i) the reduced presence of H_2 and ii) lower concentrations of CO. Please notice that the aforementioned factors are generated due to reduced CH_4 conversions. Additionally, a surface plot of CO concentration through the reactor module is shown in Figure 7.16 to illustrate the effect of the water-gas-shift catalyst. At first, CO is generated on the first MSR catalyst bed section, followed by its consumption by the WGS reaction zone. The next MSR induces the production of more CO which is later reduced by the following WGS. Finally, the MSR catalyst at the end of the PBR increases the overall CO concentration inside the reactor.

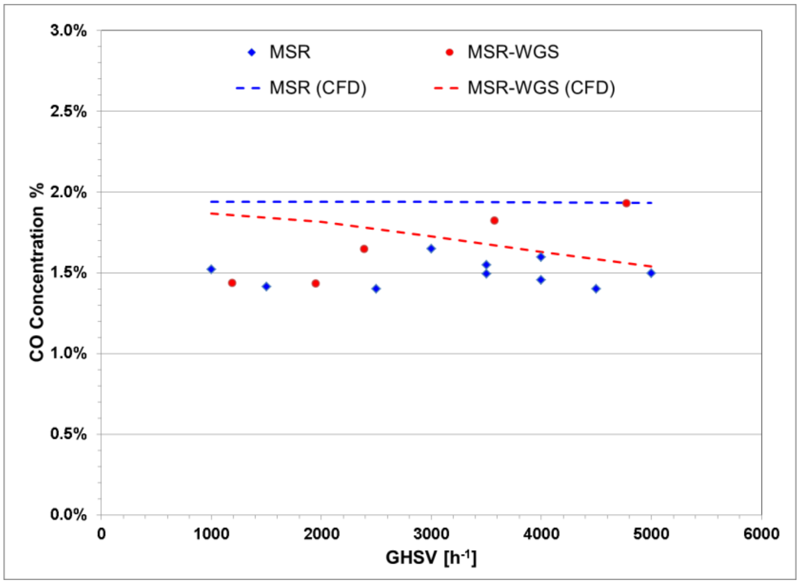

Figure 7.15. Concentration CO in conventional PBRs containing a single MSR catalyst and dual MSR-WGS catalyst at a pressure of 2 bar, a temperature of 475 °C and a S/C=5.

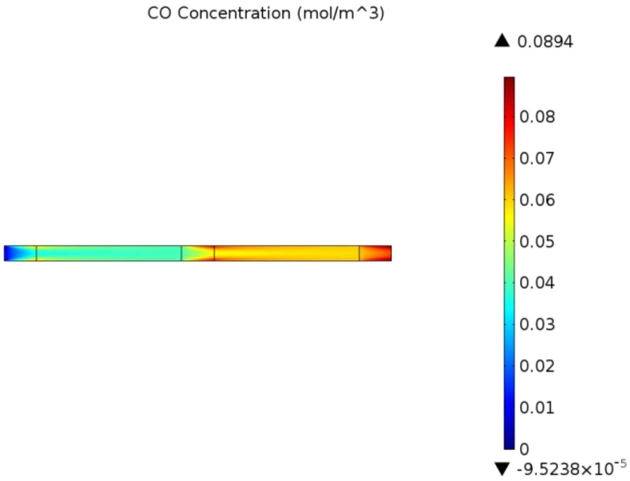

Figure 7.16. Concentration profile of CO inside in a PBR containing MSR-WGS catalysts.

7.3.7. MSR/WGS in a catalytic membrane reactor (CMR)

The CMR was packed with two catalysts in series with a membrane placed at the center of the reactor to remove in situ the H_2 generated by the reactions. As expected, compared to a PBR, the constant removal of H_2, shown by the hydrogen concentration profiles in Figure 7.17, changes the composition of the retentate allowing both reactions to proceed further. In Figure 7.17, it is possible to observe that the as soon as the feed stream (on the left) is in contact with the catalyst bed, H_2 is generated and increases as the reaction proceeds; this continues until the H_2 partial pressure in the retentate is high enough to provide the driving force for the membrane to start removing it. Notice that even though the reaction continues to take place in the module, an increase in H_2 concentration is no longer observed; this effect is caused the rate of removal overcoming the rate of reaction. Furthermore, it is possible to observe from top to bottom, a gradual reduction in H_2 concentration caused by the presence of the membrane. This reduction in H_2 concentration adjacent to the surface of the membrane causes a H_2 depleted boundary layer formed by low radial diffusion rates. This effect is often referred as concentration polarization and it can significantly reduce the performance of the membrane [109].

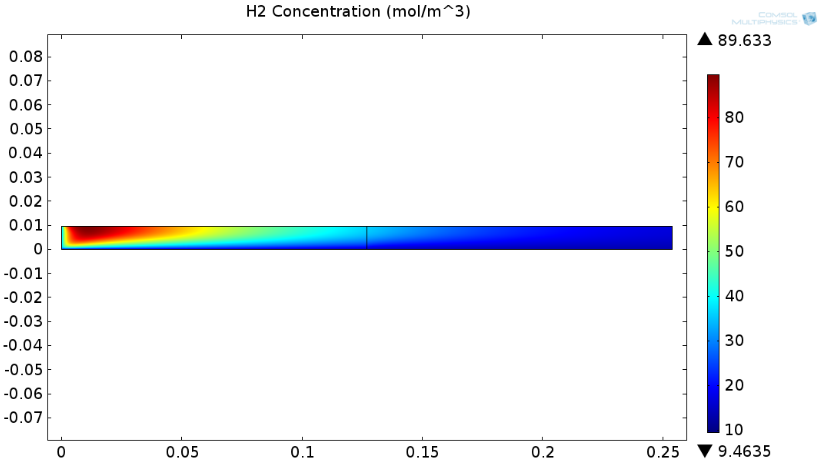

Figure 7.17. Concentration profile of H_2 inside in a dual MSR-WGS catalytic membrane reactor.

The experimental CH_4 conversion results are shown Figure 7.18 for different steam-to-carbon ratios, a temperature of 475°C and a pressure of 5 bar. The highest conversion achieved was of 43.3% at a steam-to-carbon-ratio of 5 and a space velocity of 1172 h^{-1}. Furthermore, it is found that as the GHSV is increased, the conversion of methane decreased accordingly; this is caused by the reduction of residence time in the reactor. In addition, the amount of water influenced the reaction significantly; a steam-to-carbon ratio of 5 produced about 20% higher CH_4 conversion than a ratio of 3. Notice that the H_2 purity generated by MA-170 was of 99.94% throughout a testing time of 350 hours under MSR/WGS conditions. The best flux achieved by these CMR under optimum conditions was over 500 NL/day. After the experiments were terminated, the surface of the membrane did not show carbon deposition for the reason that the protective cage separated effectively the reaction zone from the membrane. The reactor performance indicator for process intensification was quantitatively analyzed based on through the Δ-index previously reported by Ma et al. [102]. This index is represented in Equation 7.2 as the difference between the CH_4 conversion achieved by the CMR and the one by PBR under similar conditions.

$$\Delta = X_{CH4}^{CMR} - X_{CH4}^{PBR} \tag{7.2}$$

It is important to mention that the PBR was not operated experimentally at 475°C and 5 bar; consequently, the CFD performance outcome of the conventional PBR was utilized to estimate the Δ-index of this work. The Δ-index represented in Figure 7.18 shows that at all GHSV the conversion of methane increases when sized against a conventional reactor. Nevertheless, the concept of process intensification is better appreciated at low space velocities since H_2 has better rate of removal and the contact time of the gases with the catalysts increases.

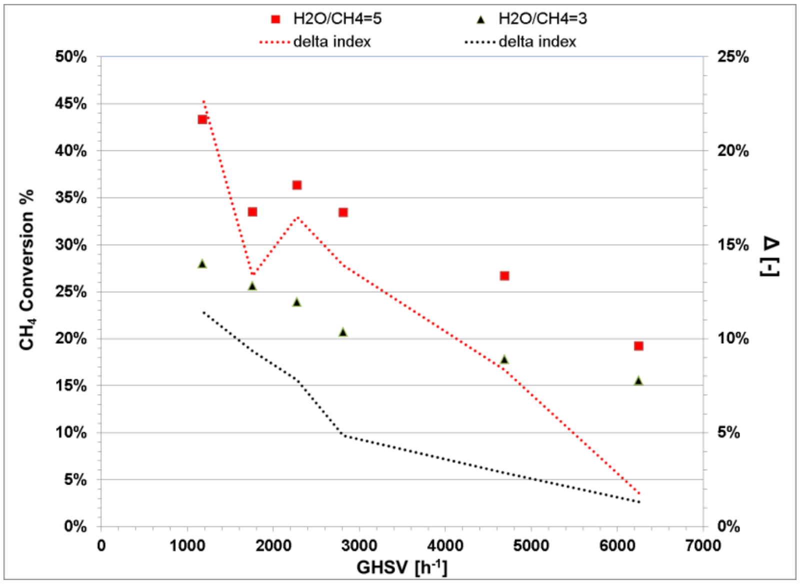

Figure 7.18. Experimental methane conversion of the dual catalyst CMR represented as scatter points and difference between CMR and PBR at 5 bar, a temperature of 475 °C.

To further characterize the performance the membrane reactor the product of Damkohler and Peclet numbers (DaPe number) is utilized since it provides the ratio of maximum reaction rate over maximum permeation rate per volume [110]. In PBRs, the Damkohler number (Da) exemplifies the performance of the reactors, since it shows the ratio of the reaction rate over the convective mass transport of the reactant; while in membrane technology, the Peclet number shows the relative convection transport rate over the diffusive rate (permeation). Consequently, the product DaPe dictates the overall effectiveness of the CMR; for instance, having a DaPe > 1, means that the permeation rate is low and thus the H_2 rate of removal through the membrane is the limiting factor of the reactor's productivity. As reported by Battersby et al. [110], the DaPe number can be estimated as shown in Equation 7.2 where $X_{equilib}$ is the conversion achieved when the reaction is thermodynamically at equilibrium and X_{actual} is the conversion displayed by the membrane reactor. Most of the DaPe numbers displayed by this CMR, shown in Table 7.3, are lower than one; this implies that the rate of H_2 removal is high enough to change the pseudo-equilibrium state favorably to achieve higher conversions. Please notice that the term "pseudo-equilibrium" is used to describe the situation where the reaction product (H_2) is independently manipulated, by the use of a permeable membrane [110]. Furthermore, Table 7.3 shows that at high GHSV, the DaPe number approaches to one, implying that the rate of reaction matches the maximum permeation equivalent. It is important to mention that it is considered that the optimum design of a CMR should operate at a theoretical DaPe =1.

$$DaPe = \frac{X_{equilib}}{X_{actual}} \tag{7.3}$$

Table 7.3. DaPe number of the dual catalyst CMR at different space velocities at 5 bar and 475 °C.

GHSV [h^{-1}]	1170	1750	2270	2810	4680	6250
DaPe number	0.47	0.61	0.56	0.61	0.77	1.07

It is important to mention that the concentration of CO in the system was undetectable in this dual catalytic CMR. However, it is not clear if this is the result presence of the secondary WGS catalyst or if it is caused by the presence of a H_2 permeable membrane as previously reported. For instant, Lin et al. described a reduction of CO yield from 50% to <2% in a Pd-based CMR. Therefore, to observe the effect of the secondary catalyst, a simulation of both single and dual catalyst CMRs was performed. In Figure 7.19a), it can be observed that the CO yield increases in both CMRs as the temperature is increased and the GHSV is reduced. Nonetheless, the effect of the secondary catalyst is also observed by reducing the CO yield, especially at higher operating temperatures. For instance, at the lowest GSHV and 650°C, the CO yield at the retentate is reduced from 9% on the CMR with one catalyst to 6.5 % on the dual CMR, while at 450°C, it is reduced from 0.2% to <0.05%.

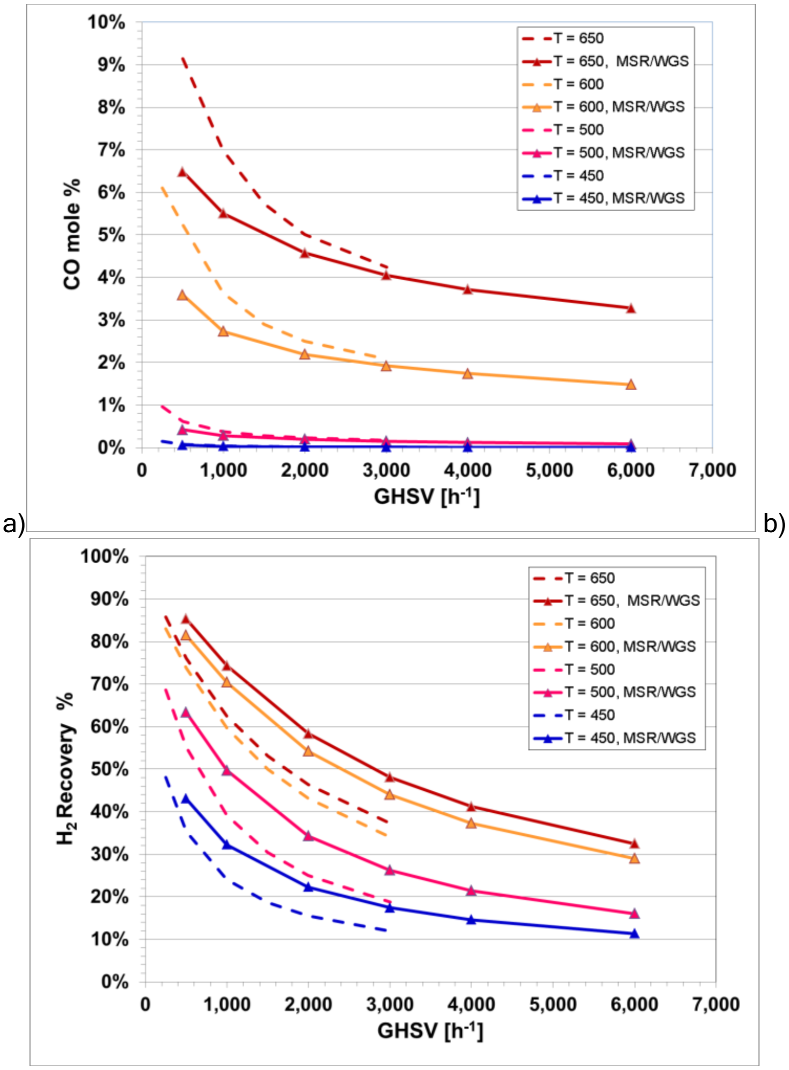

Figure 7.19. a) CO yield and b) H_2 recovery for single and dual CMRs at 5 bar and a carbon-to-steam ratio of 5.

Additionally, Figure 7.19b) shows the H_2 recovery obtained by the CMRs at different space velocities and temperatures. In both CMRs, H_2 recovery increases with higher temperatures and reduced GHSV since these conditions are favorable for higher CH_4 conversions. Additionally, it can clearly be seen that H_2 recovery increases in the dual CMR particularly as the temperature increases. For instance, the operation of the dual bed at 600°C is expected to produce more H_2 than that the conventional single stage CMR. Additionally, lower CO yields intrinsically mean not only higher H_2 generation and enriched CO_2 streams at the retentate, but also the potential reduction of CO poisoning of the membrane. Several studies have shown that severe reductions in H_2 permeance occurs in the presence of CO mainly caused by the adsorption of CO on the Pd surface hindering the active sites available for H_2 to adsorb [111]. Reacting CO with H_2O in the catalyst section allows the membrane to be less exposed to CO reducing poisoning. Furthermore, the presence of WGS can potentially decrease coking when operating at low steam-to-carbon ratios, as carbon formation is thermodynamically favored by the dissociation of CO [112].

$$2CO \leftrightarrow C + CO_2 \tag{14}$$

The results obtained in the present work were compared against those shown in the literature for methane steam reforming, as shown in Figure 7.20a. The conversion of methane in traditional PBRs (TR) and membrane reactors (MR) of different literature sources was plotted against different temperature and it is shown to be in agreement with previously reported values. Furthermore, various CO mole fractions at the outlet of the reactor were graphically represented as a function of different methane conversions as shown in Figure 7.20b. The composition of CO shown experimentally by this work is significantly lower those shown in other sources, suggesting that the additional WGS catalyst in the CMR helped in decreasing the residual CO.

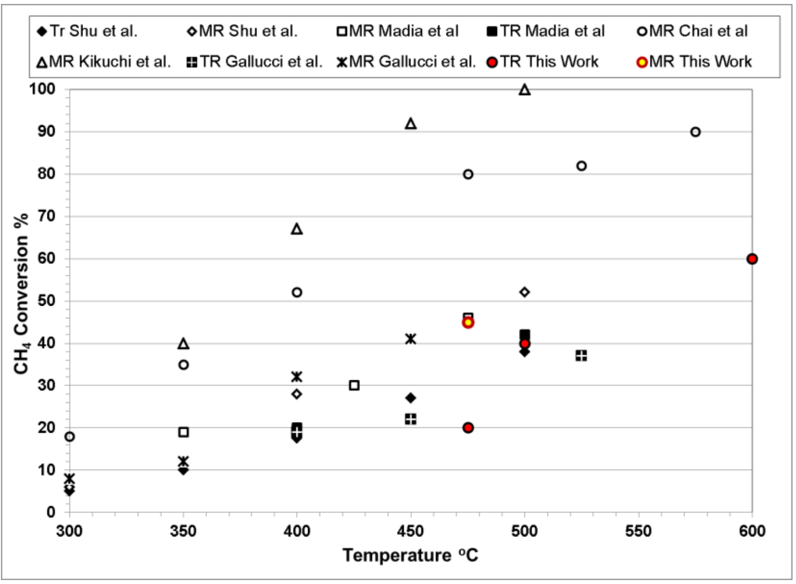

a)

b)
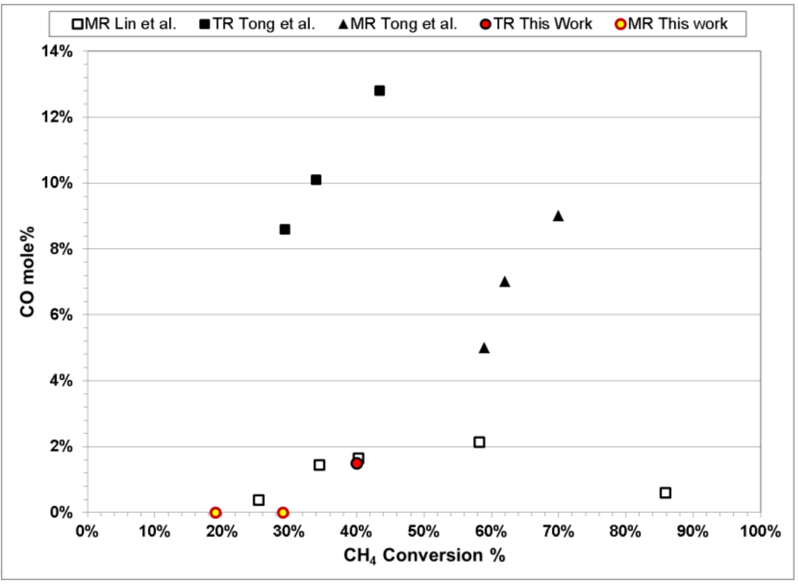

Figure 7.20. Comparison of the results presented in this work against those presented in the literature for a) methane conversion and b) CO yield at 450-500°C and pressures 2-5 bar [64,113]

7.4. Ethanol Steam Reforming

The diversification of hydrogen production sources has tremendous energy and environmental implications making of ethanol steam reforming (ESR) an essential process that requires further investigation. Hence, the purpose of this section is to investigate the performance of a pilot-scale catalytic membrane reactor (CMR) used to enhance the efficiency of ESR by the in-situ removal of H_2 from the reactor module. The rector module consisted of a tubular membrane located at the center of the module and surrounded by a commercial Nickel-based catalyst. A thin, defect-free composite asymmetric membrane was prepared as a Pd/Au/Pd/Au, then characterized and tested under reacting conditions. Ethanol steam reforming was conducted under different conditions such as steam-to-carbon ratios, liquid hourly space velocities (LHSV), operating pressures and temperatures. A 1-D model and 2-D computational fluid dynamics (CFD) model were developed, validated experimentally and used to explore further the features of this reaction. The CMR module was operated for 300 hours showing 100% conversion of ethanol in all conditions and producing H_2 with a purity of 99.9%.

Description

The membrane MA-170 with a surface area of 150 cm^2 was synthesized on a porous stainless steel (PSS) support from Mott Metallurgical Corp. The porous support had a 0.5 in. OD and a 15 in. length with a porous media grade of 0.5 µm. The porous tube was capped at one end and welded to stainless steel tube at the other. The synthesis of the membrane was carried out using previously reported procedures [75,90,100]. At first, the support was cleaned utilizing isopropanol in an ultrasonic bath followed by its oxidation on air for 12 h at 600 ^oC. The support was graded with two types of pre-activated 2 wt% Pd-alumina particles obtained from Johnson Matthey (UK). The first type consisted of coarse particles with an average size of 1-3 µm, followed by fine 0.6 µm particles. The grading layer was cemented via electroless plating of palladium. After grading, the membrane was activated with $SnCl_2$ and $PdCl_2$ [77] and a layer of Pd was subsequently plated. In addition, gold was deposited on the surface of the membrane through conventional electroplating [92]. Gold was chosen as the alloy of the membrane since it has been shown to improve the stability and lifetime of Pd membranes under harsh conditions. The thickness of the Pd and Au layers were estimated through gravimetric measurements while its effectiveness determined through He leak tests. Figure 7.21 shows the He leak characterization tests as a function of the membrane thickness at each synthesis step. The membrane was used for H_2 separation after it reached the minimal He flux located at a thickness of 13 µm. At this moment the membrane displayed a H_2 permeance of 80 $Nm^3m^{-2}h^{-1}bar^{-0.5}$at 450^{o}C. The membrane showed a He leak increase and thus, it was further plated with Pd and Au to enhance its stability and reduce the leak. The final structure and thickness presented in this membrane was Pd 6.9 µm /Au 0.2 µm /Pd 6.7 µm /Au 0.1 µm.

After synthesizing the membrane, it was arranged in a protective cage (shown in Figure 7.22) which held the membrane in close proximity with the catalyst. This cage was used to separate the catalyst particles from the surface of the membrane, avoiding any defects caused by the particle-surface interaction. The catalyst, a Nickel-based (HiFUEL R110, form Alfa Aesar), was first crushed and sieved (16/+40 mesh) before its confinement in the protective-membrane cage, which was loaded with 220 g of crushed catalyst. The characterization of the H_2 permeance and the reaction were conducted in a pilot-scale module described in detailed by Catalano et al. [72]. Notice that before initiating the H_2 permeation tests, pure He was fed to the system overnight in order to remove any air and moisture from the CMR. The reactions were carried out at different conditions with 65 ml/min of He on the tube side, which was used as sweep gas in order to increase the driving force of the separation.

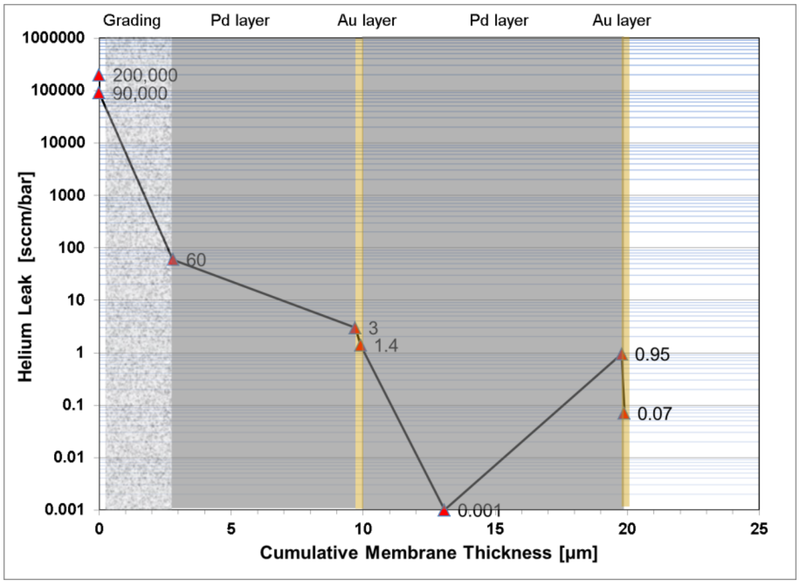

Figure 7.21. Helium leak tests as a function of the different synthesized layers.

Figure 7.22. Picture of the membrane, membrane-cage assembly and shell of the CMR module.

7.4.1 Framework of the1-d and 2-d simulation models

Ethanol steam reforming is a highly endothermic reversible reaction, which is favored by high temperatures, low pressures and low space velocities. The kinetic properties of ESR for different catalysts have been studied throughout the literature and different mechanisms have been proposed [52,114,115,116,117,118,119,120]. Nonetheless, it is considered that the reactions shown in Equations 7.4-7.7 are the most representative for the performance of the process [121]:

ESR $\mathrm{C_2H_5OH \leftrightarrow CH_4 + CO + H_2}$ (7.4)

WGS $\mathrm{CO + H_2O \leftrightarrow CO_2 + H_2}$ (7.5)

MSR $\mathrm{CH_4 + H_2O \leftrightarrow CO + 3H_2}$ (7.6)

MSR $\mathrm{CH_4 + 2H_2O \leftrightarrow CO_2 + 4H_2}$ (7.7)

At first, a 1-d model was developed utilizing Polymath with the purpose of understanding the operating conditions needed in the experimental rig. The kinetic expressions for a Ni-based catalyst proposed by Sun et al. [121] and Xu et al [122] were utilized in this study and are presented in Table 7.4. These kinetic parameters were used to simulate ESR in conventional reactors; and the results were compared with experimental results presented in the literature [119,123]. The kinetics showed > 99% accuracy in predicting the performance of ESR.

The H_2 flux across the membrane was simulated according to Sieverts' law and utilizing the experimental value of the permeance ($\overline{P_{H_2}}$) as shown in Equation 7.8, where $P_{H_2}^{shell}$ and $P_{H_2}^{tube}$ represent the H_2 partial pressure on the shell and inside the tube, respectively. On the retentate side (reaction zone) a negative H_2 flux through the membrane boundary was defined utilizing Sieverts' law. On the permeate side of the membrane boundary, the same expression, but positive, was defined to simulate the H_2 concentration profile.

$$-n \cdot N_i = \overline{P_{H_2}}[\sqrt{P_{H_2}^{shell}} - \sqrt{P_{H_2}^{tube}}] \tag{7.8}$$

Furthermore, a 2-d computational fluid dynamics (CFD) finite element simulation model was developed in COMSOL Multiphysics 5.0 to further explore the intrinsic physics of this CMR. The geometry utilized for the development of this simulation model is shown in Figure 7.23. The following assumptions were included to simplify the proposed CFD framework:

i) The effect of the protective cage used to hold the loaded catalyst is negligible and does not cause any disturbance in the flow pattern
ii) A 2-d axisymmetric geometry with two domains (shell and tube) was used for this model
iii) The system is isothermal
iv) Laminar flow

Notice that due to the presence of a sweep gas stream, the H_2 partial pressure of the permeate is subject to change since it depends on the permeate H_2 flux.

Table 7.4. Summary of the kinetic expressions used in the simulation framework.

$\mathrm{r_1} = \mathrm{k_1 P X_e}$	$[\mathrm{mol\ g_{cat}^{-1} s^{-1}}]$	(7.9)
$\mathrm{r_2} = \frac{\mathrm{k_2 P}}{\mathrm{X_h den^2}}[\mathrm{X_{co} X_w} - \frac{\mathrm{X_{CO_2} X_h}}{\mathrm{K_2}}]$	$[\mathrm{mol\ g_{cat}^{-1} s^{-1}}]$	(7.10)
$\mathrm{r_3} = \frac{k_3}{X_h^{2.5} den^2 \sqrt{P}}[X_M X_W - \frac{X_{CO} X_h^3 P^2}{K_3}]$	$[\mathrm{mol\ g_{cat}^{-1} s^{-1}}]$	(7.11)
$\mathrm{r_4} = \frac{k_4}{X_h^{3.5} den^2 \sqrt{P}}[X_M X_W^2 - \frac{X_{CO_2} X_h^4 P^2}{K_4}]$	$[\mathrm{mol\ g_{cat}^{-1} s^{-1}}]$	(7.12)
$\mathrm{k_1} = \frac{4.55 \times 10^{-5}}{T} \exp(-\frac{2030}{T})$	$[\mathrm{mol\ Pa^{-1} g_{cat}^{-1} s^{-1}}]$	(7.13)
$\mathrm{k_2} = 5.43 \times 10^{-3} \exp(\frac{-8074.33}{T})$	$[\mathrm{mol\ Pa^{-1} g_{cat}^{-1} s^{-1}}]$	(7.14)
$\mathrm{k_3} = 3.711 \times 10^{14} \exp(\frac{-28879}{T})$	$[\mathrm{mol\ Pa^{-1} g_{cat}^{-1} s^{-1}}]$	(7.15)
$\mathrm{k_4} = 8.960 \times 10^{13} \exp(\frac{-29336.1}{T})$	$[\mathrm{mol\ Pa^{-1} g_{cat}^{-1} s^{-1}}]$	(7.16)
$\mathrm{K_2} = \exp(\frac{4400}{\mathrm{T}} - 4.036)$		(7.17)
$\mathrm{K_3} = 1 \times 10^{10} \exp(\frac{-26830}{T} + 30.114)$	$[Pa^2]$	(7.18)
$\mathrm{K_4} = K_2 K_3$	$[Pa^2]$	(7.19)
$\mathrm{den} = 1 + \mathrm{P}(K_{CO} X_{CO} + K_h X_h + K_M X_M) + \frac{K_W X_W}{X_h}$		(7.20)
$K_{CO} = 8.230 \times 10^{-10} \exp(\frac{8497.71}{T})$	$[Pa^{-1}]$	(7.21)
$K_M = 6.640 \times 10^{-9} \exp(\frac{4604.28}{T})$	$[Pa^{-1}]$	(7.22)
$K_h = 6.120 \times 10^{-14} \exp(\frac{9971.13}{T})$	$[Pa^{-1}]$	(7.23)
$K_W = 1.770 \times 10^{5} \exp(\frac{-10666.35}{T})$		(7.24)
$\mathrm{R_{C\_CO}} = \mathrm{r_1} - \mathrm{r_2} + r_3$		(7.25)
$\mathrm{R_{C\_CO2}} = \mathrm{r_2} + \mathrm{r_4}$		(7.26)
$\mathrm{R_{C\_H2}} = \mathrm{r_1} + \mathrm{r_2} + 3 \cdot \mathrm{r_3} + 4 \cdot \mathrm{r_4}$		(7.27)
$\mathrm{R_{C\_H2O}} = -\mathrm{r_2} - \mathrm{r_3} - 2 \cdot \mathrm{r_4}$		(7.28)
$\mathrm{R_{C\_CH4}} = \mathrm{r_1} - \mathrm{r_3} - \mathrm{r_4}$		(7.29)
$\mathrm{R_{C\_C2H5OH}} = -\mathrm{r_1}$		(7.30)

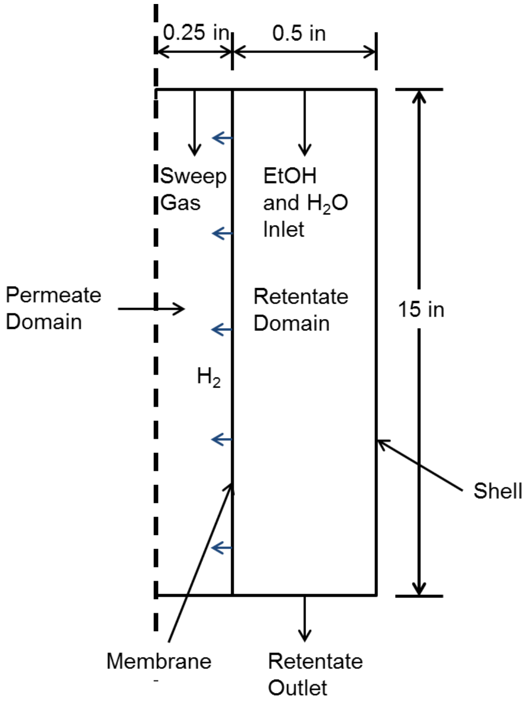

Figure 7.23. Geometry used in the 2-d CFD simulation model.

In COMSOL, the physics used for this model was “Reacting Flow in Porous Media” and “Transport of Diluted Species” for the retentate side and permeate side, respectively. The equation of motion, continuity and species continuity equations (Equations 7.31 and 7.32) were solved simultaneously within the geometric mesh, which contained 25,121 elements.

$$\begin{gathered}\rho(u\cdot\nabla)u=\nabla\cdot[-pI+\mu(\nabla u+(\nabla u)^T]+F\\ \nabla\cdot(\rho u)=0\end{gathered}\tag{7.31}$$

$$\nabla\cdot(-\mathfrak{D}_i\nabla c_i)+u\cdot\nabla c_i=R_i\tag{7.32}$$

Notice that the density (ρ) of the gas mixture was specified to be a function of composition and thus changes as the reaction and separation proceed. Furthermore, the diffusion coefficients ($\mathfrak{D}_{AB}$) were calculated as shown in Equation 7.33:

$$\mathfrak{D}_{AB}=0.0018583\sqrt{T^3(\frac{1}{M_A}+\frac{1}{M_B})}\frac{1}{p\sigma_{AB}^2\Omega_{\mathfrak{D},AB}}\tag{7.33}$$

Where σ_{AB} is obtained from the Lennard-Jones parameters, T is the temperature of the gases, p the pressure and $\Omega_{\mathfrak{D},AB}$ the collision integral [104].

7.4.2. Membrane Characterization

The membrane module was first flushed with He and the retentate pressure increased by 1 bar. Figure 7.24 shows the permeation and He leak tests of the membrane at different temperatures. The temperature (Figure 7.24) of the reactor was increased to 350°C at 1°C per minute under Helium. A leak test performed on the module showed a He flux of 0.2 sccm/bar. Hydrogen was fed to the system for 20 hours displaying a H_2 permeance of 11 $Nm^3m^{-2}h^{-1}bar^{-0.5}$. The temperature of the module was then increased to 450°C and the H_2 permeance was measured continuously for 20 hours. The membrane's permeance increased gradually reaching a steady value of 21 $Nm^3m^{-2}h^{-1}bar^{-0.5}$, which is 50% higher than at 350 °C. The He leak at this temperature increased to 1 sccm/bar. The membrane had estimated ideal H_2/He selectivities of 10,800 and 1,139 at temperatures of 350 °C and 450 °C, respectively. Afterwards, the temperature was increased to 600 °C for 2 hours under pure H_2 in order to activate the catalyst, as specified by the provider. The membrane showed a good thermal stability since, after activation, no He leak was found on the membrane at a pressure difference of 1 bar, while the H_2 flux remained stable.

The H_2 permeance of the membrane was tested when its composition and thickness was 6.9 μm Pd/ 0.2 μm Au/ 3.2 μm Pd; its permeance was 80 $Nm^3m^{-2}h^{-1}bar^{-0.5}$ at 450°C. There was a 70% reduction in H_2 permeance after the membrane was replated. The decline in H_2 permeance occurred as the thickness of the membrane was increased, inferring higher resistance to the diffusion of protons through the Pd lattice. Furthermore, there is an overall increase in the gold content of the membrane, which can significantly influence the solubility of H_2 in the active sites of the membrane, as reported by Ma et al. [124]. Nonetheless, the H_2 permeance of the membrane is in agreement with the values presented in the literature for Pd and Pd/Au membranes [94,95] and with 20 μm free standing foils, which have a theoretical permeance of 15 and 23 $Nm^3m^{-2}h^{-1}bar^{-0.5}$ at 350 °C and 450 °C, respectively. Notice that the resistance of the support is not taken into consideration for the theoretical calculation of the free standing foils, suggesting that the selective layer of the membrane presented in this work has enhanced properties and/or the resistance of the support is negligible.

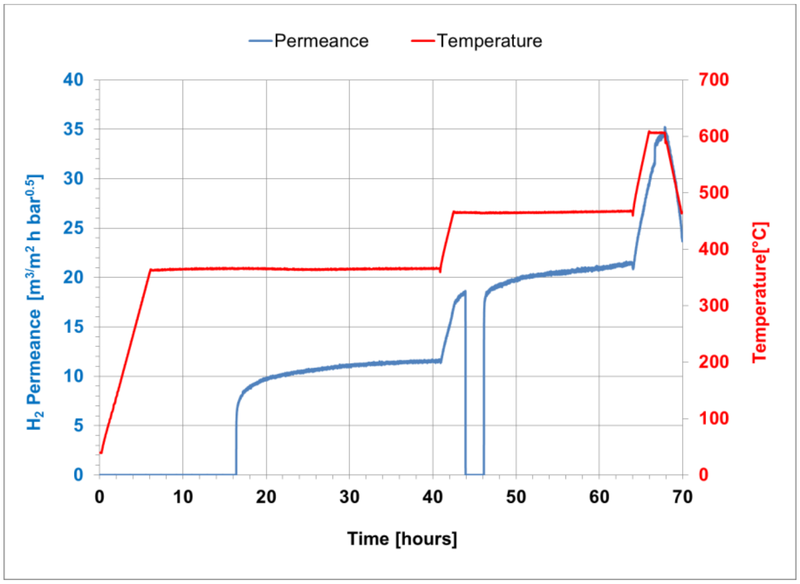

Figure 7.24. Hydrogen permeance at different times and temperatures.

7.4.3. Performance of the 1-d and 2-d simulation models

The 1-d and 2-d simulation models were compared to the experiments carried out in the pilot-scale catalytic membrane reactor presented in this work. Experimental outcomes, such as the mole fraction of the components at the retentate, H_2 flux through the membrane and others, were compared against those found through the simulation models, as shown in Figure 7.25. Both simulations predicted accurately the tendency of the reaction; however, the result of the 2-d model shows a higher accuracy than that of the 1-d simulation. While the 1-d model showed 93% accuracy; the 2-d improved its performance to 95%. The 2-d model takes into consideration the effect of radial mass transfer limitations, which can significantly affect the performance of CMRs.

The discrepancies found between the simulation results and the experiments could be triggered by four main effects or combination them:

i) The permeance of the membrane is assumed to be constant under reacting conditions. Experimentally, the permeance of the membrane has shown to be affected by components such as CO and steam [111], which are unevenly distributed along the reactor.
ii) Carbon deposition in the catalytic bed is negligible by the simulation models. The possibility of coking can lead to a decrease in the activity of the catalyst as well as in the permeance of the membrane. Nonetheless, operating at mild temperatures (350-450^{o}C) significantly reduces the possibility of coking for MSR and WGS reactions [112].
iii) Potential temperature gradients along the catalytic bed are neglected. The CMR used in this study had a length of 39.4 in. and its temperature was supplied by a furnace (Watlow 1.6 kW) with a length of 31.5 in. Although, the connections and auxiliary equipment were thermally insulated to avoid cold spots; temperature gradients were observed, as reported previously by Catalano et al. [72].
iv) The simulation model inputs are based on lab-scale parameters. The current CMR was performed on a pilot-scale bench, which can induce changes in the operational and modelling properties of the system [125].

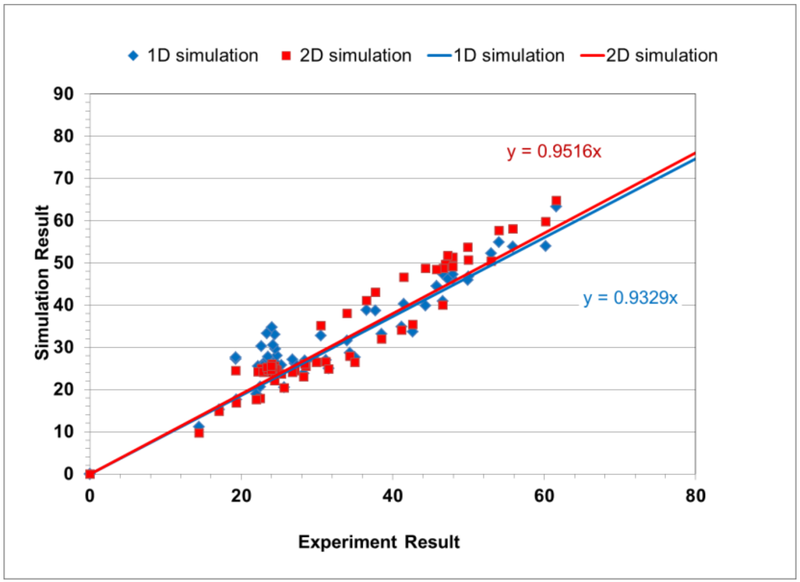

Figure 7.25. Comparison of the simulation and experimental results found in the present study.

7.4.4. Performance of the catalytic membrane reactor

The CMR module was tested continuously for 300 hours, generating H_2 with a purity of 99.9%. The conversion of ethanol was 100% for every condition, in agreement with the results reported by Kumar et al. [126], where it was shown that noble metal catalysts achieve 100% ethanol conversion with a selectivity near to 99% depending on the type of support and loading metal. A Hydrogen flux of 0.38

grams of H_2 per hour was achieved by the module. The following subsections describe in details the performance of the CMR when the operational variables were modified.

7.4.4.1. Effect of space velocity

At first, the effect of space velocity in the performance of the CMR for ESR was explored at 450°C and a steam-to-ethanol ratio (S/E) of 3. Figure 7.26 shows the mole fraction on a dry basis at the retentate outlet as a function of the space velocity for the experiments performed (scattered points), the 1-d model (solid line) and the 2-d CFD simulation (dashed line). It can be observed that in all cases H_2 appears to grow as the space velocity increases; this could be the result of a reduction in H_2 contact time with the surface of the membrane. For instance, at low space velocities, the generation of H_2 proceeds as soon as the feed gas is contact with the catalyst, leaving more membrane surface area available to remove the H_2 generated. In contrast, at higher space velocities, H_2 is generated further down the catalytic bed, implying that the available surface area of the membrane for H_2 permeation is reduced. Although, higher space velocities resulted in lower H_2 recoveries; an increase in H_2 production on the permeate stream was observed.

The mole fraction of methane at the retentate appears to have a slight decrease at higher velocities for the 2-d simulation and for the experimental results. The 1-d model showed a steady behavior where CH_4 appeared constant at all velocities. In CMRs, the process of MSR is expected to proceed further when operating at reduced feed flow rates, assuming that the reaction is not kinetically limited but rather controlled by the permeation rate of the membrane. This phenomenon has been previously reported in the literature [102,127], where methane conversion, reduces as the space velocity is increased. In Figure 7.26, CH_4 appears to decrease rather than increase, indicating that the reaction is being hindered by the presence of H_2 in the reaction zone. In other words, higher velocities influence the rate of H_2 removal stronger than the reaction rate. Similarly occurs with carbon dioxide, where it appears to have a slight decrease towards higher velocities. A reduction in CO_2 can be caused by a reduced conversion of ethanol and/or methane. As mentioned before, the total conversion of ethanol was achieved and since CH_4 is reduced, it is suggested that the lower CH_4 conversions caused the reduction in CO_2 at higher flow rates.

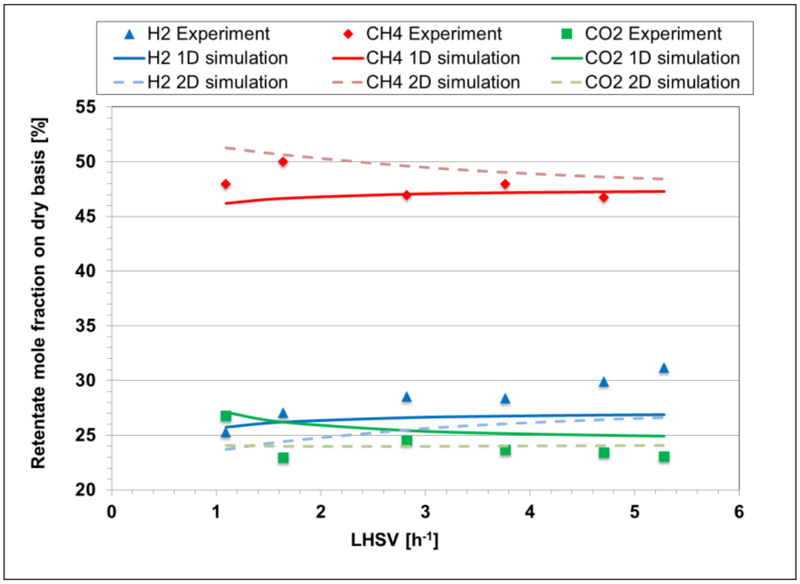

Figure 7.26. Retentate composition at different LHSV and 450°C, 3 bar and a S/E = 3.

7.4.4.2. Effect of pressure and steam content

After the analysis of the space velocity, the liquid feed flow rate was fixed to a 2.48 cm^3/min or a LHSV of 3.77 h^{-1}. The CMR module was tested at different pressures and S/E ratios as shown in Figure 7.27. At first, the S/E was fixed to 3 and the pressure was varied from 2 to 10 bar. It can be observed that as the operating pressure increases, the H_2 mole fraction of retentate decreases implying that the H_2 removal through the membrane is intensified as the driving force for permeation is increased. Moreover, higher pressures enlarged the concentration of CH_4 at the retentate. This effect does not indicate that the content of CH_4 increases, but rather that, due to the removal of H_2, the concentration of methane appears higher. This hypothesis is valid in all conditions, since no ethanol was detected at the retentate. The same effect appears to occur for CO_2, where as the pressure increases, the CO_2 mole fraction of the retentate increases. In conventional reactors, ESR [128] and MSR [102] show a negative response to pressure as it is thermodynamically unfavorable, as described by Le Chatellier's principle. Nonetheless, the removal of H_2 from the reaction zone, changes the composition of the reaction zone, improving the overall performance of the reactions. The effect of pressure at different S/E ratios did not seem to influence the aforementioned trend. Indeed, as pressure increases the H_2 mole fraction of the retentate decreased, CH_4 increased and CO_2 increased.

An increase in the driving force of H_2 transport certainly has an important contribution in the performance of CMR technology. Figure 7.28 shows how much H_2 is generated in CMRs when compared to traditional packed bed reactors (PBR) at different membrane permeances and pressures and thus the term (σ) was used to describe this effect (Equation 7.34).

$$\sigma[\%] = \frac{(F_{H2}^{per} + F_{H2}^{ret})_{CMR} - (F_{H2}^{ret})_{PBR}}{(F_{H2}^{ret})_{PBR}} \cdot 100 \tag{7.34}$$

The effectiveness of CMR technology in generating H_2 directly depends on the total amount of H_2 removed from the reaction zone. One method to improve this rate of removal is by increasing the driving force for H_2 transport or the H_2 partial pressure difference between the retentate and the permeate. Therefore, higher retentate pressures significantly improved the generation of H_2 (Figure 7.28). In Figure 7.28, an increase in pressure, not only made the CMR more efficient; but simultaneously, reduced the performance of conventional PBRs. Therefore, the term (σ) appears to significantly ameliorate the generation of H_2 as pressure was increased.

Another factor that influences the rate of H_2 removal from the reactor is the permeance of the membrane. Low permeances in CMRs imply analogous features with conventional PBRs; however, as the permeance increases, the generation of H_2 enhances. This boost, shown in Figure 7.28, reaches a plateau which occurs when the permeance of the membrane is hindered by a low driving force for H_2 transport. In other words, as more hydrogen is depleted from retentate and collected on the permeate, the hydrogen partial pressure difference becomes equal, making the driving force close or equal to zero. After reaching this condition, an increase in H_2 permeance does not reflect the effect of process intensification. This phenomenon can be confirmed when analyzing the point where the plateau is reached. The plateau appears at higher permeance values when the operating pressure is increased (Figure 7.28); this effect will continue until the diving force becomes limited by the kinetics of the reaction.

Steam showed an enhancing effect to the production of H_2 and the reaction overall. As the S/E ratio increased, the H_2 mole fraction at the retentate increased. This outcome indicates that the rate of H_2 removal is the limiting process within the CMR, and that an increase in pressure will generate more H_2. On the other hand, the mole fraction of CH_4 and CO_2 in the retentate decreased and increased, respectively, as the S/E increased. This trend indicates that the conversion of CH_4 in the process improves in the presence of higher steam content. Although, the presence of steam appears to be beneficial to the overall production of H_2, Li et al. [111] reported that steam significantly affects the permeability of Pd membranes as it has shown strong adsorption ability on Pd surfaces. This suggests that there is a tradeoff between operating at high S/E ratios to improve the kinetics of the reaction while maintaining high permeability properties in the membrane.

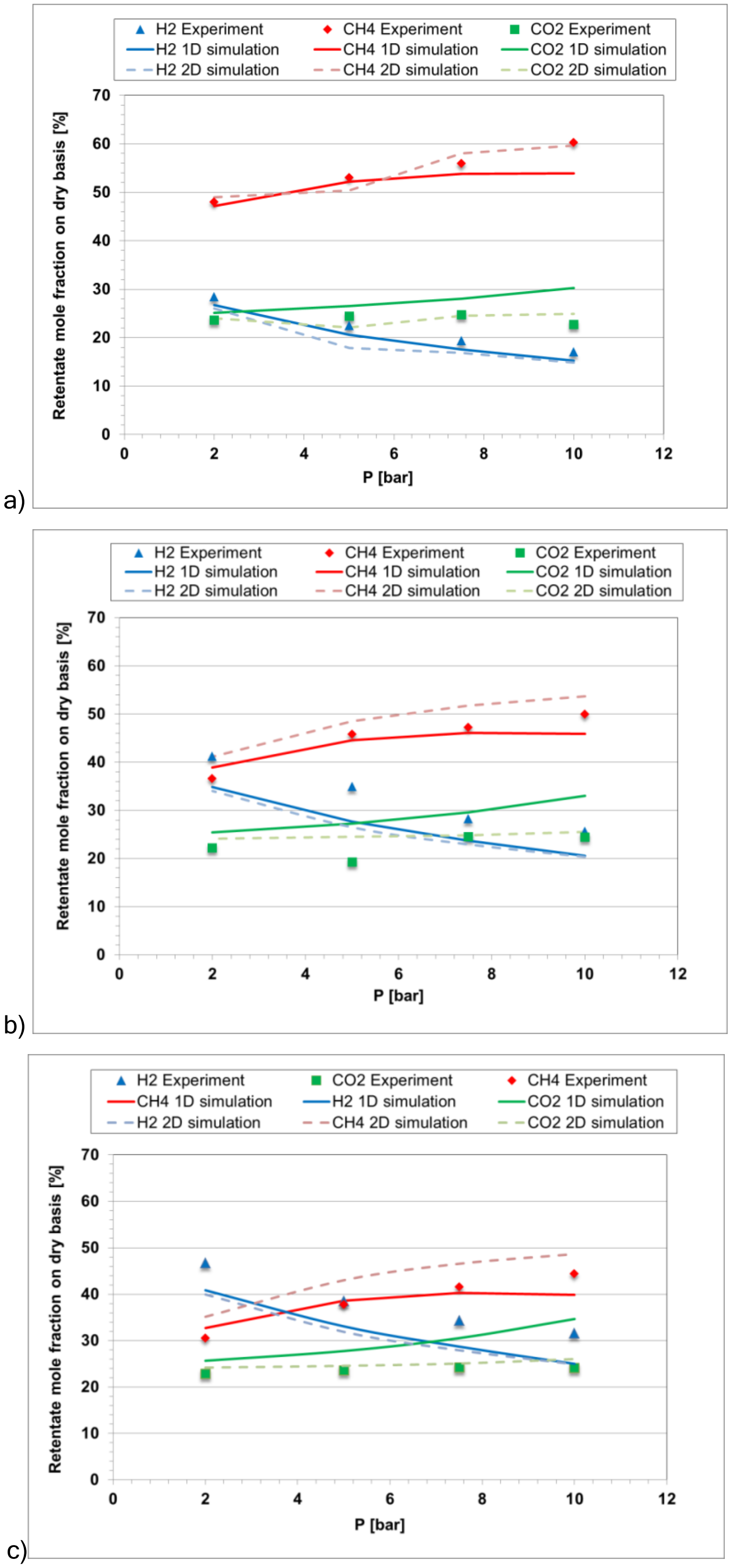

Figure 7.27. Composition of the retentate at different pressures at 450°C, LHSV=3.77 $h^{-1}$and a) S/E= 3, b) S/E= 5 and c) S/E= 7.

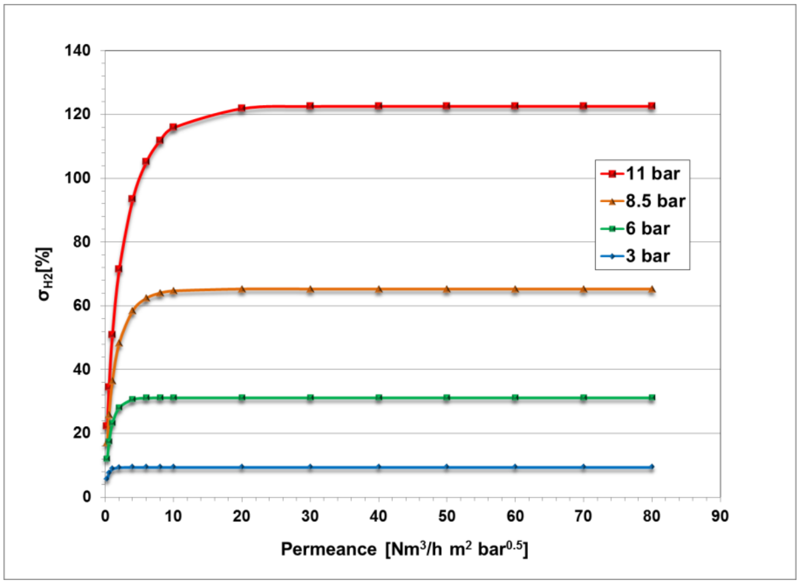

Figure 7.28. Hydrogen production improvement at different membrane permeances and retentate pressures.

7.4.4.3. Effect of temperature

The highly endothermic characteristic of ESR indicates that the process is thermodynamically favored by high temperatures. In CMR technology, temperature is a critical factor since it strongly relates to the H-diffusion through the Pd lattice and the activation energy for solution. To analyze the influence of temperature, the experiment was carried out under a fixed LHSV of 3.77 h^{-1}, a S/E ratio of 5 and a retentate pressure of 6 bar. The temperature was studied in the range of 350°C - 500°C. As shown in Figure 7.29, as the temperature increased, the H_2 mole fraction at the retentate increased, as a consequence of different elements. The first one relates to an increase in the kinetic properties of the catalyst, which induces higher CH_4 conversions, as previously shown in the literature [129]. Another factor is the membrane's H_2 permeance, which increases at higher temperatures, enhancing the effect of process intensification and thus improving the generation of H_2. It is important to mention that the trend was accurately depicted by the 1-d and 2-d simulation models; but, the experimental H_2 mole fraction appeared to be underestimated in Figure 7.29. This difference in the performance of the simulation and experimental results could be caused by the inhibition of the H_2 permeance, caused by the presence of components such as CO, steam, CO_2 and ethanol [96]. The simulation model did not consider variances in H_2 permeance; in other words, the model assumes that all gas species, excluding H_2, act as inert components.

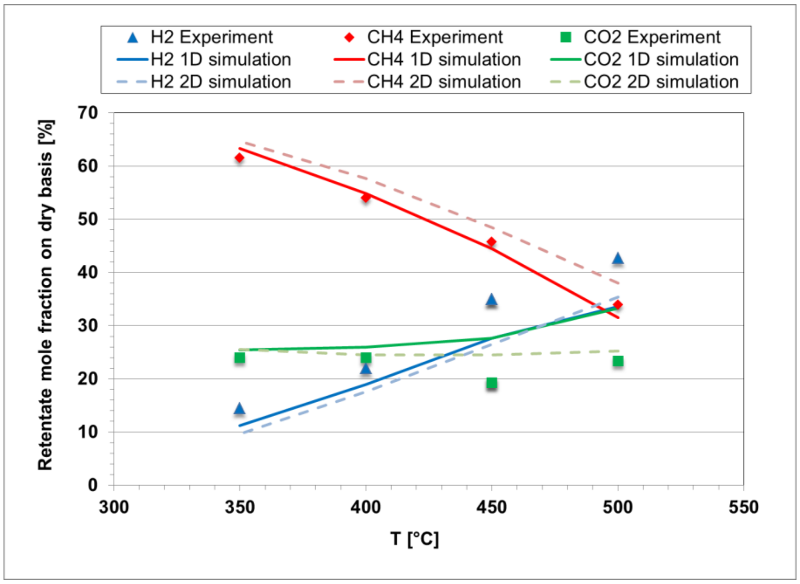

Figure 7.29. Composition of the retentate at different temperatures, a retentate pressure of 6 bar and S/E=5.

The mole fraction of methane decreased as temperature increased since the methane steam reforming reactions (Equations 7.4-7.7) are enhanced with temperature. The effect of temperature on methane during ESR (Equations 7.6-7.7) was studied in Figure 7.30, where the molar flow rate of CH_4 is computed at different membrane reactor lengths. It can be seen, at first, that CH_4 is generated early in the catalytic bed by breaking down ethanol (Equation 7.4); once ethanol is completely consumed, the process of MSR limits the generation of H_2. In Figure 7.30, the conversion of CH_4 ($\mathrm{X_{CH4}}$) was defined as:

$$\mathrm{X_{CH4}}[\%] = \frac{F_{CH4}^{max} - F_{CH4}^{ret}}{F_{CH4}^{max}} \cdot 100 \tag{7.35}$$

Where F_{CH4}^{max} and F_{CH4}^{ret} are the maximum CH_4 molar flow rate identified and the CH_4 molar flow rate at the outlet of the retentate, respectively. Figure 7.30 shows that the conversion of the generated methane, during the ESR process, improves as temperature increases.

Methane steam reforming was studied under “MSR conditions only” (CH_4 and steam) and labelled as MSR-CMR and “ESR conditions” and labelled ESR-CMR. The purpose was to compare the performance of the MSR-CMR and the ESR-CMR. Notice that the maximum CH_4 molar flow rate identified in the ESR-CMR was used as the feed stream for the MSR-CMR. Table 7.5 shows the theoretical methane conversion of the ESR-CMR and MSR-CMR. Under MSR conditions, the CH_4 conversion is higher than under ESR conditions. The reason is that the pseudo-composition formed in the reaction zone is different in both cases. For instance, in ESR, when ethanol reacts, it produces CH_4, CO and H_2; at this moment, CO immediately reacts in the WGS process (Equation 7.5) to generate more H_2 and CO_2. Meanwhile, CH_4 reacts, at a slower rate, in the MSR process (Equations 7.6 and 7.7); nonetheless, the presence of CO, CO_2 generated from the other reactions, thermodynamically inhibits the conversion of CH_4. In contrast, under MSR conditions only, when CH_4 starts reacting, no products are present and that the generated compounds are in stoichiometric balance, allowing higher CH_4 conversions. It is important to mention that the presence of a H_2 selective membrane in the reactor improves the generation of H_2 for ESR; however, when compared to MSR, the effect of “process intensification” is reduced.

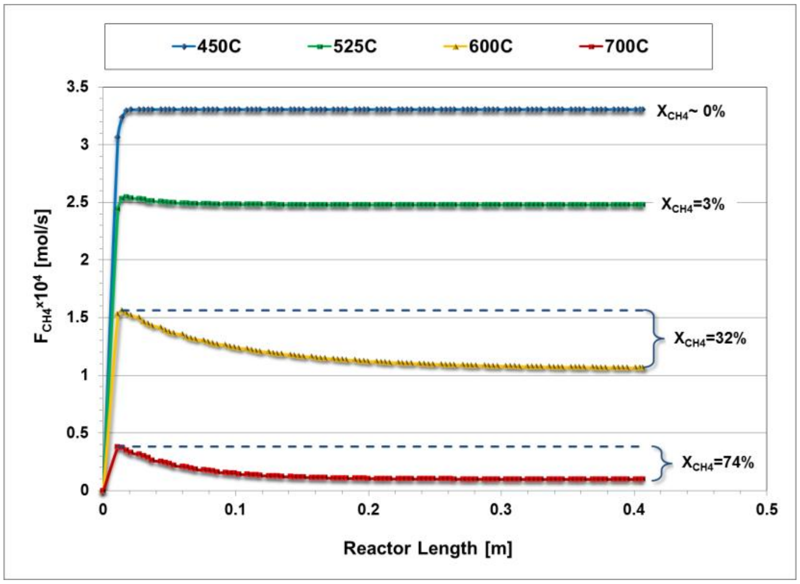

Figure 7.30. Methane molar flow rate along the length of the membrane at different temperatures, a retentate pressure of 3 bar and S/E=5.

Table 7.5. Comparison of CH_4 conversion in ESR and MSR conditions.

Temperature (°C)	X_{CH4} in ESR-CMR (%)	X_{CH4} in MSR-CMR(%)
450	0	28
525	3	60
600	32	95
700	74	100

For the case of CO_2, Figure 7.29 shows a stable performance as a function of temperature, possibly due to the integrated effect of WGS reaction and MSR. At high temperatures, the reaction rate of MSR increases, but the activity of WGS decreases. In contrast, at low temperatures, the WGS reaction improves while the MSR deteriorates, as reported by Sahoo et al. [130] and Murmura et al. [131]. It is important to mention that CO was not detected in the present work; nonetheless, to further explain the phenomenon observed in Figure 7.29, the tradeoff between MSR/WGS during the process of ESR in CMRs is presented in Figure 7.31. The selectivity of CO_2/CO, defined in Equation 7.36, was computed at different temperatures and a retentate pressure of 3 bar.

$$S_{CO2/CO} = \frac{F_{CO2}^{ret}}{F_{co}^{ret}} \tag{7.36}$$

At high temperatures (Figure 7.31), the generation of CO is expected to rise, as WGS is a moderately exothermic reaction, which is repressed at high temperatures (>450°C). As the temperature decreases, the selectivity towards CO_2 increases exponentially, since WGS becomes more active. The maximum CO_2/CO selectivity is presented at a temperature of 320°C; lower temperatures, showed a sharp decrease in selectivity. The reduction in selectivity at the colder temperatures can be attributed to i) the reduction in permeance of the membrane and ii) a slower ESR reaction rate. The reaction of ethanol is expected to proceed later in the catalytic bed, as the ESR reaction rate is reduced; consequently, the process of WGS will have lower residence times for the reaction to proceed. This reduction in residence time potentially affects the total CO concentration. Furthermore, as the permeance of the membrane decreases with reduced temperatures, it is expected to have higher a H_2 concentration in the reaction zone. The presence of H_2 allows the system to reach a thermodynamic equilibrium faster, inhibiting the WGS reaction and thus resulting in higher CO levels.

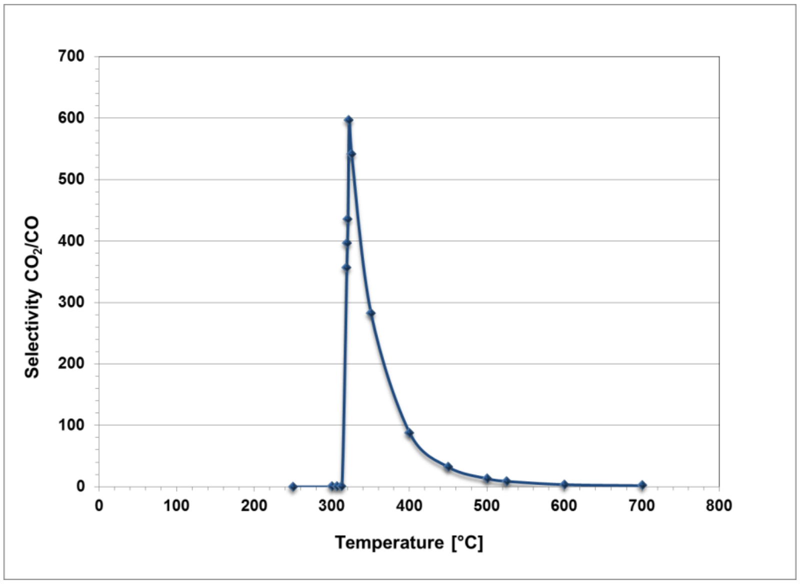

Figure 7.31. Selectivity of CO_2/CO of the Ni-based reforming catalyst under ESR-CMR conditions

8. TECHNOECONOMICAL EVALUATION

Summary

The development of an economic analysis based on test results is one of the main objectives of the project. Given the lack of industrial data useful for the valuation of membrane technology's economic performance, the assessments of membrane reactor modules is shown in the presence of uncertainty through the integration of Monte Carlo techniques. Furthermore, this section analyzes the economic performance of Palladium-based technology integrated to different processes such as in Integrated Gasification Combined Cycle (IGCC) power plants and coal and natural gas-derived hydrogen production plants. The plants with embedded membrane technology were evaluated under different market and regulatory environments. The assessments included sensitivity studies in order to obtain a deeper understanding of the constraints that currently limit the application of membrane technology in a commercial level. This chapter explores potential financing methods that could facilitate the deployment of the membranes.

8.1. Methodology of the Economic Performance Evaluation Framework in the Presence of Uncertainty

Our starting point is the recognition that conventional economic models such as the Total Capital Cost (TCI), Total Product Cost (TPC), Net Present Value (NPV) and the levelized cost (LC) are inherently uncertain and driven by various irreducible market, regulatory and other uncertainties. Therefore, an economic performance evaluation framework of a technology option based on expected/average/baseline values for all the above uncertainty sources (the uncertain TCI/TPC/NPV/LC model inputs) leads to single-point estimates and quite often to unsatisfactory economic appraisals [132,133]. This is known as the "flaw of averages" according to which the economic performance evaluated at average/baseline conditions does not necessarily represent the average economic performance [132]. Furthermore, a Monte Carlo simulator integrated into the proposed framework can simultaneously take into account multiple uncertain model inputs associated with the future state of the economic, regulatory and process operating environment as opposed to the conventional sensitivity analysis where one input variable is allowed to vary while keeping all others fixed [132]. In light of the above, the present study's key objective is the development of a methodologically sound economic performance evaluation framework for the integration of membrane technology in different settings by explicitly taking into account various sources of uncertainty. Consequently, the derivation of TCI, TPC, NPV and LC distribution profiles is sought that allows the statistical characterization of "risks and opportunities/rewards" in the presence of uncertainty [132,31]. For the attainment of such a goal the following methodological path is pursued (Figure 8.1):

1) Step 1: Comprehensive baseline functional TCI/TPC/NPV/LC-models are developed first (please see the following sub-sections)
2) Step 2: Key uncertain model input variables are identified admitting reasonable probabilistic representations through appropriately selected distribution profiles. Using Monte Carlo techniques and random sampling from the above distributions, model input uncertainties are propagated through the TCI/TPC/NPV/LC-model, generating distribution profiles for TCI/TPC/NPV/LC that can be characterized in a statistical/probabilistic sense. Please notice that the expected value of the above sample of TCI/TPC/NPV/LC values generated by Monte Carlo simulations represents an unbiased estimator of the expected value of TCI/TPC/NPV/LC, and thus the aforementioned "flaw of averages" can be effectively overcome [132].

As mentioned above, integrating standard Monte Carlo simulation methods into the proposed framework allows the inherent uncertainty of key model inputs to be explicitly recognized. Indeed, the Monte Carlo simulator generates a broad range of economic performance outcomes, and therefore allows the statistical/probabilistic characterization of the impact of uncertain future states on the economic performance of the CMR module as well as the entire plants. In the present study, the software package XLSim was used for conducting the Monte Carlo simulation runs [132]. All uncertain model inputs considered are listed along with the corresponding probability distributions in each subsection. Please notice that the lack of accumulated operating experience and the dearth of plant data at the commercial scale pose significant challenges to any economic performance evaluation of membrane-related plants. In this study, we considered three different types of probability distributions for the uncertain model input variables:

i) In the presence of available historical data the associated distributions were developed using standard re-sampling techniques [132].

ii) In the absence of any reliable data at the commercial scale, simple uniform and triangular distribution forms were considered (minimum, maximum and most likely values; [132]) that span the range of estimates reported in recent comprehensive studies/reports (cited in the list of bibliographical references).

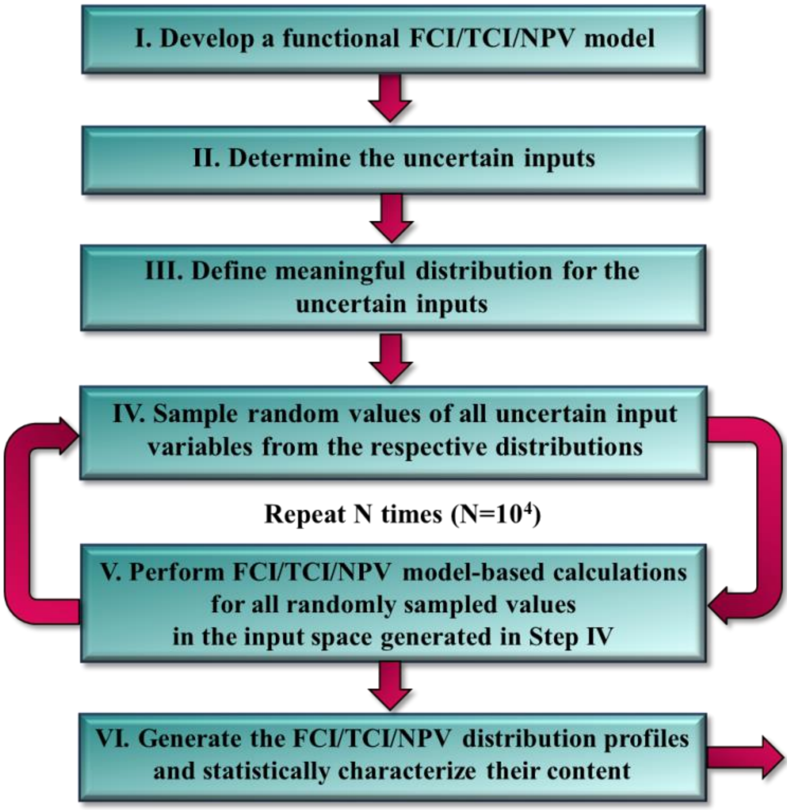

Figure 8.1. Methodological steps in the Monte Carlo simulation procedure.

8.2. A Cost Assessment Study for a Pilot-Scale Water Gas Shift Catalytic Membrane Reactor Module

A comprehensive economic performance evaluation framework for an actual pilot-scale water-gas-shift Pd-based catalytic membrane reactor (CMR) module for hydrogen production is presented. Since a detailed assessment of the technical performance of the CMR, built at WPI, was reported previously in section 6, the present research study focuses on an assessment of the module's economic performance characteristics. The proposed evaluation framework encompasses comprehensive baseline models for both Fixed Capital Investment (FCI) and Total Capital Investment (TCI) while various sources of uncertainty are identified whose effect on CMR's economic performance is explicitly taken into account using Monte Carlo techniques. As a result, insightful distribution profiles of FCI and TCI are derived rather than single-point value estimates and more realistic distributions of CMR economic performance outcomes are generated and statistically characterized. The latter could potentially inform development efforts of this new technology option for hydrogen production

Description

8.2.1. Features of the economic framework model

The proposed economic performance evaluation framework comprehensive baseline models for the FCI and TCI are developed first, while Monte Carlo simulation methods are then integrated into the FCI and TCI baseline models to explicitly take into account the various uncertain model inputs. For instance, in the baseline functional FCI/TCI model formulation, the FCI is calculated as the sum of all direct and indirect costs while the TCI is estimated by combining the FCI with the working capital (WC) in compliance with standard practices in economic analysis of engineering systems. Table 8.1 shows the 14 cost model inputs considered in the FCI/TCI estimation along with their corresponding spread range. Please notice that the cost figures of purchased equipment involving the Pd-based CMR and assorted apparatus, such as the micro gas chromatography (GC) system, the high pressure liquid metering pump, and the pressure monitor system, are adopted from the actual pilot-scale CMR module built in the facilities of Worcester Polytechnic Institute (WPI) with their specifications listed in Table 8.2. Furthermore, the range of percentages indicated in Table 8.1 are approximations, reflecting the effect of many factors in uncertain future states on the FCI/TCI, including the module location, type of process, and complexity of the equipment. Furthermore, the cost figures obtained from the actual pilot-scale CMR module are updated by means of the Chemical Engineering Plant Cost Indexes (available for year 2014) in order to obtain the most recent equivalent cost figures [134].

Table 8.1. Estimation of the capital investment for a pilot-scale Pd-based CMR module.

I. Direct Costs

- *A. Equipment + installation + instrumentation + piping + electrical + insulation + painting*
  - 1. Purchased equipment
    - a. Micro GC system
      - (1) Micro GC × 1
      - (2) Trap (H_2O) × 2
      - (3) Big universal trap (He) × 2
    - b. High pressure liquid metering pump
    - c. Pressure monitor system
      - (1) Manometer (range: 25000 Torr) × 2
      - (2) Manometer (range: 5000 Torr) × 1
      - (3) Digital power supply and readout × 2
    - d. Drain valve
    - e. Mass flow control system
      - (1) Mass flow controller × 4
      - (2) Mass flow indicator × 2
      - (3) Pressure controller × 2
      - (4) Flow-Bus interface box × 1
      - (5) Digital readout/control unit blind front × 2
    - f. Chiller
    - g. Temperature control system
      - (1) Temperature controller × 2
      - (2) Profile Probe × 2
      - (3) Thermocouple differential analog input module × 3
      - (3) CompactDAQ chassis × 1
    - h. Computer
    - i. Preheater
      - (1) Shell casing
      - (2) Ceramic fiber heater
    - j. Pd-based catalytic membrane reactor
      - (1) Pd/Au alloy composite membrane
        - i) Pd cost
        - ii) Au cost
        - iii) 316L SS support
      - (4) High temperature shit catalyst
      - (5) Shell casing
      - (6) Ceramic fiber heater
  - 2. Installation (25-55% of purchased equipment)
  - 3. Instrumentation and controls, installed (8-50% of purchased equipment)
  - 4. Piping, installed (10-80% of purchased equipment)
  - 5. Electrical, installed (10-40% of purchased equipment)
- *B. Buildings, process and auxiliary (10-70% of purchased equipment)*
- *C. Service facilities and yard improvements (40-100% of purchased equipment)*
- *D. Land (4-8% of purchased equipment)*

II. Indirect Costs

- *A. Engineering and supervision (5-30% of direct cost)*
- *B. Legal expenses (1-3% of fixed capital investment)*
- *C. Construction expense and contractor's fee (10-20% of fixed capital investment)*
- *D. Contingency (5-15% of fixed capital investment)*

III. Fixed Capital Investment (= Direct Costs + Indirect Costs)

IV. Working Capital (10-20% of Total Capital Investment)

V. Total Capital Investment (= Fixed Capital Investment + Total Capital Investment)

*Please notice that all of costs are updated to 2014 by Chemical Engineering Plant Cost Indexes.

Table 8.2. Pd-based catalytic membrane reactor specifications used for cost analysis.

Pd thickness [µm]	6.000
Au thickness [µm]	0.510
Outer diameter of the support tube [m]	0.025
Length of the support tube [m]	0.356
Length of the porous part [m]	0.254
Outer diameter of the shell casing [m]	0.051
Wall thickness of shell casing [m]	0.00305
Inner diameter of the shell casing [m]	0.045
Length of the shell casing [m]	0.914
Membrane area [m^2]	0.0203
Volume for shell casing [m^3]	0.00143
Annular volume for catalyst packing [m^3]	0.00027
Void fraction of catalyst (assumed)	0.657
Catalyst dilution (assumed)	0.800
Solid catalyst density (calculation) [kg/m^3]	2130.000
Catalyst bed density (calculation) [kg/m^3]	1119.528
Weight of catalyst [kg]	0.302

Table 8.3. Probability distributions associated with various uncertainty drivers.

Uncertainty driver	Minimum	Most likely	Maximum
Pd unit price [$/g], RH	Historical data from 2011-2015, www.kitco.com		
Au unit price [$/g], RH	Historical data from 2011-2015, www.kitco.com		
Ratio for installation, UD[a]	25.0%		55.0%
Ratio for instrumentation and controls, installed, UD[a]	8.0%		50.0%
Ratio for piping, installed, UD[a]	10.0%		80.0%
Ratio for electrical, installed, UD[a]	10.0%		40.0%
Ratio for buildings, process and auxiliary, UD[a]	10.0%		70.0%
Ratio for service facilities and yard improvements, UD[a]	40.0%		100.0%
Ratio for land, UD[a]	4.0%		8.0%
Ratio for engineering and supervision, UD[b]	5.0%		30.0%
Ratio for legal expenses, UD[c]	1.0%		3.0%
Ratio for construction expense and contractor's fee, UD[c]	10.0%		20.0%
Ratio for contingency, UD[c]	5.0%		15.0%
Ratio for working capital, UD[d]	10.0%		20.0%

RH = Resample historical data, UD = Uniform distribution
[a] Based on purchased equipment cost, [b] Based on direct cost, [c] Based on fixed capital investment, [d] Based on total capital investment.

8.2.2. Main results

An economic performance assessment of an actual pilot-scale Pd-based CMR module has been conducted with the integration of standard Monte Carlo simulation methods that take into account inherent sources of uncertainty. Figure 8.2 shows cumulative probability distribution profiles as well as associated expected values for the FCI and TCI demonstrating the economic performance of this new technology option in a statistical and more realistic manner compared to traditional single-point-based cost studies. In particular, it is easy to observe that there is a 20% chance for the TCI to be lower than $400 K, while there is a 10% probability for the FCI to be higher than $450 K. In addition, it is useful to quantify the "value at opportunity" and the "value at risk" at a predetermined probability level for further study and discussion. In the present study, the "value at opportunity" is defined as P_5, representing the 5 % probability for a capital investment cost to be lower than the P_5 threshold-value; while the "value at risk" is characterized as P_{95}, showing the possibility for the capital investment cost to be higher than the 5% threshold-value. Furthermore, the expected values of the TCI and FCI (ETCI/EFCI) have an outcome frequency of 52% as shown in Figure 8.2. The features of the cumulative distribution profiles for EFCI, ETCI, P_{95} and P_5 for the CMR module are summarized in Table 8.4.

The module cost per membrane unit area for the actual pilot-scale system, P_{95}, P_5, and the expected values for the FCI/TCI shown in the present study surpass the industrial-scale CMR module cost previously reported. The ETCI for an industrial-scale CMR is $18,805/m^2 which is approximately 1100 times lower than the ETCI delineated in this work or $22,268 K/m^2. Based on the six-tenths factor rule [135], the cost reduction in large-scale units can be attributed to a scale-up effect, which induces reasonable cost-reducing prospects on equipment costs at higher capacities. Furthermore, the design of a multiple tube membrane module and the elimination of the potentially overlapping auxiliary process components and assorted apparatus contribute further to the discrepancies in economic outcomes between the industrial- and pilot-scale CMR modules. It should be pointed out that the key cost components of the FCI/TCI models are strongly dominated by the purchased equipment cost and consequently, the lower module cost per membrane area presented in an industrial-scale seems reasonable.

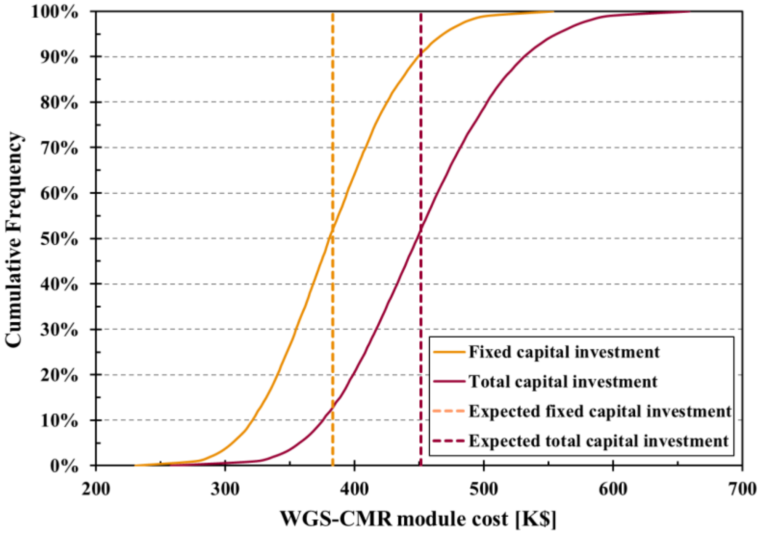

Figure 8.2. Cost distribution of a WGS-CMR module.

Table 8.4. WGS-CMR module cost summary.

	Fixed capital investment		Total capital investment	
	[K\$]	[K\$/m^2]	[K\$]	[K\$/m^2]
P_{95}	468.5	23,127	556.0	27,447
Expected value	383.0	18,906	451.1	22,268
P_5	305.3	15,072	357.2	17,632

The effects of uncertainty on the ETCI value for the pilot-scale CMR module are analyzed through the Tornado diagram presented in Figure 8.3. In such a manner, a Tornado diagram graphically illustrates the relative impact on the TCI profile of variations of the different uncertain model inputs considered in the present study. Specifically, the change of the ETCI caused by the variation of each input over its prescribed range from the lowest to the highest value is depicted with a bar in the Tornado diagram, under the assumption that all other model inputs remain at their baseline values. Afterwards, all bars are sorted from long to short, in order to clearly distinguish between the relative impact of various uncertain model inputs on TCI-relevant performance characteristics [136]. Therefore, the major advantage of using a Tornado diagram in this study is to illustrate which uncertain model inputs have the greatest impact on the expected value of the TCI.

The ETCI-Tornado diagram of the pilot-scale CMR module is based on the following values: Pd unit price: 18.6-28.2 \$/g; Au unit price: 36.5-57.0 \$/g, installation to purchased equipment ratio range: 25-55%; instrumentation and controls, installed to purchased equipment ratio range: 8-50%; piping, installed to purchased equipment ratio range: 10-80%; electrical, installed to purchased equipment ratio range: 10-40%; buildings, process and auxiliary to purchased equipment ratio range: 10-70%; service facilities and yard improvements to purchased equipment ratio range: 40-100%; land to purchased equipment ratio range: 4-8%; engineering and supervision to direct cost ratio range: 5-30%; legal expenses to fixed capital investment ratio range: 1-3%; construction expense and contractor’s fee to fixed capital investment ratio range: 10-20%; contingency to fixed capital investment ratio range: 5-15%; working capital to total capital investment ratio range: 10-20%; capacity of purchased equipment: ± 20%.

As shown in Figure 8.3, the capacity of purchased equipment has the most significant impact on the TCI performance, suggesting that the purchased equipment cost greatly determines the value of TCI. Please also notice that the TCI increases by 11% when the capacity of purchased equipment is increased by 20%, while the TCI decreases by 13% when the capacity of purchased equipment is reduced by 20%, indicative of the significant impact of the CMR module capacity on TCI performance. As a result, since the purchased equipment costs for a larger capacity, such as in an industrial-scale CMR module case, would be significantly reduced from those presented in the pilot-scale CMR module; a significant reduction in cost for an industrial-scale CMR seems indeed a valid conjecture. Additionally, membrane features such as Pd and Au unit price show a marginal effect on TCI performance when compared to the capacity of purchased equipment.

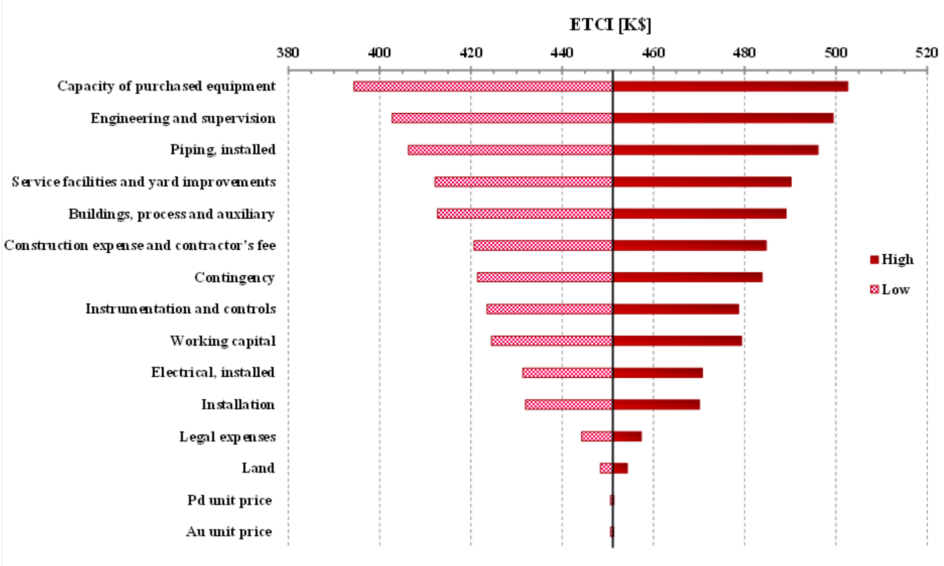

Figure 8.3. Tornado diagrams for the Total Capital Investment.

8.3. Natural Gas in Hydrogen Production: A cost Study

A comprehensive economic performance evaluation framework for palladium (Pd)-based industrial-scale catalytic membrane reactor (CMR) modules integrated into hydrogen (H_2) production systems (HP-CMR) through methane steam reforming has been developed. Within the above context, this subsection develops comprehensive baseline models for total capital investment (TCI) and total product cost (TPC) to evaluate the economic performance of CMRs. Various sources of uncertainty (raw material market prices, labor costs, membrane lifetime and maintenance costs, financing costs, etc.) are recognized and their effect on TCI and TPC is explicitly taken into account using Monte Carlo techniques. As a result, insightful distribution profiles of TCI and TPC are derived rather than single-point value estimates and more realistic distributions of CMR economic performance outcomes are generated. Furthermore, tornado diagrams are developed, establishing the predominant effect of palladium unit price, membrane lifetime and financing interest costs on TCI and TPC.

Description

8.3.1. Baseline TCI/TPC-model development

The following set of tables (Table 8.5,Table 8.6 and Table 8.7) encompass key model inputs. In particular, cost figures involving the industrial-scale membrane reactor module and assorted equipment were adopted from Criscuoli et al. [137] and the DOE/NTEL report by Chou and Kuehn (2010) [138]. Please notice that equipment costs included in the present study do not take into account the cost-reducing potential of future technological advances and “learning”.

The various cost components of the analysis conducted and all pertinent details of the associated baseline TCI and TPC models can be found in Table 8.8 and Table 8.9 respectively. Standard practice in engineering economic analysis requires the calculation of the Fixed Capital Investment cost (FCI) first as the sum of all direct and indirect costs, followed by the calculation of the Total Capital Investment (TCI) as the sum of FCI and Working Capital [139]. Furthermore, the Total Product Cost (TPC) is calculated by forming the sum of Manufacturing Cost, General Expenses as well as Membrane and Catalyst Replacement Costs [139]. In particular, Table 8.8 and Table 8.9 encompass a detailed list of all cost components (FCI/TCI/TPC model inputs) and the displayed numerical estimates correspond to the average/expected values (representing the baseline case) of the probability distributions of the various model inputs considered as inherently uncertain in the sequel. Please notice that a relatively thick Pd-layer of 75 μm was used in the above baseline calculations in agreement with the Criscuoli et al. [137] for comparison purposes, even though further cost reduction would be possible by decreasing the Pd-layer thickness as demonstrated in the next Sub-section. Please notice that since key components of FCI (pertaining for example to installation and engineering & supervision) depend on equipment cost, the FCI cost of the membrane reactor module increases proportionally with the reactor equipment cost. Furthermore, membrane replacement costs are explicitly taken into account in our study and calculated by dividing the membrane reactor module equipment cost by the membrane life-time (also treated as an uncertain model input in the sequel). It should be pointed out that Pd-based membrane reactors have to be tested under actual reaction conditions within a long-term horizon to more accurately determine the membrane lifetime. Evidently a higher membrane lifetime would lead to a reduction in replacement costs. Finally, please notice that neither the Pd-recovery nor the membrane reactor leasing option was considered in the present study; these options however would almost surely lead to additional economic benefits.

Table 8.5. Cost data used in the economic performance assessment framework (Cost base: 2012).

Raw material [$/year]	2,088,854
Catalyst [$/kg]	5
Steam [$/ton year]	119,454
Compressor (from 1 to 16 atm) [$]	580,674

Table 8.6. Electricity, steam consumption and labor cost data (Cost base: 2012).

	Conventional technology option	CMR
Electricity consumption [kW-h]	-	2,616,897
Steam consumption [Ton/year]	4.9	1.0
Labor hour [h]	8,844	8,844

Table 8.7. Economic parameters used in cost analysis.

Euro to US Dollar exchange rate	In 2000	1.083
Chemical engineering plant cost indexes	In 2000	394.1
	in 2012	584.6

Table 8.8. Estimation of total capital investment (TCI) for the membrane reactor module (Cost base: 2012).

I. Direct Costs				
A. Equipment + installation + instrumentation + piping + electrical + insulation + painting				
1. Purchased equipment	**WGS reactor**	**HTS catalyst**	**Pd membrane**	**Compressor**
	$525,497	**$9,675**	**$8,948,562**	**$580,674**
Total membrane module	$10,064,408			
2. Installation (40% of A1.)	$4,025,763			
3. Instrumentation and controls, installed (29% of A1.)	$2,918,678			
4. Piping, installed (45% of A1.)	$4,528,984			
5. Electrical, installed (25% of A1.)	$2,516,102			
Equipment total	$24,053,935			
B. Buildings, process and auxiliary (40% of A1)	$4,025,763			
C. Service facilities and yard improvements (70% of A1)	$7,045,085			
D. Land (6% of A1)	$603,864			
Sub-total	$35,728,648			
II. Indirect Costs				
A. Engineering and supervision (17.5% of direct cost)	$6,252,513			
B. Legal expenses (2% of fixed-capital investment)	$1,150,169			
C. Construction expense and contractor's fee (15% of fixed-capital investment)	$8,626,266			
D. Contingency (10% of Fixed-capital investment)	$5,750,844			
sub-total	$21,779,792			
III. Fixed capital investment (= Direct costs + Indirect costs)	$57,508,440			
IV. Working capital (15% of V)	$10,148,548			
V. Total capital investment (= III + IV)	$67,656,988			

Table 8.9 Estimation of total product cost (TPC) for the membrane reactor module (Cost base: 2012).

I. Manufacturing cost (= Direct production costs + Fixed charges + Plant overhead costs)	
A. Direct production costs	
1. Raw materials	$2,088,854
2. Operating labor	$311,701
3. Direct supervisory and clerical labor (15% of operating labor)	$46,755
4. Utilities	$380,515
5. Maintenance and repair (6% fixed-capital investment)	$3,450,506
6. Operating supplies (0.75% of fixed-capital investment)	$431,313
7. Laboratory charges (15% of operating labor)	$46,755
8. Patents and loyalties (3% of product cost)	$878,225
Total direct production costs	$7,634,626
B. Fixed charges	
1. Depreciation (10% of fixed-capital investment)	$5,750,844
2. Local taxes (2.5% of fixed-capital investment)	$1,437,711
3. Insurance (0.7% of fixed-capital investment)	$402,559
Total fixed charges	$7,591,114
C. Plant overhead costs (10% of product cost)	$2,927,418
Sub-total	$18,153,158
II. General expenses	
A. Administrative costs (3.5% of product cost)	$1,024,596
B. Distribution & selling costs (11% of product cost)	$3,220,160
C. R&D costs (5% of product cost)	$1,463,709
D. Financing interest (8% of total capital investment)	$5,412,559
Sub-total	$11,121,025
III. Total product cost	
A. Membrane replacement	$2,982,854
B. HTS catalyst replacement	$1,935
C. Product cost (= Manufacturing cost + General expenses)	$29,274,183
Total	$32,258,972

8.3.2. Probabilistic Representation of Cost Model Input Uncertainty- Monte Carlo Simulator

The proposed TCI/TPC-modeling framework with the integrated Monte Carlo simulator was employed in order to conduct a membrane reactor module cost analysis in the presence of uncertainty. In our analysis instead of seeking the "best cost forecast" as a single-point estimate under conditions of irreducible uncertainty (for a technology option which has also not yet been demonstrated on the commercial scale), the focus is placed on the derivation of a range of economic performance outcomes (along with a probabilistic characterization) for a more realistic and potentially useful economic appraisal. Within the proposed context, the FCI, TCI, TPC cumulative probability distribution profiles for the industrial-scale membrane reactor module considered in this section are shown in Figure 8.4, Figure 8.5

and Figure 8.6 respectively for various Pd-thickness values as well as the distribution profile of the associated costs in the traditional technology option case for comparison purposes. Please notice that each of these distribution profiles and the corresponding statistical characterization offer valuable pieces of information regarding the economic performance of the technology options considered in the present study:

i) The probability (vertical axis) that the FCI/TCI/TPC falls below a desirable cost target level (horizontal axis) as well as the complementary probability for the cost to be higher than the aforementioned target level can be easily deduced. For example, there is a 10% probability for TPC to be lower than 8 $M in the 20 µm Pd-thickness case (Figure 8.6)

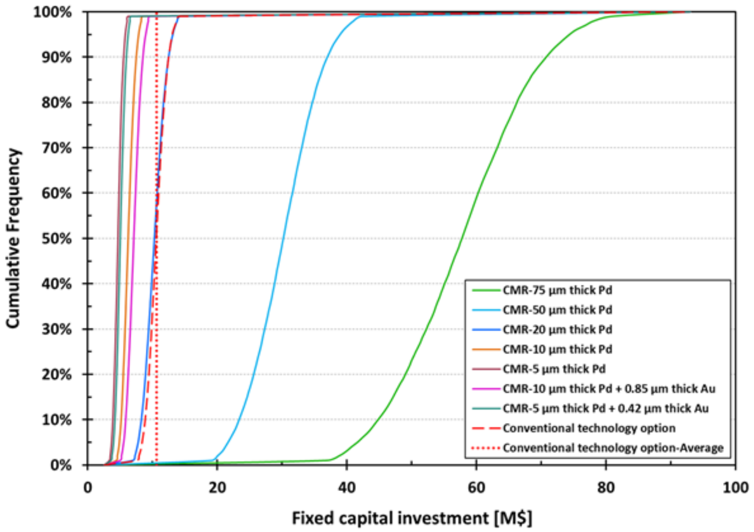

Figure 8.4. Distribution profiles of fixed capital investment for various Pd-thickness values.

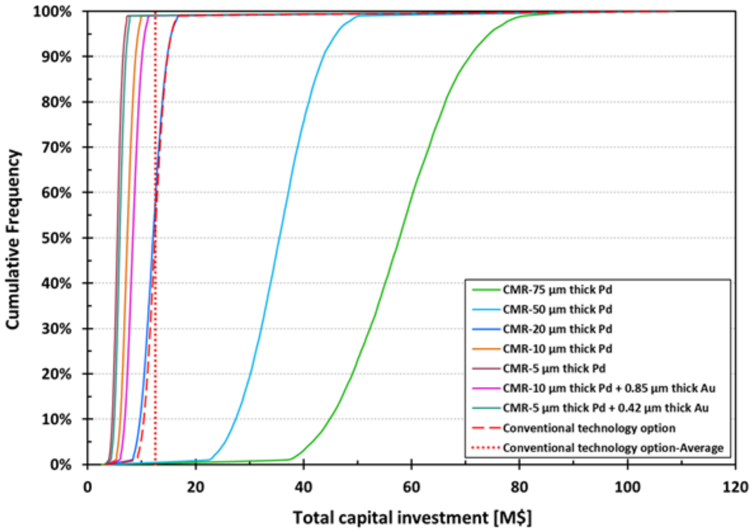

Figure 8.5.Distribution profiles of total capital investment for various Pd-thickness values.

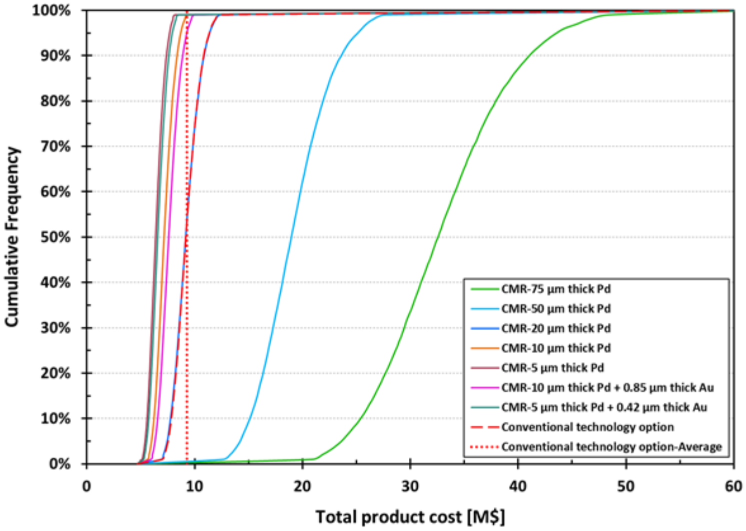

Figure 8.6. Distribution profiles of total product cost for various Pd-thickness values.

ii) The expected values of the FCI, TCI, TPC distribution profiles (tabulated also in Table 8.10) as well as the associated value ranges (a measure of dispersion/spread of possible economic performance outcomes) can be also readily deduced.

iii) The downside risk (also known as “value at risk”; Savage 2003) can be quantified at a pre-specified level. For example a FCI/TCI/TPC threshold-value can be easily identified for which there is a 10% probability of a higher cost to be realized (usually denoted as the P90 value; the 90th-percentile). For example, there is a 10% probability for TPC to be higher than 10 $M (and a 90% probability to be lower than 10 $M) in the 20 µm Pd-thickness case (Figure 8.6).

Table 8.10. FCI/TCI/TPC expected values for various Pd-thickness values.

Expected Value	Conventional Technology Option (Criscuoli et al., 2001)	CMR-75 µm thick Pd	CMR-50 µm thick Pd	CMR-20 µm thick Pd	CMR-10 µm thick Pd	CMR-5 µm thick Pd	CMR-10 µm thick Pd and 0.85 µm thick Au	CMR-5 µm thick Pd and 0.42 µm thick Au
Fixed-capital investment [M$]	10.64	57.81	30.22	10.34	6.29	4.69	7.16	5.07
Total capital investment [M$]	12.54	68.07	35.59	12.18	7.41	5.52	8.43	5.97
Total product cost [M$]	9.28	32.94	19.19	9.26	7.24	6.44	7.67	6.63

From Table 8.10 it can be easily inferred that the expected values of FCI, TCI and TPC obtained from the respective distribution profiles are higher in the CMR-based technology option than the ones associated with the conventional technology platform option for Pd-thicknesses greater than 20 μm. However, FCI, TCI and TPC distribution profiles for CMRs start shifting towards the left of the vertical axis and thus becoming economically appealing especially when Pd -thickness falls below the 20 μm level. This behavior conforms also to the intuitively expected one since lower Pd-thickness values lead to lower membrane areas required for the attainment of the same hydrogen recovery target level, and consequently to lower costs. Please notice that the observed shift of the distribution profile curves to the left with decreasing Pd-thickness implies a higher chance of costs falling below a certain target level/threshold, and thus enhanced economic performance. It should be also noted that over the years thin membranes with Pd-thicknesses within the 5 μm - 10 μm range have been synthesized at WPI's Center for Inorganic Membrane Studies and the attainment of high performance levels has been experimentally validated and patented. Finally, given the enhanced environmental performance prospects of the methane steam reforming-based HP-CMR technology option, the results of our cost analysis under uncertainty also demonstrate a significant window of opportunity for the proposed technology option to favorably compete on the overall techno-economic performance front with the traditional/conventional option, and therefore to be seriously considered for the provision of the requisite incentives aiming at the acceleration of its demonstration on the commercial scale.

Within a range of Pd-thickness values, Figure 8.7, Figure 8.8 and Figure 8.9 aim at a comparative appraisal of FCI, TCI and TPC for CMRs and also against the conventional non-membrane-based technology option on the average/expected value level as well as at equal levels of probability associated with potential "risks and opportunities" such as the P95 and P5 values (the 95th-percentile and 5th-percentile respectively). The upper P95 line (a possible means of quantifying "risks") graphically shows that there is a 5% chance of incurring a cost higher than the value on the line (equivalently a 95% chance of a cost lower than the value on the line), and similarly, the lower P5 line graphically shows the 5% chance of incurring a cost lower than the value on the line (a possible means of identifying "opportunities"). The middle line provides the expected cost value for the various Pd-thicknesses considered. Please notice that as the Pd-thickness decreases not only the FCI, TCI and TPC values decrease as noted earlier, but so does the spread/variability (quantified as P95-P5) of the various costs, i.e. the dispersion of possible economic performance outcomes. Since the palladium unit price has by far the most significant effect on cost (as will be established through Tornado diagrams presented in the sequel) the observed reduction in the variability/spread of the various costs with decreasing Pd-thickness can be attributed to the fact that thinner membranes require less Pd-amounts for the attainment of the same hydrogen recovery level.

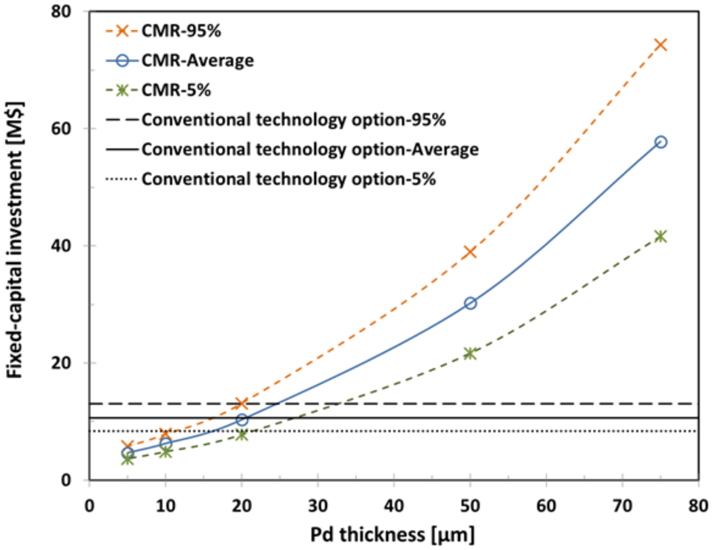

Figure 8.7. P95, P5 and expected value lines of fixed capital investment for various Pd-thickness values.

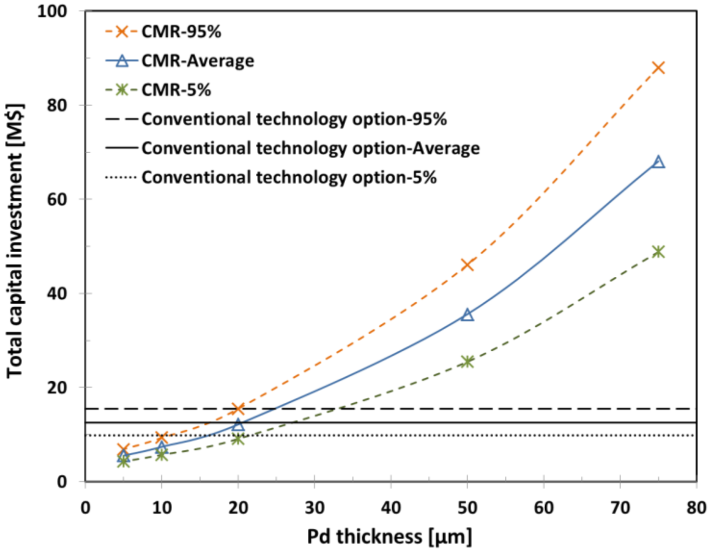

Figure 8.8. P95, P5 and expected value lines of total capital investment for various Pd-thickness values.

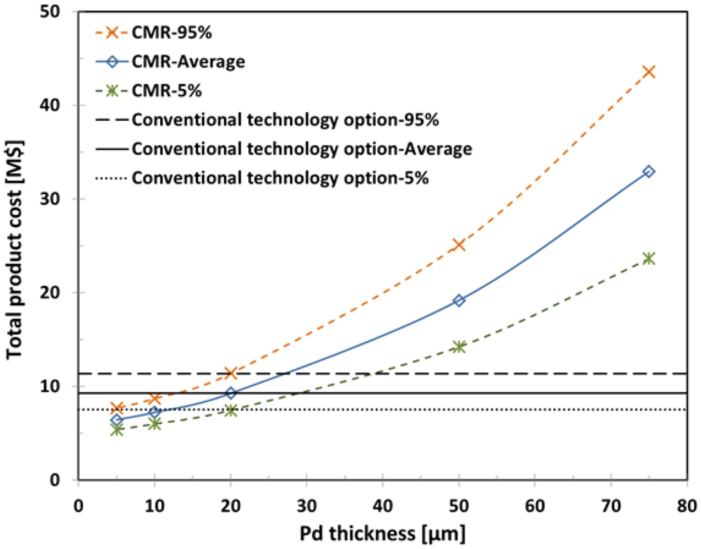

Figure 8.9. P95, P5 and expected value lines of total product cost for various Pd-thickness values.

Next the useful tool of a Tornado diagram is employed in order to conduct a sensitivity analysis and draw useful insights into the sources of uncertainty with the highest impact on FCI, TCI and TPC. A Tornado diagram graphically summarizes the relative impact of variations of the various uncertain model inputs considered in the present study over their respective ranges (from the lowest to the highest value) under the assumption that all other model inputs remain at their baseline values (fixed at their average/expected values of the corresponding probability distributions). Therefore, within such a context, a Tornado diagram nicely illustrates which uncertain model inputs most affect an economic performance index or metric (in this study the expected value of FCI, TCI and TPC). In a Tornado diagram each model input is represented by a bar as it varies over its prescribed range depicting its impact on the above performance index, and all bars are sorted from the long ones at the top to the shorter ones at the bottom. In this manner, a Tornado diagram prioritizes the most consequential inputs (sources of uncertainty) in terms of bar length and facilitates the visualization of their impact on economic performance primarily in cases of large-scale multi-input models. Figure 8.10 and Figure 8.11 provide representative Tornado diagrams for TCI and TPC. Pd-price, working capital, membrane reactor and catalyst cost constitute the set of model inputs (uncertainty sources) with the highest impact on TCI in descending order, whereas Pd-price, membrane lifetime, financing interest rate, working capital, raw materials and reactor cost constitute the set of model inputs with the highest impact on TPC (in descending order as well). In light of the above Tornado diagrams, the upper right zone of a TCI distribution profile curve (Figure 8.5) represents the “zone of adverse economic performance outcomes (risks)” corresponding to relatively higher Pd-prices, working capital levels, membrane reactor and catalyst costs, whereas the lower left zone represents the “zone of enhanced economic performance outcomes (opportunities)” corresponding to lower Pd-prices, working capital levels, membrane and catalyst costs. Similarly, the upper right zone of a TPC distribution profile curve (Figure 8.6) represents the “zone of adverse economic outcomes (risks)” corresponding to relatively higher Pd-prices, financing interest costs, working capital levels, raw materials costs and shorter membrane lifetimes, whereas the lower left zone represents the “zone of enhanced economic performance outcomes (opportunities)” corresponding to lower Pd-prices, financing interest costs, working capital levels, raw material costs as well as longer membrane lifetimes.

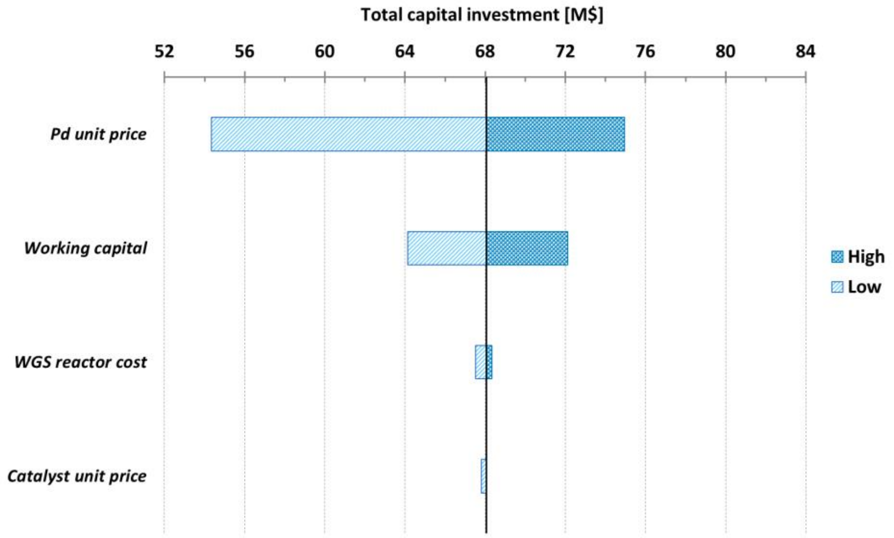

Figure 8.10. Tornado diagram for total capital investment (Pd unit price: 16.9-24.4 $/g; CMR module: baseline ± 10%; catalyst unit price: baseline ± 10%; Working capital to total capital investment ratio range 10-20%).

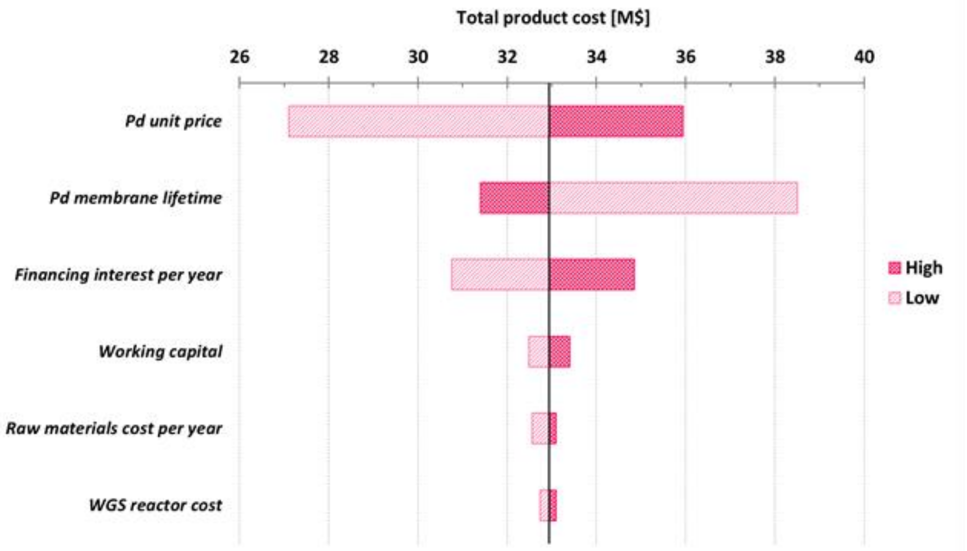

Figure 8.11.Tornado diagram for total product cost (Pd unit price: 16.9-24.4 $/g; Pd membrane lifetime: 1-5 years; CMR module: baseline ± 10%; Raw material cost per year: baseline ± 10%; Working capital to total capital investment ratio range: 10-20%; Financing interest to total capital investment ratio range: 6-10%).

8.4. Integration of Membrane Technology into Hydrogen Production Plants Based on Coal Gasification With CO_2 Capture

An economic performance evaluation framework for hydrogen production (HP) plants with integrated catalytic membrane reactor (CMR) modules) through coal gasification is presented (HP-CMR). A detailed comprehensive Net Present Value (NPV) model is first developed to assess the economic viability of HP-CMR plants, while irreducible sources of market and regulatory uncertainty are identified and their effect on the plant's economic performance is explicitly taken into account through Monte-Carlo techniques. As a result, the proposed economic performance evaluation framework for an HP-CMR plant allows the derivation of distribution profiles of economic performance outcomes rather than single-point value estimates that often lead to unsatisfactory valuation assessments by overlooking significant uncertainty effects over the plant's lifetime. Within the above framework, the HP-CMR plant is comparatively assessed against the conventional HP plant with and without Carbon Capture and Sequestration (CCS) systems. It is shown that future regulatory action on CO_2 emissions leads to comparatively appealing distribution profiles of economic performance outcomes for HP-CMR plants in the presence of uncertainty, thus offering a window of opportunity for this new technology option to emerge as a viable one for hydrogen production in a carbon-constrained world. Finally, the provision of a set of incentives is considered that could potentially facilitate the demonstration stage of the HP-CMR technology option on the commercial scale.

Description

8.4.1. Technology options integrated into coal-fired H_2 production plants for CO_2 capture: Absorption versus Membrane Technology

Several approaches for CO_2 capture applicable to fossil fuel-based electricity and H_2 co-production process systems have been thoroughly studied in the relevant body of literature [140,141,142,143], primarily falling into four categories: absorption, adsorption, chemical looping and membrane-based separation. The most common approach for CO_2 capture is physical absorption which uses solvents such as Selexol, Rectisol, Purisol, Sepasolv MPE and Fluor Solvent [144,145]. Specifically, the integration of a Selexol unit into conventional HP plants for CO_2 capture has been recommended in the DOE/NETL report [138,145] as shown in Figure 8.13. Therefore, a conventional coal-fired HP plant with CO_2 capture consists of five basic processes:

(1) Gasification. In this process pulverized coal reacts with O_2 (supplied by an air separation unit (ASU)) in the gasifier at elevated pressure and temperature (56 bar and 677 °C) to produce syngas, primarily composed of CO, CO_2, H_2, H_2O and other particulate impurities.
(2) Particulate removal. Syngas is treated with water in a scrubber to remove chlorides, alkali, and particulate matter.
(3) WGS reaction. The CO present in syngas reacts with steam in a series of WGS reactors (high temperature and low temperature reactors) to convert CO and H_2O into H_2 and CO_2.
(4) Gas clean up. This step involves three process units: the sour water stripper, the mercury removal, and the Selexol unit. First, the syngas passes through the sour water stripper to remove NH_3, SO_2, and other impurities from the scrubber. Then, 95% of mercury is removed through a carbon bed. Finally, both H_2S and CO_2 removal is performed in the Selexol unit. The Selexol unit used in this study is a dual stage one and the attainable efficiency of CO_2 capture can reach a level as high as 90% [146].
(5) H_2 Purification. Solid adsorbents, such as 5A zeolite, alumina, and activated carbon, in the pressure swing adsorption (PSA) unit adsorb all gas species contained in the syngas, except for H_2. Typically, the PSA unit is operated at 51 bar to yield 99.99% pure H_2 with a recovery efficiency of 80% [138,147].

The integration of Pd-based membrane technology in power plants is recognized as a quite promising technology option [148,149,150]. Indeed, CMR modules for the simultaneous CO_2 capture and high purity H_2 production embedded in Integrated Gasification Combined Cycle (IGCC) with CCS systems have been shown to generate rather good prospects for enhanced environmental and economic performance especially under future CO_2 emissions regulations [149]. In the present research work, motivated by the above considerations, preliminary studies and pertinent recommendations found in [151] whereby the HP-CMR technology option for future clean hydrogen production is supported, the integration of industrial scale Pd-based CMR modules into coal-fired H_2 production plants is economically evaluated under uncertainty within a systematic and comprehensive framework. The process block flow diagram of HP-CMR plant with CO_2 capture, based on the design of the DOE/NETL report [138], is presented in Figure 8.13.

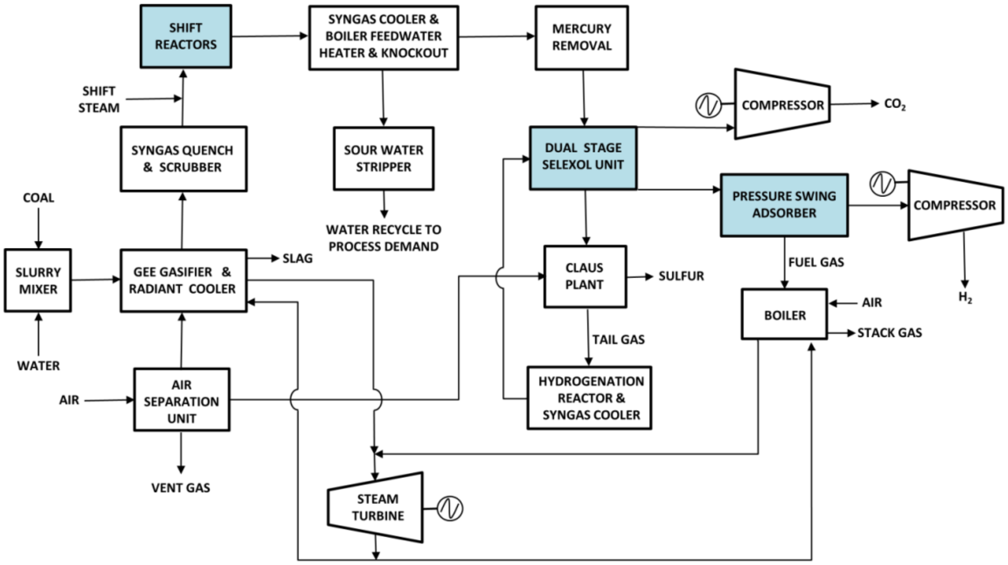

Figure 8.12. Process block flow diagram of the conventional coal-based H_2 production plant with CO_2 capture, based on the design of the DOE/NETL report [138].

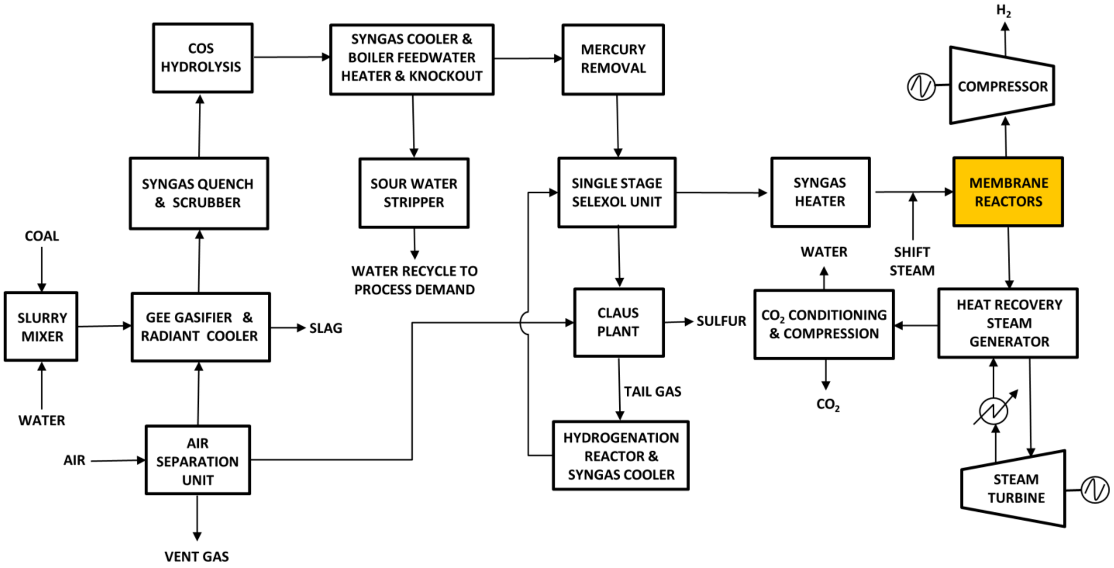

Figure 8.13. Process block flow diagram of the coal-based H_2 production plant integrated with membrane technology.

Compared to the conventional HP process system, the higher attainable CO conversion levels in an industrial scale CMR module allows for lower operating temperatures. Thereby, potential gains in terms of prolonged catalyst lifetime, lower production costs and reduced material costs can be realized [102,152]. Furthermore, combined with higher H_2 recovery levels, production of high-pressure CO_2 readily available for sequestration purposes takes place [148,149]. Therefore, the HP-CMR technology option exhibits great potential in enhancing the productivity of HP plants as well as the associated environmental performance in a cost-effective manner. It is important to mention that the main disadvantage of HP-CMR technology lays in the lack of accumulated operating experience and the absence of plant data at the commercial scale and therefore, the 33 uncertain model inputs considered are listed along with the corresponding probability distributions in Table 8.11. Other technical disadvantages of the CMR technology include the membranes' sensitivity to sulfur poisoning as well as challenges in the membrane preparation and process scale up stages [72,94,95,153].

Table 8.11. Probability distributions associated with various uncertain model inputs.

Uncertainty driver	Minimum	Most likely	Maximum
Pd unit price [$/g], RH	Historical data from 2010-2014, www.kitco.com		
Au unit price [$/g], RH	Historical data from 2010-2014, www.kitco.com		
Labor cost per hour [$/h], RH	Historical data from 2010-2014, www.bls.gov		
Coal price [$/tonne], RH	Historical data from 2010-2014, www.eia.gov		
Inflation rate, RH	Historical data from 2010-2014, U.S. Dept. of Lab. [2014]		
H_2 delivery cost [$/kg], RH	350 bar H_2 dispensing pathways, www.hydrogen.energy.gov [2013]		
	Pipeline	Pipeline-tube trailer	Tube trailer
	4.44	3.16	3.00
316L PSS support price [$/cm^2 for a 24 cm^2 support area], TD	10.2	11.3	12.4
Pd/Au membrane lifetime, TD[a]	1	3	5
Nominal discount rate for HP-CMR plant, TD[b]	14.4%	16.0%	17.6%
CO_2 transport & storage cost [$/tonne], TD	9	10	11
CO_2 tax rate (start at 2015) [$/tonne], TD	27	30	33
Annual growth rate of CO_2 tax, TD	5.4%	6.0%	6.6%
H_2 selling price [$/kg], TD	9	10	11
Combined state and local sales tax rates, TD	0.0%	6.4%	9.5%
Ratio for market value of plant after 30 years, TD[c]	13.5%	15.0%	16.5%
Ratio for Installation, UD[d]	25.0%		55.0%
Ratio for instrumentation and controls, installed, UD[d]	8.0%		50.0%
Ratio for piping, installed, UD[d]	10.0%		80.0%
Ratio for electrical, installed, UD[d]	10.0%		40.0%
Ratio for buildings, process and auxiliary, UD[d]	10.0%		70.0%
Ratio for service facilities and yard improvements, UD[d]	40.0%		100.0%
Ratio for land, UD[d]	4.0%		8.0%
Ratio for engineering and supervision, UD[e]	5.0%		30.0%
Ratio for legal expenses, UD[c]	1.0%		3.0%
Ratio for construction expense and contractor's fee, UD[c]	10.0%		20.0%
Ratio for contingency, UD[c]	5.0%		15.0%
Ratio for insurance, UD[c]	0.4%		1.0%
Ratio for working capital, UD[f]	10.0%		20.0%
Ratio for financing interest, UD[f]	6.0%		10.0%
Ratio for plant overhead costs, UD[g]	5.0%		15.0%
Ratio for patents and loyalties, UD[g]	0.0%		6.0%
Ratio for administrative costs, UD[g]	2.0%		5.0%
Ratio for marketing costs, UD[g]	2.0%		6.0%

RH = Resample historical data, TD = Triangular distribution, UD = Uniform distribution

[a] Based on available lab-scale data and estimates reported in the literature [154], [b] Notice that the nominal discount rate used for the conventional plants was 12.95% [138], [c] Based on fixed capital investment, [d] Based on purchased equipment cost, [e] Based on direct cost, [f] Based on total capital investment, [g] Based on total product cost.

8.4.2. Capital investment cost estimation under uncertainty: The CMR module case

A CMR module cost analysis in the presence of uncertainty is conducted with the integration of standard Monte Carlo simulation methods into the FCI/TCI model presented earlier. The cumulative probability distribution FCI and TCI profiles as well as the associated expected values for industrial scale CMR modules are presented in Figure 8.14. It is possible to observe that there is a 10% probability for the FCI to be lower than 225 M$ and a 90% probability for the TCI to be higher than 400 M$. The "value at risk" and the "value at opportunity" are quantified at pre-specified probabilistic levels of 95% and 5% (P_{95} and P_5) respectively. A threshold-value of P_{95} represents that there is a 5% probability of incurring a cost higher than this value, while there is a 5% probability of incurring a cost lower than a P_5 threshold-value. P_{95}, P_5, and expected values of FCI/TCI for the CMR module are summarized in Table 8.12.

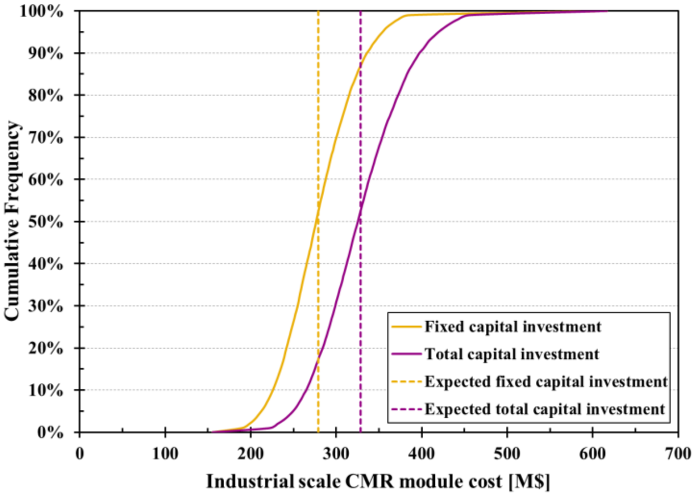

Figure 8.14. Cost distribution of an industrial scale CMR module.

Table 8.12. Industrial scale CMR module cost summary.

	Fixed capital investment		Total capital investment	
	[M$]	[$/m^2]	[M$]	[$/m^2]
P_{95}	354.3	20,275	419.7	24,018
Expected value	279.1	15,969	328.6	18,805
P_5	212.5	12,161	249.6	14,284

8.4.3. Economic Assessment of HP Technology Options

The technical performance of HP-CMR plants is first comparatively evaluated in terms of coal feed requirements and CO_2 production and emission levels against conventional HP plants that utilize PSA as a purification unit (HP-PSA plants). Pertinent results are graphically shown in Figure 8.15. Correspondingly, plant specifications and capital investment costs associated with all technology options considered in this study are tabulated in Table 8.13. These results show that the higher efficiency displayed by the HP-CMR plant reduces the coal feed requirements to achieve the same H_2 production levels by 16% compared to the conventional HP-PSA plants. The reduction in the coal feed requirements is attributed to process intensification-relevant benefits attributed to CMRs in which the WGS reaction and separation are simultaneously carried out. Furthermore, the lower CO_2 production level is directly reflected on the lower carbon feed requirements in the HP-CMR case, as shown in Figure 8.15. Please also notice that HP plants with integrated CCS systems lead to a substantial reduction of the amount of CO_2 emissions, but their degree of efficiency varies. The HP-PSA plant has an efficiency of 90% while the

HP-CMR plant displays an efficiency of 98%. Considering both the lower CO_2 production levels and the higher CO_2 capture efficiency achieved by the HP-CMR technology option, the HP-CMR plant emits 0.07 Mtonnes of CO_2 per Mtonnes of coal feed compared to a value of 0.23 for the conventional HP plant, leading to an overall reduction in CO_2 emissions of 70%. Other than higher levels of technical performance displayed by the HP-CMR plant, lower capital investment costs for the same H_2 production target level can be also achieved using the HP-CMR technology option as seen in Table 8.13. Notice that the benefits of the HP-CMR technology option lead to a reduction of the TCI costs for HP by 26%. Indeed, process intensification opportunities combined with the simultaneous CO_2 capture and extra purity H_2 production enabled by CMRs allow a significant reduction in the pertinent TCI costs by reducing the size of the process equipment needed and replacing the traditional WGS reactors, PSA as well as Selexol units.

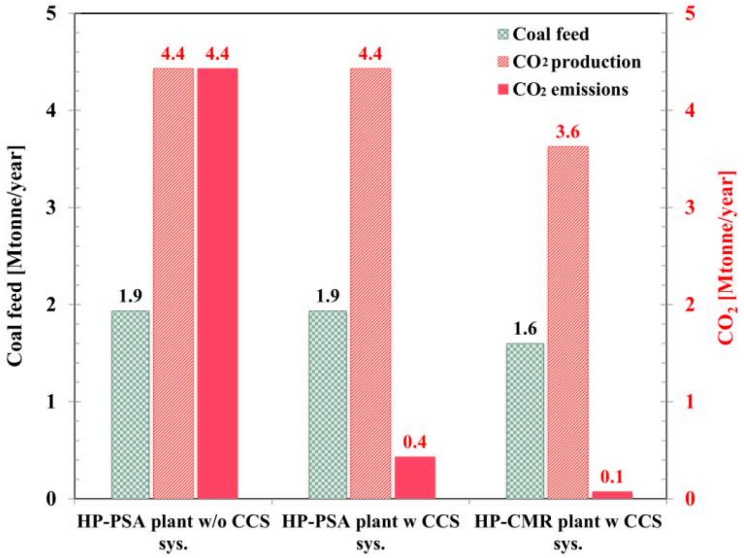

Figure 8.15. Coal feed, CO_2 production, and CO_2 emissions of hydrogen production plants for various technology options.

Table 8.13. Hydrogen production plant specifications and capital investment costs for various technology options.

	TCI [B$]	Plant size [TPD]	H_2 production [TPD]	Coal feed [TPD]	CO_2 production [TPD]	CO_2 captured [TPD]	CO_2 emissions [TPD]
HP-PSA plant w/o CCS sys.*	1.82	685	616.5	5,302	12,137	0	12,137
HP-PSA plant w CCS sys.*	2.14	685	616.5	5,302	12,137	10,954	1,183
HP-CMR plant w CCS sys.	1.58	685	616.5	4,384	9,936	9,737	199

TPD = Tonne Per Day

*For the pertinent data sources of the HP-PSA plants, please see DOE/NETL report [138]

Considering all uncertain model inputs, the economic performance of HP plants and range of potential outcomes are comparatively evaluated amongst the various technology options by conducting detailed simulation studies. As it will be demonstrated below, the inclusion of regulatory action on carbon has a significant effect on the NPV distribution profiles of all technology options considered in the present study, generating comparative economic performance advantages and noticeably promising prospects in the HP-CMR case. Indeed, it is shown that HP-CMR could become an economically appealing technology option under a certain set of regulatory conditions, thus deserving attention as a potentially meritorious option whose realization prospects of an initial fleet of demonstration plants at the commercial scale ought to be seriously considered.

The simulation results of NPV distribution profiles in the absence and presence of regulatory action on carbon are presented in Figure 8.16 (a) and (b), respectively. It should be pointed out that the initial CO_2 tax rate of \$30 per tonne of CO_2 considered represents a reasonable first estimate based on current market conditions and average "best" estimates provided by experts. Furthermore, \$30 per tonne of CO_2 indicates an initial tax level higher than the CO_2 abatement cost, thus providing an incentive for HP plant owners/operators to invest in CCS systems. At this point, it should be pointed out that a price on emissions (of any type) conforming to a simple stochastic model that makes use of an initial emissions price and an annual growth rate (such as the one presented) could have been considered within the context of the present research study. We chose the "carbon tax" term since such a type of emissions price is now widely acknowledged of generating the appropriate price signals that can be internalized by the pertinent markets in the most direct and seamless manner. In Figure 8.16 (a), notice that in the absence of CO_2 tax, the conventional HP-PSA plant without any CCS system installed has the most attractive NPV distribution profile, and therefore, the graphically depicted results naturally reproduce the current state of affairs in the field of hydrogen production. Moreover, it also confirms the fact that the capital investment and O&M costs associated with the installation and operation of a CCS system would result in less attractive economic outcome profiles in all cases in the absence of a CO_2 tax. However, under the conditions considered and in the presence of regulatory action on carbon the NPV distribution profile of HP-CMR emerges as a comparatively appealing one. Indeed, one observes that key performance assessment metrics deduced from the above NPV-distribution profiles such as ENPV, P_{95} and P_5 -threshold values ("value at opportunity", "value at risk") are improved compared to the ones associated with the NPV distribution profiles of the traditional technology option with CCS. This outcome can be jointly attributed to the fact that superior efficiency gains in the HP-CMR case coupled with higher regulatory cost savings (versus CCS-operating costs) realized when compared to the traditional option result in enhanced economic performance in an uncertain carbon-constrained world over the plant's lifetime. In light of these findings, a stronger justification basis could be built for the provision of the right incentives aiming at the realization of technology demonstration projects at the commercial scale for a technology option such as HP-CMR, thus supporting broader energy and environmental policy goals briefly presented in the Introduction section.

Finally, it would be worth noticing that the conventional HP-PSA plant without a CCS system appears to be the most sensitive to future regulatory action, while the HP-CMR plant appears to be less sensitive due to the fact that the degree of change of the NPV distribution profiles is mainly determined by the "carbon tax penalty" which is computed through the amount of CO_2 emissions and the CO_2 tax rate (thus allowing the HP-CMR plant to exhibit more appealing economic performance outcomes under the stated regulatory conditions).

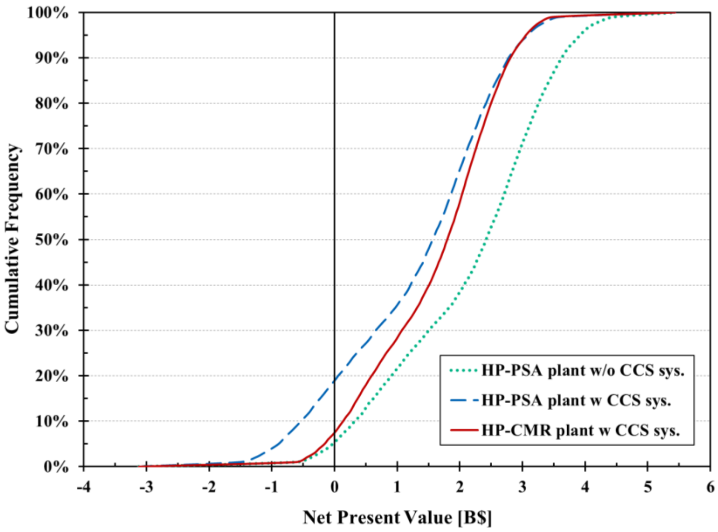

(a)

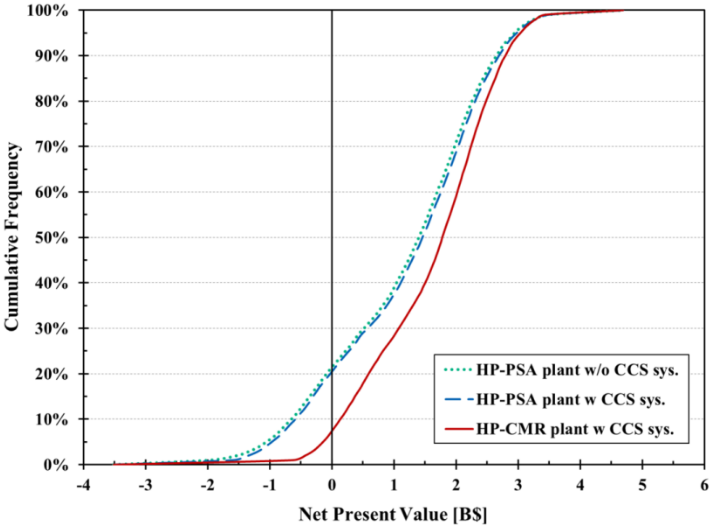

(b)

Figure 8.16. Cumulative probability distribution profiles of the Net Present Value for various technology options in (a) the absence of CO_2 tax and their ENPV rates with displayed rate changes and (b) under an initial tax rate of $30 per tonne of CO_2.

The effects of uncertainty on the expected NPV-value (ENPV) for the various technology options integrated with CCS systems are also analyzed through Tornado diagrams and presented in Figure 8.17. A Tornado diagram summarizes graphically the relative impact of variations of the numerous uncertain NPV-model inputs over their respective ranges (from the lowest to the highest value) under the assumption that all other model inputs remain at their baseline values (fixed at their expected values). In a Tornado diagram each model input is represented by a bar as it varies over its prescribed range depicting its impact on the above performance indexes, and all bars are sorted from the long ones at the top to the shorter ones at the bottom in a decreasing impact order. In this manner, a Tornado diagram prioritizes the most consequential inputs (sources of uncertainty) in terms of bar length and facilitates the visualization of their impact on economic performance, primarily in cases of large-scale multi-input models. Figure 8.17(a) and Figure 8.17 (b) provide representative ENPV-Tornado diagrams for the case of the traditional HP as well as the HP-CMR option. The uncertain model inputs considered and their respective prescribed ranges used include the following: Pd unit price: 16.9-25.9 \$/g, Au unit price: 39.4-53.7 \$/g, coal price: 61.0-48.5 \$/tonne, inflation rate: 1.46-3.16%, H_2 delivery cost: 3.0-4.4 \$/kg, Pd/Au membrane lifetime: 1-5 years, CO_2 transport & storage cost: 9-11 \$/tonne, annual growth rate of CO_2 tax: 5.4-6.6%, H_2 selling price: 9-11 \$/kg, combined state and local sales tax rates: 0-9.5%, financing interest to total capital investment ratio range: 6-10%, and plant overhead costs to total product cost ratio range: 5-15%. Please notice that hydrogen selling price, hydrogen delivery cost, plant overhead costs, financing interest costs, taxation levels and inflation rate constitute the set of model inputs with the highest impact on ENPV.

As shown in Figure 8.17, hydrogen selling price has the most significant impact on NPV in both cases, suggesting that economic performance of HP plants greatly depends on the revenue generated through hydrogen sales. Additionally, since the H_2 selling price is mainly determined by production costs, production cost disruption (referring to situations where production costs undergo significant departures from their expected values used to design the coordination scheme which aligns the plans and objectives of the project undertaken) can significantly influence the H_2 economy by shifting selling prices. However, in the short and medium term, production cost disruptions in the H_2 economy are unlikely to happen unless alternative energy prices become increasingly competitive, H_2 demand grows rapidly and/or a breakthrough in H_2 production technology occurs. Finally, when comparing the two cases, it is found that HP-PSA plants appear to be more sensitive to the selling price than HP-CMR plants, implying that the effect of the selling price on NPV-based performance evaluation is jointly determined by production costs and the nominal discount rate of the various HP options. H_2 delivery cost is another uncertainty driver that exerts a significant effect on the NPV of HP plants. The delivery cost is determined by the geographic and market characteristics, such as transport distance, delivery chain, density demand, etc. Yang and Ogden [61] reported that compressed gas truck delivery is ideal for small stations with low demand, while cryogenic liquid trucks of liquefied H_2 is preferred for long distances and robust, healthy demand patterns. Within such a context, any geographic and market characteristics should be considered and carefully evaluated for customization of H_2 delivery in order to enhance the economic performance of HP plants. Furthermore, it should be pointed out that considerably high costs for H_2 delivery would drive the ENPV value of HP-PSA plants to become negative, while HP-CMR plants can withstand the effect of delivery costs to maintain a positive ENPV due to their production cost.

The lifetime of Pd/Au membranes is an uncertain model input that affects the ENPV of HP-CMR plants. A long lifetime would reduce the total product cost by lowering the membrane replacement cost, thus increasing the plant's ENPV. Since the replacement cost is jointly determined by the membrane cost and lifetime, the effect of lifetime is also correlated with the Pd unit price as well as the membrane thickness. When the membrane cost is relative low by using thinner membranes, the impact of the membranes' lifetime on the ENPV could be higher than the Pd unit price (see Figure 8.17 (b)); in contrast, when the membrane cost dominates the membrane replacement cost in cases of thicker membranes use, the Pd unit price could have a greater effect on ENPV than membrane lifetime. It should be pointed out that currently the fabrication of thin membranes with high durability characteristics is attainable and has been demonstrated by Augustine et al. [154]. Moreover, lifetime extension can be also achieved by repairing defects on the membranes and/or through post-treatment for reactivation of contaminated membranes [155,156,157]. Given the current pace of advancements in membrane science and technology, it is reasonably expected that the effect of membrane lifetime could be further minimized in the future. Please notice that this feature was not included in the present evaluation framework.

Comparing the Tornado ENPV diagrams of the traditional HP-PSA plant to an HP-CMR plant, one infers that the HP-PSA plant appears to be more sensitive to financing interest costs, while HP-CMR plants appear to be more susceptible to combined state and local sales tax rates. Please notice that federal corporate tax rates, as mentioned before, depend on the reportable income and therefore are not shown as uncertainty drivers in the Tornado diagrams; however, they are expected to have a high impact on the ENPV of the plants. Indeed, higher capital investment costs for HP-PSA plants (Table 8.13) generate higher financing interest costs. In contrast relatively lower capital investment costs for HP-CMR plants could mitigate the effect of corresponding financing interest costs on ENPV. Please also notice that combined with a relatively low total product cost, tax rates become critical in the calculation of net cash flows. As a result, tax rates can have a more substantial impact on the ENPV than financing interest costs under low capital investment and total product costs. Focusing on the effect of taxation levels, tax incentives have been occasionally introduced by states to influence business relocation, expansion, or start-up formation-relevant decision-making [158]. However, tax incentives in isolation could not determine “optimal” technology choices and plant locations since they do not represent the only criterion in an inherently complex decision-making process (other factors include developments in hydrogen markets and distribution challenges, macroeconomic conditions, state of regulatory framework and geopolitical stability).

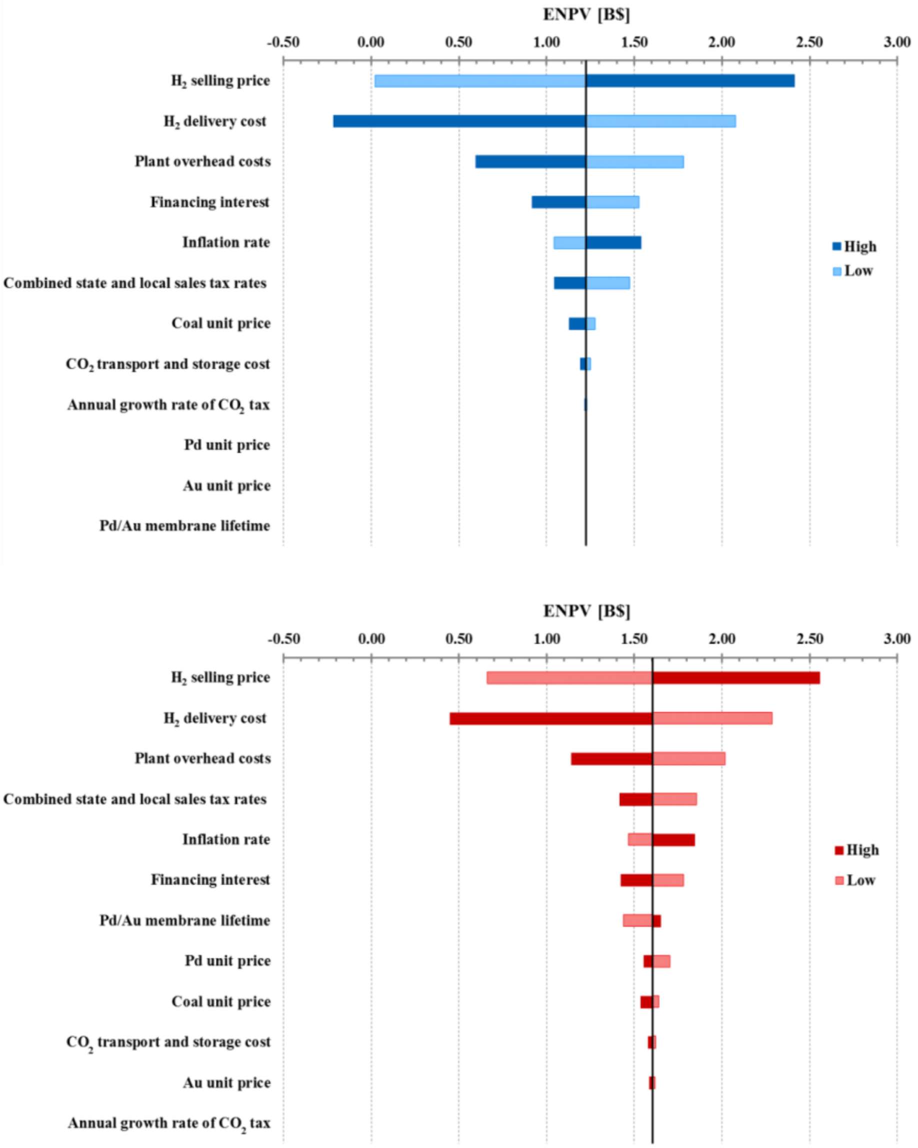

(a)

(b)

Figure 8.17. Tornado diagrams for the NPV of various technology options in the presence of CO_2 tax for (a) HP-PSA plant w CCS sys. (b) HP-CMR plant w CCS sys.

The effect of regulatory action (with an initial CO_2 tax rate starting on 2015) on ENPV is further examined in the following three technology option cases: i) Case A refers to an HP-PSA plant without any CCS system installed; ii) Case B corresponds to an HP-PSA plant with a CCS system installed, and iii) Case C corresponds to an HP-CMR plant with a CCS system installed. The ENPV in the three cases considered is computed and tabulated at different initial CO_2 tax rates as shown in Table 8.14. From this table, it can be inferred that the ENPV of conventional HP plants without CCS varies significantly as the initial CO_2 tax rate increases, becoming economically problematic when the rate reaches $65 per tonne of CO_2 and the associated regulatory compliance costs become quite significant. However, conventional HP plants with CCS systems do not display negative ENPVs within the range of CO_2 tax rates considered since the regulatory compliance cost savings exceed the costs associated with the operation of the CCS system.

The technology options considered were then evaluated under a set of different tax rates in order to visualize their impact on the associated ENPVs as shown in Table 8.15. First an economic performance comparison involving Cases A and B was performed and labeled as the "Traditional technology option." This case demonstrates the economic effect of having a CCS system installed in a traditional HP plant under future regulatory action on CO_2 emissions. As shown in Table 8.15, the ENPV difference favors the use of CCS systems when the tax rate is higher than $25 per tonne of CO_2. Lower tax rates do not seem to incentivize the integration of CO_2 capture technologies in HP plants. Similar conclusions have been previously drawn and discussed in the context of coal-fired power plants with CCS units installed [159,160].

The second economic comparison, performed in this study, was between Case C and A, which was labeled as "Membrane technology option." This option shows the economic effect of integrating membrane technology into HP plants in the presence of future CO_2 emission regulations. Based on the proposed NPV-based assessment framework, the analysis indicates that Case C, i.e. the HP-CMR option becomes comparatively economically appealing when the regulatory tax rate reaches $15/tonne of CO_2. Therefore, it is possible to conclude that, depending on the course of action of future regulatory policies on carbon, there is a window of opportunity for HP-CMR to be perceived as an economically robust, if not superior, competitor to the incumbent technology option exhibiting also enhanced environmental performance in a carbon-constrained world. However, in the absence of regulatory action, the conventional HP options would remain uncontested when economic metrics dominate decision making in selecting the best technology options. It would be also worth noting that the HP-CMR option, when compared to the traditional HP with CCS, attains a positive ENPV at lower regulatory tax rates.

Table 8.14. ENPV performance (B$) of technology options under various CO_2 tax scenarios.

Case	Case Explanation	Initial CO_2 tax rate [$/tonne CO_2]														
		0	5	10	15	20	25	30	35	40	45	50	55	60	65	70
Case A	HP-PSA plant w/o CCS sys.	2.17	2.01	1.84	1.67	1.50	1.34	1.16	0.99	0.81	0.63	0.45	0.26	0.07	-0.13	-0.33
Case B	HP-PSA plant w CCS sys.	1.32	1.31	1.29	1.27	1.26	1.24	1.23	1.21	1.19	1.18	1.16	1.14	1.13	1.11	1.09
Case C	HP-CMR plant w CCS sys.	1.62	1.61	1.61	1.61	1.61	1.61	1.60	1.60	1.60	1.60	1.60	1.59	1.59	1.59	1.59

Table 8.15. ENPV difference (B$) between two technology options under various CO_2 tax scenarios.

ENPV difference	Initial CO_2 tax rate [$/tonne CO_2]														
	0	5	10	15	20	25	30	35	40	45	50	55	60	65	70
Traditional technology option (Case B – Case A)	-0.85	-0.70	-0.55	-0.40	-0.25	-0.09	0.06	0.22	0.38	0.54	0.71	0.88	1.06	1.24	1.43
Membrane technology option (Case C – Case A)	-0.56	-0.39	-0.23	-0.06	0.10	0.27	0.44	0.61	0.79	0.96	1.15	1.33	1.52	1.72	1.92

The rate under which the ENPV changes as a function of the initial carbon tax (shown in Equation 8.1) is considered in all cases as a measure of sensitivity or robustness of economic performance to future regulatory action on CO_2 emissions

$$r = -\frac{\Delta\, ENPV}{\Delta\, Initial\ CO_2\ tax\ rate} \tag{8.1}$$

Notice that the above ratio captures the degree of sensitivity of economic performance of an HP-relevant technology option (when evaluated through the ENPV-metric) with respect to a future carbon price. The calculated values of the rate *r* are: 0.035, 0.003 and 0.0004 [B$] per $/tonne of CO_2 for cases A, B and C, respectively. In Figure 8.18, NPV distribution profiles for all HP technology options considered are depicted in the absence of any regulatory action along with their respective rates. Furthermore, since the magnitude of the rate *r* is smaller in the HP-CMR case than in the traditional HP (Cases A and B), the NPV-profile of the HP-CMR finds itself located to the right of the NPV-profiles of Cases A and B (as also previously depicted in Figure 8.16(b) under an initial CO_2 tax rate of $30 per tonne CO_2), thus starting to become comparatively more appealing under regulatory taxes greater than $15/tonne of CO_2. It is important to mention that the NPV profile of the HP-CMR plants undergoes a smaller shift compared to the traditional technology option in response to the introduction of a carbon tax, thus demonstrating the relative robustness of its economic performance under regulatory uncertainties. Please notice that the arrows shown in Figure 8.18 represent the rate under which the NPV-curve of each technology option is displaced towards less attractive valuation zones when a carbon price is imposed.

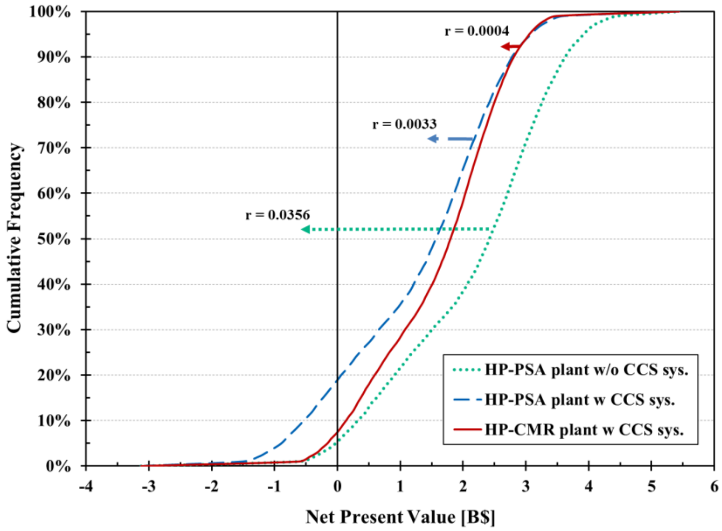

Figure 8.18. Net present value cumulative probability distribution profiles for various technology options in the absence of CO_2 tax and their ENPV rates.

8.4.3 The role of discount-rate in the valuation of HP-CMRs: Sensitivity analysis

The discount rate at which future cash flows are discounted represents a key determinant of any technology investment project valuation approach, particularly in cases involving capital intensive projects where their respective NPV distribution profiles depend crucially on the choice of the discount rate. It should be pointed out that the aforementioned discount rate depends essentially on two factors: (i) the perceived risk of the specific project (ii) as well as its financing mechanism [133,136,161]. Indeed, investment in advanced energy-relevant technology projects encompasses a diverse set of risks such as: macro-economic ones related to global economic growth and demand for hydrogen as well as availability of labor and capital, regulatory risks, technology reliability risks, price and volume risks in the hydrogen markets and fuel price (coal, natural gas) risks. Please notice that these project risks could affect different technology options in different ways. Focusing solely on capturing project risk, 100% equity financing is usually assumed, and the most common practice is to add a project specific risk premium to the risk free rate of return when estimating the discount rate (the risk free rate of return is generally determined by the long-term rates of return of government bonds in the United States) [133,136,161]. It should be pointed out that the estimation of the risk premium could become quite complex. If the risk of the project under consideration is similar to other ones undertaken by the firm, and if the firm's common stock is traded on open markets then in principle the risk premium can be estimated using published historical stock price data [133,136,161]. As mentioned earlier, the nominal discount rate used by the DOE for evaluating investments in conventional hydrogen production is 12.95% [138]. When the financing structure of the project is also taken into account, the risk-adjusted nominal discount rate is a weighted average of the cost of funds obtained from shareholders ("cost of equity") and borrowed from debt-holders ("cost of debt") with relative amounts of equity and debt being the respective weights (known as the Weighted Average Cost of Capital) [133,136,161]. In competitive hydrogen markets, what matters to the investor is the profitability of the investment against the risk to the capital employed. In particular, the level of risk anticipated by an investor in a hydrogen production plant will be reflected on the level of return expected on that investment. Moreover, the greater the business and financial risks, the higher the overall return that will be demanded. Since it is quite difficult for the traditional levelized cost-based methodology to incorporate risks and uncertainty effectively, the proposed approach using a detailed NPV model coupled with a Monte Carlo simulator represents a methodologically appropriate and sound approach to effectively cope with multiple risk and uncertainty sources by generating a range of economic performance assessment outcomes for a new technology option such as HP-CMR [133,136,161]. Within the above context, we complemented the valuation assessment with a sensitivity analysis conducted for different representative values of the discount rate that span a reasonable range (between 10 and 20% in nominal terms) associated with business and financing risks. Lower values of the discount rate could correspond to a more stable environment of the producing firm (low macro-economic risks, acceptable technology reliability levels, an available captive market and long-term contracts, availability of capital, low financing risks) whereas higher values of the discount rate could correspond to conditions of elevated risks in the firm's (macroeconomic, operating, financing, market) environment. The simulation results derived are tabulated in Table 8.16. Please notice the expected adverse impact of a higher discount rate on the economic performance and valuation profile of HP-CMR reflected on all indicators: a deteriorating ENPV, an increasing probability of loss, a decreasing range of upside opportunities and a deteriorating "value at risk" pattern (downside risk). It becomes therefore apparent that creatively structured financing mechanisms leading to a reduction of the cost of capital/discount rate could induce more appealing economic performance outcomes and valuation profiles, thus unlocking the investment potential of a clean hydrogen production project that utilizes the HP-CMR technology option.

Table 8.16. Sensitivity analysis results of the NPV-based economic performance assessment for HP-CMR plants with various discount rates.

	Discount rate [%]										
	10	11	12	13	14	15	16	17	18	19	20
P_5 [B$]	0.73	0.52	0.35	0.21	0.08	-0.04	-0.14	-0.24	-0.31	-0.38	-0.46
ENPV [B$]	3.56	3.11	2.72	2.39	2.10	1.84	1.60	1.42	1.24	1.08	0.94
P_{95} [B$]	5.87	5.22	4.64	4.16	3.75	3.35	3.04	2.77	2.51	2.27	2.06
Standard deviation [B$]	1.61	1.47	1.35	1.24	1.15	1.07	1.00	0.94	0.88	0.83	0.79
Probability of loss	2%	2%	3%	4%	5%	6%	8%	10%	12%	14%	17%

8.5. Membrane Technology Embedded into IGCC Plants with CO_2 Capture

The economic performance assessment framework has been developed for membrane reactor modules embedded into Integrated Gasification Combined Cycle (IGCC) power plants with CO_2 capture (IGCC-MR). A functional Net Present Value (NPV) model has been developed first to evaluate the economic viability of IGCC-MR plants. The project value of IGCC-MR is compared to other competing technology options such as Supercritical Pulverized Coal-fired and traditional IGCC power plants with and without CO_2 capture. As in previous sections, sources of irreducible uncertainty as well as technology risks are explicitly recognized and the effect of these uncertainty drivers on the plant's/project's value is taken into account using Monte-Carlo techniques. Therefore, more realistic distribution profiles of the plant's economic performance outcomes are generated rather than single-point value estimates. It is shown that future regulatory action on CO_2 emissions could induce appealing NPV-distribution profiles for IGCC-MR in the presence of uncertainty and technology risks. Finally, a creatively structured portfolio of technology-push and/or market-pull policy incentives could lead to more attractive profiles, suggesting possible means for accelerating the realization of demonstration projects.

Description

8.5.1. Integration of Pd/Au-based membrane reactors into IGCC plants

The integration and structural configuration of membrane reactor modules into coal-fired power plants has to be performed in a way that ensures maximum net plant efficiency. It should be also pointed out that the specific type of sulfur, nitrogen oxides, particulate matter and mercury removal system represents one of the determinants of net plant efficiency for membrane reactor modules integrated into IGCC plants. Even though the utilization of hot gas desulfurization and removal of trace metal contaminants at elevated temperatures [162,163] has the potential to decrease the waste heat, operating experience associated with such pollution/emission control systems remains limited. Conventional gas cleaning systems such as the combination of Selective Catalytic Reaction (SCR), fabric filters and Flue Gas Desulfurization (FGD) or Selexol units are considered in this study because ofthe sufficient technical information provided, particularly by the US Department of Energy [145]. Furthermore, due to the specific operating requirements of the gasification system used when Pd-based membrane reactor technology is integrated into IGCC plants, the GE Energy (GEE) gasifier is considered in the present study. The flow diagram of the IGCC plant with CO_2 capture and conventional packed bed reactors (IGCC-PBR) reported in [145] is structurally compared with the flow diagram of IGCC-MR. The two detailed block flow diagrams are shown in Figure 8.19 and Figure 8.20 respectively. Notice that reaction and separation take place simultaneously in the membrane reactor module, and therefore, both the high and low temperature shift reactors as well as the Selexol unit used for H_2 separation in the conventional IGCC can now be removed from the corresponding flow diagram. Furthermore, notice that the membrane reactor module is located after the gas clean-up equipment in order to prevent membrane poisoning by the sulfur potentially present in the syngas. Within the IGCC-MR context the separation quality of hydrogen from CO_2 is of paramount importance, and the presence of a Pd-based membrane with high selectivity would produce extra purity H_2 (99.9999%). In contrast, the utilization of Pd-based membranes exhibiting leaks and thus low selectivity values could result in the attainment of lower purity H_2 levels (94%) could still be used to generate electricity whereas extra purity H_2 (99.9999%) could be sold for other purposes such as de-hydrogenation/hydrogenation. In the present study, all of the separated H_2 exiting the membrane reactor module is used solely for electricity generation purposes in order to facilitate a fair comparative economic performance assessment of IGCC-MR with other traditional and currently available technology diagrams are shown in Figure 8.19 and Figure 8.20, respectively.

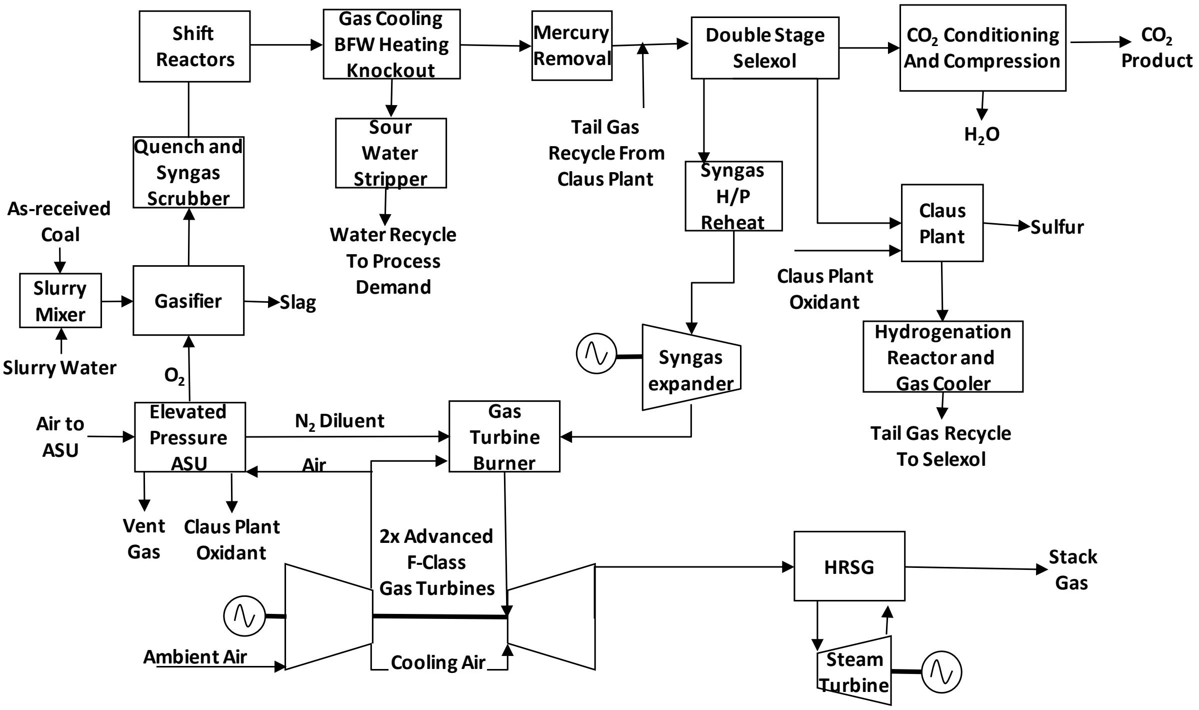

Figure 8.19. Schematic block flow diagram of the GEE IGCC with CO_2 capture using conventional packed bed reactors [145].

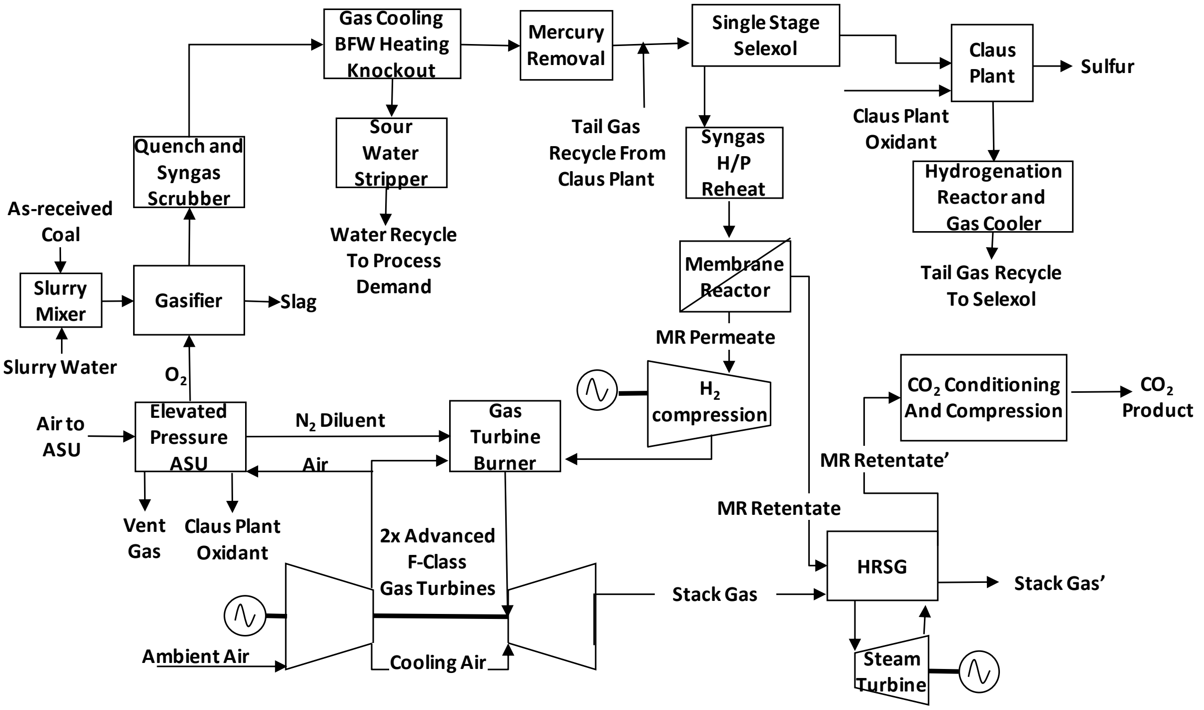

Figure 8.20 Schematic block flow diagram of the GEE IGCC with CO_2 capture using Pd-based membrane reactors.

Table 8.17. Probability distributions associated with the various uncertain model inputs.

Parameter↓	Distribution		
	Minimum	**Most Likely**	**Maximum**
CO_2 tax (\$/ t CO_2), TD	0	25	75
CO_2 tax growth rate, TD	0	3	8
Nominal discount rate, TD	6	7	9
For IGCC-MR	6	8	9
For SCPC without CO_2 capture		6-fixed	
Plant capacity factor [%], TD	70	80	85
For IGCC-MR	65	70	80
For SCPC without CO_2 capture		85-fixed	
Inflation rate [%], RH	1979-2011 Historical data, U.S. Dept. of Lab. [2012]		
Electricity selling price [cents/kWh], RH	1979-2011 Historical data, U.S. Energy Inf. Adm.		
Pd price [\$/g], RH	1979-2011 Historical data, www.kitco.com		
Au price[\$/g], RH	1979-2011 Historical data, www.kitco.com		
Support price [\$/cm^2 for lab scale], TD	2.3	5	7.5
Membrane life time [years], TD	1	3	5
H_2 selling price [\$/kg]	1.1	1.6	2.3

*TD: triangular distribution, RH: resample historical data

8.5.2. Membrane reactor module cost

A cost analysis encompassing manufacturing and capital investment costs as well as general expenses for the industrial scale membrane reactor module of interest was first conducted and all pertinent details can be found in Table 8.18 and Table 8.19, respectively. A relatively thick Pd/Au layer of 7.4 μm was used in the above calculations, even though further cost reduction would be possible by decreasing the layer thickness. If the support cost of the membrane reactor module does not follow the six-tenths-factor rule [139], the support cost figure in Table 8.18 would be the numerically dominant contributor to capital investment cost. In addition, the PSS support considered in the present study represents an inexpensive option whereas an Inconel support would be more expensive than the 316L PSS supports. Since key components of fixed-capital investment (pertaining for example to installation and engineering & supervision) depend on equipment cost, the fixed-capital investment of the membrane reactor module increases proportionally with the membrane bundle equipment cost. Furthermore, the variable operating costs of IGCC-MR considered in this study include membrane replacement costs calculated by dividing the membrane bundle equipment cost by the membrane life-time (i.e. US M\$ 22.5/3 years). The Pd/alloy based membrane reactors have to be tested under actual reaction conditions within a long-term horizon to determine the membrane lifetime and, evidently a higher membrane lifetime would lead to a reduction in replacement costs. Finally, please notice that neither Pd recovery nor membrane reactor leasing were considered in the present study; however these options would almost surely generate additional economic benefits. The target cost of the membrane module was set at 1000 US\$/ft^2 for 2010 (1500 US\$/ft^2 for 2006 status, <500 US\$/ft^2 for 2015) by the US Department of Energy (US/DOE; Fuel Cell Technologies Program, 2011). The cost figures for the water gas shift membrane reactor were summarized in Table 8.20. It is important to note that the US Department of Energy cost targets were specified for H_2 usage in fuel cells. Even though the cost figures listed in Table 8.20 were derived for an industrial scale water gas shift Pd/Au-based membrane reactor, they were still competitive in relation to the high standards associated with the US-DOE target levels

8.5.3. Plant costs and operating and maintenance costs

The total plant costs and also operating and maintenance (O&M) costs for six different plants listed below were estimated by using the data provided by the DOE/NETL report [145]. The net energy output of all plants was fixed at 550 MWe. Cases without CO_2 capture unit/equipment:

1. IGCC baseline
2. IGCC-MR without CO_2 compression/transport/sequestration
3. SCPC Cases with CO_2 capture unit/equipment:
4. IGCC-PBR (with traditional packed bed reactors)
5. IGCC-MR
6. SCPC with CO_2 capture

The plant cost of the IGCC-MR was determined by using the IGCC baseline cost figures. Notice that there is no COS hydrolysis unit in the IGCC-MR case. Furthermore, the IGCC-MR option considered encompasses a CO_2 compression system and a bigger size Heat Recovery Steam Generator (HRSG). Therefore, the corresponding cost differences from the IGCC baseline case were taken into account in the development of the corresponding IGCC-MR cost figures and indexes. Finally, the cost of the entire membrane reactor module listed in Table 8.19 has been included into the total plant cost. The annual operating labor costs associated with the operation and maintenance of the membrane reactor module were added to the O&M costs of the IGCC-MR plant. In the calculation of the operating labor cost figures for the membrane reactor module one assumes 55 employee hours/day/processing step, where two major steps are involved in the membrane reactor case under consideration, namely heat transfer and reaction/separation [139]. A product capacity of 718 tons H_2 per day was used by assuming 80% plant capacity for the IGCC-MR plant. The hourly labor rate of 24$/h (US/DOL, 2012) was used in the calculations and the resulting annual labor cost was approximately US M$0.7. Furthermore, the variable O&M cost component includes membrane replacement costs. The auxiliary power load needed in the IGCC-MR case was determined by including the energy requirements related to reheating the feed steam for the membrane reactor, cooling the retentate stream before CO_2 compression, the H_2 compression of the module's permeate stream before the gas turbine and finally CO_2 compression.

Table 8.18. Estimation of capital investment cost for the membrane reactor module (550MWe-plant).

I. Direct Costs				
A. Equipment + installation + instrumentation + piping + electrical + insulation + painting				
1. Purchased equipment	Reactor	HTS catalyst	Pd Membrane	
	$28,758.4	$1,756,783.8	Pd Cost	$17,346,343.1
			Au Cost	$3,622,542.1
			Support [316L SS]	$3,094,501.4
			Total	$24,063,386.6
Total membrane module	$25,848,928.8			
2. Installation (%40 of A1.)	$10,339,571.5			
3. Instrumentation and controls, installed (%18 of A1.)	$4,652,807.2			
4. Piping installed (%45 of A1.)	$11,632,017.9			
5. Electrical, installed (%25 of A1.)	$6,462,232.2			
Equipment total	$58,935,557.6			
B. Buildings, process and auxilary (20% of A1)	$5,169,785.75			
C. Service facilities and yard improvements (40% of A1)	$10,339,571.51			
D. Land (4% of A1)	$1,033,957.15			
Sub-total	$75,478,872.02			
II. Indirect Costs				
A. Engineering and supervision (%17.5 of direct cost)	$13,208,802.6			
B. Construction expense and supervision (18% of direct cost)	$13,586,197.0			
C. Contingency (%10 of Fixed-capital investment)	$11,363,763.5			
Sub-total	$38,158,763.1			
III. Fixed-capital investment = direct + indirect costs	$113,637,635.1			
IV. Working capital (15% of V)	$20,053,700.3			
V. Total capital investment = III + IV	$133,691,335.4			

Table 8.19. Estimation of total product cost for the membrane reactor module (550MWe-plant).

I. Manufacturing cost = direct production cost + fixed charges		
A. Direct production costs		
1. Raw materials (30% of total product cost)		$86,772,567.99
2. Operating labor (15% of total product cost)		$43,386,283.99
3. Direct supervisory and clerical labor (17.5% of operating labor)		$7,592,599.70
4. Utilities (15% of total product cost)		$43,386,283.99
5. Maintenance (6% fixed-capital in.)		$6,818,258.11
6. Operating supplies (0.75% of fixed-capital in.)		$852,282.26
7. Laboratory charges (15% of operating labor)		$6,507,942.60
8. Patents and loyalties (3% of total product cost)		$8,677,256.80
	Sub-total	$203,993,475.44
B. Fixed charges		
1. Depriciation (assumed 10% of fixed-capital in.)		$11,363,763.51
2. Local taxes (4% of fixed-capital in.)		$4,545,505.40
3. Insurance (0.7% of fixed-capital in.)		$795,463.45
Subtotal		$16,704,732.36
II. General expenses = administrative + distribution & selling + R&D costs		
A. Administrative costs (4% of total product cost)		$11,569,675.73
B. Distribution & selling costs (11% of total product cost)		$31,816,608.26
C. R&D costs (5% total product cost)		$14,462,094.66
D. Financing (interest - 8% of total capital investment)		$10,695,306.83
	Subtotal	$68,543,685.49
III. Total product cost		
Membrane replacement		$8,616,309.59
Manufacturing cost + general expenses		$289,241,893.29
	Total	$297,858,202.88

Table 8.20. Membrane reactor module cost summary.

	w CO_2 capture	w/o CO_2 capture
Fixed-capital investment [\$/m^2] ([\$/ft^2])	7585 (705)	7617 (708)
Total capital investment [\$/m^2] ([\$/ft^2])	8919 (829)	8962 (833)
Total product cost [\$/m^2] ([\$/ft^2])	19311 (1795)	19387 (1802)

The power requirements for the H_2 compression were calculated by assuming a multi-stage intercooled compressor (7 stages, cooling down to 196◦C which was the inlet temperature of the gas turbine). The energy requirements and gains for the heating and cooling steps were determined by assuming 40% efficiency to convert thermal energy to electric power, and vice versa. The O&M costs and the plant costs for the six cases listed above are shown in Figure 8.21(a). The plant capacity factor (CF) for SCPC was assumed to be 85% whereas the rest of technology options shown in Figure 8.21 assumed to exhibit an 80% CF due to higher inherent technology risks. It is also not surprising that the O&M costs for an SCPC plant(without CO_2 capture) are typically the lowest [164]. As it is also expected, O&M costs in the IGCC-MR, IGCC-PBR and SCPC with CO_2 capture cases were higher than in cases where CO_2 capture units/equipment are not integrated into the respective plants. Higher O&M costs in the presence of CO_2 capture units installed can be primarily attributed to the significant energy and material requirements needed for a well-functioning CO_2 compression unit. The use of a less efficient CO_2 removal system (such as Econamine with 90% CO_2 recovery) combined with the operating pressure in a traditional SCPC plant result in higher O&M costs. The Selexol system used in the IGCC-PBR case is typically more efficient (92% CO_2 recovery) than the Econamine system for CO_2 removal. However, additional costs related to the packed bed reactor operation as well as inherent technology differences between IGCC (gasification) and SCPC (boiler) cause the O&M costs in the IGCC-PBR case to be higher than the ones in the SCPC with CO_2 capture case. The IGCC-MR option had the highest O&M costs as shown in Figure 8.21. It can be inferred, that the most important components/contributors to the O&M costs in the IGCC-MR case were the additional costs associated with scheduled membrane replacement and also labor costs associated with the operation of the membrane reactor module.

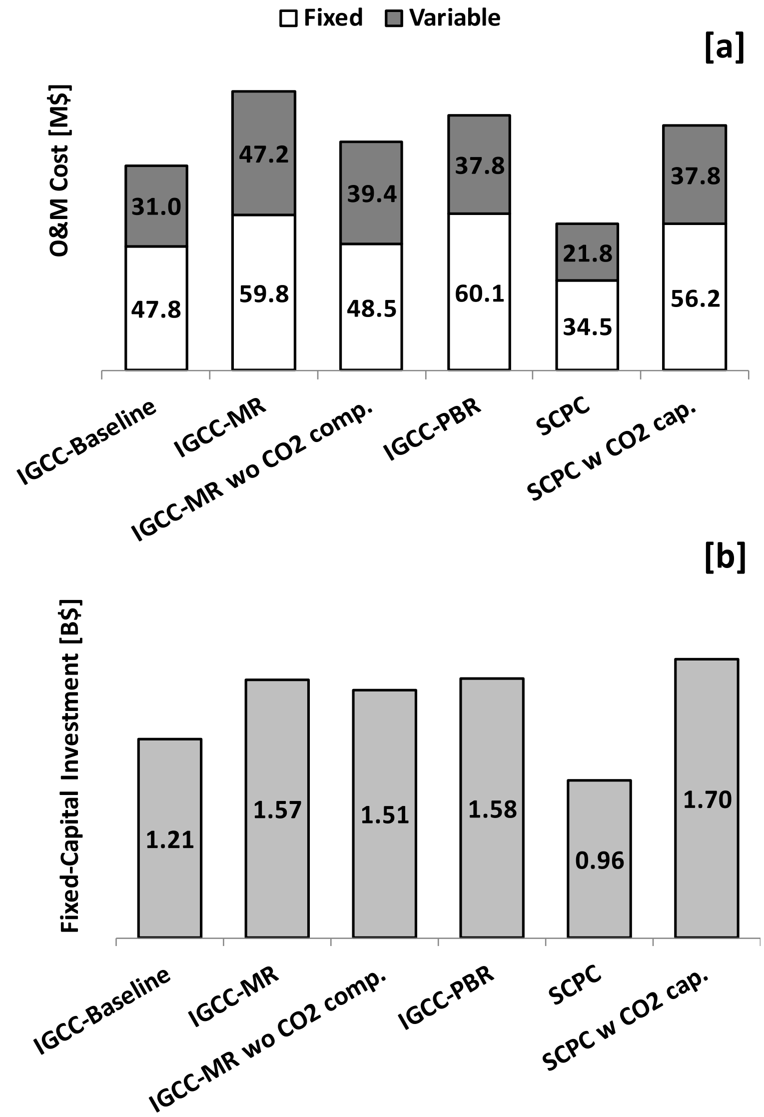

Figure 8.21. [a] O&M and [b] Plant costs for the listed coal-fired power plants.

The plant costs in the IGCC baseline and SCPC without CO_2 capture cases were the lowest as shown in Figure 8.21(b)(as expected) due to the smaller size plants, the reduced coal feed requirements listed in Table 8.21, as well as the absence of any additional units for CO_2 capture/compression. In contrast, the SCPC with CO_2 capture case had the highest total plant cost because of the large plant size and the presence of costly CO_2 removal/compression units. The removal and compression unit costs in the SCPC with CO_2 capture case represent a substantial portion of the total plant cost: 29%. Moreover, the required coal feed in the SCPC with CO_2 capture case was the highest of all as listed in Table 8.21 to compensate for the higher energy needs associated with the CO_2 removal and compression tasks. The total plant cost in the IGCC-MR and IGCC-PBR cases were quite similar (the IGCC-MR case exhibiting a slightly lower cost value). The energy requirement for isothermal H_2 compression before directing the H_2 flow to the gas turbine represented 40% of the total auxiliary power requirement. Innovative membrane reactor design options would be essential at this point to reduce the total H_2 compression costs, such as membrane reactor modules in series: one operating at a higher permeate side pressure and the next one at a lower permeate side pressure to remove as much H_2 as possible. If the H_2 compression costs could be reduced, the size of the IGCC-MR could be smaller while attaining the same level of net power output. Another parameter worth mentioning is the amount of CO_2 product listed in Table 8.21. The extents of CO_2 product for all the above cases except for the IGCC-MR one were adopted from [145]. The total CO_2 product for the IGCC-MR was determined based on the retentate composition of the membrane reactor which was calculated with the aid of the reactor model. It should be pointed out that the differences in the extent of the CO_2 product could vary due to the type of gasifier and also the amount and type of coal feed.

Table 8.21. Coal feed and CO_2 product levels.

Power Plant Type	Coal Feed [Mtonne/year]	Captured CO_2 [Mtonne/year]	Released CO_2 [Mtonne/year]
SCPC	1.4	0.0	3.3
SCPC w CO_2 Capture	1.8	3.8	0.4
IGCC/PBR w CO_2 capture	1.6	4.1	0.4
IGCC-MR w/o CO_2 comp.	1.5	0.0	4.3
IGCC-MR	1.7	4.7	0.1
IGCC Baseline	1.3	0	3.0

8.5.4. NPV-based economic assessment in the absence of uncertainty

In the present research study, a carbon charge in the form of a direct tax is considered as a CO_2 emission control mechanism. Within such a context, both the level and timing of the aforementioned carbon charge/tax do matter in the comparative economic performance assessment of the technology options considered. In particular, it is assumed that regulatory action on carbon in the form of a direct tax is introduced in the year 2015. A standard sensitivity analysis with respect to the initial CO_2 tax level was performed to evaluate its impact on the NPV estimates of all six power plant options considered. The single point projected NPV results presented in Figure 8.22 were all based on current market conditions and average figures/best guesses for all pertinent NPV model inputs in the absence of uncertainty.

For the zero CO_2 tax scenario (absence of any regulatory action on carbon), one easily concludes by a simple inspection of Figure 8.22(a) that the SCPC without CO_2 capture option is undoubtedly the preferred one. Even though all of the plant options had the same net power output of 550 MWe and the same stream revenues, the resulting NPV values in the IGCC baseline and IGCC-MR cases were lower than in the SCPC one due to higher plant and O&M costs (Figure 8.22). However, it should be pointed out that the IGCC-MR option could become competitive when compared to SCPC without CO_2 capture if the net plant efficiency were increased from 40% to 60% due to anticipated future technological advancements coupled with the possibility of an additional stream of revenues coming from selling the high-purity hydrogen that is co-produced (sales of which are not considered in this study). As shown in Figure 8.22, SCPC without CO_2 capture remains the potentially most profitable and attractive option as long as the initial CO_2 tax stays below the value of 30 \$/tons CO_2. Consequently, SCPC plants could still be operated by just paying the requisite emission taxes without capturing the CO_2 product if these taxes stay below the 30 \$/tons CO_2 figure (with 3% growth rate). However, for initial CO_2 tax levels higher than 30 \$/tons CO_2, the IGCC-MR starts emerging as an attractive option with a good investment potential as evidenced in Figure 8.22(d). Finally, within the range of CO_2 tax levels shown in Figure 8.22(b)-(d), the IGCCMR plant appears to be the least affected by the increased CO_2 taxes mainly because of the attainment of higher CO_2 recovery levels. In addition, negative NPV values in the baseline IGCC plant case for initial CO_2 taxes higher than 15 \$/tons CO_2 suggest that the baseline IGCC could not compete with SCPC if CO_2 capture were not pursued.

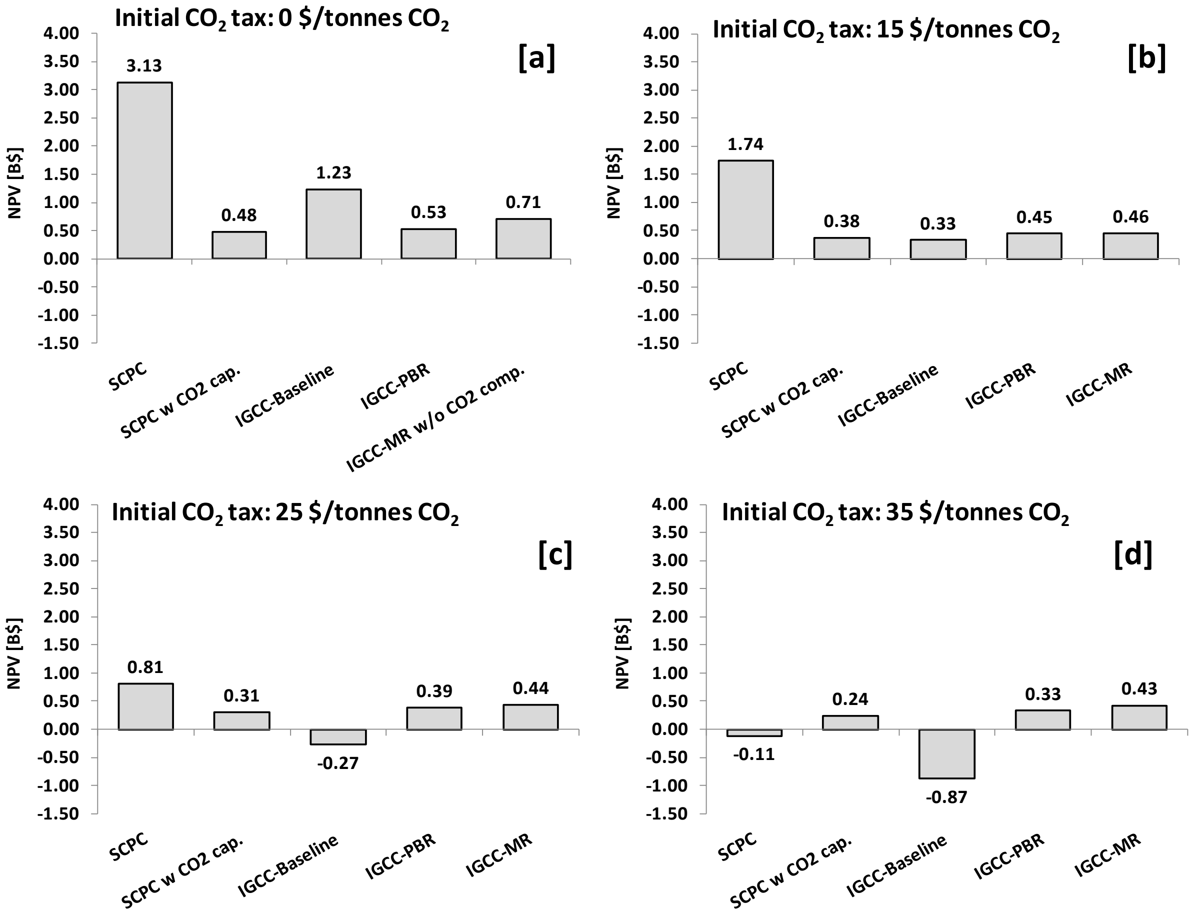

Figure 8.22. Sensitivity analysis on initial CO_2 tax.

8.5.5. Economic assessment in the presence of uncertainty: membrane reactor module cost

The NPV-modeling framework with the integrated Monte Carlo simulator was first employed in order to conduct a membrane reactor module cost analysis in the presence of uncertainty. Specifically, Pd, Au, and membrane support prices as well as membrane life time were the uncertain drivers (model inputs) considered of the fixed-capital, total capital (fixed-capital + working capital) as well as total product costs with manufacturing cost and general expenses included. The probability distribution profile of the membrane reactor module cost is shown in Figure 8.23. In addition to the module cost distribution profiles, the average cost value, maximum and minimum cost figures of all economic performance outcomes generated through the Monte Carlo simulator are listed in Table 8.22. The upper right zone of Figure 8.23 is the "risk zone" corresponding to higher Pd, Au and membrane support prices as well as shorter membrane lifetime. Furthermore, the lower left zone of Figure 8.23 is the "reward zone" corresponding to lower Pd, Au, support prices and longer membrane lifetime. The average value of the total product cost for the membrane reactor module was determined at 1464 US$/ft^2 which exceeds the target value of the DOE for 2010. As mentioned earlier, the DOE targets were introduced with fuel cell grade H_2 production in mind, and therefore, costs related to the water-gas shift reaction that takes place in the IGCC-MR context were not included. In light of this remark, the total product cost of 1464 US$/ft^2 for the water-gas shift membrane reactor module under consideration is deemed quite satisfactory. Moreover, the fixed-capital and total capital cost of the membrane reactor module listed in Table 8.22 could also be compared to the DOE target level. Indeed, the average fixed-capital investment of 575 US$/ft^2 and the average total capital investment of 677 US$/ft^2 were both close to the 2015 DOE target leve. As a final remark, it should be noted that the reactor module cost could be further reduced by using thinner Pd-based membranes, alloying with cheaper metals such as Cu or decreasing the required membrane area with the application of vacuum from the permeate side.

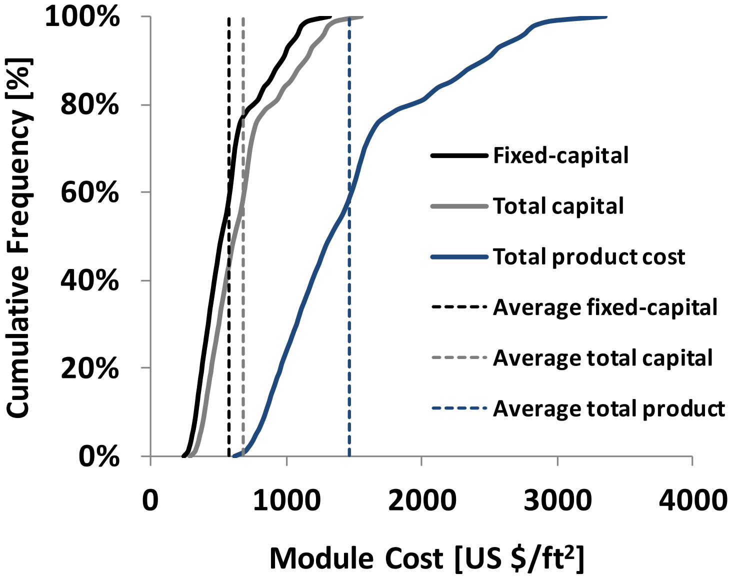

Figure 8.23. Membrane reactor module cost distributions.

Table 8.22. Membrane reactor module cost summary [US$/m^2] (US$/ft^2).

	Fixed-capital		Total capital		Total product cost	
Average	6186	(575)	7283	(677)	15750	(1464)
Max	14180	(1318)	16665	(1549)	36073	(3353)
Min	2625	(244)	3088	(287)	6681	(621)

8.5.6. Absence of regulatory action on carbon emissions

In the absence of any regulatory action on carbon, the simulation results are presented in Figure 8.24. Since pulverized coal power plants have been operating for a significant period of time, the associated nominal discount rate and plant capacity values were fixed at 6% and 85%, respectively. Under no CO_2 taxes, as expected, SCPC without CO_2 capture exhibits the most attractive NPV-distribution profile with negligible risk of losing money as shown in Figure 8.24(a). It is interesting to note that, even though the NPV-positive zone in the baseline IGCC distribution profile is not as broad as the one of SCPC, the baseline IGCC plant was still found to be a quite attractive investment option with a relatively low probability of losing money (notice also that the likelihood of losing money is about 13% for IGCC-MR without CO_2 compression/transportation/sequestration and 1% for IGCC baseline as shown in Figure 8.24(a)). Furthermore, IGCC options could become more attractive and competitive against SCPC plants when environmental performance criteria are considered in addition to economic ones. If one focuses on the NPV distribution profile of IGCC-MR, the well-known barrier and reluctance of investors to consider an active involvement in the realization of demonstration projects for an advanced energy technology option such as IGCC-MR becomes apparent. Indeed, in the absence of any government incentives, any regulatory action on carbon and in the presence of technology risks associated with this new technology option for which no accumulated operating experience is available, the SCPC NPV profile remains the most attractive one. Please notice that in the present study, to demonstrate the above challenge, the capacity factor (related to technology risks and reliability) and also the nominal discount rate values in the IGCC-MR case were selected in a manner reflecting the above considerations.

The NPV distribution profiles of the plants with CO_2 capture capability are shown in Figure 8.24(b) namely, SCPC with capture, IGCC with traditional packed bed reactors and with an embedded membrane reactor module. In the absence of regulatory action on carbon, all profiles are of course shifted to the left compared to those without CO_2 capture due to higher plant and O&M costs related to the CO_2 capture units as well as expenses for CO_2 transportation and sequestration. The NPV profile of the IGCC-MR plant in a no-CO_2 taxes regime was not better than the IGCC-PBR and SCPC with capture, but the difference was not as significant as the results obtained in cases without CO_2 capture shown in Figure 8.24(a). It is important to note that even though membrane reactor technology currently introduces higher technology risks due to a lack of operating experience, IGCC-MR is still capable of producing a statistically significant range of positive NPV outcomes as shown in both Figure 8.24(a) and (b). Finally, the expected NPV (ENPV) as well as the maximum and minimum NPV values are summarized in Table 8.23.

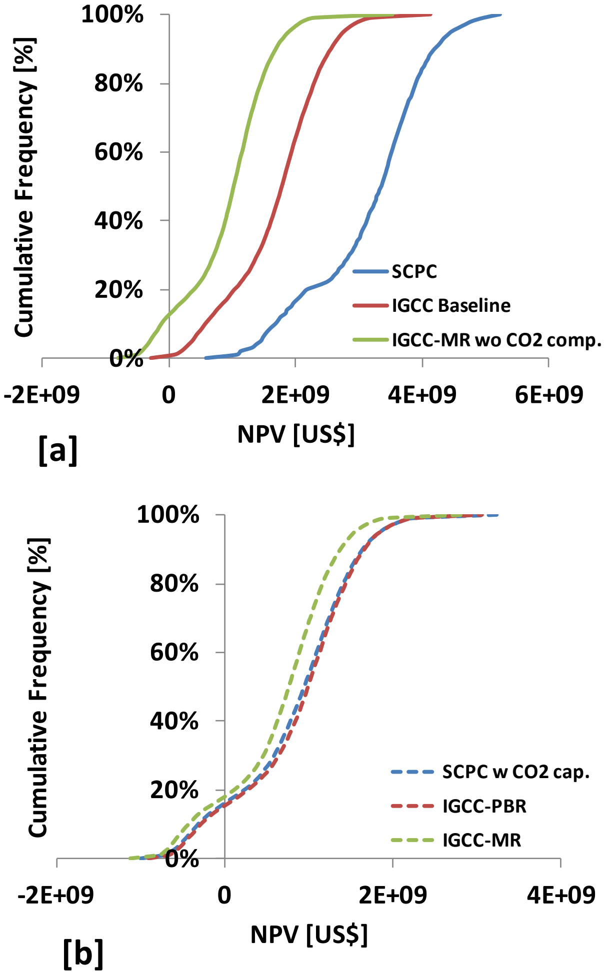

Figure 8.24. NPV distribution profiles in the absence of regulatory action on carbon for plants [a] without and [b] with CO_2 capture.

Table 8.23. NPV results summary in the absence of carbon tax [US B$].

	Without CO_2 capture			With CO_2 capture		
	SCPC	IGCC Baseline	IGCC-MR wo CO_2 comp.	SCPC w CO_2 cap.	IGCC-PBR	IGCC-MR
ENPV	3.1	1.7	0.93	0.83	0.87	0.64
Max	5.2	4.1	3.5	3.2	3.0	2.9
Min	0.58	-0.3	-0.8	-1.0	-0.9	-1.1

8.5.7. Future regulatory action on carbon emissions

Let us now examine the results of simulation scenarios where all uncertainty drivers are included, i.e. cases where the combined effect of regulatory and market uncertainties, as well as technological risks on the plant value is analyzed within the proposed economic assessment framework. As it can be easily deduced, the inclusion of regulatory action on carbon has a direct effect on the NPV-distribution profiles for all options considered, starting also to confer noticeable advantages to IGCC-MR (Figure 8.25). The latter now appears as an appealing technology option worthy of further attention and a good candidate for the provision of the requisite incentives package to stimulate the deployment of demonstration plants. In particular, apparent differences between Figure 8.24(a) and Figure 8.25 (a) highlight the consequences of any future CO_2 taxes on the economics of the power plants which were not equipped with CO_2 capture and sequestration units (SCPC and baseline IGCC are no longer competitive or even viable options under the CO_2 taxation scenario/trajectory considered). Moreover, IGCC-MR exhibited the highest level of CO_2 recovery, namely 98%, compared to the CO_2 recovery levels in the SCPC and IGCC-PBR cases which were 90% and 92% respectively. Thus, in the case of future regulatory action on carbon, IGCC-MR displays a comparative advantage with significant implications in its overall economic performance potential (Figure 8.25 (b)). Under the assumptions that underlie the particular scenario considered, the lower probability value of losing money (in percentage terms 17%) and the highest ENPV value of 0.8 US B$ for the IGCC-MR plant render it a promising option and investment choice in a carbon constrained world.

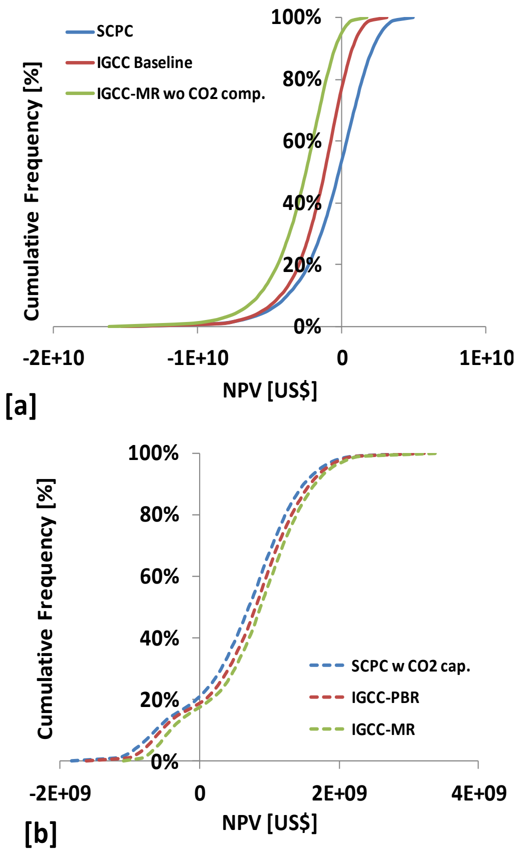

Figure 8.25. NPV distribution profiles in the presence of regulatory action on carbon for plants [a] without and [b] with CO_2 capture.

8.5.8 Potential improvements on IGCC-MR NPV-distribution profiles through technology-push and/or market-pull policy incentives

The main objective of this section is to examine possibilities for the potential improvement of NPV-distribution (risk-reward) profiles for the IGCC-MR technology option through technology push and/or market-pull policy incentives. One may envision a typical technology-push policy incentive where direct government support makes the accumulation of valuable operating experience possible through demonstration plants resulting in a reduction in the uncertainty related to the availability factor [165]. Furthermore, the case of a market-pull policy incentive could also be envisioned where a reduction of the cost of capital, and thus the cost of electricity production, is attained through a carefully structured financing mechanism for an IGCC-MR plant. Within such a context, a recent thoughtful and innovative approach is the “3 Party Covenant Financing” which has been proposed by the Energy Technology Innovation Project Group, J.F. Kennedy School of Government, Harvard [165] and represents a “technology-risk tolerant financing and regulatory program” aiming at addressing one of the main hurdles that inhibit the realization of IGCC demonstration projects. Let us succinctly describe the above financing mechanism’s main objectives, its three participants as well as its primary ideas and tools. For further regulatory and legislative details of this program the interested reader is referred to [165]. The deployment of an “initial fleet” of IGCC demonstration plants at the commercial scale in order to establish technical feasibility and economic viability of IGCC-related technology options constitutes the program’s primary objective [165]. The program requires the participation of three parties:

(i) The government that provides loan guarantees at a low budget cost (the fiscal burden is lower than other forms of government support such as direct subsidies) and the coveted AAA credit rating on debt financing.

(ii) (ii) A regional/state utility commission or a utility rate setting authority that provides an assured stream of revenues to the power producer and establishes cost recovery mechanisms while closely monitoring plant performance.

(iii) (iii) An equity investor (electric utility or an independent power producer) who provides equity financing and know-how with the required guarantees from an EPC firm (nowadays most of the major utility companies have their own EPC-arms).

The main underlying ideas and tools that the “3 Party Covenant Financing” program introduces are the following: First, due to the government’s participation (through the loan guarantee program) the cost of debt is reduced from 6.5% (a typical return on debt associated with a mid-grade utility bond) to 5.5% reflecting the higher AAA credit rating that accompanies the proposed debt financing mechanism. Secondly, an increase of the debt-to-equity financing ratio from 55/45 (associated with traditional utility financing) to 80/20 is shown in Figure 8.26. As a result, the nominal weighted average cost of capital (WACC) can be significantly reduced, and thus the cost of electric energy production since its cost of capital component is quite significant (Figure 8.26).

Let us now examine the possible effect of technology-push and market pull policy incentives such as the “3 Party Covenant Financing” (3PCF) mechanism on the NPV-distribution profile of the IGCC-MR technology option. It should be also pointed out that in addition to technology-push and market-pull policy incentives, the IGCC-MR technology option enjoys the advantage of allowing the co-production of extra purity H_2 which could be sold together with electricity and generate an additional revenue stream. The NPV distribution profile of the IGCC-MR was evaluated following the sequence of scenarios shown below and the associated results are provided in Figure 8.27:

- Reduce the uncertainty in the capacity factor by centering the associated distribution at a higher value of CF = 85% due to a technology-push policy incentive that allowed the accumulation of valuable operating experience through demonstration plants (a technology risk management approach).
- Center the distribution of the nominal discount rate at the “3 Party Covenant Financing” after-tax value: r = 7%.
- Include high-purity H_2 sales into the revenue stream calculation.

Please notice that electricity could be also produced in an IGCCMR plant through the use of steam turbines in addition to the production of high purity H_2. In the ensuing simulation results it is assumed that the remaining electricity after subtracting the net auxiliary power needed for the operation of IGCC-MR as well as all the amount of the H_2 produced are sold in the pertinent markets (their respective sales were included into the total revenue stream calculation). From the results graphically depicted in Figure 8.27, it can be readily deduced that the NPV distribution profile of IGCC-MR can be indeed improved (shifted to the right) and the option become even more attractive due to the implementation of a technology-push initiative, or the “3 Party Covenant Financing” market-pull policy initiative or finally due to increased revenues as a result of high purity H_2 sales.

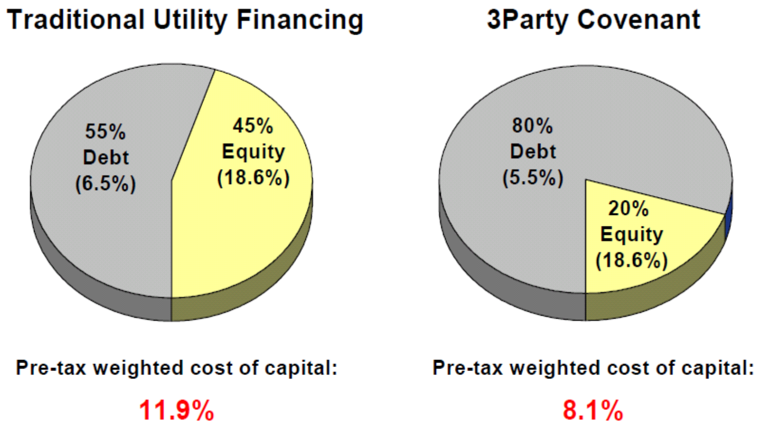

Figure 8.26. 3-Party Covenant Financing mechanism [165].

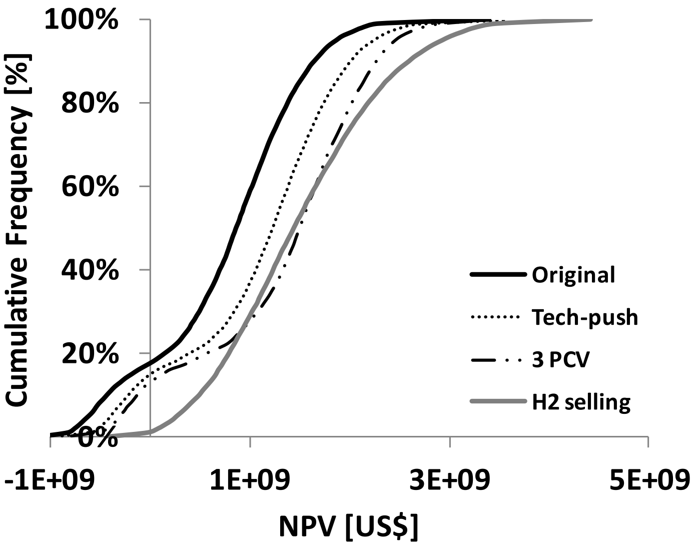

Figure 8.27. The effect of Tech-push, 3 Party Covenant Financing mechanisms and H_2 selling on the NPV distribution profile of IGCC-MR.

9. CONCEPTUAL DESIGN OF A POST-PHASE II TEST SYSTEM

Summary

Based on the results obtained in Phase II of this project, a conceptual design of a post-Phase II test system is provided. In Phase II, a model of the membrane reactor process has been developed providing the basis for rationalizing the design and performance of pilot-scale reactors to be built in a post-Phase II. The proposed process intensification relies on powerful tools that make the overall approach comprehensive, realistically efficient and capable to support readiness of the proposed technology for operation at the scale(s) envisioned. The production and separation performance of the post-Phase II device will show the feasibility of scale up to a commercial sized unit producing a minimum of four (4) tons per day of H_2. Therefore, the goal of a post-Phase II program is to prepare a detailed engineering design of a four (4) ton/day H_2 membrane reactor. To achieve this goal, the following tasks should be performed:

9.1.Task 1: Membrane Reactor Studies

In Phase II, the technology was scaled up to a seven tube membrane module with a total surface area of 1050 cm^2 that processed 6 lb of H_2 per day. Membrane reactor studies with the 100 lb/day H_2 unit should continue at NCCC, using prototype reactors of increasing size. The ability of the reactors to handle plant upsets and high levels of contaminants need to be determined. Reactor life needs to be established and the optimum operating conditions determined. During Task 1.0 of this Phase, it is expected to:

- Do preliminary membrane scale up and WGS modeling studies for a 100 lb/day H_2 pilot system – MTR, WPI
- Scale up membrane production and construct a 100 lb/day H_2 pilot system – MTR, WPI
- Operate the pilot system at the NCCC. – MTR, WPI

9.2. Task 2: Development of the Process Flow Sheet

A thorough evaluation of the performance of a commercial-sized CMR under actual process operating conditions embedded in an IGCC plant needs to be made, based on actual reactor performance data. Final modifications of the proposed process intensification strategy should be performed, as well as an update of the economic evaluation of the technology while in actual use in a commercial sized IGCC plane. Indeed, the engineering design of the complete plant able to process 9,000 lb/day (4 tons/day of H_2) requires preparation. Such a plant would contain about 1,000 meters of tubing. As part of the prototype, a module containing 50 tubes each one meter long would be prepared. Such module will be comparable to the size of a module likely to be used in a commercial IGCC plant. Such a plant would use 100 to 200 of these modules in a parallel/series array. During Task 2.0 of this Phase, it is expected to:

- Construct prototype industrial scale membrane reactor modules – MTR
- Evaluate industrial-scale membrane reactor modules at NCCC. – MTR, WPI
- Design a four (4) ton/day H_2 full scale WGS membrane reactor. Integrate it into syngas/IGCC process. – MTR, WPI.

9.3. Task 3: Prepare an Engineering Design Package

In this task, the Full Engineering Design of a unit capable of producing a minimum of four (4) tons/day H_2 will be performed. The WPI and Siemens teams will assess the compatibility of commercial-sized HSMR reactors with Siemens gasifier designs, for integration into a commercial-sized IGCC. The engineering design package can be developed through a Process Engineering Flow Simulation package such as Aspen Plus. In Figure 1, a flow diagram of membrane embedded IGCC plant with CO_2 capture is presented. This figure shows the potential set up of the units within the IGCC plant and can be used as basis for this task. Furthermore, it is important to mention, the performance of the catalytic membrane reactor would require to be externally coded, as there is no equipment within Aspen Plus to enable this.

9.4. MTR Recommendations

Over the course of this project, field tests capturing high purity H_2 from a coal-fired gasifier stream scaled up from initial single tube tests capturing 2 lb. H_2/day to a seven tube membrane module capturing 6 lb. H_2/day. To further scale up this technology to a level of capturing 4 tons H_2/day, a research program should including the following efforts:

- Continued testing at NCCC with scaled-up membrane modules and catalytic membrane reactor modules
- Long term testing of a membrane module on a small scale at an alternative coal gasification site for lifetime technology analysis
- Develop commercial scale prototype modules for both gas separation and catalytic membrane reactors

Continued testing at NCCC allows for the unique perspective of comparing scaled-up (in both number of tubes and membrane area) membrane modules to single tube performance under the exact same operation conditions. With a heated area of 48” x 20” x 24”, the oven located on the WPI skid can hold a significantly larger membrane module. While the current membrane module designs include a pre-heating coil, this could easily be removed to allow for larger membrane modules and replaced by an explosion-proof, indirect gas heater adjacent to the skid oven to assist with heating requirements. Upgrading the flowmeters and other skid components for higher syngas flow rates would be included in testing of scaled-up modules.

By testing membrane modules of various sizes under the same conditions as a single Pd tube, any issues with the membrane module design could be identified by comparing normalized membrane performance. Possible issues with gas-separation module design include gas maldistribution, feed-to-residue pressure drop, and concentration polarization. These issues can be minimized by reviewing module designs previously tested at NCCC to determine any current issues and using CFD modeling as a design aid in future scale-up modules. WPI has shared CFD modeling of multi-tube membrane modules in previous quarterly reports during this project that has given significant insight into gas distribution and velocity profiles that will aid in module design. As most multi-tube module designs to date have been a shell and tube style, CFD modeling can guide future membrane module design with respect to the inclusion of baffles. The size, number, and placement of baffles in a membrane module will heavily influence the extent of gas maldistribution, feed-to-residue pressure drop, and concentration polarization in a module. In addition, a balance between different module issues can be determined with CFD modeling. For example, optimizing the number the baffles in a module will balance the minimization of gas maldistribution and concentration polarization while maintaining a manageable feed-to-residue pressure drop.

While scale-up and performance testing of multi-tube membrane modules continues at NCCC, it would be beneficial to identify another coal gasifier site for long term testing. While facilities and support at NCCC are world class, the gasifier runs intermittently throughout the year due to their testing schedule. An alternative site that is operating full-time would allow for long term exposure and lifetime performance analysis. The small slipstream skid could be engineered to be remotely monitored. While operating on only a single tube membrane module, the performance data from this type of testing would be instrumental in determining proper membrane area needs for any scale of H_2 recovery.

The final research emphasis for creating a path towards a Pd-membrane based system for removal of 4 tons H_2/day is the design and development of commercial scale membrane or catalytic membrane reactor modules. As mentioned above, CFD modeling is a valuable tool that aids in the design of a module that maximizes membrane performance. With respect to catalytic membrane reactor design, CFD modeling can aid not only in determining gas flow patterns within the module but also the module temperature profile. This subject is often overlooked in catalytic membrane reactor journal articles but, without proper heat management design, membrane damage or hot spots could occur in commercial sized modules. For an exothermic reaction such as the water gas shift, a combination of process design and module design are needed to balance the heat produced. Specifically for the module design, the incorporation of a fluid jacket as a heat sink to remove heat from the module would be an engineering heat solution.

Beyond the need for heat management of commercial size catalytic membrane reactor modules, the design should also take into account the ease of fabrication, installation of membrane tubes, and protecting the membrane surface from catalysts during loading and operation. While keeping the specific needs of a catalytic membrane reactor in mind, the module design should not vary considerably from a simple heat exchanger shell and tube design due the ease of fabrication, cost, and relative availability of heat exchanger components. In addition, welding membrane tubes into standard tube sheets would keep module costs competitive. The module design should also include protection of the membrane surfaces from scratching that could occur during loading or replacement of catalyst pellets as well as module operation. Shown below are some preliminary engineering drawings of a catalytic membrane reactor module that includes a membrane sleeve to guide in catalyst placement and limit catalyst movement during operation.

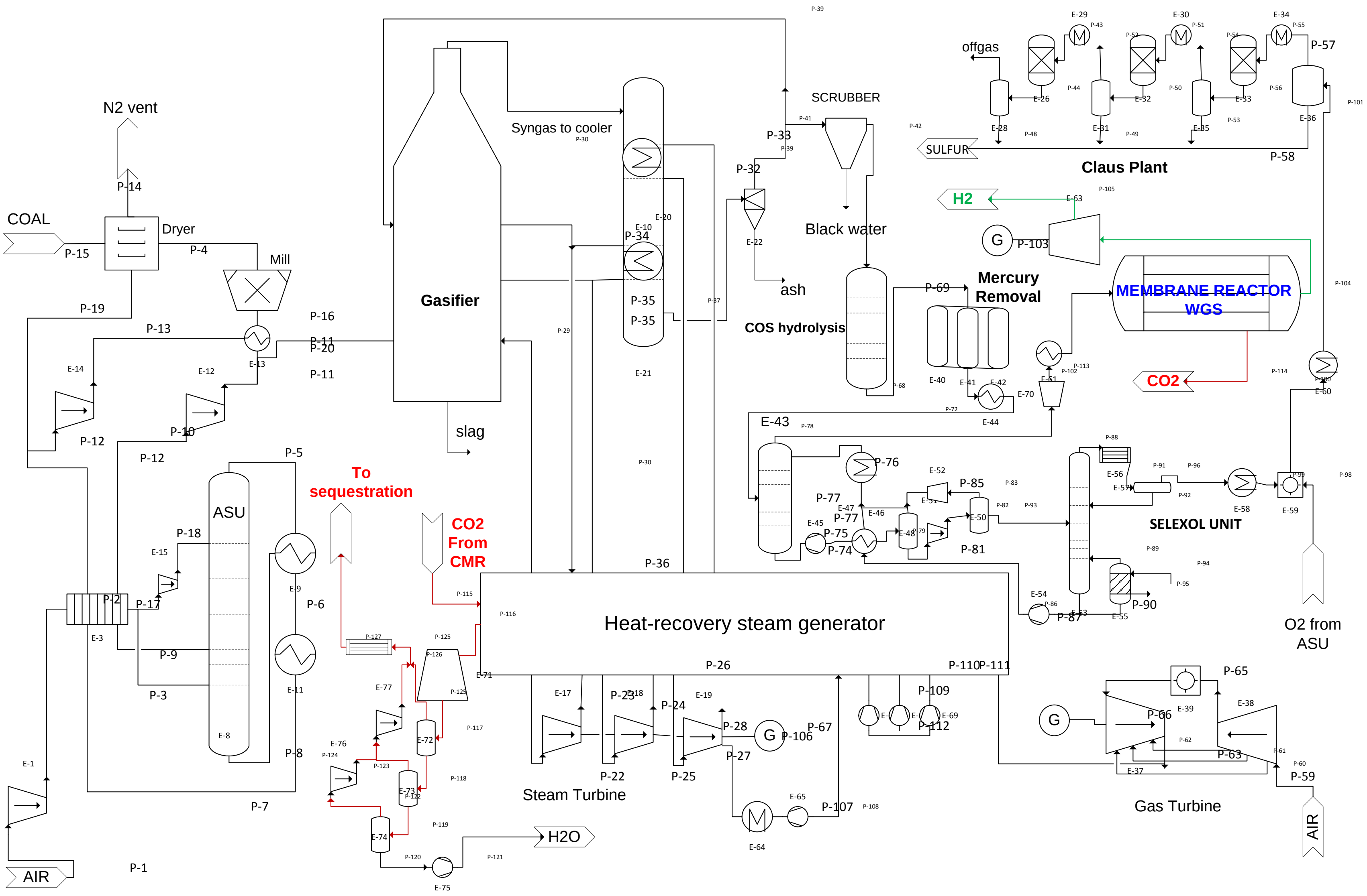

Figure 9. 1. Process flow diagram of an IGCC plant with membrane technology embedded.

10. CONTRIBUTION OF T3 SCIENTIFIC

T3 was responsible for two subtasks comprising Task 4.0 of Phase II of the project. Each task is thoroughly described in the following subsections.

10.1. Optimization of MembraGuard^{TM} coating for Phase II scale-up (completed Q4 2015)

T3 has optimized MembraGuard^{TM} coating for high flux membranes. The coating was tested under pure H_2 and DOE test protocol 2A for mixed gases with high H_2S content. The coating was also tested for long term thermal stability. A MembraGuard^{TM} HT was developed and optimized for operations at temperatures higher than 450°C. All the items were satisfactorily completed.

Description

10.1.1. Optimization of coating

T3 has experimented with various coating formulations to optimize the performance of MembraGuard^{TM} coating for H_2 permeation. The experiments were performed on palladium membranes with ½" OD stainless steel tubing for in-house testing. Palladium membranes prepared were checked for H_2 permeance, H_2 purity and stability under high temperatures.

We also developed a method to remove the protective coating without affecting the membrane. This allows us to compare various coating formulation on the same membrane to optimize the performance for versatile contaminant-containing gas stream. Table 10. 1 shows the results of several studies. Tube A10 in Table 10. 1 is an example of the quality achieved. The performance of the membrane was stable throughout the test. Only membranes passed quality test of H_2 permeance and purity were further used for fine tuning MembraGuard^{TM} coating against trace contaminants in the gas stream. Tube A10 is the base palladium membrane. Tubes A10-A, A10-B and A10-C are membranes with various coating formulations. Note that the time in H_2 stream is only an indication of the duration tested. The membranes did not degrade at the end of the test. Tube A10-A and A10-B were studied for the optimal coating thickness without added resistance. As shown in Table 10. 1, Tube A10-A had lower H_2 permeance than Tube A10, thus the coating thickness is not optimal. Tube A10-B had the same H_2 permeance as Tube A10 at 350°C (permeace at 450°C not measured), thus the coating thickness is optimal. Tube A10-C was modified with a surface modifier. H_2 permeance of Tube A10-C at 350°C was the same as A10, indicating that coating with a surface modifier does not add any flow resistance. The effect of this surface modifier is being studied for other performance matrices. The goal is for optimal contaminant protection and membrane performance for Phase II scale testing.

Table 10. 1. Optimization studies of MembraGuard^{TM} coating

	Permeance@450°C / @350°C	**H_2 purity**[1]	**Time in H_2 stream**[2]
Tube Number	$m^3/(m^2\ hr\ bar^{0.5})$	(%)	(hrs)
A10	34 / 20	>99.97	800
A10-A	13.1 / 9.5	>99.97	80
A10-B	*/ 20	>99.97	80
A10-C	*/ 20	>99.97	120

A10: pure Pd membrane
A10-A: non-optimal thickness of MembraGuard^{TM}
A10-B: optimal thickness of MembraGuard^{TM}
A10-C: optimal thickness of MembraGuard^{TM} with surface modifier
*: No data
Note 1: H_2 purity is limited by equipment accuracy

Note 2: Time only reflected the duration of test, not the lifetime of membrane

10.1.2. Coated tested under H_2S

MembraGuard^{TM} coating was applied to MA-83 membrane provided by WPI. Hydrogen feed stream containing 25ppm H_2S was introduced to the membrane retentate side. The permeation experiment was conducted at 400°C for 150 hours. No helium leak was observed at the beginning and at the end of the experiment, indicating complete hydrogen separation. Results are shown in Figure 10. 1 which indicates stable hydrogen permeation through the membrane for 150 hours. Note that without MembraGuard^{TM}, the hydrogen permeation rate is expected to drop significantly within first couple hours upon exposure to 25ppm H_2S as reported throughout the literature for palladium/alloy membranes.

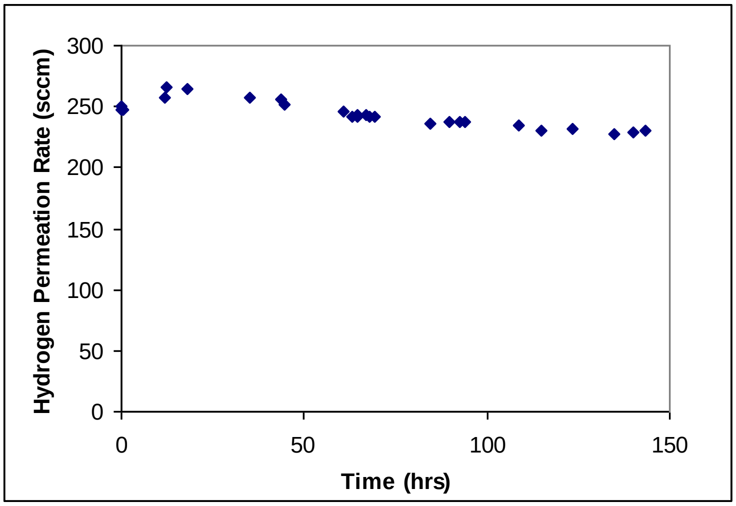

Figure 10. 1. Performance of MA-83 membrane (24cm^2 membrane area) coated with MembraGuard^{TM}. Experiment was performed at 400°C with hydrogen feed gas containing 25ppm H_2S.

10.1.3. Coating tested under DOE test protocol

MembraGuard^{TM} coating was coated on a 25 mm thick Pd membrane. Test equipment was modified to handle the mixed gas with water vapor condition. The coated membrane was tested at gas composition similar to DOE test protocol 2A at 400°C, 60 psi dP with 200 sccm feed gas comprised 50% H_2, 1%CO, 30% CO_2, 19% H_2O and trace gases including 100 ppm H_2S (5x the test protocol). The test duration was 55 hours. Figure 10. 2 shows the results. H_2 flux was stable throughout the test.

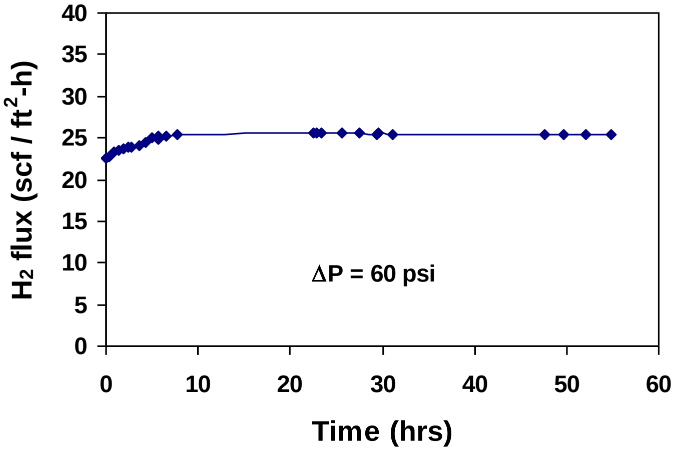

Figure 10. 2. MembraGuard™ coated 25 µm Pd membrane tested at gas composition similar to DOE test protocol 2A but with 100 ppm H_2S.

10.1.4. Long term stability

Thermal stability of MembraGuard™ coated palladium membrane (25 µm thick Pd foil) was tested under H_2 for 1200 hours at 400°C. H_2 permeance increased gradually to reach a steady state of 94 scf/ft^2-h-100psi. Membrane remained nitrogen and helium tight throughout the testing. Thermal stability of MembraGuard™ coated membrane was proved for at least 1200 hours.

10.1.5. Process tools development

During optimization and development, we realized the need to shorten process time. T3 has developed a fast and easy method to check the coating quality of MembraGuard™ coating. A visual method was developed to easily achieve the purpose without the use of permeation measurements. 30% H_2O_2 was used as an indicator of the coating quality. 30% H_2O_2 is a strong oxidant. Pure Pd will be oxidized and produce bubbles. MembraGuard™ coated Pd should be protected from the oxidant and no bubble should be produced. Figure 10. 3 shows the effect of an uncoated Pd foil and a MembraGuard™ coated Pd foil. The uncoated Pd foil bubbles vigorously on both the bottom and top surfaces of the foil. The foil essentially floats with the buoyancy of the bubbles. The left side of Figure 10. 3 shows the uncoated Pd foil with lots of bubbles. The part without bubbles is above the liquid line. If one pushes it down, it will bubble. The right side of Figure 10. 3 shows the MembraGuard™ coated Pd foil. There is no bubbles seen showing a good quality coating and the effectiveness of the MembraGuard™ coating.

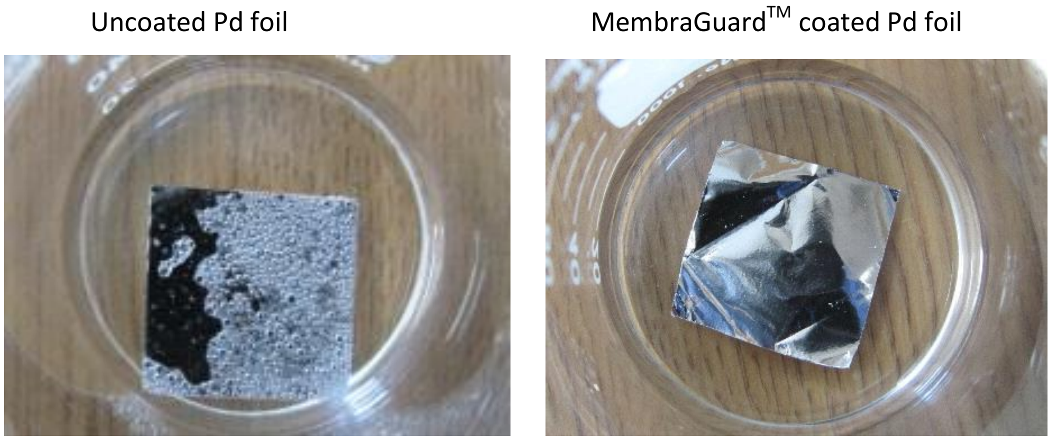

Uncoated Pd foil

MembraGuard^{TM} coated Pd foil

Figure 10. 3. MembraGuard^{TM} coated and uncoated Pd foil were put in 30% H_2O_2. The left figure showed the uncoated sample with many bubbles. The right figure showed the MembraGuard^{TM} coated sample with no bubble.

10.1.6. High temperature coating

There are several advantages to operate process stream at temperatures exceeding 450°C. The expected advantage of higher operating temperature is higher hydrogen permeation flux and the effect of reduced surface gas adsorption. MembraGuard^{TM} coating needs to be optimized for higher temperatures. In preparation for this experiment, several aspects needed to be addressed: thermal stability of the support, thermal stability of the intermetallic barrier layer, thermal stability of thin film and the performance of the MembraGuard^{TM} coating. Instead of using porous stainless steel supports, we used Hastelloy alloy porous supports which are known to be stable at temperature above 450°C. Both of these alloys cost more than stainless steel but the added cost potentially can be offset by using less material due to higher hydrogen flux, the benefit of increase in substrate stability, enabling process simplification and intensification and the benefit of economic of scale in production when technology is embraced by end users.

Although the structure of porous substrate is stable at higher temperature according to the manufactures, the intermetallic diffusion barrier layer which in contact with thin palladium film needed to be verified. The first experiment was conducted at 700°C for 25 micron thick palladium membrane on top of standard alumina barrier layer. Figure 10. 4 shows high hydrogen flux (35 m^3/m^2-hr-bar$^{0.5}$) was achieved and no nitrogen leak was detectable until almost 80 hrs into the testing. A slight decrease of hydrogen permeance was observed under pure hydrogen feed condition. An onset nitrogen leak was observed after 80 hours and the leak increased continuously throughout the rest of the test. Based on this result, 700°C seemed to be too high for the combination of the materials. The logical approach was to lower down the temperature.

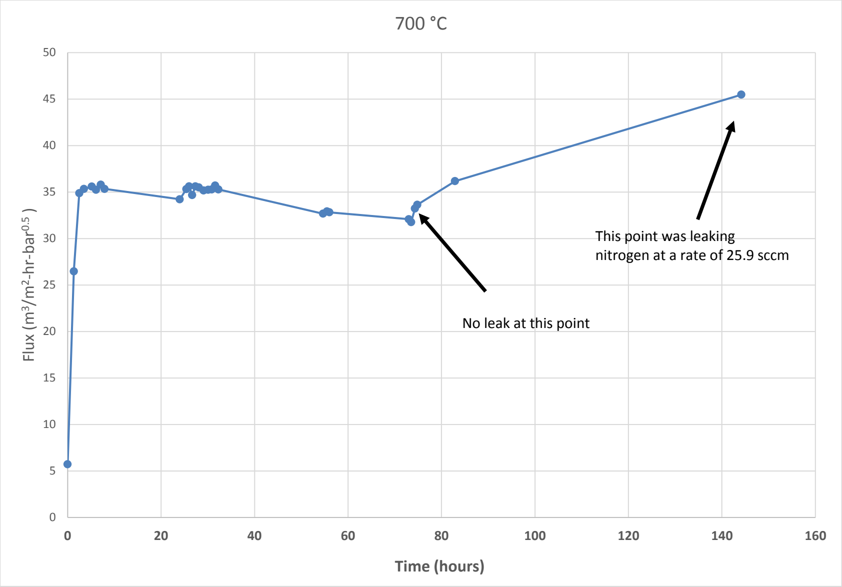

Figure 10. 4. Hydrogen permeation test at 700°C

The second experiment was performed at 600°C. Figure 10. 5 shows a Pd membrane coated with MembraGuard HT coating tested at 600°C. The test was carried out in two steps. The first step was under pure hydrogen. The second step introduced 100 ppm H_2S to test for sulfur resistance. The initial permeance under pure hydrogen feed was around 28 m^3/m^2-hr-$bar^{0.5}$. When a 100ppm of H_2S was introduced into pure hydrogen feed at about 40 hours into the testing. The H_2 permeance dropped slightly to 25 m^3/m^2-hr-$bar^{0.5}$ within 100 hours and remained stable afterward. This preliminary result showed promise for using MembraGuard HT for higher temperature operation.

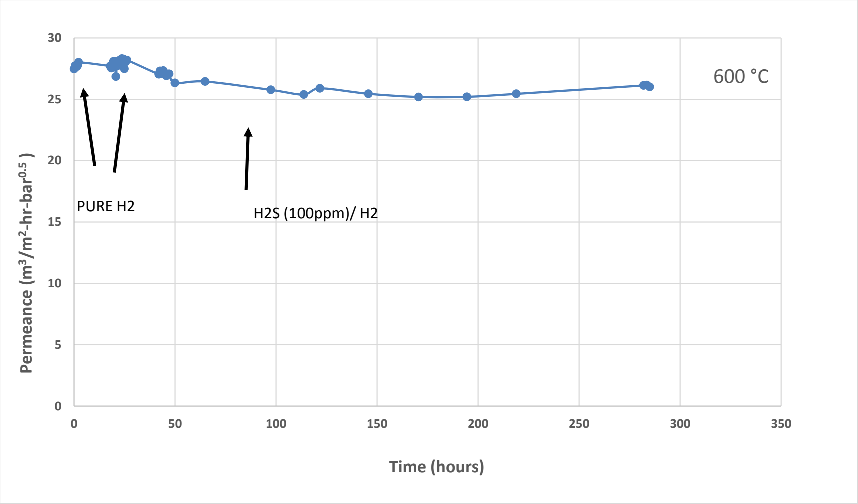

Figure 10. 5. Hydrogen permeation test at 600°C with 100 ppm H_2S

Building on the success, we fabricated supported thin films on high temperature porous tubes with a high temperature barrier layer, FuseGuard HT. The as-received support was 0.2 grade porous Hastelloy. The supports were calcined at 600°C for 12 hours prior to the deposition of FuseGuard HT barrier layer.

We tested two membranes (X101 and X103). The area of the membranes was estimated to be around 20 cm^2 since some porous area around joints between nonporous and porous was affected by high heat of welding for Hastelloy. There was no detectable N_2 leak for X101 at 470°C. X103 was fabricated with improved process, resulting in lower support resistance. The lower support resistance of X103 was reflected by lower activation energy of X103 compared to X101. The H_2/N_2 separation factor for X103 was around 3400. Note that only X103 was selected to be coated with MembraGuard HT protective layer on top of Pd membrane because of its high H_2 permeance. Only membranes with high H_2 permeance are selected to test with H_2S. The test was performed using industrial-grade pure hydrogen. Figure 10. 6 shows a picture of membrane X101.

We also prepared a thin film Pd alloy membrane (X104) that is expected to be more high temperature stable. It is known that adding a second metal to Pd can provide Zener pinning effect of the grain boundary at high temperature, thus stabilizing thin electroplated membrane to prevent pinhole formation during long term high temperature testing. We co-plated palladium and ruthenium on the surface of a Pd thin film membrane supported by high temperature grading layer and Hastelloy porous support. The thickness of the Pd-Ru layer is estimated to be 1 µm and the Pd layer is estimated around 7 µm. The test was performed using industrial-grade pure hydrogen. The membrane was annealed at 500°C for over 24 hours. The area of the membrane was around 20 cm^2.

Figure 10. 6. Seven µm thick supported palladium membrane (X101) with ~20 cm^2 surface area on top of a high temperature barrier layer and Hastelloy porous support.

Figure 10. 7 shows the comparison of hydrogen permeances of X101(Pd), X103 (Pd with MembraGuard^{TM} coating) and X104 (Pd-Ru alloy). X103 shows a much higher permeance than X101 mainly due to lower support resistance and thinner membranes (ca. 4 µm vs. 7 µm after grading). The permeance of X103 reaches 57 m^3/m^2-hr-$bar^{0.5}$ under pure hydrogen feed at 600°C. Hydrogen feed containing 20ppm H_2S was introduced into the membrane testing module at 600°C. The permeance of H_2 when H_2S was present was essentially the same and maintained closed to 57 m^3/m^2-hr-$bar^{0.5}$ (red triangle (with H_2S) in Figure 10. 7 overlapped with green square (without H_2S)). The result is in consistent with earlier results using Pd foil coated with MembraGuard^{TM} HT and tested under H_2S. At 600°C, MembraGuard^{TM} HT is able to protect Pd membrane (foil and thin film) under H_2S conditions. This preliminary result shows it is promising to use the supported thin membrane with MembraGuard^{TM} HT protective coating for sulfur containing feed gas stream. X104 shows a lower permeance which is likely due to support resistance. In addition, the activation energy is also lower, which may be partially due to the incursion of ruthenium into the palladium matrix.

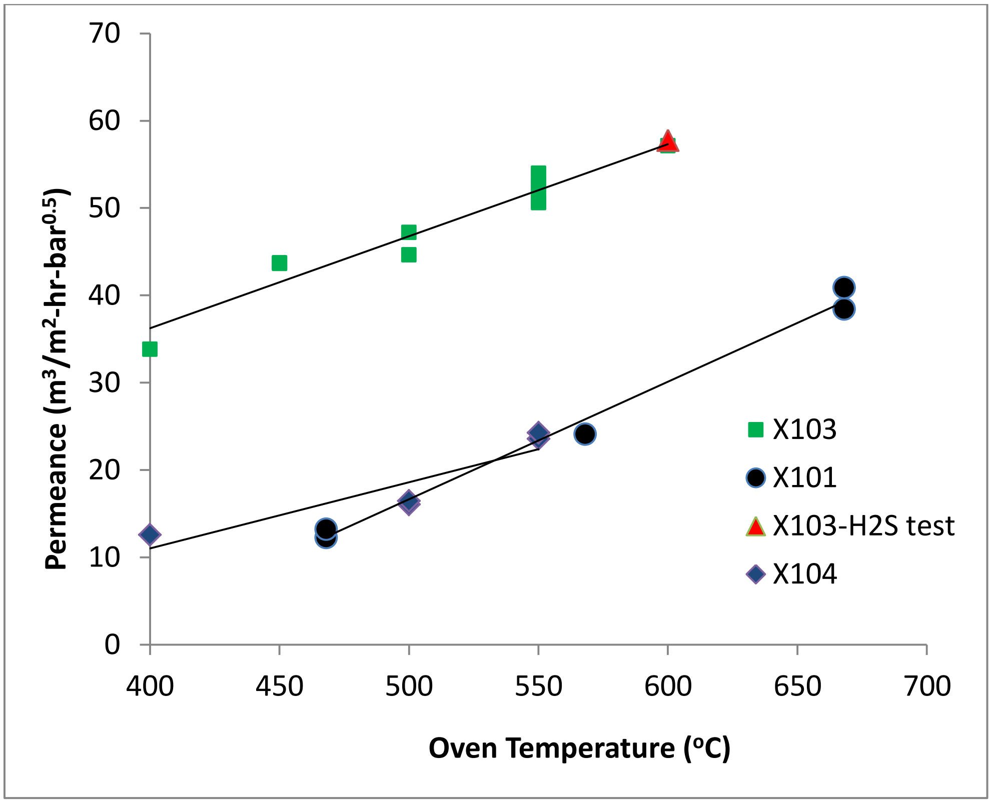

Figure 10. 7. Comparison of permeances as a function of temperature for thin supported palladium membranes with ~20 cm^2 surface area on top of FuseGuard^{TM} HT barrier layer and Hastelloy porous support.

10.2. MembraGuard^{TM} coated membrane for gasifier testing

T3 has coated multiple tubes and sent to WPI for further testing. Among the tubes, Ma-138C was tested in NCCC in R09 slip stream testing. Before NCCC test, WPI had tested Ma-138C and confirmed that MembraGuard^{TM} coating had no negative impact on membrane performance. Also, after MembraGuard^{TM} coating, leak rate was reduced and the growth of leak rate was also reduced. During R09 run, the tube had excellent stability and provided excellent H_2 purity. (Completed Q1 2013)

Coordination with NCCC in preparation for additional testing of membranes coated with MembraGuard^{TM} coating

R09 did not fully evaluate the effectiveness of MembraGuard^{TM} coating because the testing condition was slightly different than conditions tested at T3 facilities. T3 visited NCCC to discuss additional testing. T3 also coordinated with NCCC and other vendors to prepare testing of membrane coated with MembraGuard^{TM}. After many discussion and revisions of plan submitted for NCCC approval, program schedule was changed and the submitted plan was not pursued.

11. SUMMARY OF ACCOMPLISHMENTS

Throughout this project, WPI successfully prepared composite Pd and Pd-alloy membranes demonstrating the effectiveness of the patented technology. The accomplishments of Phase I and II can be summarized as follows:

(1) A total of thirteen single-tube membranes were tested for a cumulative time of > 4,000 hours at the National Carbon Capture Center (NCCC) in coal-derived syngas and industrial conditions.. These membranes showed high permeance and selectivity values and outstanding long-term performances under actual coal derived syngas never reported before. Permeances as high as 30 $Nm^3m^{-2}h^{-1}bar^{-0.5}$ and H_2/He selectivities over 160,000 were achieved, producing H_2 with purity as high as 99.95%.

(2) Palladium and Pd-Au composite membranes showed outstanding long term performances in actual coal derived syngas never reported before in the literature. They also showed a very high robustness/resilience towards gasifier trips and process upsets in industrial conditions.

(3) The permeance of composite Pd-Au alloys was demonstrated to be 100% recoverable when exposed to pure H_2 or by short treatment in air at temperatures ranging from 300-350°C

(4) A pilot-scale multitube membrane module was tested under industrial conditions at NCCC, producing 6 lb of hydrogen per day and displaying an excellent stability for 800 hours.

(5) A computational fluid dynamics model was developed and used to predict and optimize the performance of Pd-based membrane technology.

(6) The implementation of a large-scale catalytic membrane reactor module for water gas shift, ethanol steam reforming and methanol steam reforming enhanced the generation of H_2 and clearly proved the concept of process intensification. The large scale water-gas-shift membrane reactor produced 1.2 lb of H_2/day.

(7) A comprehensive economic performance assessment framework has been developed for this membrane-based technology option in the presence of irreducible (market, regulatory, technological) uncertainty that allows the derivation and insightful characterization of a range of economic performance outcomes (instead of single-point valuation estimates) through the integration of Monte Carlo techniques. Within such a framework, it was demonstrated that in the absence of any regulatory action on CO_2 emissions this new advanced technology option cannot compete with incumbent ones on the economic front. However, in the presence of regulatory action on CO_2 emissions, quite appealing economic performance outcomes surface regarding our technology option when comparatively assessed against the current conventional ones in a carbon-constrained world.

12. CONCLUSIONS

(1) The NCCC tests under actual coal derived syngas further demonstrated that the membrane manufacturing technology is mature and ready for licensing to other parties.

(2) This membrane technology is now ready for its application at larger-scales and for its commercialization.

(3) A regulatory action on carbon emissions needs to be implemented to incentivize the realization of demonstration projects of this innovative technology.

13. LIST OF PUBLICATIONS/CONFERENCES UNDER THE PROJECT

Peer-reviewed publications

- B. Castro-Dominguez, I.P. Mardilovich, R. Ma, N. K. Kazantzis, A.G. Dixon, Y.H. Ma, Performance of a Pilot-scale Multitube Membrane Module under Coal-Derived Syngas for Hydrogen Generation, *Energy* (submitted)
- L.C. Ma, B. Castro-Dominguez, N. Kazantzis, Y.H. Ma, Design Flexibility for Hydrogen Production Plants Integrated with Membrane Technology: An Economic Performance Evaluation Study, *Int. J. Greenhouse Gas Control* (submitted)
- L.C. Ma, B. Castro-Dominguez, N. Kazantzis, Y.H. Ma, A Cost Assessment Study for a Pilot-Scale Water Gas Shift Catalytic Membrane Reactor Module in the Presence of Uncertainty, *Sep. Purif. Techn.* (submitted).
- L.C. Ma, B. Castro-Dominguez, N. Kazantzis, Y.H. Ma, Integration of Membrane Technology into Hydrogen Production Plants with CO_2 Capture: An Economic Performance Assessment Study, *Int. J. Greenhouse Gas Control* 42 (2015) 424-438.
- L-C. Ma, N. Kazantzis and Y. H. Ma, Natural Gas in H_2 Production: A Cost Study of Membrane Modules, *Energy, Institution of Civil Engineers (ICE Proc.)* 168 (2015) 61-73.
- I. P. Mardilovich, B. Castro-Dominguez, N. Kazantzis, T. Wu, Y.H. Ma, A Comprehensive Analysis of Pilot-Scale Pd and Pd/Alloy Membranes under Long-Term Coal Derived Syngas Atmosphere Testing, *Int. J. Hydrogen Energy* 40 (2015) 6107-6117.
- Y.H. Ma, I.P. Mardilovich Simultaneous Production of H_2 and High pressure CO_2 for sequestration by composite Pd and Pd./Alloy membranes, American Chemical Society, Division of Energy & Fuels (2014), 59(1), 383-384., At 247th ACS National Meeting and Exhibition 2014: Dallas, Texas, USA, 16-20 March 2014
- R. Koc, N.K. Kazantzis, Y.H. Ma, Membrane technology embedded into IGCC plants with CO_2 capture: An economic performance evaluation under uncertainty, *Int. J. Greenh. Gas Con.*, 26 (2014) 22-38.
- F. Guazzone, J. Catalano, I.P. Mardilovich, T. Wu, R.C. Lambrecht, S. Datta, J. Kniep, S. Pande, N.K. Kazantzis, Y.H. Ma, Enhancement of the Long-Term Permeance, Selectivity Stability, and Recoverability of Pd-Au Membranes in Coal Derived Syngas Atmospheres, *Energy Fuels*, 2013, 27 (8), pp 4150–4160
- R. Koc, N. Kazantzis, W.J. Nuttall, Y.H. Ma, An Economic Evaluation Framework for Membrane Reactor Modules in the Presence of Uncertainty: The Case for Process Safety Investment and Risk Reduction, *J. Loss Prevention in the Process Industries* 26 (2013) 468-477.
- J. Catalano, F. Guazzone, I.P. Mardilovich, N.K. Kazantzis, Y.H. Ma, Hydrogen Production in a Large Scale Water-Gas Shift Pd-Based Catalytic Membrane Reactor, *Ind. Eng. Chem. Res.*, 2013, 52 (3), pp 1042–1055.
- Y.H. Ma, C.H. Chen, J. Catalano, F. Guazzone, E.A Payzant, Synthesis, Annealing and Performances of Pd-Au Asymmetric Composite Membranes for Hydrogen Purification, *Ind. Eng. Chem. Res.,* 2013, 52 (26), 8732–8744.
- F. Guazzone, J. Catalano, Ivan P. Mardilovich, J. Kniep, S. Pande, T. Wu, R.C. Lambrecht, S. Datta, N.K. Kazantzis, Y.H. Ma, Gas permeation field tests of composite Pd and Pd-Au membranes in actual coal derived syngas atmosphere, *Intl. J. Hydrogen Energy*, 37(2012), 14557-14568.

- A.S. Augustine, Y.H. Ma, I.P. Mardilovich, N.K. Kazantzis, Durability of PSS-supported Pd-membranes under mixed gas and water-gas shift conditions, *J Memb. Sci.,* (2012) 415 - 416, 213-220
- R. Koc, N. Kazantzis, W. J. Nuttall, Y.H. Ma, Economic Rationale for Safety Investment in Integrated Gasification Combined-Cycle Gas Turbine Membrane Reactor Modules, Cambridge Working Paper in Economics, No. 1226. University of Cambridge, Cambridge, UK.(2012)
- R. Koc, N. Kazantzis, Y.H. Ma, A Process Dynamic Modeling and Control Framework for Performance Characterization and Enhancement of Pd-Based Membrane Reactors Used in Hydrogen Production, *Int. J of Hydrogen Energy* 36, (2011) 4934-4951.

Conferences

- R. Ma, B. Castro-Dominguez, A.G. Dixon, Y.H. Ma, Three-dimensional CFD Model of a Multitube Pd/Au Membrane Module for Hydrogen Purification, 2015 AICHE Annual Meeting, Salt Lake City, November 8 to 13, 2015.
- B. Castro-Dominguez, I. P. Mardilovich, A.G. Dixon, N. Kazantzis, Y.H. Ma, A CFD Model of an Integrated Reforming-WGS Membrane Reactor Module, North American Membrane Society (NAMS) Conference 2015.
- L.C. Ma, B. Castro-Dominguez, N. Kazantzis, Y.H. Ma, An economic performance evaluation study of membrane steam reformer modules used in H_2 production, North American Membrane Society (NAMS) Conference 2015.
- R. Ma, B. Castro-Dominguez, A.G. Dixon, Y.H. Ma, Water Gas Shift Membrane Reactor Module: A Heat Transfer Analysis, North American Membrane Society (NAMS) Conference 2015.
- I. P. Mardilovich, B. Castro-Dominguez, N. Kazantzis, Y.H. Ma, Long-term testing and recovery of Pd/Au membranes, North American Membrane Society (NAMS) Conference 2015.
- B. Castro-Dominguez, et al., A CFD Analysis of the Operating Conditions of a Multitube Pd Membrane for H_2 Purification, COMSOL Conference Boston, October 2014.
- Y.H. Ma, F. Guazzone, J. Catalano, Ivan P. Mardilovich, N. Kazantzis, Characterization of New Pd, Pd-Au and Pd-Au-Pt Large Scale Membranes in Actual Coal Derived Syngas Atmospheres, 13 AIChE Annual Meeting (2013)
- Ivan P. Mardilovich, F. Guazzone, N. Kazantzis, Y.H. Ma, Long Term H2 Permeance and Selectivity Stability of Pd and Pd-Au Large Scale Membranes in Actual Syngas Atmospheres, 12 AIChE Annual Meeting (2012)
- Y.H. Ma, Ivan P. Mardilovich, F. Guazzone, J. Catalano, Performances and Stability of Pilot Scale Composite Pd and Pd-Au Membranes in Actual Coal Derived SynGas, Conference: 2012 AIChE Spring National Meeting
- F. Guazzone, Ivan P. Mardilovich, J. Catalano, Y.H. Ma, Gas permeation field tests of composite Pd and Pd /Au membranes in coal derived syngas atmospheres, Conference: Preprints of Symposia - American Chemical Society, Division of Fuel Chemistry (2012), 57(1), 643-644., At 243rd ACS National Meeting & Exposition, San Diego, CA, United States, March 25-29, 2012 (2012)

NOMENCLATURE

P_i	Partial pressure of component *i* in the reaction zone
F_i	Molar flow rate of component *i*
Pe	Peclet number
Da	Damkohler number
r_i	Reaction rate
k_i	Reaction rate constant
K_i	Equilibrium constant
GHSV	Gas hourly space velocity
N_i	Flux of component *i*
j_i	Mass flux of component *i*
w_i	Mass fraction of component *i*
c_i	Concentration of component *i*
R_g	Ideal gas constant
κ	H_2 solubility
$\overline{P_{H2}}$	Hydrogen permeance of the membrane
T	Temperature
Δ, t	Thickness of the membrane
Δ	Delta index
X	Conversion of methane
D_{AB}	Binary diffusion coefficient between components A and B
M_i	Molecular weight of component *i*
$\varphi_{D,AB}$	Collation integral for diffusion
σ_{AB}	Lennard-Jones potential between molecules A and B
$\mathrm{J}_{\mathrm{H}_2}$	H_2 flux
θ	Surface coverage.
$\mathrm{k_d}$ and $\mathrm{k_a}$	Rate constants of desorption and adsorption
u	Velocity vector of the fluid
ΔH_{H_2}	Enthalpy of adsorption
ΔS_{H_2}	Entropy of adsorption
$S_{A}/_{B}$	Selectivity of A with respect to B

APPENDIX A: SKEMATIC OF THE MULTITUBE MEMBRANE MODULE

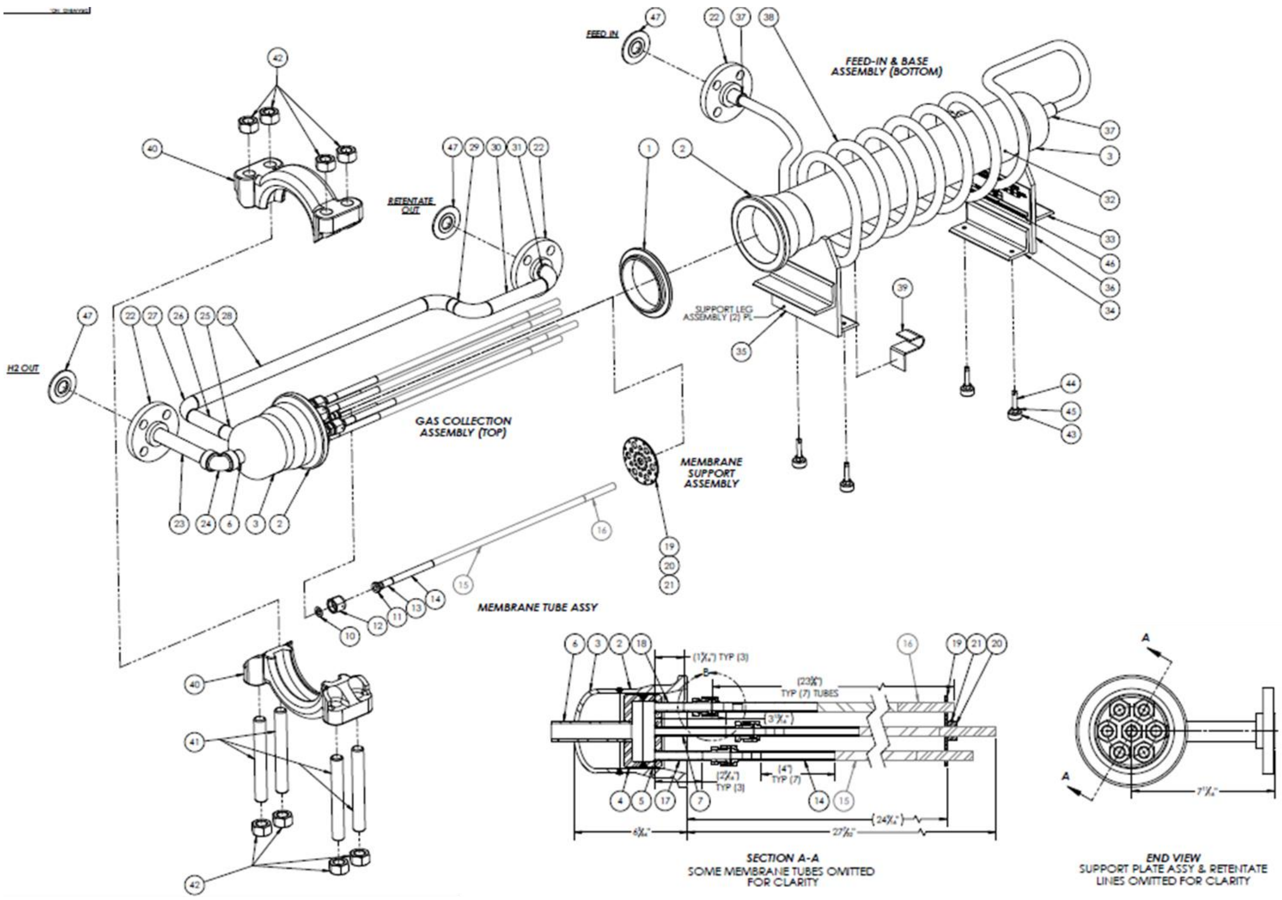

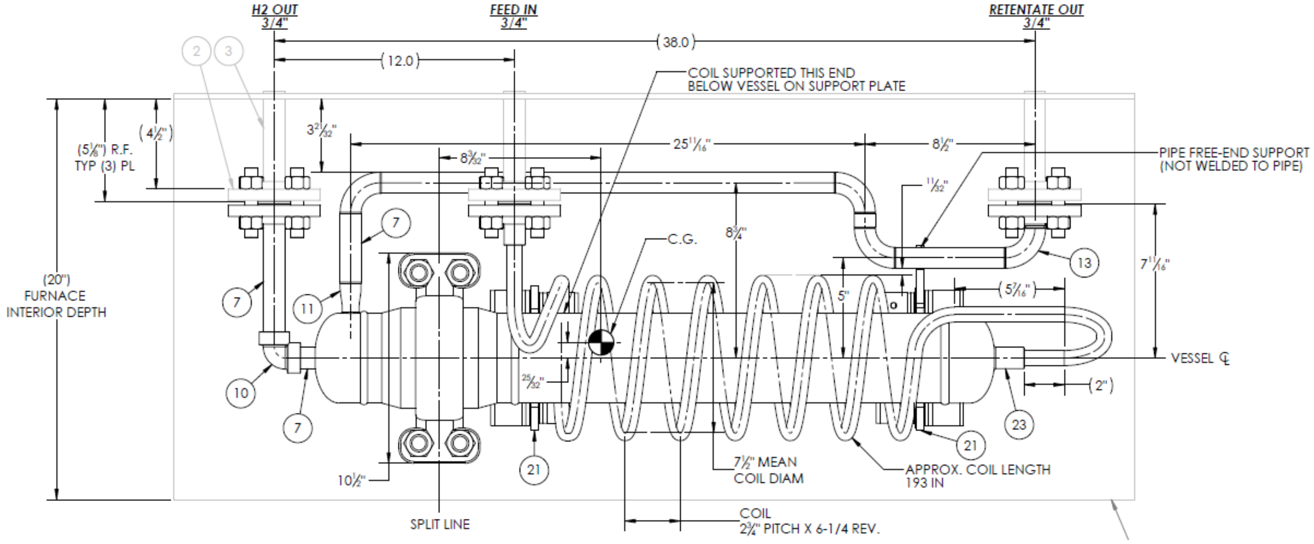

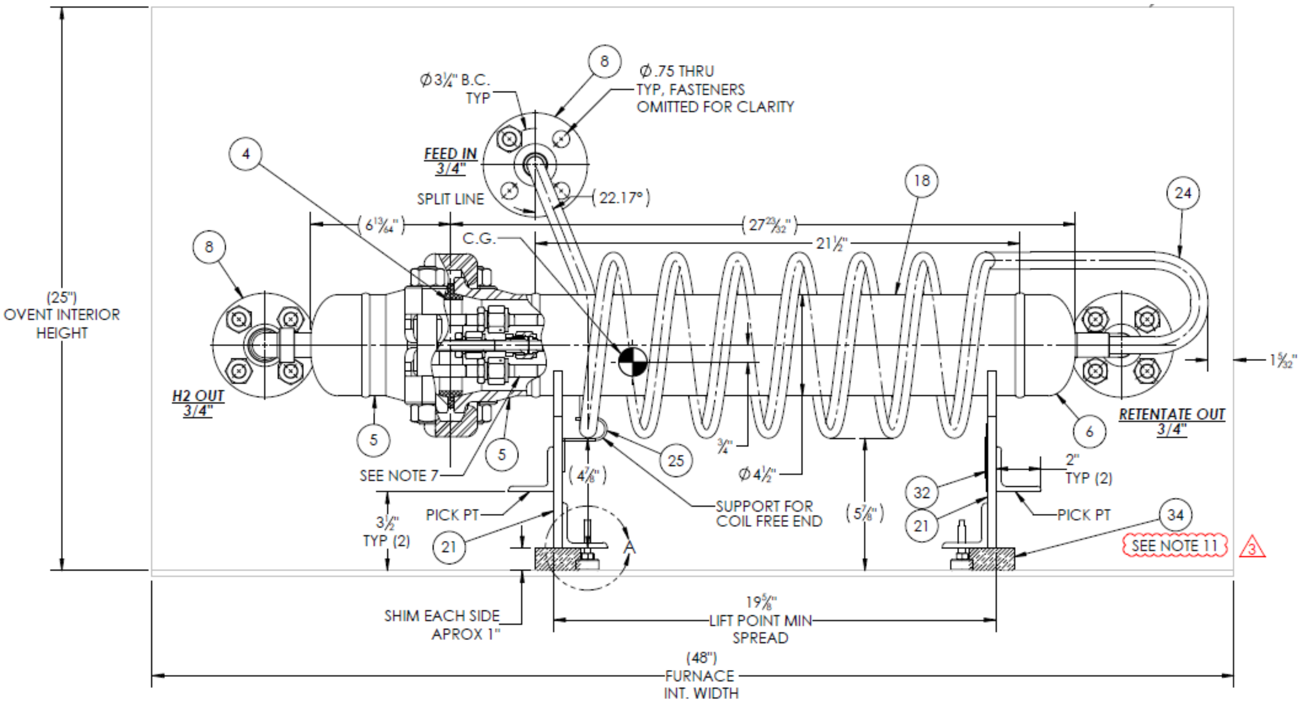
8
Ø 3¼" B.C.
TYP
Ø .75 THRU
TYP, FASTENERS
OMITTED FOR CLARITY
4
FEED IN
3/4"
18
24
SPLIT LINE
(22.17°)
(6 13/64")
(27 23/32")
8
C.G.
21½"
(25")
OVENT INTERIOR
HEIGHT
1 5/32"
H2 OUT
3/4"
RETENTATE OUT
3/4"
5
6
5
25
¾"
SEE NOTE 7
(4⅞")
Ø 4½"
2"
TYP (2)
32
3½"
TYP (2)
PICK PT
SUPPORT FOR
COIL FREE END
(5⅞")
21
PICK PT
34
21
A
SEE NOTE 11
3
SHIM EACH SIDE
APROX 1"
19⅝"
LIFT POINT MIN
SPREAD
(48")
FURNACE
INT. WIDTH

APPENDIX B: SUMMARY OF ALL SYNTHESIZED MEMBRANES

Table B1. List of all lab scale membranes prepared on Mott 1”OD – 10” L and 0.5”OD – 6” L PSS 316L, different media grade supports

#	Support: - Grade -He Permeance (m^3/m^2 h bar)	Anodization Yes/no	Oxidation: -Temp (°C) -He Permeance (m^3/m^2 h bar)	Grading: -Technique -Thickness (mm) - He Permeance (m^3/m^2 h bar)	Pd/Ag -Thickness (µm) -He Permeance (m^3/m^2 h bar)	Dense layer Pd-(µm) Gravi.	Initial He leak at RT (sccm)	Expected Permeance at 450°C Scfh/ft^2-psi$^{0.5}$	Comments
MA-125	-0.2 µm 153	Yes	380 153	α-alumina + sol gel cementing note: performed after the PdAg	4.3 + grading on the left Annealed at 530°C in H_2 56	8.1	7	24.5	Tested + Extra Pd Plating+ Protective Coating
MA-125b	Se above					11	6	23.4	Cut. Studied with SEM
MA-126	- 0.2 µm 159	Yes	380 161	α-alumina + sol gel cementing Calcination at 500°C 54	no	6.9	0.5	26.9	Tested Extra Pd Plating+ +0.2 µm Au layer
MA-126b	See above					9	0.2‡	24.3	Tested in NCCC 1st run (5.2.3/Q4) Recovered at WPI Section 5.2.4.1/Q5
MA-126c	See above					~4 + 0.26 Au + 0.29 Pt	0.2‡	Not possible to predict due to Au Pt layer	Tested at WPI Section 5.2.1.1/Q6
MA-127	- 0.2 µm 179	Yes	400 158	α-alumina + sol gel cementing	no	7.3	19	31.9	Tested + Extra Pd Plating+ Protective Coating

				Calcination at 500°C 75					
MA-127b	See above					9	<0.2	26.6	Tested (gas mixtures) at WPI Section 2.5.2/Q3
MA-127c	See above					11	< 0.2	23.4	Tested in WGS reaction at WPI Section 5.2.2/Q4 Cut/SEM-EDX
MA-128	- 0.2 µm 167	Yes	425	α-alumina + sol gel cementing Calcination at 500°C 94	0.5 91	5.9	9	35.9	Tested Extra Pd Plating+ +0.2 µm Au layer
MA-128b	See above					12.5	< 0.2‡	20.3	Tested in NCCC 1st run (Section 5.2.3/Q4)
MA-128 C	See above					9.6	< 0.2‡	33	Tested in NCCC 2nd run (Section 5.2.3/Q5)) Recovered at WPI (Section 5.2.4.4/Q5) Cut/SEM-EDX
MA-129	- 0.2 µm 137	Yes	Sol gel + Calcination at 500°C 80	α-alumina + Pd cementing ~4 65	no	13.5	2.2	21.3	Tested + Extra Pd Plating+ Protective Coating
MA-129b	See above					15	< 0.2‡	19.7	Tested in NCCC 1st run (Section 5.2.3 in Q4) Recovered at WPI Section 5.2.4.3/Q5

MA-129c	See above					~14+0.9 Au	0.0125	Not possible to predict due to Au layer	Tested at WPI (Q4/5.2.1.1) Oxidation tests (Q10) Propylene tests (Q10) Sent to NCCC for Run R10 syngas (Q11 report)
MA-130	- 0.2 µm 173	Yes	Sol gel + Calcination at 500°C 80	α-alumina + Pd cementing ~4 65	no	12	0.8	23.1	Tested + Extra Pd Plating+ Protective Coating
MA-130b	See above					13.5	< 0.2‡	21.3	Tested at WPI Section 5.2.1/Q4 Thermal cycle test at WPI Section 5.2.3/Q6
MA-131	- 0.2 µm 144	No	Coarse α-alumina + Sol gel+calcination at 500°C 130	α-alumina + Pd cementing 1.3 97	no	7	0.8	38.4	Tested + Extra Pd Plating+ Protective Coating
MA-131b	See above					9	<0.2‡	32	Tested at WPI under WGS Section 5.2.2/ Q4 SEM study in Q10
MA-134	- 0.2 µm 159	The synthesis of Ma-134 was terminated due to large spots of corrosion. The membrane was cut and the microstructure was studied with SEM / See section 5.2.1.6 in Q4							
MA-135	- 0.2 µm 157	Ready to be prepared- support discarded							
Ma-136	- **0.5 µm** 444	No	2 X Coarse α-alumina + Sol gel+calcination at 500°C 262	α-alumina + Pd cementing 0.6 241	No	10.3	0.3	35.5	Tested at WPI Section 5.2.1 / Q4

MA-136b	See above					10.3 +0.33 Au + 0.085 Pt	2	Not possible to predict due to Au Pt layer	Tested at WPI Section 5.2.1.1/Q7 Oxidation tests (section 5.2.4 in Q9) Coated with T3 protective layer
MA-136b + T3	See above					**Ma-136b + T3 coating**			**Tested at NCCC in R13 Q14**
MA-137	- **0.5 µm** 463	No	227	α-alumina + Pd cementing 180	No	7.1	1.1	40.5	Tested at WPI
MA-137 B	See above					8.7+ 0.45Au	<0.2‡	Not possible to predict due to Au layer	Tested at WPI Tested in NCCC 2nd run Section 5.2.2/Q5 Recovered at WPI Section 5.2.4.1/Q6 Tested at EERC Results in Q7 Recovered at WPI Section 5.2.3/Q7 Section 5.2.5/Q8
MA-138	- **0.5 µm** 463	No	Ag plating + 2 X Coarseα-alumina + sol gel; 1 X fine α-alumina +so gel (3 layers) + calcination at 600°C 183	Fine α-alumina + Pd cementing not measured ~110	No	6.5 Pd +2.6 Ag +2 Pd	1.5	45.6	Tested at WPI
MA-138b	See above					Ma-38 +0.35 Au + 0.020 Pt	n.m	Not possible to predict due to Au Pt layer	Tested at WPI Section 5.2.1.2/Q6
MA-	See above					Ma-38b	2	Not	Tested at WPI

138c						+ 0.040 Pt +weld plating		possible to predict	Section 5.2.1.2/Q7 Oxidation tests (section 5.2.4 in Q9) Coated with T3 protective layer
MA-138c + T3	See above					**Ma-138c + T3 coating**			Tested at WPI section 5.2.4. in Q9 Tested at NCCC section 5.2.2. in Q9 Recovered at WPI
MA-139	- **0.5 µm** 429	No	1 X Coarse α-alumina + Sol gel+ +3 extra sol gel layers +calcination at 600°C 140	α-alumina + Pd cementing not measured 115	No	Synthesis terminated			-
MA-140	0.2 µm thin wall 265	No	No oxidation Au - 1.4 µm	α-alumina + Pd cementing 1.7 212	Yes 6 31	6.1	3.3	31.7	Tested / annealed at 525°C Surface treatment+ Pd plating
MA-140b	See as above					7.1	0.6	29.2	Tested at WPI Section 5.2.1/Q4 Tested again at WPI
MA-141	0.2 µm thin wall 278	No	600 177	Ag+In/Ga 12 10.5	Yes 7.3 46	7.1	<0.2	Not possible to predict	Tested at WPI 5.2.1.3/Q6
MA-141b	Same as above					Synthesis terminated			
MA-142	0.2 µm thin wall 254	No	600 162	-JM Pre-activated alumina (catalyst)+ Pd cementing	Yes -3.3 -133	9.6	0.4	34.5	Tested at WPI Tested at NCCC in run R10 (Q10) <u>Not</u> recovered It was cut for SEM;

				-1.25 -139					Q11
MA-143	0.5 µm 0.5” OD 58 cm^2 1254	No	600 750	α-alumina + Pd cementing 6.3 401	Yes 5.9 14.9	6.1	1	Not possible to predict due to Pd/Ag	Tested at WPI Results not reported due to errors
MA-143b	See above					7.6	<0.2	Not possible to predict due to Pd/Ag	Tested at WPI 5.2.1.4/ Q6 Mechanically damaged at URS/NETL
MA-143c	See above					7.9	<0.2	Not possible to predict due to Pd/Ag	Sent to URS/NETL for testing
MA-144	0.5 µm 0.5” OD 58 cm^2 1337	No	600 897	α-alumina + Pd cementing 5.2 418	Yes 5.5 19.2	6.1	5.9	Not possible to predict due to Pd/Ag	Tested at WPI Section 5.2.1.4/Q6
MA-144b	See above					7.5	<0.2	Not possible to predict due to Pd/Ag	Tested at WPI Section 5.2.1.4/Q6 Sent to URS/NETL for testing
MA-145	0.2 µm thin wall ~235	No	1 X Coarse α-alumina + Sol gel+ +calcination at 500°C 140	+ Pd cementing n.m. 83	No	7.1	n.m.	39	Tested at WPI Section 5.2.1.4/Q7
MA-145b	See above					7.1 + 0.35 Au + 80 nm Pt	<0.2	Not possible to predict due to Au+Pt	Tested at WPI Section 5.2.1.4/Q7 Tested at NCCC R08 run Section 5.2.2/Q8 Recovered at WPI Section 5.2.3/Q8 Ethylene/propylene tests complete; results can be found in Q11

MA-146	0.2 µm thin wall ~235	No	1 X Coarse α-alumina + Sol gel+ +calcination at 500°C 145	α-alumina + Pd cementing n.m. 119	No	Pd-Au sequential plating			Tested at WPI
MA-147	0.2 µm thin wall ~260	No	Sol gel+calcination at 500°C Not measured	-α-alumina + Pd cementing - 0.5 - 192	Yes 3.3 1	7.1	7.7	38.6	Tested at WPI
MA-147b	See above					+1.7 Pd +1.2 Au	1.6	Not possible to predict due to Au	Tested at WPI
MA-148**	0.2 µm thin wall ~260	No	Sol gel+calcination at 500°C Not measured	-α-alumina + Pd cementing	No	Synthesis terminated Support Corrosion			-
MA-149	1.0 µm - 0.5”OD-6”L ~1100	No	Sol gel+calcination at 600°C -785	-α-alumina + Pd cementing ~3 -8.9	No	~4.5	1.5	76.7	Tested at WPI Q10 Repaired at the welds Sent to PRAXAIR for testing
MA-150	0.2 µm thin wall ~265	No	500 -165	-α-alumina + Pd cementing 2.4 36	No	5.0	0.1	75.3	Tested at WPI Section 5.2.1.1 / Q11
MA-150b	See above					+0.8 Au +0.9 Pd	0.8	Not possible to predict due to Au	Tested at WPI Section 5.2.1.2 / Q11 Sent to NCCC for testing in run R11
MA-151	0.2 µm thin wall ~265	No	500 -145	-α-alumina + Pd cementing	No	3.9	0.7	80.8	Tested at WPI Section 5.2.1.3 / Q11

				3.0 31.5					
MA-151b	See above					+0.5 Pt +0.9 Pd	0.7	Not possible to predict due to Pt	Tested at WPI Section 5.2.1.1/Q12 Sent to NCCC for testing in run R11; Tested at NCCC in run R12
MA-152	1.0 µm - 0.5"OD-6"L ~1100	No	Sol gel+calcination at 600°C -780	-α-alumina + Pd cementing 2.9 0.4	No	2.0	0.8	113.7	Tested at WPI Section 5.2.1.4 / Q11 Repaired at the welds Sent to PRAXAIR for testing
MA-153	0.5 µm - 0.5"OD - 6"L ~450	No	Sol gel+calcination at 600°C No data	-α-alumina + Pd cementing 4.0 4.4	No	6.8	0.1	59.9	Tested at WPI Q12 Repaired at the welds Sent to Parker Hannifin Corp. for testing
MA-154	0.5 µm - 0.5"OD - 6"L ~450	No	Sol gel+calcination at 600°C No data	-α-alumina + Pd cementing No data 213	No	7.5	0.01	54.4	Tested at WPI Q12 Sent to Johnson Matthey for further testing
MA-155	0.5 µm - 0.5"OD - 6"L ~450	No	Sol gel+calcination at 600°C No data	-α-alumina + Pd cementing No data 121	No	10.6	0.01	44.6	Sent to Johnson Matthey for further testing
MA-156	0.5 µm - 0.5"OD - 6"L ~450	No	Sol gel+calcination at 600°C No data	-α-alumina + Pd cementing 4.0 0.33	No	6.0	0.3	68.0	Tested at WPI Q13
MA-157	0.5 µm - 0.5"OD - 6"L	No	Sol gel+calcination at 600°C No data	-α-alumina + Pd cementing	No	2.7 Pd +0.1 Au	1.1	Not possible to predict	Tested at WPI Q13

	~450			4.2 0.06				due to Au	
MA-158	0.2 µm thin wall ~265	No	Sol gel+calcination at 500°C -145	-α-alumina + Pd cementing 1.2 54	No	4.8 Pd +0.45 Pt	0.4	Not possible to predict due to Pt	Tested at WPI Q12 Sent to NCCC for testing in run R12
MA-159	1.0 µm - 0.5"OD-6"L ~1100	No	Sol gel+calcination at 600°C No data	-α-alumina + Pd cementing 2.9 0.1	No	5.0 Pd +0.4 Au	0.01	Not possible to predict due to Au	Tested at WPI Q15
MA-160	0.5 µm - 0.5"OD - 6"L ~450	No	Sol gel+calcination at 600°C No data	-α-alumina + Pd cementing 3.3 0.1	No	4.6 Pd +0.1 Au	0.01	Not possible to predict due to Au	Tested at WPI Q14; Q15
MA-161	- 0.2 µm 160	No	Sol gel+calcination at 600°C No data	-α-alumina + Pd cementing 3.8 45	No				Synthesis of this membrane is in progress
MA-162 A	- 0.2 µm 160	No	Sol gel+calcination at 600°C No data	-α-alumina + Pd cementing 3.7 45	No				Synthesis of this membrane is in progress
MA-162	0.5 µm - 0.5"OD - 15"L ~790	No	Sol gel+calcination at 600°C ~340	-α-alumina + Pd cementing 2.4 0.3	No	7.4 Pd +0.4 Au	0.15	Not possible to predict due to Au	The membrane is being kept at WPI for multi-tube module testing
MA-163	0.5 µm - 0.5"OD - 15"L ~790	No	Sol gel+calcination at 600°C ~340	-α-alumina + Pd cementing 2.6 0.7	No				Synthesis of this membrane is in progress
MA-	0.5 µm -	No	Sol gel+calcination at 600°C	-α-alumina	No	7.8	0.4	52.3	Synthesis of this

164	0.5”OD - 15”L ~790		~340	+ Pd cementing 1.8 0.5					membrane is in progress
MA-165	0.5 µm - 0.5”OD - 15”L ~790	No	Sol gel+calcination at 600°C ~340	-α-alumina + Pd cementing 1.2 0.1	No	5.6 Pd +0.5 Au	0.25	Not possible to predict due to Au	The membrane is being kept at WPI for multi-tube module testing
MA-166	0.5 µm - 0.5”OD - 15”L ~790	No	Sol gel+calcination at 600°C ~340	-α-alumina + Pd cementing 2.6 0.3	No	4.5 Pd +0.3 Au	0.25	Not possible to predict due to Au	The membrane is being kept at WPI for multi-tube module testing
MA-167	0.5 µm - 0.5”OD - 15”L ~790	No	Sol gel+calcination at 600°C ~340	-α-alumina + Pd cementing 2.6 0.3	No	4.6 Pd +0.4 Au	0.35	Not possible to predict due to Au	The membrane is being kept at WPI for multi-tube module testing
MA-168	0.5 µm - 0.5”OD - 15”L ~790	No	Sol gel+calcination at 600°C ~340	-α-alumina + Pd cementing 2.7 0.2	No	5.2 Pd +0.4 Au	0.2	Not possible to predict due to Au	The membrane is being kept at WPI for multi-tube module testing
MA-169	0.5 µm - 0.5”OD - 15”L ~790	No	Sol gel+calcination at 600°C ~340	-α-alumina + Pd cementing 3.2 0.3	No	5.5 Pd +0.4 Au	0.1	Not possible to predict due to Au	The membrane is being kept at WPI for multi-tube module testing
MA-170	0.5 µm - 0.5”OD - 15”L ~790	No	Sol gel+calcination at 600°C ~340	-α-alumina + Pd cementing 2.8 0.3	No	5.1 Pd +0.2 Au	0.9	Not possible to predict due to Au	The membrane is being kept at WPI for future testing
MA-171	0.5 µm - 0.5”OD - 15”L ~790	No	Sol gel+calcination at 600°C ~340	-α-alumina + Pd cementing 2.9 0.2	No	4.9 Pd +0.4 Au	0.15	Not possible to predict due to Au	The membrane is being kept at WPI for multi-tube module testing

MA-172	0.5 µm – 0.5”OD – 6”L ~592	No	Sol gel+calcination at 600°C ~394	-α-alumina + Pd cementing 4.5 2.5	No	10.5	0.01	38.8	The membrane is being kept at Praxair for further testing
MA-173	0.5 µm – 0.375”OD – 6”L ~815	No	Sol gel+calcination at 600°C ~552	-α-alumina + Pd cementing 2.2 14.9	No	12.8	0.15	31.8	Sent to Stanford University Energy Res. Eng. Dpt. for testing
MA-174	0.5 µm – 0.375”OD – 6”L ~821	No	Sol gel+calcination at 600°C ~578	-α-alumina + Pd cementing 2.6 1.2	No				Sent to Stanford University Energy Res. Eng. Dpt. for testing
MA-175	1.0 µm – 0.5”OD-6”L ~2263	No	Sol gel+calcination at 600°C ~1890	-α-alumina + Pd cementing 2.6 58.4	No	6.5	0.01	74.2	The membrane is being kept at Praxair for further testing
MA-176	Nano-coated – 0.5”OD-6”L ~1135	No	Oxidation at 600°C ~17.5	No	No	9.9	0.01	41.2	Tested at WPI Q16
MA-177	Nano-coated – 0.5”OD-6”L ~966	No	Oxidation at 600°C ~5.8	No	No				Synthesis of this membrane is in progress
MA-178	0.2 µm – 1”OD – 10”L ~183	No	Sol gel+calcination at 600°C ~106	α-alumina + Pd cementing 4.8 0.3	Yes				Tested at WPI Q19

‡ The He leak at RT was undetectable; however, in order to estimate selectivity at high pressures we assumed a value of 0.2 sccm/bar for the undetectable He leaks at RT.

**The sol gel layer on MA-148 had spots that peeled off of the support. MA-147 had a nice sol-gel layer.

APPENDIX C: JOHNSON MATTHEY’S CONTRIBUTION

Summary

In this project, Johnson Matthey (JM) has developed an improved method to manufacture Pd membranes based on WPI’s original procedure. The developed manufacturing routes at JM lead up to 80% fewer manufacturing steps compared to WPI’s original procedure. In addition, the procedure developed for the 6” long Pd membrane has been scaled to fabricate membranes up to 24” length. The reproducibility of this procedure was demonstrated through synthesizing a batch of ten 15” long Pd membranes. Theses membrane exhibits the required quality, with the He permeance and the Pd thickness within the range reported by WPI. Although very low inert leaks across the membranes were obtained, the synthesis parameters can be further optimized to reduce the thickness of the Pd layer. The batch of ten Pd membranes was supposed to be tested in the multi-tubular module at the National Carbon Capture Centre. However due to delays in the project, the testing of the Pd membranes synthesized at JM was not realized.

The palladium-containing Hg sorbent jointly developed by NETL and JM in the late 2000s was successfully tested at NCCC. Both fresh and regenerated Pd sorbent was found to be as effective in removing Hg, As and Se from sweet and sour syngas streams.

A-C.1. Introduction

Johnson Matthey (JM) participated, as a subcontractor to WPI, in Phase II of the project entitled “Design of Advanced H_2-CO_2 Pd and Pd/Alloy Composite Membrane Separations and Process Intensification,” from 01 Aug 2013 to 31 Dec 2015. JM joined this project from the perspective of being a potential Pd membrane manufacturer and also a technology supplier if Pd membrane technology were to be commercialized.

The specific project objectives which involve JM are:

- Design of a multi-tube shell-and-tube H_2 separation module with sufficient H_2 production rate to generate engineering and performance data to allow further design for a large H_2 separation system. (WPI – MTR – JMTC)
- Development of strategies for handling contaminants. (WPI – T3 – JMTC)
- Perform an economic analysis based on test results obtained by the end of Phase II and estimates of costs for commercial equipment and membranes. (WPI – JMTC)
- Perform conceptual design of a post-Phase II test system and proposed plan for long-term testing of membranes at smaller scale. (WPI – MTR –JMTC)

Based on the general project objectives, the scope of work WPI expect from JM are:

- Fabricate Pd membranes for the large multi-tubular module.
- Develop novel manufacturing routes to fabricate Pd and Pd-alloy membranes.
- Provide Pd-sorbent bed for contaminant removal.

In addition, JM have agreed to contribute to the following tasks:

- Discussion on the collected performance, engineering and recovery data for the multi-tubular module.
- Discussion on the process flowsheet for the membrane system, its interfaces with the IGCC plant and the effects of those interface streams on the IGCC plant

JM has successfully completed the majority of the tasks as stated in the agreement with WPI with the following exceptions with justifications summarized in Table A-C. 1.

Table A-C. 1. Summary of tasks not completed during the project and its justification.

Task not fully met	Justification
Provision of membranes for MembraGuard^{TM} coatings	The project has not proceeded to the stage where the MembraGuard^{TM} coatings have to be coated on the membranes. However, JM have synthesized a batch of ten 15"L Pd membranes that could be sent to T3 for coating of MembraGuard^{TM}.
Development of novel routes to the generation of alloy membranes	In addition to PdAu membranes, WPI has also developed a novel PdAuPt membrane. Although PdAuPt membranes show higher H_2 permeance during the gasifier test, PdAu membranes exhibited lower permeance drop, higher H_2 purity and stability. Focus was therefore kept on optimising the manufacture of the PdAu membranes.
Sealing technology for the membranes in the module	As stainless steel support was used in this project, the membrane can be effectively sealed to the module using established method such as welding or compression tube fitting. Initial discussions with JM experts in metal joining were initiated to find possible alternatives to the compression tube fitting technology used in the current module. Brazing was identified as a promising substitute sealing technology and this technology can be implemented in a post-Phase II test system. If required, JM Metal Joining will be able to provide the relevant expertise in selecting the most suitable filler metal alloy.
Flux and recovery optimization – Process economic analysis	JM have discussed with Dr Nikolaos Kazantzis the possibility to contribute on the process optimization and economics analysis. However, at the end WPI did not require JM input.

A-C.2. Pd membranes synthesized at JM

Throughout the project, JM has synthesized 72 Pd membranes on different supports. Most of the investigation was performed on Mott 0.5" OD, 6" L PSS (porous stainless steel) supports. The synthesis process was then scaled-up to fabricate Pd membranes on Mott 0.5" OD, 15"L supports, which have the same dimensions as the membranes used for the multi-tubular module test trials at National Carbon Capture Centre (NCCC) located at Wilsonville, Alabama. Towards the end of the project, JM has further scaled the synthesis process to fabricate Pd membranes on Mott 0.5" OD, 24"L. The technology has not been further scaled up to synthesize longer membranes since existing Mott's technology is only able to fabricate a continuous 24" length PSS tube. Longer tubes are made by welding individual ones. In addition, JM has also explored the possibility of using PSS supports from other suppliers.

The quality of the Pd membranes at each stage of the synthesis process was evaluated by estimating the thickness of the Pd layer and also measuring the inert leak across the membrane. The thickness of the Pd layer is directly related to the rate at which H_2 is transported across the Pd membrane; hence a thinner Pd layer is desired. The thickness of the Pd layer can be measured by gravimetric methods, XRF or analysing the cross-section of the membrane by SEM. The gravimetric method is used predominantly as it is easy to apply, but XRF can provide both the thickness and composition profile along the membrane. Analysing the cross section of the membrane using SEM is an invasive method but provides direct visual evidence of the thickness and morphology of the Pd layer. The inert leak across the Pd membrane measures the defects present and gives an indication of non-selective transport of gas through it. A variation of the inert leak test is the water rise test, which is used to locate the specific location of defects on the membrane. A schematic diagram of the inert leak and water rise test set-up is shown in Figure A-C. 21.

The properties of all the membranes synthesized at JM are given in Appendix B. Table A-C. 15-Table A-C. 17 summarizes the properties of the Pd membranes synthesized on 6" L, 15" L and 24"

L Mott supports, respectively. The properties of the Pd membranes synthesized on PSS from other suppliers are disclosed in Table A-C. 17.

A-C.3. Development of Pd membrane manufacturing routes

WPI has developed the state-of-the-art Pd membrane technology based on continuous understanding, modification and improvements to their synthesis method over the years. The four main processes used by WPI to synthesize a pure Pd membrane are shown in Figure A-C. 1.

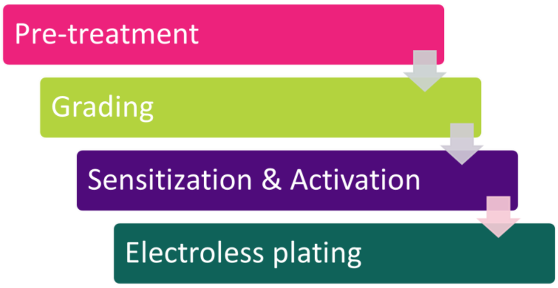

Figure A-C. 1. Main processes involved in WPI synthesis of pure Pd membranes.

Based on the knowledge gained during the technology transfer phase on the detailed Pd membrane synthesis procedure, JM has converted WPI's synthesis procedure into one requiring fewer manufacturing steps. The total number of manufacturing steps required to prepare a Pd membrane using the original WPI method is 75. The number of manufacturing steps required for each of the main processes is summarized in Table A-C. 2.

Apart from the large number of steps involved in WPI's method, some of them are highly dependent on the person performing the synthesis. This makes these steps difficult for manufacturing and scaling up.

Table A-C. 2. Summary of the methods and number of manufacturing steps required to fabricate Pd membranes.

	WPI's original	**JM-v1**	**JM-v2**	**JM-v3**	**JM-v4[1]**	**JM-v5[1]**
Pre-treatment	5	5				
Grading	34	27				
Sensitization and activation	26	26				
Electroless plating	10	10				
Total number of steps	**75**	**68**	**46**	**43**	**34**	**17**

[1] These modifications are only possible if PSS supports from an alternative supplier is used.

The first modifications made to WPI's original Pd membrane synthesis procedure (JM-v1) were to eliminate all operator dependent steps to improve the reproducibility of the membranes. After these changes, the synthesis using JM-v1 required only slightly fewer steps than WPI's original procedure. However the methods used to replace the operator dependent steps are easy to scale up to produce more membranes and with larger dimensions.

The subsequent goal of the work at JM was to decrease the number of synthesis steps. This led to the development of JM-v2 and JM-v3 synthesis procedures. Further reduction could not be achieved using the existing Mott porous stainless steel supports. However, if PSS supports from an alternative supplier are used, the synthesis procedure can be considerably shortened as shown for JM-v4 and JM-v5.

The development made to the pre-treatment, grading, sensitization and activation and electroless plating will be discussed in detail in the following subsections.

A-C.3.1. Pre-treatment of the PSS support

The pre-treatment of the PSS supports involves cleaning and also formation of the intermetallic diffusion barrier via calcination of the support. WPI's original pre-treatment consists of 5 steps as shown in Figure A-C. 2.

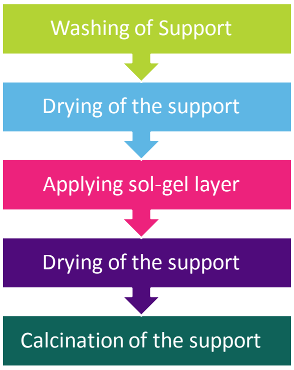

Figure A-C. 2. Steps involved in the pre-treatment of the PSS support.

Most of the steps in the pre-treatment of the PSS support can be scaled-up easily, except the method used to apply the sol-gel solution. The sol-gel solution is applied onto the support by carefully painting the surface of the support with an alumina sol-gel solution and removing the excess solution remaining on the support. Due to the difficulty in scaling up and reproducing the painting method used by WPI in a manufacturing environment, dip-coating and spray-coating were investigated as possible alternatives.

Figure A-C. 3 shows the PSS support weight increase and relative decrease in the He permeance when different methods were used to apply the sol-gel solution. The increase in PSS weight is an indication of the amount of alumina introduced. Greater increase in the PSS weight of the dip coated support is reflected by higher reduction in the He permeance. Dip coating resulted in the highest increase in weight of the PSS and also the greatest decrease in He permeance. The sol-gel applied by spray coating led to comparable weight increase and He permeance to the painting method. Although dip coating appears to be a more effective pre-treatment method due to lower He permeance, the effectiveness of the sol-gel coating method must be evaluated based on the grading quality since the main purpose of the pre-treatment is to prepare the support for grading.

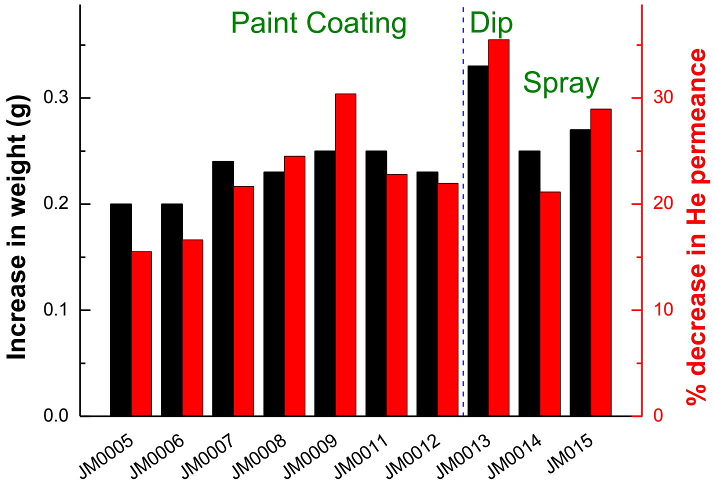

Figure A-C. 3. Weight increase and decrease in He permeance after calcination of the PSS support.

Figure A-C. 4 shows the He permeance and the thickness of the Pd after grading. The PSS supports prepared by spray-coating (JM0014 and JM0015) showed comparable He permeance and Pd thickness to the support prepared by paint-coating (JM0012). In contrast, the He permeance through the support prepared by dip-coating was found to be unexpectedly high. For JM0013, the He permeance could not be decreased even after an additional fine powder grading. With the highest reduction in the He permeance after calcination, one would expect that JM0013, prepared by dip-coating, would yield the lowest He permeance after grading. A possible explanation for this observation is that the sol-gel enters deep into pores of the support during dip-coating resulting in poor conditioning of the surface and more significant decrease in the He permeance. This hypothesis is supported by Electron Probe Micro-Analyser (EPMA) and Scanning Electron Microscope (SEM) elemental mapping analysis, where Al was found deep in the pores of the PSS support for the dip-coated sample.

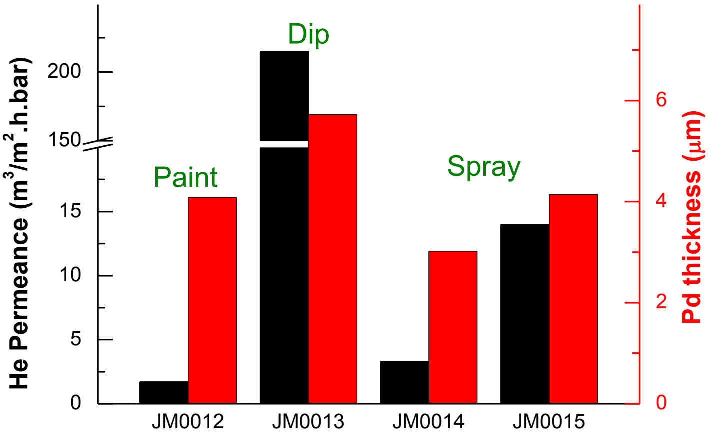

Figure A-C. 4. He permeance and Pd layer thickness of the membrane after grading.

A-C.3.2. Grading

The purpose of the grading step is to prepare the support surface for the deposit of the final dense Pd layer. This is the most crucial part of the fabrication process as it will significantly impact the final quality of the membrane. WPI's original grading procedure consists of 34 steps: 5 steps are for pre-washing, 16 steps for coarse grading, 12 steps for fine grading and 1 step for the post synthesis drying.

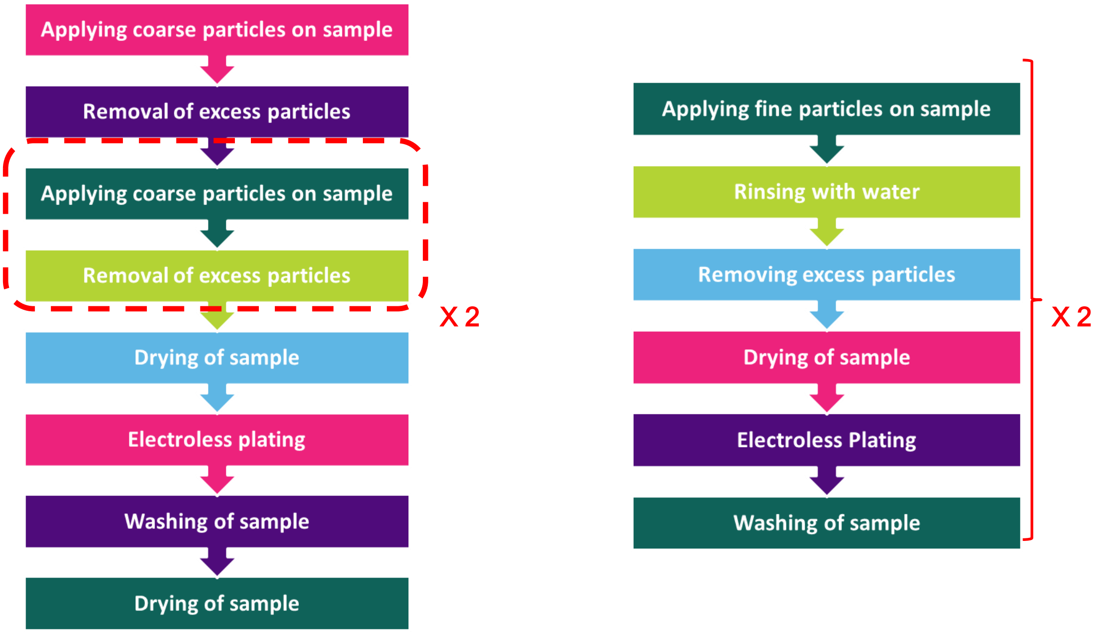

(a) Coarse grading (b) Fine grading

Figure A-C. 5. WPI's original grading procedure excluding the pre-washing and post-drying steps.

The original WPI's process for coarse and fine grading is outlined in Figure A-C. 5. During the grading process, 4 μm 2%Pd/γ-Al_2O_3 and 0.6 μm 2%Pd/α-Al_2O_3 are used for coarse and fine grading respectively. This method involves a large number of manufacturing steps and also multiple steps that strongly depend on the skills of the person performing the task, such as the method used to apply and remove both the coarse and fine particles from the support. Overall, the grading process has poor control and is difficult to scale up. The poor reproducibility in the membrane quality using WPI's original particle deposition and removal method is shown in Figure A-C. 22, Table A-C. 14. The He permeance obtained using WPI's grading method (JM0001 to JM0012) ranges between 2 to 300 $Nm^3/m^2/bar/h$. Hence, in-order to develop a proper manufacturing route for the grading process, it needs to be shortened and the operator dependent steps must be replaced with alternative methods with better control.

Particle deposition method

JM's proprietary thin film coating technique was investigated as a possible alternative to WPI's method to improve the reproducibility. Figure A-C. 6 compares the He permeance and grading layer thickness for membranes prepared by the two different grading methods. Ma153 is a reference membrane synthesized by WPI as part of the technology transfer and JM0012 is a second reference membrane which has the lowest He permeance synthesized at JM using a modified WPI's grading process. JM0016 is the first sample which uses JM's proprietary thin film coating technique to apply the grading layer. Although the grading layer is about 2 μm thicker than JM0012, the He permeance is one order of magnitude lower. JM0017 was synthesized using the exact same procedure as JM0016, but optimizing some of the parameters. JM0017 yields comparable He permeance to JM0016 and similar grading layer thickness to Ma153 and JM0012.

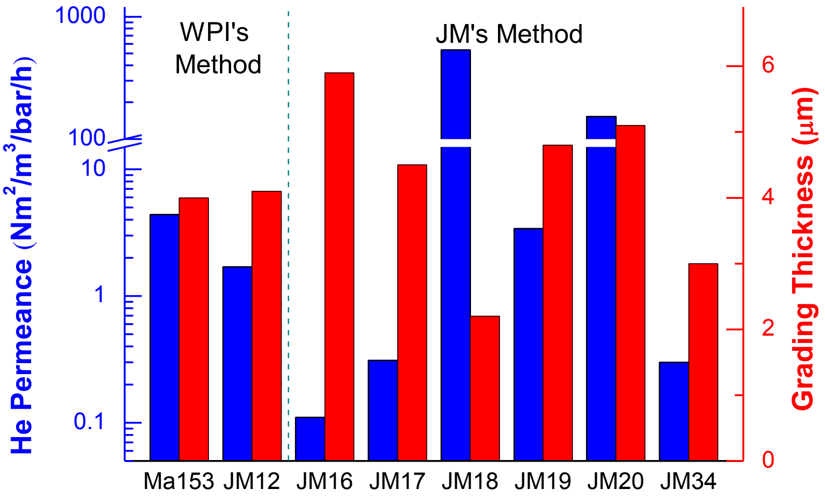

Figure A-C. 6. Weight increase and He permeance after grading of the pre-treated PSS supports.

Number of synthesis steps

Although JM's proprietary thin film coating technique is able to improve the reproducibility of the grading process, the whole grading still involves a large number of steps. JM's proprietary thin film coating technique is a more efficient technique for the particles deposition on the PSS support, and only a single deposition and removal step is required for each of the coarse grading layer (steps removed are highlighted in the red box Figure A-C. 5a). In order to further decrease the number of synthesis steps, the grading process was examined and all the redundant steps were eliminated. The above mentioned two modifications resulted in a reduction of the number of steps down to 23 (Table A-C. 3 Entry 3).

Table A-C. 3. Number of steps required for different grading methods

Entry	**Sample**	**Grading method**	**Number of grading steps**	**Grading He perm.** Nm^3/m^2.h.bar
1	Ma153 JM0001 to JM0006	WPI's grading method	34	4 21 to 350
2	JM0007 to JM0015	WPI's method with additional grading	40	0.2 to 14[a]
3	JM0016 to JM0017	JM-Grading-A	23	0.1 to 0.3
4	JM0019	JM-Grading-B	19	3.4[b]
5	JM0020	JM-Grading-C	15	150[b,c]
6	JM0034	JM-Grading-D	21	0.3
7	JM0018	Pre-treatment+Grading	6	540[b,c]

[a] Exclude JM0013 as different pre-treatment method was used. [b] Only single experiment was performed. Experiments need to be repeated. [c] Required quality was not obtained.

The first attempt to decrease the number of steps was to combine the pre-treatment and grading and activation steps (Table A-C. 3 Entry 7, Figure A-C. 6, JM18). For this, the sol-gel solution, both the coarse and fine 2%Pd/Al_2O_3 particles were deposited on the PSS support before calcination. Although this synthesis method involves only 6 steps, the He permeance through JM0018 is very high, hence the desired quality of the graded membrane was not obtained.

Another approach tested is to modify the grading procedure.

In the first attempt, the number of grading steps was reduced to 15 (JM-Grading-C) but it yield poor grading quality as reflected by the high He permeance and thicker Pd layer as compared to the reference membrane (Table A-C. 3 Entry 6, Figure A-C. 6 JM20). When the number of grading steps was reduced to 19 (JM-Grading-B), the He permeance obtained was comparable to WPI's reference but the grading layer was 1 μm thicker (Table A-C. 3 Entry 5, Figure A-C. 6 JM19). However, further experiments showed that this procedure resulted in the membrane being very sensitive to the fabrication process and the reproducibility is poor.

In the next attempt the procedure was modified to increase the stability of the grading layer by increasing the number of steps to 21 (JM-Grading-D). This method is able to obtain a graded membrane with lower He permeance and Pd thickness compared to WPI's and JM's reference (Table A-C. 3 Entry 4, Figure A-C. 6 and 7a JM34). However, when this modified procedure was used to prepare 15" Pd membranes it was unsuccessful. Although JM3004 and JM3005 attained the required membrane quality, peeling of the graded layer was observed on JM3003 and JM3006 (Figure A-C. 7b). From these results, it can be deduced that extreme care needs to be taken while using JM-Grading-D to prevent delamination. Hence it was decided not to implement this modified grading method.

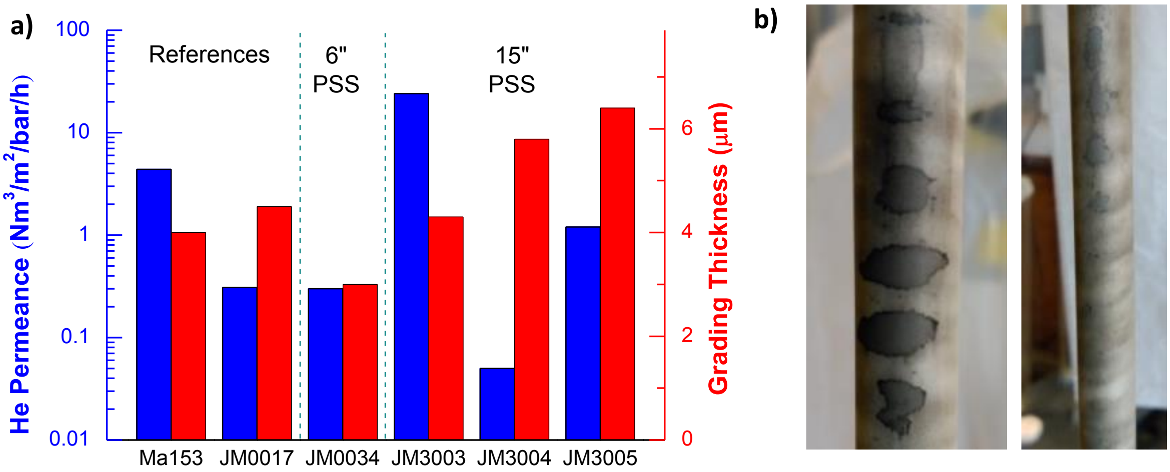

Figure A-C. 7 a) He permeance and Pd thickness for membranes prepared using the modified grading procedure. b) Image of the grading layer of JM3006 showing areas where the coating has been peeled off.

In conclusion, only JM-Grading-A is suitable. This process prepares the surface of the PSS for the deposition of the dense Pd layer and also improves the stability to the membrane.

Particle removal method

WPI's original method to remove the excess particles from the PSS support is to rub the support with gloved hands. This step has very poor reproducibility and depends significantly on the skills of the person synthesizing the membranes. In order to enhance the reproducibility of the grading process, the current method needs to be replaced. Table A-C. 4 summarizes different methods tested to remove the excess particles more systematically. However, none of these methods were able to achieve the expected He permeance obtained except when using one of JM's in-house methods.

Table A-C. 4. Grading layer He permeance for samples prepared using different methods to remove the excess of Pd/Al_2O_3 particles.

Excess Particles Removal Method	Sample Number	Grading He permeance $Nm^3/m^2.h.bar$
Rubbing with a gloved hand	JM0019	3.4
Dipping into water + Rubbing with O-rings	JM0021	348
Rubbing with O-ring	JM0022	80
Four step grading + Rubbing with O-ring	JM0023	23
JM's in-house method	JM0026	0.1

Figure A-C. 8 shows the results when the excess particles are removed using JM's in-house method, which is able to improve the reproducibility but keeps the same number of steps. Initial trials (JM0026 and JM0028) to remove the excess particles using JM's in-house method show comparable He permeance and Pd thickness to WPI's and JM's reference (Ma153 and JM0017). JM's method on 1 μm median grade tubes received from WPI yield similar He permeance as the references (JM0035 and JM0036). As expected, thicker Pd layers were obtained due to the larger median grade of the supports.

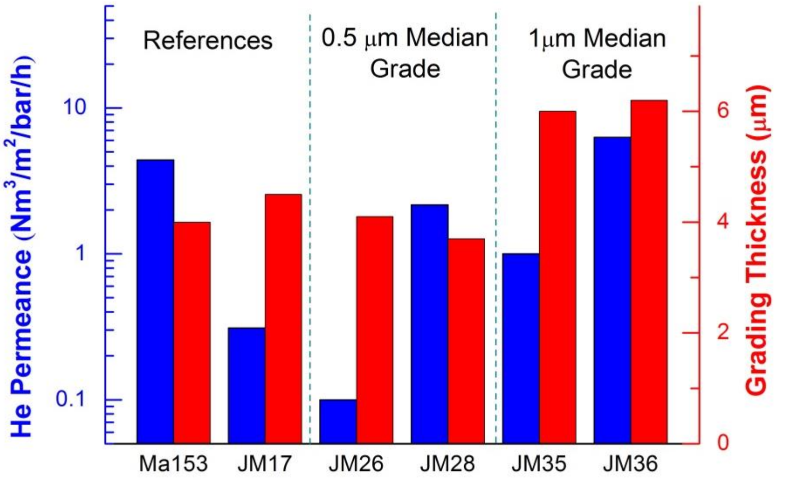

Figure A-C. 8. He permeance and Pd thickness using alternative particle removal method on different supports.

A-C.3.2. Activation and sensitization

The current activation method based on WPI's procedure involves multiple steps where the graded membrane is dipped into different solutions. Several alternative methods were tested to reduce the number of steps required for activation. The trials were carried out on ceramic supports because they give a very clear visual indication of the effectiveness of the activation step and they are much cheaper.

Activation method 0

This activation method is developed based on WPI's original activation method and will allow more effective deposition of the Pd seeds. This method is applied in synthesis method JM-v2 shown in Table A-C. 2.

Activation method A

This activation method was developed at Colorado School of Mines (A.E. Lewis et al., J Membrane Sci. 437 (2013) 257-264). The procedure consists of (1) spraying solution containing Pd acetate dissolved in chloroform onto the ceramic tube, (2) drying the support, (3) performing thermal treatment as described in Figure A-C. 9, and (4) dipping the support into a bath containing hydrazine and ammonium hydroxide before plating.

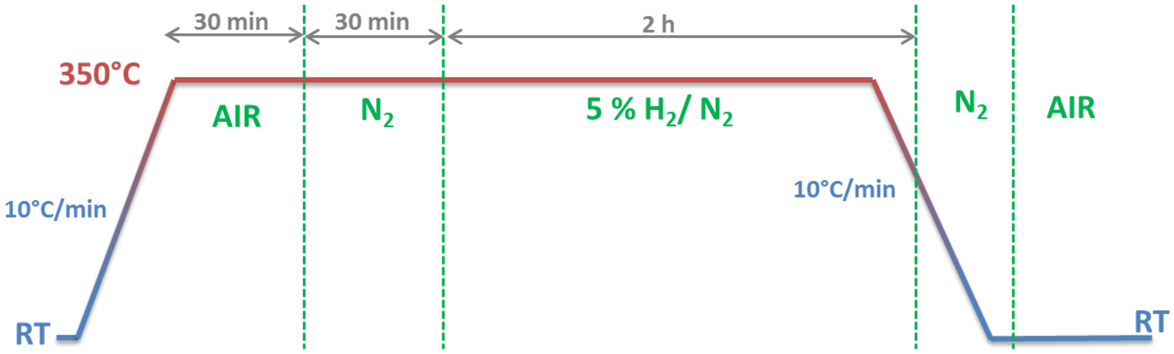

Figure A-C. 9. Temperature profile of the treatment used to activate the graded membrane according to the Colorado School of Mines method.

Initially, Pd acetate gives the surface a yellowish colour after drying, but after thermal treatment a homogeneously metallic grey surface is observed (see photographs in Figure A-C. 10). The final plating covers the entire surface homogeneously so it seems a suitable activation method. However, this method involves thermal heat treatment and it is more time consuming compared to WPI’s Pd-Sn activation method. Hence, alternative activation methods were explored.

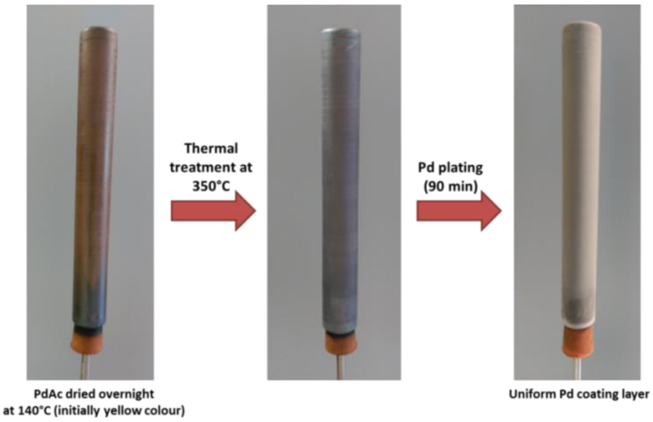

Figure A-C. 10. Photographs taken during the Pd acetate activation. From left to right: after deposition of Pd acetate and drying overnight, after the thermal treatment at 350°C and after plating for 90 minutes.

Activation method B

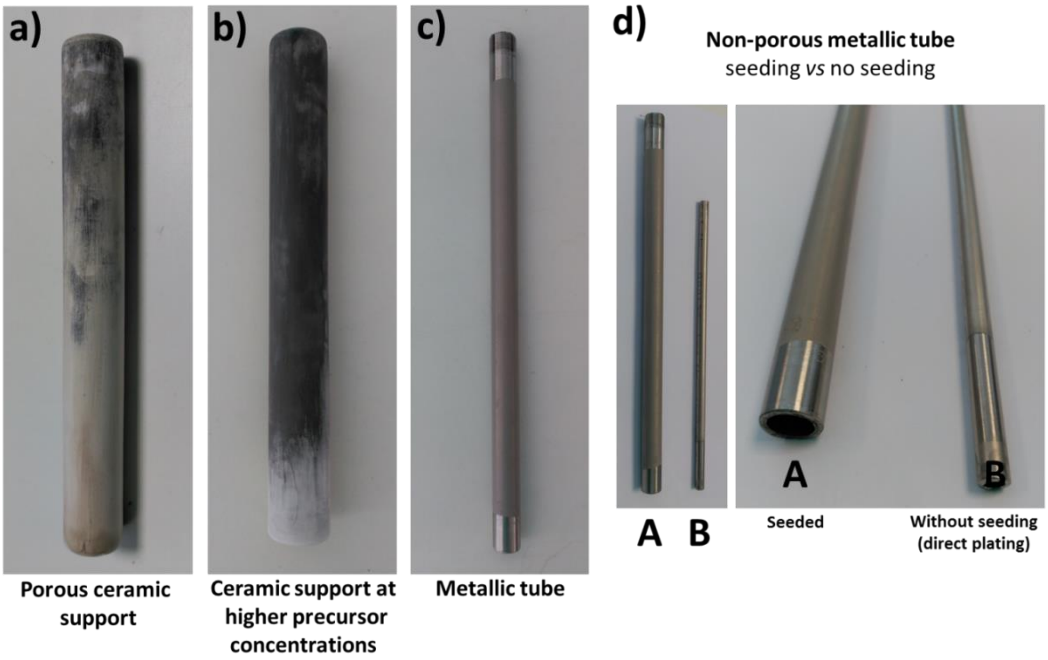

Figure A-C. 11. a) Photograph of a plated ceramic support activated using method B. b) Photograph of a plated ceramic support activated using method B with higher concentration and plating. c) Photograph of a sample prepared using the same procedure as in b) but on a non-porous metallic tube. d) Photograph comparing the Pd layer obtained by seeding and successive plating (A) and a directly plated metallic tube (B).

This method uses JM's expertise in PGM chemistry and will avoid the need of thermal treatment used in Activation Method A. In our first attempt, low concentration of Pd was used and this resulted in poor and uneven plating (Figure A-C. 11a). When a higher concentration of Pd was used, the uniformity of the Pd coating improved considerably (Figure A-C. 11).

In order to verify that this procedure can be also implemented on PSS supports, dense stainless steel tubes were used as supports. The dense stainless steel tube, shown in Figure A-C. 11c, exhibits a uniformly coated Pd surface. In Figure A-C. 11d, the uniformly coated tube is compared to a dense stainless steel tube electroless plated without any activation. It can be observed that the tube without any activation has a thinner and less uniform Pd surface. This suggests that this activation method can be implemented on the PSS support.

Activation method C

This is a modification of method B and is also meant to avoid the high temperature treatment used in method A. After activation, the surface of the ceramic tube presents a greyish black colour and after electroless plating a homogeneous metallic layer is observed (**Error! Reference source not ound.**).

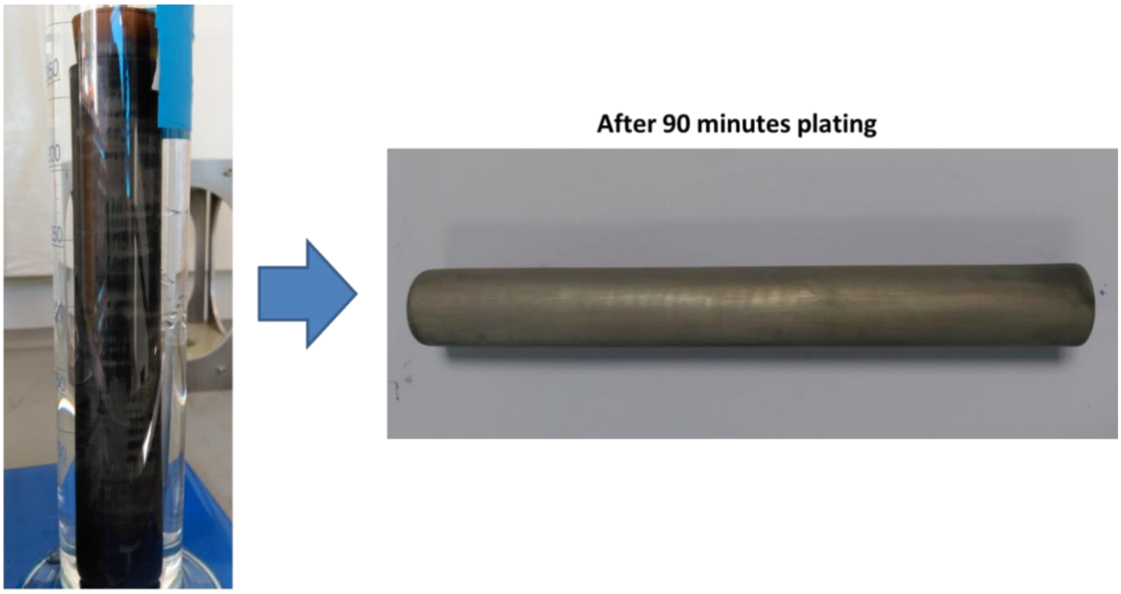

Ceramic tube after seeding

After 90 minutes plating

Figure A-C. 12. Photograph of a ceramic tube seeded with activation method C and after successive plating.

Activation method D

This method uses another of JM's proprietary technologies. In the first trial (A in Figure A-C. 12) the surface of the ceramic tube was not very uniformly coated and shows a blackish colour. This suggests that nanoparticles, instead of a Pd film, are formed on the surface of the support. By increasing the concentration used for activation, a more uniform metallic coating was obtained after plating (B in Figure A-C. 13). This method seems to be a promising strategy to replace WPI's original activation method. However, better understanding on the influence of the additives added needs to be investigated.

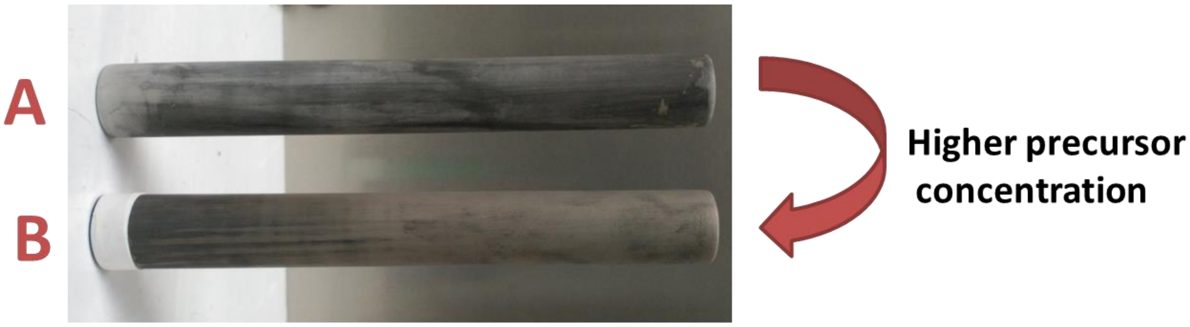

Figure A-C. 13. Photograph of two ceramic membranes prepared using method D. A has lower activation concentration than B.

A-C.3.4. Pd membrane synthesis

The entire synthesis procedure to fabricate the Pd membranes was examined and the changes described in the above sections were implemented in order to further reduce the number of steps. Table A-C. 5 summarizes the total number of steps required to synthesize the different dense membranes.

By using JM's proprietary thin film coating technology in the grading procedure, the Pd membrane synthesis can be reduced to 68 steps. As discussed earlier, the use of JM's proprietary thin film coating technology is mainly to improve the reproducibility of the membrane synthesis.

The next major modification made to the synthesis procedure is able to reduce the number of steps to 46, which has 39% step reduction in WPI's original synthesis procedure. Further modification made allows Pd membranes to be synthesized in 43 steps.

Table A-C. 5. Total number of steps required to synthesize the Pd membranes.

Method	Description	Sample	Total # of synthesis steps	Steps reduction
WPI	Original WPI's procedure	Ma153 (reference)	75	-
JM-v1	WPI's procedure but using JM's proprietary thin film coating technology during grading	JM0017	68	9%
JM-v2	-	JM0026, JM0036	46	39%
JM-v3	-	JM0028, JM0035	43	43%

Figure A-C. 13 shows that the modifications made to the membrane synthesis procedure did not change the properties of the membranes at room temperature. The He permeance and the Pd thickness of the membranes synthesized using the modified procedures are comparable to WPI's and JM's reference. JM35 and JM36 have approximately 2 μm thicker grading layers due to the use of 1 μm grade PSS supports instead of the usual 0.5 μm grade.

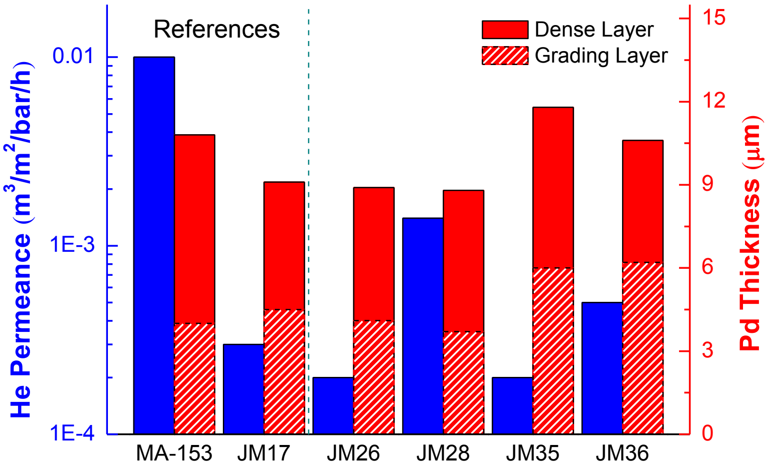

Figure A-C. 14. He permeance and Pd thickness for the dense membrane synthesized using a modified procedure.

A-C.3.5. Porous Stainless Steel Supports

The characteristics of the PSS support have a significant influence on the quality of the Pd membrane being synthesized. For instance, different batches of PSS supports provided by Mott with the same specifications yield very different membranes.

PSS supports from an alternative supplier were also investigated to determine if a similar procedure could be used to synthesize Pd membranes with the required quality as supports supplied by Mott. For this purpose, JM obtained two types of PSS supports from alternative suppliers.

Type 1 Supports

As shown in Table A-C. 6, the Type 1 PSS supports were found to have lower initial N_2 permeance than Mott tubes. In general, the Pd membranes prepared on Type 1 supports have a lower He leak than those prepared on Mott ones.

JM2001 and JM2002 (Table A-C. 6) were synthesized using the grading procedure developed using JM's proprietary thin film coating technology (same procedure as JM0017, 28 and 26). The He permeance after grading the support from the new supplier is comparable to the He permeance of the dense Pd membrane prepared on Mott supports (compare JM2001/2 to JM0017).

It was found that the polishing procedure used on Mott tubes has a detrimental effect on the He permeance of the graded membrane prepared on Type 1 supports. As seen in Figure A-C. 15a, an increase in He permeance was observed after the polishing. This indicates that the polishing has introduced additional defects to the graded membrane. By omitting the polishing step, very low He leak on the dense Pd membrane can be achieved after two electroless plating steps (Figure A-C. 15b).

Table A-C. 6. Comparison between nitrogen and helium flux for the PSS tubes supplied by Mott and an alternative supplier. J is given in $Nm^3/m^2/h/bar$ and thickness in µm.

Sample	Method	PSS Supplier	J_{N2} bare tube	J_{N2} after sol-gel and calcination	Grading		Dense membrane		Total # of steps	Step reduction[c]
					J_{He}	Pd thickness	J_{He}	Pd thickness		
JM0017	JM-v1	Mott	1082	817	0.31	4.5	0.0003	4.4	68	9%
JM0028	JM-v3		1018	854	2.17	3.7	0.0014	5.1	43	43%
JM0026	JM-v2		1132	716	0.10	4.1	0.0002	4.8	46	39%
JM2001	JM-v3	Other	620	499	0.05	3.6	0.0016	6.3	43	43%
JM2002	JM-v3[b]		663	529	0.006	2.9	0.0006	4.4	38	49%
JM2003	JM-v4		614	494	6.80	2.6	0.0065	5.8	34	55%
JM2004	JM-v4a		636	441	2.79	2.7	1.36	4.5	32[a]	57%

[a] Total synthesis steps would be 34 steps, however due to poor quality of the membrane, the synthesis was stopped prior the last plating step. [b] Membrane was synthesized using JM-v3 method, however the polishing step after the grading was omitted. [c] Step reduction with reference to WPI's original 75 steps procedure.

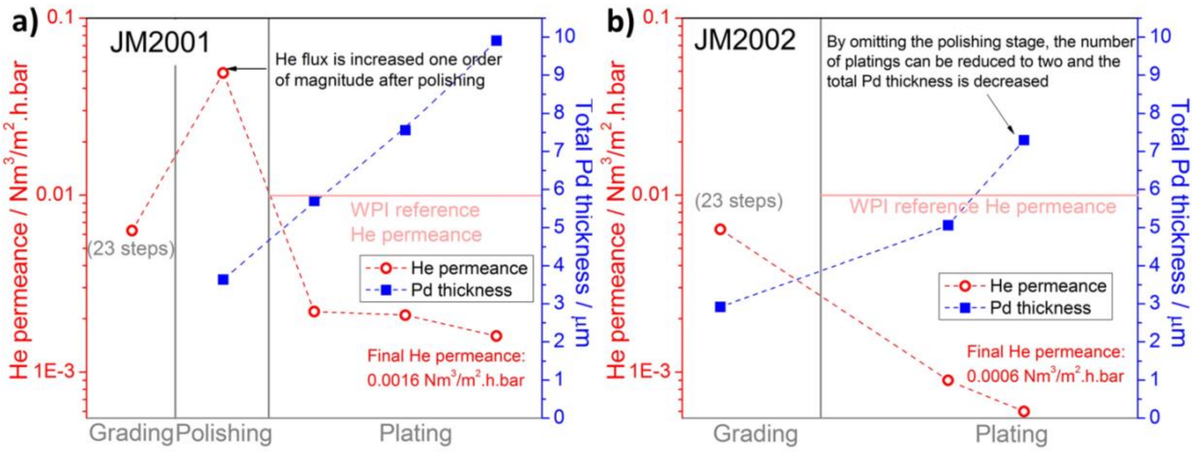

Figure A-C. 15. a) Evolution of He permeance and Pd thickness for a) JM2001 and b)JM2002 during the different synthesis stages.

Although the number of plating steps can be reduced using the Type 2 supports, the priority is to decrease the total number of steps by shortening the grading procedure as it is more difficult to scale up. JM's proprietary thin film coating method was modified to reduce the number of steps. Two different strategies were used: the first still used both 4 µm and 0.6 µm particles for grading (shown in Figure A-C. 16a) and the second used only the 0.6 µm particles (shown in Figure A-C. 16b). Figure A-C. 16a shows that by using both 4 µm and 0.6 µm particles for grading, the final dense Pd membrane has lower He permeance compared to WPI's reference (JM-v4, JM2003). However, if only 0.6 µm particles are used, the He permeance of the dense Pd membrane is one order of magnitude higher than WPI's reference permeance (Figure A-C. 16b, JM-v4a, JM2004).

From these results, it can be concluded that by using Type 1 supports, Pd membrane with the required quality can be synthesized in 34 steps using method JM-v4.

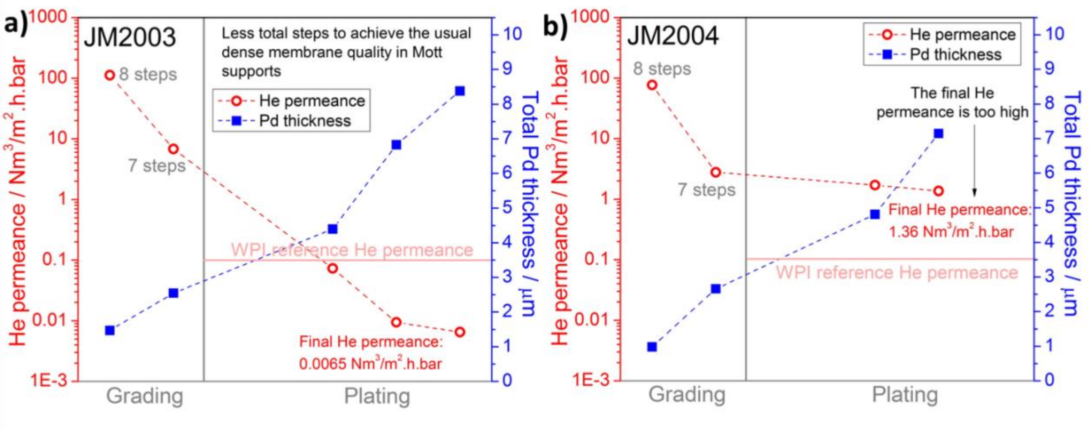

Figure A-C. 16. a) Evolution of He permeance and Pd thickness for a) JM2003 and b) JM2004 during the different synthesis stages.

Type 2 Supports

The initial nitrogen flux through these Type 2 supports is ~ 100 Nm^3/m^2/h/bar (see Table A-C. 7). This value is much lower than in Mott (~ 1000 Nm^3/m^{2}hbar) and Type 1 (~ 700 Nm^3/m^2/h/bar) PSS supports. The use of Type 2 supports to fabricate the Pd membrane has the potential to significantly reduce the number of synthesis steps.

Table A-C. 7. Nitrogen and helium flux for the membranes prepared in supports provided by an alternative supplier. J is given in Nm^3/m^2/h/bar and thickness in µm.

Sample	**J_{N2} bare tube**	**Grading**			**Dense membrane**		**Total synthesis steps**	**Step reduction[4]**
		Grading method	**Pd thickness**	**J_{He}**	**Pd thickness**	**J_{He}**		
WPI Ref.	-	WPI's original grading method	-	4.4	6.8	0.01[b]	75	-
JM Ref.[1]	854	JM's proprietary thin film coating technology	3.7	2.2	5.1	0.0014	43	43%
JM4001	78	Modified method using JM's proprietary thin film coating technology	1.0	13.0	7.0	0.0015	19	75%
JM4002	102	Modification 1	2.0	0.1	3.9	0.0053	17	77%
JM4003	93	Modification 2	-	-	-	-	-	-
JM4004[2] (JM-v5)	86	Modification 3	2.1	0.03	5.4	0.0001	17	77%
JM4005 (JM-v5)	112	Modification 3	1.7	0.14	6.1	N.D.[3]	17	77%

[1] Pd membrane fabricated on Mott support at JM with the least number of synthesis steps (JM0028). [2] Shorter tubes was used. [3] N.D. indicates He flow was not detected after synthesis. [4] Step reduction with reference to WPI's original 75 steps procedure.

The synthesis procedure was modified and the characteristics of the resulting membranes are summarized in

The initial nitrogen flux through these Type 2 supports is ~ 100 Nm^3/m^2/h/bar (see Table A-C. 7. The general trend is that Pd membranes can be synthesized on Type 2 supports with fewer than 20 steps. This is significantly shorter than both WPI's and JM's reference membranes.

The grading method used for JM4001 and JM4002 led to uniform Pd surfaces.. However, the grading method used to synthesize JM4003 was not effective and the surface was irregularly plated (Figure A-C. 17).

In order to rectify the issue with JM4003, Modification 3 was used in the synthesis. This synthesis method resulted in membranes showing very low He permeance and a very significant decrease in the overall number of synthesis steps. The use of this method may ultimately lead to lower manufacturing cost to fabricate the Pd membranes.

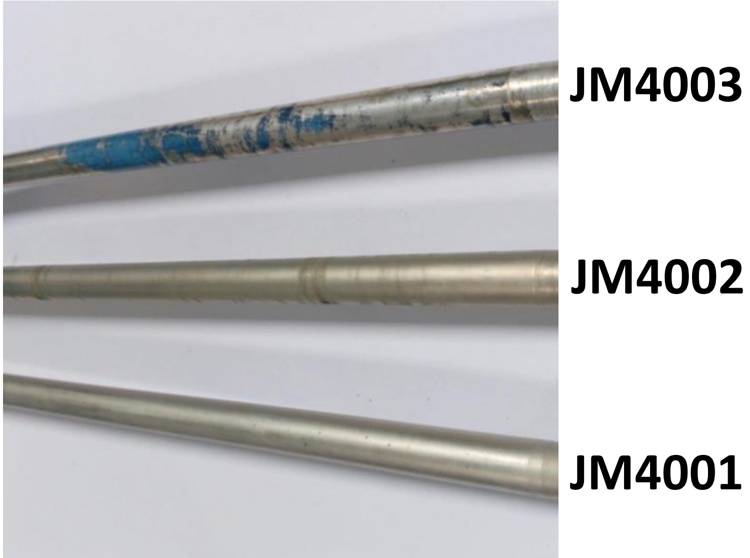

Figure A-C. 17. Photograph of the membranes JM4001, JM4002 and JM4003.

For the US DOE funded program, WPI's preferred PSS supplier is Mott; the use of Type 1 and Type 2 support was not thoroughly investigated.

A-C.3.6. High temperature test

The Pd thickness and He leak tests give an indication of the quality of the Pd membrane at room temperature. Two different methods are used to evaluate the performance of the Pd membrane upon exposure to high temperature. The first method is the "High Temperature Aging Test", developed and performed at JM, consists of measuring the inert gas leak across the membrane before and after exposing the membrane to high temperature aging in 5% H_2/N_2 atmosphere. The second method is the "High Temperature H_2 Permeance Test", which is measured at WPI and mimics the operation conditions of the membrane. It evaluates both the H_2 flux and the inert leak across the membrane at high temperature.

High Temperature Aging Test

As the Pd membrane setup at JMTC is not equipped to test the membrane performance at high temperature, an aging test was performed to evaluate the formation of defects on the membrane after exposing it to a high temperature reducing atmosphere. Figure A-C. 18a shows the temperature profile used for the high temperature aging test. The samples were heated under N_2 flow to 450°C before switching to a 5% H_2/N_2 mixture. The sample was kept at 450°C under reducing atmosphere for approximately 5 days before being cooled to room temperature under an inert atmosphere. He permeance was measured before and after the ageing test at room temperature.

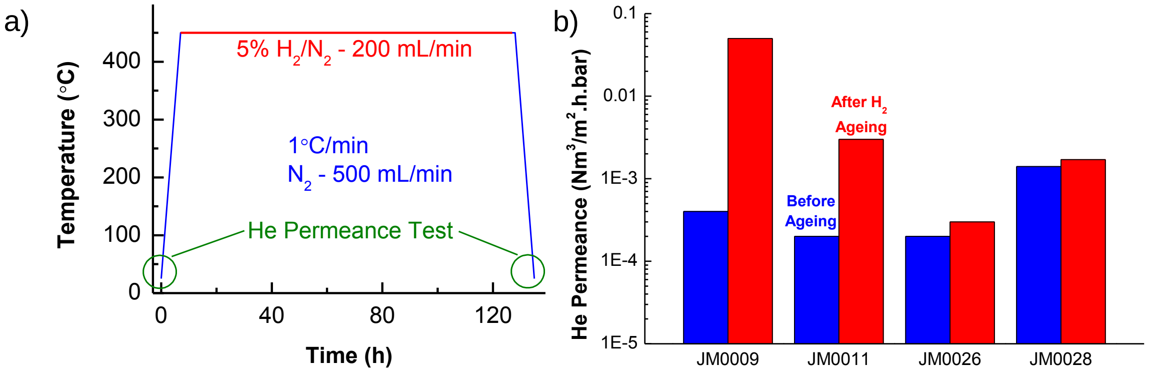

Figure A-C. 18. (a) Temperature profile used for high temperature hydrogen aging and (b) He permeance through the dense Pd membrane before and after aging.

Figure A-C. 18b shows the He permeance through the dense Pd membrane before and after high temperature aging. Both JM0009 and JM0011 are very early versions of the Pd membrane prepared using a method similar to WPI. JM0026 and JM0028 were synthesized using JM-v2 and JM-v3 as described in Table A-C. 2 and Table A-C. 5. After high temperature H_2 aging, the He permeance through the membrane increased by two orders of magnitude for JM0009 and JM0011. However, He permeance through JM0011 is still lower than the He permeance of the reference support prepared at WPI prior aging (Table A-C. 14, Ma-153). The He permeance of the aged JM0009 is of similar order of magnitude but slightly higher than the un-aged reference (Ma-153). No visible change in the membranes was observed via physical inspection and using an optical microscope. Suspected causes for the increase in He permeance include (1) joint failure and (2) formation of bigger pin holes on the membrane. The exact cause of the membrane failure was not identified at that point of time as the water rise test setup was not available to determine the leak location.

For JM0026 and JM0028, the high temperature aging has only minimum influence on the He permeance, suggesting that these membranes have better stability than JM0009 and JM0011. The better stability for JM0026 and JM0028 is probably due to the improvement made to the grading by using JM's proprietary thin film coating method and also JM's in-house method to remove the excess particles.

The high temperature aging test was also performed on Type 1 and Type 2 PSS support. The He permeance for Type 2 support (JM4005 and JM4006) increased one order of magnitude after the high temperature aging (see Table A-C. 8). However these values are still comparable to WPI's reference membrane prior heat treatment.

For Type 1 support (JM2002), the membrane was unaffected by the high temperature aging.

Table A-C. 8. He permeance for Pd membranes prepared on Type 2 supports. Values have been taken before and after the ageing treatment at 450°C in 5% H2/N2.

Sample	**J Dense membrane /** Nm^{3}m^{-2}h^{-1}bar^{-1}	**J after thermal treatment /** Nm^{3}m^{-2}h^{-1}bar^{-1}
JM2002	0.0006	0.0006
JM4005	No leaks detected	0.0284
JM4006	0.0017	0.0098

High Temperature H_2 Permeance Test

Through the project, eight membranes (JM0011, JM0017, JM0019, JM0035, JM0036, JM0028, JM2005 and JM4007) were sent to WPI for a high temperature H_2 permeance test. The difference between these samples is the number of steps required to synthesize them. The number of synthesis steps and also the properties of these membranes are summarized in Table A-C. 9.

Table A-C. 9. Properties of dense Pd membrane sent to WPI.

Sample	Method	Number of Synthesis Steps	Thickness (μm)			He Permeance at RT ($Nm^3/m^2/bar/h$)		
			Grading	Dense	Total	JM	WPI	JM[a]
JM0011	Modified WPI	84	4.5	4.4	8.9	0.0030	0.0031	-
JM0017	JM-v1	68	4.5	4.6	9.1	0.0003	0.0014	-
JM0019	-	63	4.8	5.4	10.2	0.0200	0.0370	-
JM0036	JM-v2	46	6.2	4.4	10.6	0.0005	-	0.0006
JM0035	JM-v3	43	6.0	5.8	11.8	0.0002	-	0.0019
JM0028	JM-v3	43	3.7	5.1	8.8	0.0014	-	-
JM2005	JM-v4	34	3.8	6.0	9.8	0.0021	-	-
JM4007	JM-v5	17	2.1	4.3	6.4	0.0003	-	-

[a] He permeance measured at JM after high temperature permeance test at WPI.

From Figure A-C. 19 it can be observed that all the membranes which were sent to WPI exhibit good thermal stability during the test period except JM0019. The H_2 permeance remained relatively stable and the He permeance is low for all the stable membranes. For JM0019, the H_2 permeance increases gradually overtime, however this gradual increase is due to the increase in non-selective transport of gases across the membrane. This is evident by a drastic increase in the He leak for JM0019.

Table A-C. 10. Performance of different Pd membrane tested at high temperature.

Sample	Method	Number of Synthesis Steps	H_2 Permeance at 450°C ($Nm^3/m^2/h/bar^{0.5}$)	H_2/He ideal selectivity after 200h at 450°C
JM0011	Modified WPI	84	35	5 200
JM0017	JM-v1	68	42	1 400
JM0019	-	63	15	123
JM0035	JM-v3	43	30	370
JM0036	JM-v2	46	10	22 000
JM0028[a]	JM-v3	43	-	-
JM2005	JM-v4	34	27	5 000
JM4007	JM-v5	17	17	35 000

[a] Very high He leak was detected at WPI and high temperature permeance test was not carried out. The membrane was probably damaged during transport.

The H_2 permeance and H_2/He ideal selectivity for the Pd membranes synthesized using different method is summarized in Table A-C. 10. For the Pd membrane synthesized on Mott supports, the membrane with the least defect at high temperature is synthesized using JM-v2, JM0036, and the membrane which exhibits the highest H_2 permeance is synthesized on JM0017.

JM4007 exhibits the least defects amongst all the membrane as it has the highest H_2/He ideal selectivity. This is probably due to the modifications made at JM and also the support used from the alternative supplier. The Pd layer is thinner on JM4007 than JM2005 and the synthesis procedure used for both membranes are very similar. Hence the lower H_2 permeance for JM4007 is probably due to the nature of Type 2 support supplied by the alternative supplier.

Based on the high temperature H_2 permeance results, the Type 1 support supplied by the alternative supplier is able to synthesize Pd membrane comparable to those synthesized on Mott's support. JM2005 can be synthesized using only 34 steps and it exhibit comparable H_2 permeance and H_2/He to the other membranes.

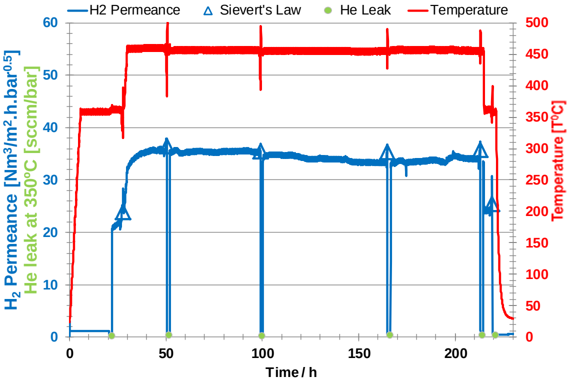

(a) JM0011

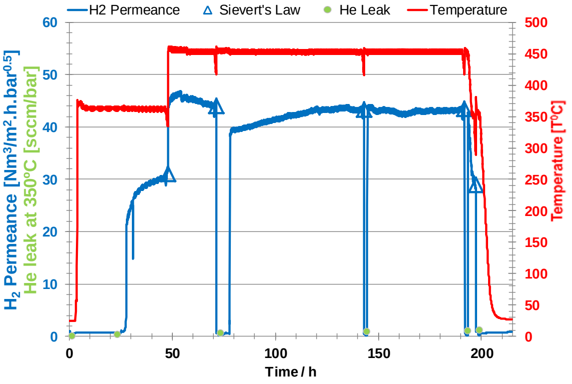

(b) JM0017 (JM-v1)

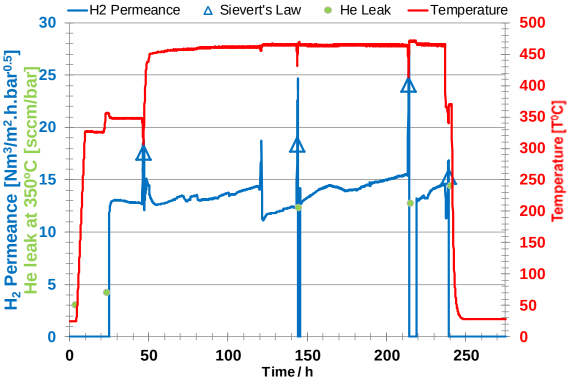

(c) JM0019

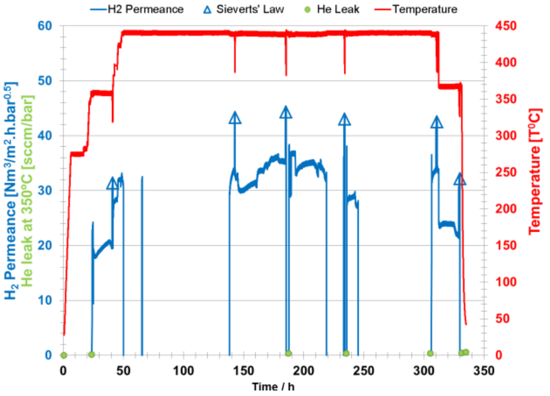

(d) JM0035 (JM-v3)

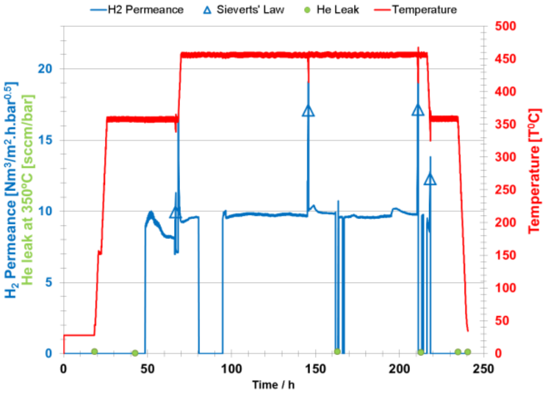

(e) JM0036 (JM-v2)

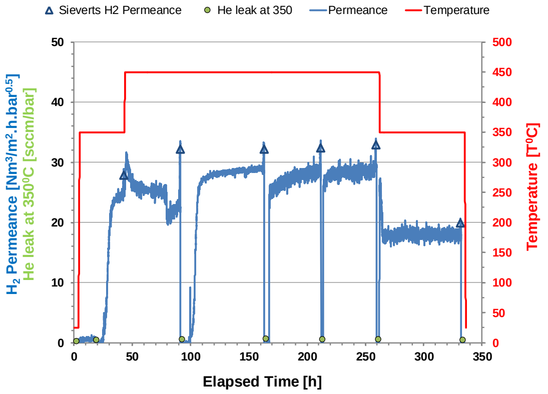

(f) JM2005 (JM-v4)

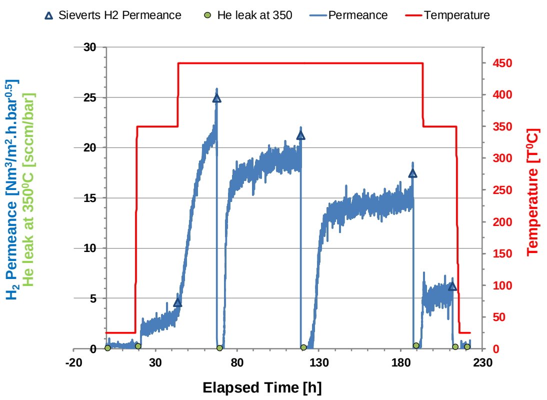

(g) JM4007 (JM-v5)

Figure A-C. 19. H_2 permeance and He leak as a function of time and temperature for Pd membrane synthesized using different methods.

A-C.4. Pd membrane synthesis scale-up

The development of the synthesis method for Pd membrane described in Section 3. The aim was to acquire a manufacturing method for Pd membranes which can be scaled to produce longer and larger quantities of Pd membranes if future business opportunity arises. Although automation and further process optimization needs to be implemented to the method for large scale manufacturing of Pd membranes, the developed method was used to synthesized membranes up to 24” length and also a batch of ten 15” Pd membranes to evaluate its scalability. These results are being discussed in this section.

A-C.4.1. Synthesis of longer membranes

The procedure for the Pd membrane synthesis was predominantly developed using 6” PSS support from Mott. The method developed was then used to synthesize 15” and 24” Pd membranes. 15” PSS support was selected, as the muti-tubular membrane module used in the current DOE project is designed to accommodate Pd membranes of this length. 24” membrane was selected based on the maximum continuous length PSS support which can be supplied by Mott.

Table A-C. 11. Pd membranes prepared on Mott 0.5” OD - 24” L PSS 316L, 0.5 µm median grade supports.

Sample	Sample Length	Pre-treatment	Grading		Plating		Total thickness µm
		J_{N2} $Nm^3m^{-2}h^{-1}bar^{-1}$	Thickness µm	J_{He} $Nm^3m^{-2}h^{-1}bar^{-1}$	Thickness µm	J He $Nm^3m^{-2}h^{-1}bar^{-1}$	
Ma153[1]	6”	430	-	4.4	6.8	0.01	-
JM0017	6”	817	4.5	0.3	4.6	0.0003	9.1
JM3001	15”	729	2.8	1.9	6.5	0.0017	9.4
JM6001	24”	956	6.7	3.2	8.1	0.0015	14.8

[1] Membrane synthesized at WPI is given as a reference.

Table A-C. 11 shows that the Pd membrane synthesis method developed at JM can be easily scaled to synthesize 15” membranes. The total Pd thickness for the 6” and 15” Pd membranes are comparable. Although the He permeance of the dense membrane and grading is higher for the 15” compared to the 6” membrane, it is still thinner than the membrane synthesized at WPI.

The synthesis method was also successfully applied to synthesize 24” length Pd membrane. The He permeance after grading and the dense membrane is comparable to the values for both the 6” and 15” membrane. However the Pd layer for the 24” Pd membrane is thicker compared to the shorter membranes for both the grading and dense layer. This is probably due to the need to optimize the conditions used for electroless plating. Since the aim of the DOE funded project does not require 24” membrane to be synthesized, the plating conditions for the 24” Pd membrane was not optimized.

A-C.4.2. Synthesis of multiple membranes

The procedure for the Pd membrane synthesis was applied to synthesize a batch of ten 15” Pd membranes. Although the same synthesis procedure is used, the grading layer for the batch of ten Pd membranes is almost twice as thick as those synthesized earlier with no significant decrease in the He leak (JM3001 and JM3002). Table A-C. 12 shows that the estimated thickness for the graded layer of the first two 15” membranes is below 3.5 µm, while for those prepared as part of ten membrane batch it is around 6 µm (JM3007 to JM3018). Several parameters which will affect the plating during grading were evaluated to elucidate the origin of the increase in Pd thickness for the grading layer.

Table A-C. 12. Pd membranes prepared on Mott 0.5” OD - 15” L PSS 316L, 0.5 µm median grade supports.

Sample	Pretreatment	Grading			Plating		Total thickness µm
	J_{N2} Nm^{3}m^{-2}h^{-1}bar^{-1}	Loading mg/cm^2	Thickness µm	J_{He} Nm^{3}m^{-2}h^{-1}bar^{-1}	Thickness µm	J_{He} Nm^{3}m^{-2}h^{-1}bar^{-1}	
JM3001	729	3.4	2.8	1.9	6.5	0.0017	9.4
JM3002	729	4.3	3.5	0.1	6.2	0.0005	9.7
JM3007	804	7.7	6.4	0.8	7.4	0.0007	13.8
JM3008	839	7.5	6.2	0.6	7.4	0.0007	13.6
JM3009	768	5.8	4.7	5.6	6.5	0.0011	11.1
JM3010	778	7.1	5.9	0.1	5.5	0.0042	11.4
JM3011	781	7.9	6.5	3.7	6.8	0.0008	13.4
JM3013	746	7.7	6.4	1.6	7.0	0.0020	13.4
JM3014	738	7.4	6.1	0.5	6.1	0.0040	12.2
JM3015[1]	719	5.8	4.7	0.6	6.1	0.0318	10.8
JM3016	799	7.1	5.8	3.4	6.3	0.0054	12.1
JM3017[1]	753	6.6	5.4	2.5	8.1	0.0822	13.5
JM3012	718	7.6	6.3	0.4	8.2	0.0059	14.5
JM3018	719	6.5	5.3	0.1	6.4	0.0019	11.7
Average[2]	769 ± 39	7.2 ± 0.6	6.0 ± 0.6	1.7 ± 1.9	6.8 ± 0.8	0.0027 ± 0.0020	12.7 ± 1.2

[1] Membrane were damaged during the synthesis of the final dense layer. [2] Exclude reference (JM3001 and JM3002) and damaged membranes (JM3015 and JM3017).

Temperature

An increase in the plating temperature could accelerate rate of Pd deposition. JM3012 was prepared with more an accurate temperature control and without pre-heating the cold cylinders prior to plating. The thickness of the graded layer prepared in these conditions is 6.3 µm (Table A-C. 12, JM3012) which suggests that temperature is not the cause.

Hydrazine

Hydrazine is known to slowly degrade with time. Another possible hypothesis is that the hydrazine used for the reference JM3001 and JM3002 was aged, hence resulting in a thinner Pd layer. The activity of hydrazine was assessed by titration with sulphuric acid to determine the equivalence point. The titration curve, given in Figure A-C. 20, shows minor differences between a freshly prepared hydrazine solution and after 20 days storage. From the equivalent point, the concentration can be calculated. By assuming that hydrazine is fully dissociated (this is not true as hydrazine is a weak acid and will be governed by its dissociation equilibrium), the concentration has decreased from 1.07 M to 1.03 M. This change does not seem significant enough to cause the observed changes in Pd thickness.

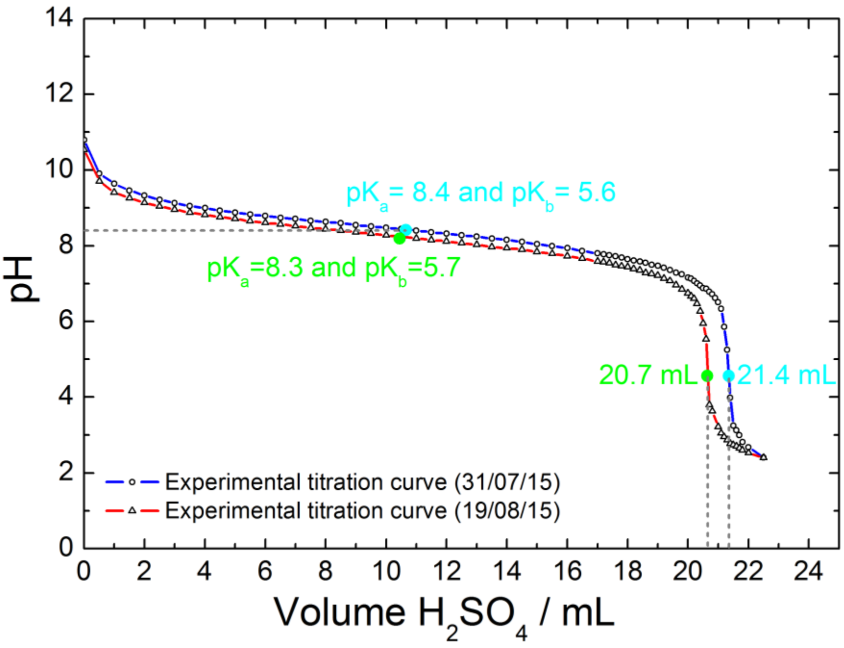

Figure A-C. 20. Hydrazine titration curve for 20 mL of hydrazine solution used for plating neutralized with 0.5 M H_2SO_4 solution. The blue curve was taken immediately after preparing the hydrazine solution and the red one 20 days after. Pka and equivalence points are indicated in the figure. The reported pKa of hydrazine is ~8.

Plating solution

Aging of the plating solution could reduce the thickness of the Pd layer during its deposition. In order to determine the influence of the plating solution age, the solution was kept for a week before using it for grading. The thickness of the graded layer is 5.3 µm (see JM3018 in Table A-C. 12). Although the value is one of the lowest among the membranes that we have recently prepared, it is still thicker than the first two 15" membranes. Hence, the age of the plating solution has only minor influence on the grading thickness.

Based on the studies described above, it can be concluded that the change in plating condition is not the cause for thicker Pd layer. This is also supported by the fact that the thickness of the dense Pd layer for the batch of ten membranes is comparable to the values of the reference membranes.

Further work is required to identify the cause of the thicker Pd layer, since thinner Pd layer is desired for both rate of H_2 permeance and membrane cost.

This batch of ten 15” Pd membranes was supposed to be tested at the NCCC. However due to delays in the fabrication of the multi-tubular module and the cancellation of several planned gasifier trial runs, testing of the Pd membranes synthesized at JM was not realized.

A-C.5. Pd -sorbents for contaminant removal

In an effort to increase the clean utilization of abundant global coal reserves, stakeholders such as governments, miners and power companies have been, are currently and will be for many years, seeking new technologies to improve extraction, processing and conversion of coal to energy. Whilst the majority of energy produced from coal arises from combustion processes, strategies such as gasification are being developed with the goals of achieving greater thermal efficiencies, wider chemical product diversity and better control of waste streams.

The development of mercury sorbents to replace the activated carbon beds, which are unsuitable for higher temperature operation, has seen a wide range of candidate materials trialled, the majority being modified oxides, such as those of copper and manganese, supported on inert oxide carriers. In the late 1990s – early 2000s the US National Energy Technology Laboratory (NETL) in Pittsburgh investigated a wide range of materials, including some based on the platinum group metals

(PGMs). It has been known for many years that mercury will form amalgams with the various PGMs and gold – the latter amalgams have been used in applications as diverse as gold mining, deposition of thin gold films and as sorbents in instrumentation. During laboratory trials in synthetic syngas streams, the NETL researchers found that Pt and Pd both possessed good uptake capacity for mercury vapour in the temperature range desirable for WGC.

In 2005 Johnson Matthey and NETL signed a Cooperative Research and Development Agreement to develop palladium-containing sorbent materials based upon the initial patent filing by NETL. The three-year programme was very successful, both in the range of materials examined and in the close collaboration and friendship that remains in place.

After a series of successful laboratory trials, and a positive economic assessment report, time was allocated on-stream at the pilot-scale development facility at Southern Company's plant in Wilsonville, Alabama. In July 2008, after the successful transfer of the palladium sorbents onto alumina bead carriers, the first trial of a 5wt%Pd sorbent was carried out in a sweet (desulphurized) syngas stream. In addition to successfully removing Hg, As and Se for the entire duration, the sorbent also removed the 1-5ppm H_2S that had "slipped" past the zinc oxide sorbent beds, so protecting the equipment on trial downstream. Analysis of the sorbent bed, removed in separate 2" layers, showed that the majority of the trapped Hg, As, Se and S was in the top of the bed, confirming that a large proportion of the capacity was unused.

Subsequently, eight further trials of 2wt.% and 5wt.% Pd sorbents in sweet and "sour" syngas streams derived from Mississippi lignite and Powder River Basin sub-bituminous coals have been carried out since 2008, the most recent ending in November 2015 (see Table A-C. 13 below). In all cases the palladium sorbent removed the inlet Hg, As and Se from the syngas stream for the duration of the trial, in both sour and sweet syngas.

Ease of sorbent regeneration was one of the key features targeted by the US DOE in their initial programme outlines. After Trial R-10 in April 2013 the used sorbent was returned to Johnson Matthey for regeneration. The regenerated sorbent was re-used in the three subsequent trials and successfully removed all inlet Hg, As and Se. The sorbent bed remains in place in the NCCC facility having been planned into the March 2016 gasifier trial. That the sorbent functions well after regeneration is extremely pleasing, leading the JM-NETL-NCCC team to begin drafting a publication highlighting the success.

Table A-C. 13. Summary of the conditions and results of the trials of palladium sorbents at the Southern Company PSDF (NCCC) facility in Wilsonville, Alabama.

	Run 1 (TC-25)	**Run 2 (R01)**	**Run 3 (R04)**	**Run 4 (R05)**	**Run 5 (R06)**	**Run 6 (R-10)**	**Run 7 (R-13)**	**Run 8 (G1)**	**Run 9 (G2)**	**Run 10 (G3)**
Date	**Jul-08**	**Feb-09**	**Apr-10**	**Aug-10**	**Aug-11**	**Apr-13**	**Mar-April 2014**	**Oct-Nov 2014**	**Oct-Nov 2015**	**Feb-Mar 2016**
Coal Type	MS Lignite	MS Lignite	MS Lignite	PRB	PRB	PRB	PRB	PRB	Lignite	PRB/Lignite
Syngas Quality	Sweet Syngas Shifted, HC Free (hydrocarbon cracked)	Sour Syngas Particulates-Free (hydrocarbons present)	Sour Syngas Particulates-Free	Sour Syngas Particulates-Free	Sour Syngas Particulates-Free	Sour Syngas Particulates-Free	Sweet Syngas, shifted	Sweet Syngas, shifted	Sweet Syngas, shifted	Sweet Syngas, shifted
H_2S Level (ppm)	1 – 5	1200 – 1600	1200 – 1600	300 – 500	300 – 500	317	1 – 5	1 – 5	1 – 5	
Flow Rate (lb/hr)	20 – 40	40	10	25	25	49.5	50	50	50	50
space velocity (hr^{-1})	1632-3263	3218	824	1810	1854	3708	4164	4164	4164	4164
Pd-loading (wt%)	5	5	2	5	2	2	2 (Regen^d R-10 bed	2 (Regen^d R-10 bed	2 (Regen^d R-10 bed	2 (Regen^d R-10 bed
Operating T (°F)	500	500	500	500	500	435	500	500	500	
Operating P (psig)	150 – 200	165	180	180	180	199	180	180	190	
Run Time (hr)	330 (260 with HC, 70 without)	170, last sample 166	500, last sample 467	718, last sample 642	1011, last sample 1011	492, last sample 470	540	556	680	
Hg Removal (%)	> 96	98 – 99	99.7 for 370 hr	96 – 100	96 – 100	96-100	96-100	96-100	96-100	

It was the success of the initial palladium sorbent trials that lead to the suggestion during the proposal stage of the WPI-led programme that a “polishing” bed of Pd sorbent could be incorporated upstream of the planned palladium membrane module at the NCCC facility. Although the NCCC gasification stream has hydrocarbon-cracking, sulphur removal and water-gas shift reactors downstream of the gasifier in order to sweeten the syngas, experience had shown that slippage of one or more contaminants occasionally occurred, which could lead to impaired performance of the membrane module. As part of their contribution to the programme, JM agreed to supply a sorbent bed to be installed ahead of the membrane module to “polish” the inlet syngas.

Unfortunately, the time constraints in the programme and the NCCC gasifier, and the space constraints within the WPI skid, meant that the incorporation of the palladium sorbent bed within the WPI trial was not achieved. However, the continued success of the sorbent bed within the NCCC gasifier stream provides confidence that a downstream membrane module would be adequately protected from contaminant slippage.

Further details of the NCCC gasification trials can be found on the website :

http://www.nationalcarboncapturecenter.com/Publications.htm

Conclusions

In this project, JM have successfully completed the project deliverable in Phase II of the project entitled “Design of Advanced H_2-CO_2 Pd and Pd/Alloy Composite Membrane Separations and Process Intensification,” to help WPI in meeting the overall project object.

Through this project, JM has successfully developed an improved method to manufacture Pd membranes based on WPI’s original procedure. The manufacturing method developed can be used to fabricate Pd membranes with better reproducibility and also using between 40 to 80% fewer steps than WPI’s original procedure. In addition, the developed synthesis procedure has been applied to synthesize Pd membranes up to 24”L. The developed manufacturing procedure was also applied to fabricate a batch of ten 15” length Pd membranes with good reproducibility and quality.

Both fresh and regenerated palladium-containing sorbent was successfully tested at NCCC. The Pd sorbent was able to remove Hg, As and Se from both sweet and sour syngas streams. Although there were plans to incorporate these Pd sorbent as a final “polishing” unit before the Pd membrane module, time constraints in the programme and the space constraints within the WPI skid did not allow the plan to be realized.

Appendix C-1: Schematic diagram of experimental setup

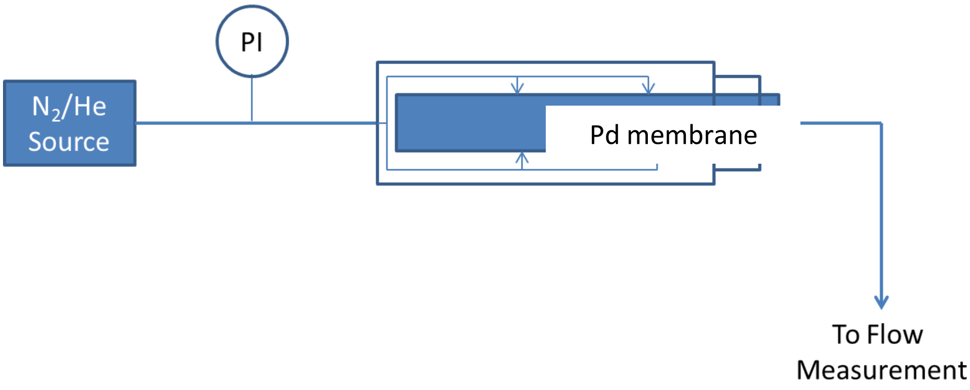

Figure A-C. 21. Schematic diagram of inert leak test experimental setup.

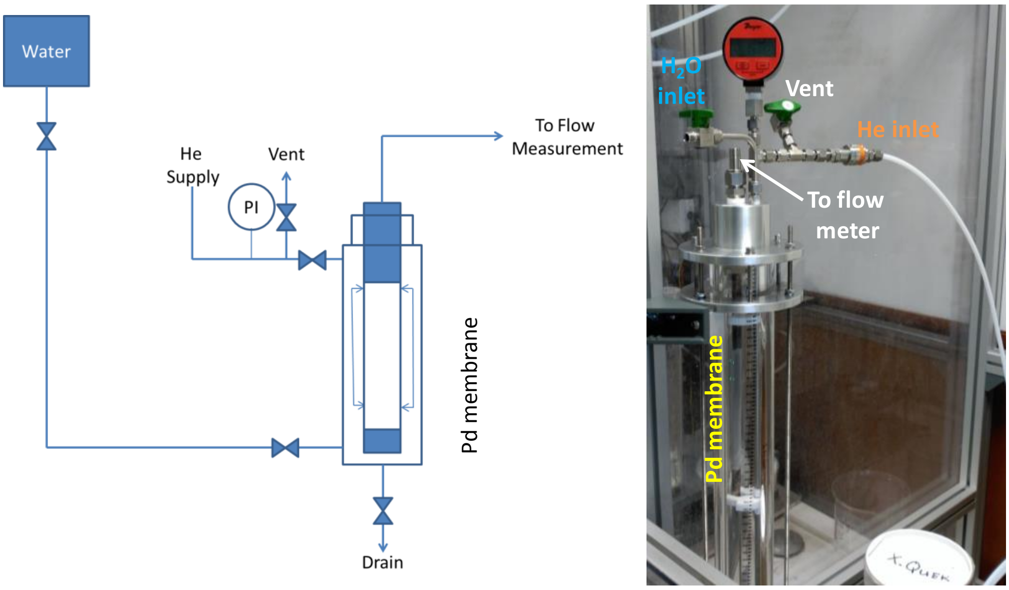

Figure A-C. 22. Schematic diagram (left) and photograph (right) of water rise test experimental setup.

Appendix C-2: Properties membranes synthesized at JM

Table A-C. 14. Pd membranes prepared on Mott 0.5" OD – 6" L PSS 316L, 0.5 µm median grade supports.

Sample	Pre-treatment	Grading[a]			Pd dense layer		Comments
	He perm. m^3/m^2.h.bar	**Loading** mg/cm^2	**Thickness** µm	**He perm.** m^3/m^2.h.bar	**Thickness** µm	**He perm.** m^3/m^2.h.bar	
Ma-153	430	-	-	4.4	6.8	0.01[b]	Reference
JM0001	712	2.7	2.2	350	-	-	Synthesis stopped[c]
JM0002	742	3.8	3.4	21	8.1	0.12[b] 0.02[b,d]	-
JM0003	-	5.8	5.0	350	6.3	0.001[b]	-
JM0004	672	7.3	5.9	248	8.8	131	• Vacuum not applied during electroless plating.
JM0005	921	6.9	5.7	74	4.5	4.3	• Use of larger water bath resulted in poor temp. control.
JM0006	878	4.9	4.0	20	12.6	0.002	• Increased heating power of water bath.
JM0007	803	6.3 9.0[e]	5.2 7.5[e]	168 7.2[e]	6.8	0.003	• Implemented stirring to water bath.
JM0008	779	5.7 8.4[e]	4.7 6.8[e]	51 1.4[e]	7.0	0.002	• Increased grading slurry to 2g/L. • Performed additional fine powder grading.
JM0009	749	6.0 9.2[e]	4.9 7.4[e]	45 0.4[e]	4.0	0.0004	• Performed additional fine powder grading.
JM0011	768	5.5	4.5	0.2[f]	4.4	0.0002	• Performed additional fine powder grading with shorter duration.
JM0012	863	5.0	4.1	1.7[f]	5.2	0.03	• Performed additional fine powder grading with shorter duration. • Membrane scratched during synthesis. Broke glass cylinder with membrane inside.
JM0013	794	7.0	5.7	215[f]	-	-	• Dip-coating was used to apply the sol-gel layer. • Applied JM0012 grading procedure in all subsequent synthesis. • Poor grading quality: Synthesis stopped.
JM0014	1044	3.7	3.0	3.3[f]	-	-	• Spray-coating was used to apply the sol-gel layer. • Synthesis in progress.
JM0015	758	5.0	4.1	14	-	-	
JM0016	872	7.2	5.9	0.1	4.6	0.01	• Grading performed using proprietary thin film coating technique. • Reduce number of grading steps. • Membrane scratched during synthesis. Broke glass

							cylinder with membrane inside.
JM0017	817	5.5	4.5	0.3	4.6	0.0003	• Repeat grading experiment for JM0016.
JM0018	-	2.7	2.2	535	-	-	• Attempted to combine steps for pre-treatment and grading. • Poor grading quality: Synthesis stopped.
JM0019	915	5.8	4.8	3.4	5.4	0.02	• Grading performed using proprietary thin film coating technique. • Reduce number of grading steps compared to JM0016.
JM0020	938	6.2	5.1	153	-	-	• Grading performed using proprietary thin film coating technique. • Reduce number of grading steps compared to JM0019.
JM0021	974	4.4	3.6	348	-	-	• Grading: Excess particles removed by dipping in water or using O-rings • Poor grading quality: Synthesis stopped.
JM0022	900	5.0	4.1	80	-	-	• Grading: Excess particles removed using O-rings • Poor grading quality: Synthesis stopped.
JM0023	1050	5.9	4.8	23	-	-	• Grading: Similar to JM0016 and JM0017 but uses O-rings to remove excess particles. • Poor grading quality: Synthesis stopped.
JM0024	721[g]	5.7	4.7	48	6.5	1.75	• First membrane synthesized by new scientist. • Performed two additional grading.
JM0025	779[g]	5.0	4.1	8.3	5.3	0.0021	• Membrane used for demonstration.
JM0026	716[g]	5.0	4.1	0.1	4.8	0.0002	• Grading: Excess particles removed by alternative reproducible method • Reduced number of synthesis steps • Aged under H_2 at 450°C
JM0027	747[g]	-	-	-	-	-	• Membrane scratched, synthesis stopped
JM0028	854[g]	4.5	3.7	2.2	5.1	0.0014	• Grading: Excess particles removed by alternative reproducible method • Reduced number of synthesis steps • Aged under H_2 at 450°C
JM0029	839[g]	9.1	7.4	0.2	5.3	0.0021	• Performed additional fine powder grading.
JM0030	834[g]	2.7	2.2	11.8	5.9	0.0011	• Grading performed using proprietary thin film coating

							technique.
JM0031	1012[g]	6.2	5.1	4.7	5.5	0.016	• New batch of Mott PSS tubes with evident surface defects • Grading: Excess particles removed by alternative reproducible method • Reduced number of synthesis steps
JM0032	1033[g]	8.6	7.03	3.8	8.0	0.18	• New batch of Mott PSS tubes with evident surface defects • Grading: Excess particles removed by alternative reproducible method • Reduced number of synthesis steps
JM0033	963[g]	6.5	5.4	6.3	6.3	0.39	• New batch of Mott PSS tubes with evident surface defects • Grading: Excess particles removed by alternative reproducible method • Reduced number of synthesis steps
JM0034	862[g]	3.7	3.0	0.3	5.4	0.013	• Grading: Excess particles removed by alternative reproducible method • Reduced number of synthesis steps • Same procedure as JM0032
JM0035	2554[g]	7.3	6.0	1.0	5.8	0.0002	• PSS supports received from WPI (media grade 1) • Grading: Excess particles removed by alternative reproducible method • Reduced number of synthesis steps • Sent to WPI for testing
JM0036	2709[g]	7.7	6.2	6.3	4.4	0.0005	• PSS supports received from WPI (media grade 1) • Grading performed using proprietary thin film coating technique. • Reduced number of synthesis steps • Sent to WPI for testing
JM0037	1074[g]	7.5	5.4	6.3	6.3	0.39	• New batch of Mott PSS after repairing the defects • Grading performed using proprietary thin film coating technique. • Defect in the vacuum pipe • Aged under H_2 at 450°C
JM0038	1180[g]	7.5	6.1	2.6	4.5	0.0023	• New batch of Mott PSS after repairing the defects • Grading performed using proprietary thin film coating

							technique. • Defect in the vacuum pipe • Aged under H_2 at 450°C
JM0039	1051[g]	7.9	6.4	16.2	5.4	0.0128	• New batch of Mott PSS after repairing the defects • Reduced number of synthesis steps • To be sent to WPI for testing
JM0040	1033[g]	-	-	-	-	-	• New batch of Mott PSS after repairing the defects • Synthesis stopped as Mott decided to re-fabricate the PSS
JM0041	1031	8.7	7.0	1.4	5.7	0.0385	• New batch of Mott PSS
JM0042	1150	8.1	6.5	0.5	4.5	0.0210	• New batch of Mott PSS
JM0043	1059	-	-	-	-	-	• PSS support were pre-treated but no further work was carried out.
JM0044	910	-	-	-	-	-	

[a] Grading performed using 2% Pd/Al_2O_3 followed by cementing. Loading refers to the mass of Pd and 2% Pd/Al_2O_3 loaded onto the support during grading. Thickness refers to the equivalent Pd thickness. [b] He permeance measured after applying Au plating on welds. [c] Synthesis was stopped as water was still leaking through the membrane after 6 h of Au plating. [d] He permeance measured after applying Au plating on welds for an additional 3 h. [e] Performed additional fine powder grading, followed by additional 90 min of electroless plating. [f] Performed additional fine powder grading but total electroless plating duration was not increased. [g] N_2 permeance was measured instead of He permeance.

Table A-C. 15. Pd membranes prepared on Mott 0.5” OD - 15” L PSS 316L, 0.5 µm median grade supports.

Sample	Pre-treatment	Grading[a]			Pd dense layer		Comments
	N_2 perm. m^3/m^2.h.bar	Loading mg/cm^2	Thickness µm	He perm. m^3/m^2.h.bar	Thickness µm	He perm. m^3/m^2.h.bar	
JM3001	729	3.4	2.8	1.9	6.5	0.0017	-
JM3002	729	4.3	3.5	0.1	6.2	0.0005	• First 15” membrane synthesized by new scientist
JM3003	779	5.3	4.3	24	-	-	• Reduced number of synthesis steps • Pd layer peeled off after grading
JM3004	821	7.1	5.8	0.05	5.0	0.0050	• Reduced number of synthesis steps (modified from JM3003 to prevent delamination)
JM3005	634	3.5	6.4	1.2	5.7	0.0750	• Reduced number of synthesis steps
JM3006	573	-	6.2	-	-	-	• Reduced number of synthesis steps • Pd layer peeled off after grading
JM3007	804	7.7	6.4	0.8	7.4	0.0007	• Batch of ten membrane intended for use in multi-tubular module test at NCCC
JM3008	839	7.5	6.2	0.6	7.4	0.0007	
JM3009	768	5.8	4.7	5.6	6.5	0.0011	
JM3010	778	7.1	5.9	0.1	5.5	0.0042	
JM3011	781	7.9	6.5	3.8	6.8	0.0008	

JM3013	746	7.7	6.4	1.6	7.0	0.0020	
JM3014	738	7.4	6.1	0.5	6.1	0.0040	
JM3015	720	5.8	4.7	0.6	6.1	0.0318	
JM3016	799	7.1	5.8	3.4	6.3	0.0054	
JM3017	753	6.6	5.4	2.5	8.1	0.0822	
JM3018	719	6.5	5.3	0.1	6.4	0.0019	• Two weeks aged plating solution and hydrazine • Included in the batch of ten membranes to replace damaged ones.
JM3012	718	7.6	5.9	0.4	8.2	0.0059	• Accurate temperature control, not above 60°C • Included in the batch of ten membranes to replace damaged ones.

[a] Grading performed using 2% Pd/Al_2O_3. Loading refers to the mass of Pd and 2% Pd/Al_2O_3 loaded onto the support during grading. Thickness refers to the equivalent Pd thickness.

Table A-C. 16. Pd membranes prepared on Mott 0.5” OD – 24” L PSS 316L, 0.5 µm median grade supports.

Sample	Pre-treatment	Grading[a]			Pd dense layer		Comments
	N$_2$ perm. m^3/m^2.h.bar	Loading mg/cm^2	Thickness µm	He perm. m^3/m^2.h.bar	Thickness µm	He perm. m^3/m^2.h.bar	
JM6001	956	-	6.7	3.2	8.1	0.0015	• Proof of concept experiment to demonstrate that the procedure developed can be scaled to synthesize longer membrane

[a] Grading performed using 2% Pd/Al_2O_3. Loading refers to the mass of Pd and 2% Pd/Al_2O_3 loaded onto the support during grading. Thickness refers to the equivalent Pd thickness.

Table A-C. 17. Pd membranes prepared on supports from alternative suppliers.

Sample	Bare tube	Grading[a]		Pd dense layer		Comments
	N$_2$ perm. m^3/m^2.h.bar	Thickness µm	He perm. m^3/m^2.h.bar	Thickness µm	He perm. m^3/m^2.h.bar	
JM2001	621	3.6	0.0063	6.3	0.0016	• Type 1 PSS supports.
JM2002	663	2.9	0.0064	4.4	0.0006	• Type 1 PSS supports. • Eliminated the polishing step
JM2003	614	2.6	6.8	5.8	0.0065	• Type 1 PSS supports. • Number of grading steps reduced
JM2004	636	2.8	2.79	4.5	1.36	• Type 1 PSS supports. • Number of grading steps reduced
JM4001	77	1.0	12.99	7.0	0.0015	• Type 2 PSS supports. • Number of grading steps reduced
JM4002	102	1.9	0.1	3.9	0.0053	• Type 2 PSS supports. • Number of synthesis steps is reduced
JM4003	93	-	-	-	-	• Type 2 PSS supports. • Activation method did not work.
JM4004	86	2.0	0.033	5.4	0.000	• Type 2 PSS supports. • Number of synthesis steps is reduced

JM4005	112	1.7	0.16	6.1	N.D.[b]	• Type 2 PSS supports. • Number of synthesis steps is reduced

[a] Grading performed using 2% Pd/Al_2O_3. Loading refers to the mass of Pd and 2% Pd/Al_2O_3 loaded onto the support during grading. Thickness refers to the equivalent Pd thickness. [3] N.D. indicates He flow was not detected.

REFERENCES

---

[1] Y. Bi, H. Xu, W. Li, A. Goldbach, Water-gas shift reaction in a Pd membrane reactor over Pt/Ce0.6Zr0.4O2 catalyst, Int. J. Hydrogen Energy. 34 (2009) 2965-2971.

[2] P. Pinacci, M. Broglia, C. Valli, G. Capannelli, A. Comite, Evaluation of the water gas shift reaction in a palladium membrane reactor, Catal. Today. 156 (2010) 165-172.

[3] A.S. Augustine, Y.H. Ma, N.K. Kazantzis, High pressure palladium membrane reactor for the high temperature water-gas shift reaction, Int. J. Hydrogen Energy. 36 (2011) 5350-5360.

[4] H. Li, J.A.Z. Pieterse, J.W. Dijkstra, W.G. Haije, H.Y. Xu, C. Bao, R.W. van den Brink, D. Jansen, Performance test of a bench-scale multi-tubular membrane reformer, J. Membr. Sci. 373 (2011) 43-52.

[5] M. De Falco, G. Iaquaniello, A. Salladini, Experimental tests on steam reforming of natural gas in a reformer and membrane modules (RMM) plant, J. Membr. Sci. 368 (2011) 264-274.

[6] Y. Shirasaki, T. Tsuneki, Y. Ota, I. Yasuda, S. Tachibana, H. Nakajima, K. Kobayashi, Development of membrane reformer system for highly efficient hydrogen production from natural gas, Int. J. Hydrogen Energy. 34 (2009) 4482-4487.

[7] D.L. McKinley, Metal alloy for hydrogen separation and purification, (1967) (3,350,845).

[8] D.J. Edlund, W.A. Pledger, Thermolysis of hydrogen sulfide in a metal-membrane reactor, J. Membr. Sci. 77 (1993) 255-264.

[9] N. Pomerantz, Y.H. Ma, Effect of H_2S on the Performance and Long-Term Stability of Pd/Cu Membranes, Ind. Eng. Chem. Res. 48 (2009) 4030-4039.

[10] J. Chabot, J. Lecomte, C. Grumet, J. Sannier, Fuel cleanup system—poisoning of palladium-silver membranes by gaseous impurities, Fusion Technol. 14 (1988) 614-618.

[11] Y. Sakamoto, F.L. Chen, Y. Kinari, F. Sakamoto, Effect of carbon monoxide on hydrogen permeation in some palladium-based alloy membranes, Int J Hydrogen Energy. 21 (1996) 1017-1024.

[12] D. Wang, T.B. Flanagan, K.L. Shanahan, Permeation of hydrogen through pre-oxidized Pd membranes in the presence and absence of CO, J. Alloys Compounds. 372 (2004) 158-164.

[13] J.K. Ali, E.J. Newson, D.W.T. Rippin, Deactivation and regeneration of Pd-Ag membranes for dehydrogenation reactions, J. Membr. Sci. 89 (1994) 171-184.

[14] F. Sakamoto, Y. Kinari, F.L. Chen, Y. Sakamoto, Hydrogen permeation through palladium alloy membranes in mixture gases of 10% nitrogen and ammonia in the hydrogen, Int J Hydrogen Energy. 22 (1997) 369-375.

[15] J. Catalano, M. Giacinti Baschetti, G.C. Sarti, Influence of water vapor on hydrogen permeation through 2.5 μm Pd-Ag membranes, Int. J. Hydrogen Energy. 36 (2011) 8658-8673.

[16] D.F. Sanders, Z.P. Smith, R. Guo, L.M. Robeson, J.E. McGrath, D.R. Paula, B.D. Freeman, Energy-efficient polymeric gas separation membranes for a sustainable future: A review, Polymer 54 (2013) 4729-4761.

[17] S. Tosti, A. Basile, L. Bettinali, F. Borgognoni, F. Gallucci, C. Rizzello, Design and process study of Pd membrane reactors, Int. J Hydr Energy 33 (2008) 5098-5105.

[18] J.C. Diniz da Costa, G.P. Reed, K. Thambimuthu, High Temperature Gas Separation Membranes in Coal Gasification, Proceedings of the 9th International Conference on Greenhouse Gas Control Technologies 1 (2009) 295-302.

[19] D. Parsley, R.J. Ciora Jr., D.L. Flowers, J. Laukaitaus, A. Chen, P.K.T. Liu, J. Yu, M. Sahimi, A. Bonsu, T.T. Tsotsis, Field evaluation of carbon molecular sieve membranes for the separation and purification of hydrogen from coal- and biomass-derived syngas, J. Memb Sci. 450 (2014) 81-92.

[20] H.É.S. Deville, L.J. Troost, Comptes Rendus 57 (1863) 965.

[21] T. Graham, On the Absorption and Dialytic Separation of Gases by Colloid Septa. Phil. Trans. R. Soc. 156 (1866) 399-439.

[22] D.R. Askeland, P.P. Fulay, W.J. Wright, The science and engineering of materials. Cengage Learning, Stamford, CT 2011.

[23] J. Shu, B.P.A. Grandjean, A. Van Neste, Catalytic Palladium-Based Membrane Reactors: A Review. Can. J. Chem. Eng. 69 (1991) 1036-1060.

[24] E. Wicke, G.H. Nernst, Phase Diagram and Thermodynamic Behavior of the Systems Pd/H_2 and Pd/D_2 at Normal Temperatures; H/D Separation Effects. Ber. Bunsen Ges. Phys. Chem. 68 (1964) 224-235.

[25] H. Frieske, E. Wicke, Magnetic Susceptibility and Equilibrium Diagram of PdHn. Ber. Bunsen Ges. Phys. Chem. 77 (1973) 48-52.

[26] L.J. Gillespie, L.S. Galstaun, The Palladium-Hydrogen Equilibrium and New Palladium Hydrides. J. Am. Chem. Soc. 58 (1936) 2565-2573.

[27] F.A. Lewis, The palladium hydrogen system. Academic Press, London, NY. 1967.

[28] T.L. Ward, T. Dao, Model of Hydrogen Permeation Behavior in Palladium Membranes. J. Membr. Sci. 153 (1999) 211-231.

[29] K. Skold, Quasielastic Neutron Scattering Studies of Metal Hydrides, in: Alefeld, G., Volkl, J., eds., 1978, Hydrogen in Metals I, Springer-Verlag, Berlin (1978) 267-287.

[30] R.C. Hurlbert, J.O. Konecny, Diffusion of Hydrogen through Palladium, J. Chem. Phys. 34 (1961).655-658.

[31] J.P. Collins, J.D. Way, Preparation and Characterization of a Composite Palladium-Ceramic Membrane. Ind. Eng. Chem. Res. 32 (1993) 3006-3013.

[32] B.D. Morreale, M.V. Ciocco, R.M. Enick, B.I. Morsi, B.H. Howard, A.V. Cugini, K.S. Rothenberger, The Permeability of Hydrogen in Bulk Palladium at Elevated Temperatures and Pressures. J. Membr. Sci. 212 (2003) 87-97.

[33] F. Guazzone, E.E. Engwall, Y.H. Ma, Effects of Surface Activity, Defects and Mass Transfer on Hydrogen Permeance and n-Value in Composite Palladium-Porous Stainless Steel Membranes. Catal. Today 118 (2006) 24-31.

[34] H. Zhao, K. Pflanz, J. Gu, A.W. Li, N. Stroh, H. Brunner, G.X. Xiong, Preparation of Palladium Composite Membranes by Modified Electroless Plating Procedure. J. Membr. Sci. 142 (1998)147-157.

[35] L. Wu, N. Xu, J. Shi, Preparation of a Palladium Composite Membrane by an Improved Electroless Plating Technique. Ind. Eng. Chem. Res. 39 (2000) 342-348.

[36] F. Guazzone, Y.H. Ma, Leak growth mechanism in composite Pd membranes prepared by the electroless deposition method. AIChE J. 54, (2008) 487–494.

[37] E.A. Mason, A.P. Malinauskas, R. B. Evans, Flow and Diffusion of Gases in Porous Media. J. Chem. Phys. 46 (1967) 3199-3118.

[38] J.M.S. Henis, M.K. Tripodi, Composite Hollow Fiber Membranes for Gas Separation: The Resistance Model Approach. J. Membr. Sci. 8 (1981) 233-246.

[39] J.B. Hunter, A New Hydrogen Purification Process, Platinum Metals Review Journal, 4(4) (1960) 130-131.

[40] G.J. Grashoff, C.E. Pilkington, C.W. Corti, The Purification of Hydrogen. A Review of the Technology Emphasizing the Current Status of Palladium Membrane Diffusion, Platinum Metals Review 27(4) (1983) 157-169.

[41] E. Wicke, H. Brodowsky, H. Zuechner, Hydrogen in palladium and palladium alloys, in: Alefeld, G., Volkl, J., eds., 1978, Hydrogen in Metals II, (1978) Springer-Verlag, Berlin, 73–151.

[42] McKinley, D. L., 1969, Method for Hydrogen Separation and Purification, (3,439,474).

[43] G.L. Holleck, Diffusion and Solubility of Hydrogen in Palladium and Palladium-Silver Alloys, J. Phys. Chem. 74(3) (1970) 503-511.

[44] Y. Sakamoto, S. Hirata, H. Nishikawa, Diffusivity and Solubility of Hydrogen in Palladium-Silver and Palladium-Gold Alloys, J. Less-Common Metals, 88(2) (1982) 387-395.

[45] J. Piper, Diffusion of Hydrogen in Copper-Palladium Alloys, J. App. Phys., 37(2) (1966) 715-721.

[46] F.N. Berseneva, N.I. Timofeev, A.B. Zakharov, Alloys of Palladium with Metals of the Platinum Group as Hydrogen-Permeable Membrane Components at High Temperatures of Gas Separation, Int. J. Hydrogen Energy, 18(1) (1993) 15-18.

[47] B.D. Morreale, M.V. Ciocco, B.H. Howard, R.P. Killmeyer, A.V. Cugini, R.M. Enick, Effect of hydrogen-sulfide on the hydrogen permeance of palladium–copper alloys at elevated temperatures, J. Membr. Sci. 241 (2004) 219-224.

[48] Way, J.D., Lusk, M., Thoen, P., 2008. Sulfur-resistance composite metal membranes. U.S. Patent 20080038567.

[49] R. Dittmeyer, V. Hollein, and K. Daub, Membrane Reactors for Hydrogenation and Dehydrogenation Processes Based on Supported Palladium. Journal of Molecular Catalysis A: Chemical, 173(1-2) (2001) 135-184.

[50] A.G. Dixon, Recent Research in Catalytic Inorganic Membrane Reactors, Int. J. Chem. Reactor Eng., 1 (2003), pp. 1–35.

[51] US. Office of Energy Efficiency & Renewable Energy, http://energy.gov/eere/fuelcells/hydrogen-production-natural-gas-reforming.

[52] M. Patrascu, M. Sheintuch, On-site pure hydrogen production by methane steam reforming in high flux membrane reactor: Experimental validation, model predictions and membrane inhibition, Chem. Eng. J. 262 (2015) 862–874.

[53] R. Koc, N.K. Kazantzis, Y.H. Ma, Membrane technology embedded into IGCC plants with CO_2 capture: An economic performance evaluation under uncertainty, Int. J. Greenh. Gas Con., 26 (2014) 22-38.

[54] L.C. Ma, B. Castro-Dominguez, N.K. Kazantzis, Y.H. Ma, Integration of membrane technology into hydrogen production plants with CO_2 capture: An economic performance assessment study, Int. J. Greenh. Gas Con., 42 (2015) 424-438.

[55] E. Kikuchi, S. Uemiya, N. Sato, Membrane Reactor using a Microporous Glass-Supported Thin Film of Palladium. Part I. Application to the Water Gas Shift Reaction, Chemistry Letters, (3) (1989) 489-492.

[56] S.W. Nam, S.P. Yoon, H.Y. Ha, Methane Steam Reforming in a Pd-Ru Membrane Reactor, Korean Journal of Chemical Engineering, 17(3) (2000) 288-291.

[57] J. Tong, Y. Matsumura, H. Suda, Experimental Study of Steam Reforming of Methane in a Thin (6 μM) Pd-Based Membrane Reactor, Ind. Eng. Chem. Res. 44(5) (2005) 1454-1465.

[58] S. Laegsgaard Jorgensen, P.E. Hojlund Nielsen, P. Lehrmann, Steam Reforming of Methane in a Membrane Reactor, Catalysis Today, 25(3-4) (1995) 303-307.

[59] A. Basile, E. Drioli, F. Santell, A Study on Catalytic Membrane Reactors for Water Gas Shift Reaction, Gas Separation & Purification, 10(1) (1996b) 53-61.

[60] A. Criscuoli, A. Basile, E. Drioli, An Analysis of the Performance of Membrane Reactors for the water-gas Shift Reaction using Gas Feed Mixtures, Catalysis Today, 56(1-3) (2000) 53-64.

[61] O. Iyoha, R. Enick, R. Killmeyer, H_2 Production from Simulated Coal Syngas Containing H_2S in Multi-Tubular Pd and 80wt% Pd-20wt% Cu Membrane Reactors at 1173 K, J. Membr. Sci. 306 (2007a) 103-115.

[62] O. Iyoha, R. Enick, R. Killmeyer, Wall-Catalyzed Water-Gas Shift Reaction in Multi-Tubular Pd and 80wt%Pd-20wt%Cu Membrane Reactors at 1173K, J. Membr. Sci., 298 (2007b) 14-23.

[63] P. Chiesa, S. Consonni, T. Kreutz, R, Williams, Co-Production of Hydrogen, Electricity and CO_2 from Coal with Commercially Ready Technology. Part A. Performance and Emissions. Int. J. Hydrogen Energy 30 (2005) 747-767.

[64] F. Gallucci, L. Paturzo, A. Famà, A. Basile, Experimental Study of the Methane Steam Reforming Reaction in a Dense Pd/Ag Membrane Reactor, Ind. Eng. Chem. Res., 2004, 43 (4), pp 928-933.

[65] J. Shu, B.P.A. Grandjean, S. Kaliaguine, Asymmetric Pd-Ag/stainless steel catalytic membranes for methane steam reforming, Catal. Today 25 (1995) 327-332.

[66] Y.M. Lin, S.L. Liu, C.H. Chuang, Y.T. Chu, Effect of incipient removal of hydrogen through palladium membrane on the conversion of methane steam reforming: Experimental and modeling, Catal. Today 82 (2003)127-139.

[67] E. Kikuchi, Y. Nemoto, M. Kajiwara, S. Uemiya, T. Kojima, Steam reforming of methane in membrane reactors: comparison of electroless-plating and CVD membranes and catalyst packing modes, Catal. Today 56 (2000) 75–81.

[68] J.M. Vásquez Castillo, T. Sato, N. Itoh, Effect of temperature and pressure on hydrogen production from steam reforming of biogas with Pd-Ag membrane reactor, Int. J. Hydrogen Energy 40 (2015) 3582-3591.

[69] H.W. Abu El Hawa, S.N. Paglieri, C.C. Morris, A. Harale, J.D. Way, Application of a Pd-Ru composite membrane to hydrogen production in a high temperature membrane reactor, Sep. Purif. Technol. 147 (2015) 388-397.

[70] S. Uemiya, N. Sato, H. Ando, E. Kikuchi, The Water Gas Shift Reaction Assisted by a Palladium Membrane Reactor, Ind. Eng. Chem. Res.,30 (1991) 585-589.

[71] D. Mendes, V. Chibante, JM. Zheng, S. Tosti, F. Borgognoni, A. Mendesa, L.M. Madeira, Enhancing the production of hydrogen via water-gas shift reaction using Pd-based membrane reactors, Int. J. Hydrogen Energy 35 (2010) 12596-12608.

[72] J. Catalano, F. Guazzone, I.P. Mardilovich, N.K. Kazantzis, Y.H. Ma, Hydrogen Production in a Large Scale Water-Gas Shift Pd-Based Catalytic Membrane Reactor, Ind. Eng. Chem. Res. 52 (2013) 1042-1055.

[73] T.A. Peters, M. Stange, H. Klette, R. Bredesen, High pressure performance of thin Pd-23%Ag/stainless steel composite membranes in water gas shift gas mixtures; influence of dilution, mass transfer and surface effects on the hydrogen flux, J. Membr. Sci. 316 (2008) 119-127.

[74] E. Fernandez, A. Helmi, K. Coenen, J. Melendez, J.L. Viviente, D.A.P. Tanaka, M. van Sint Annaland, F. Gallucci, Development of thin Pd-Ag supported membranes for fluidized bed membrane reactors including WGS related gases, Int. J. Hydrogen Energy 40 (2015) 3506-3519.

[75] Ma YH, Mardilovich PP, She Y. (2000) Hydrogen gas-extraction module and method fabrication. US Patent No. 6,152,987.

[76] I.P. Mardilovich, E. Engwall, Y.H. Ma, Dependence of Hydrogen Flux on the Pore Size and Plating Surface Topology of Asymmetric Pd-Porous Stainless Steel Membranes, Desalination, 144(1-3) (2002) 85-89.

[77] Ma YH, Mardilovich IP, Engwall EE. (2008) Method for fabricating composite gas separation modules. US Patent No. 7,390,536.

[78] S. Yun, S.T. Oyama, Correlations in palladium membranes for hydrogen separation: A review, J. Membr. Sci. 375 (2011) 28-45.

[79] Y. Guo, Z. Hongye, H. Wu, L. Zhou, H. Liu, X. Zhang, Preparation of palladium membrane by bio-membrane assisted electroless plating for hydrogen separation, Int. J. Hydrogen Energy 39 (2014) 7069-7076.

[80] K. Zhang, H. Gao, Z. Rui, P. Liu, Y. Li, Y.S. Lin, High-temperature stability of palladium membranes on porous metal supports with different intermediate layers, Ind. Eng. Chem. Res. 48 (2009) 1880-1886.

[81] S.K. Ryi, S.W. Lee, D.K. Oh, B.S. Seo, J.W. Park, J.S. Park, D.W. Lee, S.S. Kim, Electroless plating of Pd after shielding the bottom of planar porous stainless steel for a highly stable hydrogen selective membrane, J. Membr. Sci. 467 (2014) 93-99.

[82] H. Noh, T.B. Flanagan, T. Sonoda, Y. Sakamoto, Solubility and thermodynamics of hydrogen in homogeneous f.c.c. Pd-Pt alloys, J Alloys Compd 228 (1995) 164-171.

[83] F. Vigier, R. Jurczakowski, A. Lasia, Determination of hydrogen absorption isotherm and diffusion coefficient in $Pd_{81}Pt_{19}$ alloy. J. Electroanal. Chem. 588 (2006) 32-43.

[84] M. Kajiwara, S. Uemiya, T. Kojima, Stability and hydrogen permeation behavior of supported platinum membranes in presence of hydrogen sulfide, Int. J. Hydrogen Energy 24 (1999) 839-844.

[85] D.W. Kim, Y.J. Park, J.W. Moon, S.K. Ryi, J.S. Park, The effect of Cu reflow on the Pd-Cu-Ni ternary alloy membrane fabrication for Infinite hydrogen separation, Thin Solid Films 516 (2008) 3036-3044.

[86] A.M. Tarditi, L.M. Cornaglia, Novel PdAgCu ternary alloy as promising materials for hydrogen separation membranes: Synthesis and characterization, Surf. Sci. 605 (2011) 62-71.

[87] K.E. Coulter, J.D. Way, S.K. Gade, S. Chaudhari, D.S. Sholl, L. Semidey-Flecha, Predicting, fabricating and permeability testing of free-standing ternary palladium-copper-gold membranes for hydrogen separation, J. Phys. Chem. C 114 (2010) 17173-17180.

[88] E.O. Kirkendall, Diffusion of zinc in alpha brass. Trans AIME 147 (1942)104-110.

[89] H. Okamoto, T.B.J. Massalski, Phase Equilib. 6 (1985) 229– 235.

[90] Ma YH, Mardilovich IP, Engwall EE. (2007) Composite gas separation modules having high Tamman temperature intermediate layers. US Patent No. 7,255,726.

[91] Ma YH, Mardilovich IP, Engwall EE. (2007) Composite gas separation modules having intermediate porous metal layer. US Patent No. 7,175,694.

[92] Ma YH, Mardilovich IP, Engwall EE. (2007) Method for curing defects in the fabrication of a composite gas separation module. US Patent No. 7,172,644.

[93] F. Guazzone , J. Catalano, I.P. Mardilovich, J Kniep, S. Pande, T. Wu, R.C. Lambrecht, S. Datta, N.K. Kazantzis, Y.H. Ma, Gas permeation field tests of composite Pd and Pd-Au membranes in actual coal derived syngas atmosphere, Int. J Hydrogen Energy 37 (2012) 4557-4568.

[94] I.P. Mardilovich, B. Castro-Dominguez, N.K. Kazantzis, T. Wu, Y.H. Ma, A comprehensive performance assessment study of pilot-scale Pd and Pd/alloy membranes under extended coal-derived syngas atmosphere testing, Int. J. Hydrogen Energy 40 (2015) 6107-6117.

[95] F. Guazzone, J. Catalano, I.P. Mardilovich, T. Wu, R.C. Lambrecht, S. Datta, J. Kniep, S. Pande, N.K. Kazantzis, and Y.H Ma, Enhancement of the Long-Term Permeance, Selectivity Stability, and Recoverability of Pd-Au Membranes in Coal Derived Syngas Atmospheres, Energy Fuels 27 (2013) 4150-4160.

[96] J. Boon, J.A.Z. Pieterse, F.P.F. van Berkel, Y.C. van Delft, M. van Sint Annaland, Hydrogen permeation through palladium membranes and inhibition by carbon monoxide, carbon dioxide, and steam, J. Membr. Sci.496 (2015)344-358.

[97] G. He, Y. Mi, P.L. Yue, G. Chen, Theoretical study on concentration polarization in gas separation membrane processes, J. Membr. Sci 153 (1999) 243-258.

[98] S. Adhikari, S. Fernando, Hydrogen Membrane Separation Techniques, Ind. Eng. Chem. Res. 45 (2006) 875-881.

[99] M. Coroneo, G. Montante, M. Giacinti Baschetti, A. Paglianti, CFD modelling of inorganic membrane modules for gas mixture separation, Chem. Eng. Sci. 64 (2009) 1085-1094.

[100] P.P. Mardilovich, Y. She, Y.H. Ma, M.H. Rei, Defect-free Pd membranes on porous stainless-steel support. AIChE J. 44 (1998) 310.

[101] C.H. Chen, Y.H. Ma, The effect of H_2S on the performance of Pd and Pd/Au composite membrane, J. Membr. Sci. 362 (2010) 535-544.

[102] M.E. Ayturk, N.K. Kazantzis, Y.H. Ma, Modeling and performance assessment of Pd- and Pd/Au-based catalytic membrane reactors for hydrogen production, Energy Environ. Sci. 2 (2009) 430-438.

[103] R. Koc, N.K. Kazantzis, Y.H. Ma, A process dynamic modeling and control framework for performance assessment of Pd/alloy-based membrane reactors used in hydrogen production, Int. J. Hydrogen Energy 36 (2011) 4934-4951.

[104] R.B. Bird, W.E. Stewart, E.N. Lightfoot, Transport Phenomena, Second Edition, John Wiley & Sons, Inc. 2007.

[105] S. Uemiya, State of the art of supported metal membranes for gas separation, Sep. Purif. Methods 28(1), (1999) 51-85

[106] S.K. Gade, , E.A. Payzant, , H.J. Park, , P.M. Thoen, , J.D. Way, The effects of fabrication and annealing on the structure and hydrogen permeation of Pd-Au binary alloy membranes, J. Membr. Sci. 340 (2009) 227-233.

[107] V. Gryaznov, Metal containing membranes for the production of ultrapure hydrogen and the recovery of hydrogen isotopes, Sep. Purif. Methods (2000) 29.

[108] K. Atwood, M.R. Arnold, E.G. Appel, Water gas shift reaction: Effect of Pressure on Rate over an Iron- Oxide-Chromium Oxide Catalyst, Ind. Eng. Chem., 1950, 42 (8) 1600-1602.

[109] J. Zhang, D. Liu, M. He, H. Xua, W. Li, Experimental and simulation studies on concentration polarization in H_2 enrichment by highly permeable and selective Pd membranes, J. Membr. Sci. 274 (2006) 83-91.

[110] S. Battersby, P.W. Teixeira, J. Beltramini, M.C. Duke, V. Rudolph, J.C. Diniz da Costa, An analysis of the Peclet and Damkohler numbers for dehydrogenation reactions using molecular sieve silica (MSS) membrane reactors, Catal. Today 116 (2006) 12-17.

[111] A. Li, W. Liang, R. Hughes, The effect of carbon monoxide and steam on the hydrogen permeability of a Pd/stainless steel membrane, J. Membr. Sci. 165 (2000) 135-141.

[112] J.R. Rostrupnielsen, J.H.B. Hansen, CO_2-Reforming of Methane over Transition Metals, J. Catalysis 144 (1993) 38-49.

[113] J. Tong, Y. Matsumura, Pure hydrogen production by methane steam reforming with hydrogen-permeable membrane reactor, Catal. Today 111 (2006) 147-152.

[114] V.M. Mas, L. Bergamini, G. Baronetti, N. Amadeo, M. Laborde, A kinetic study of ethanol steam reforming using a nickel based catalyst, Top. Catal. 51 (2008) 39-48.

[115] V. Palma, F. Castaldo, G. Iaquaniello, P. Ciambelli, Sustainable hydrogen production by catalytic bio-ethanol steam reforming, INTECH Open Access Publisher (2012).

[116] A. Bshish, Z. Yaakob, B. Narayanan, R. Ramakrishnan, A. Ebshish, Steam-reforming of ethanol for hydrogen production, Chem. Pap. 65 (2011) 251-266.

[117] N.R. Peela, D. Kunzru, Steam reforming of ethanol in a microchannel reactor: kinetic study and reactor simulation, Ind. Eng. Chem. Res. 50 (2011) 12881-12894.

[118] O. Olafadehan, A. Ayoola, O. Akintunde, V. Adeniyi, Mechanistic kinetic models for steam reforming of concentrated crude ethanol on Ni/Al_2O_3 catalyst, J. Eng. Sci. &Tech. 10 (2015) 633-653.

[119] M. Patel, T.K. Jindal, K.K. Pant, Kinetic study of steam reforming of ethanol on Ni-based Ceria-Zirconia catalyst, Ind. Eng. Chem. Res 52 (2013) 15763-15771.

[120] W. Du, Q. Wang, D. Saxner, N. A. Deskins, D. Su, J.E. Krzanowski, I.F. Anatoly, X. Teng, Highly active Iridium/Iridium-Tin/Tin oxide heterogeneous nanoparticles as alternative electrocatalysts for the ethanol oxidation reaction, J. Amer. Chem. Soc. 133 (2011) 15172-15183.

[121] J. Sun, X.P. Qiu, F. Wu, W.T. Zhu, H_2 from steam reforming of ethanol at low temperature over Ni/Y_2O_3, Ni/La_2O_3 and Ni/Al_2O_3 catalysts for fuel-cell application, Int. J. Hydrogen Energy. 30 (2005) 437-445.

[122] J. Xu, G.F. Froment, Methane steam reforming, methanation and water-gas shift: I. Intrinsic kinetics, AIChE J. 35 (1989) 88-96.

[123] M. de-Souza, G. M. Zanin, F.F. Moraes. Parametric study of hydrogen production from ethanol steam reforming in a membrane microreactor, Braz Raz J Chem Eng. 30 (2013) 355-367.

[124] C.G. Sonwane, J. Wilcox, Y.H. Ma, Achieving optimum hydrogen permeability in PdAg and PdAu alloys, J. Chem. Phys. 125 (2006) 1-10.

[125] G. Caygill, M. Zanfir, A. Gavriilidis, Scalable Reactor Design for Pharmaceuticals and Fine Chemicals Production 1: Potential Scale-up Obstacles, Org. Process Res. Dev. 10(2006) 539−552.

[126] A. Kumar, R. Prasad, Y.C. Sharma, Steam Reforming of Ethanol: Production of Renewable Hydrogen, Int. J. Environ. Res. Dev, 4 (2014) 203-212.

[127] G. Barbieri, V. Violante, F.P. Di Maio, A. Criscuoli, E. Drioli, Methane Steam Reforming Analysis in a Palladium-Based Catalytic Membrane Reactor, Ind. Eng. Chem. Res. 36 (1997) 3369-3374.

[128] P.V Mathure, S. Ganguly, A.V. Patwardhan, R.K. Saha, Steam reforming of ethanol using a commercial nickel-based catalyst, Ind. Eng. Chem. Res. 46 (2007) 8471-8479.

[129] F. Gallucci, A. Basile, Pd-Ag membrane reactor for steam reforming reactions: a comparison between different fuels, Int. J. Hydrogen Energy. 33 (2008) 1671-1687.

[130] D.R. Sahoo, S. Vajpai, S. Patel, K. K. Pant, Kinetic modeling of steam reforming of ethanol for the production of hydrogen over Co/Al_2O_3 catalyst, Chem. Eng. J. 125 (2007) 139-147.

[131] M.A. Murmura, M. Patrascu, M.C. Annesini, V. Palma, C. Ruocco, M. Sheintuch, Directing selectivity of ethanol steam reforming in membrane reactors, Int. J. Hydrogen Energy. 40 (2015) 5837-5848.

[132] L.S. Savage, Decision Making with Insight, Brooks/Cole, Belmont, CA (2003).

[133] R.A. Brealey, S.C. Myers, F. Allen, Principles of Corporate Finance, 9th edition, McGraw-Hill, New York (2008).

[134] Chemical Engineering Plant Cost Indexes. Available from: http://www.che.com/pci (accessed 20.06.15).

[135] W.D. Seider, J.D. Seader, D.R. Lewin, Product and Process Design Principles, Synthesis, Analysis and Evaluation, Second Edition, John Wiley and Sons, Inc. 2004.

[136] R. de Neufville, S. Scholtes, Flexibility in Engineering Design, MIT Press, Cambridge, MA (2011).

[137] A. Criscuoli, A. Basile, E. Drioli, O. Loiacono. An economic feasibility study for water gas shift membrane reactor, J. Membr. Sci. 181(1) (2001) 21-27.

[138] V.H. Chou, N.J. Kuehn (2010) Assessment of Hydrogen Production with CO_2 Capture. National Energy Technology Laboratory, US Department of Energy, Pittsburgh, PA, USA. See http://netl.doe.gov/File%20Library/Research/Energy%20Analysis/Publications/DOE-NETL-2010-1434-H2ProdwCO2CaptureVol1-2010.pdf (accessed 20/06/2014).

[139] Peters, M.S., Timmerhaus, K.D., 1991. Plant Design and Economics for Chemical Engineers, 4th ed. McGraw Hill, New York

[140] G.J. Stiegel, M. Ramezan, Hydrogen from coal gasification: An economical pathway to a sustainable energy future, Int. J. Coal Geol., 65 (2006) 173 – 190.

[141] K. Jordal, R. Bredesen, H.M. Kvamsdal, Integration of H_2-Separating Membrane Technology in Gas Turbine Processes for CO_2 Capture. Energy 29(9-10) (2004) 1269-1278.

[142] R. Bredesen, K. Jordal, O. Bolland, High-Temperature Membranes in Power Generation with CO_2 Capture, Chem. Eng. Process. Process Intensif., 43(9) (2004) 1129-1158.

[143] K. Damen, M. Troost, A. Faaij, A Comparison of Electricity and Hydrogen Production Systems with CO_2 Capture and Storage. Part A: Review and Selection of Promising Conversion and Capture Technologies, Prog. Energy Combust. Sci., 32(2) (2006) 215-246.

[144] J.D. Figueroa, T. Fout, S. Plasynski, H. McIlvried, R.D. Srivastava, Advances in CO_2 Capture Technology-The U.S. Department of Energy's Carbon Sequestration Program, Int. J. Greenh. Gas Con., 2 (2008) 9–20.

[145] J.L. Haslbeck, N.J. Kuehn, E.G. Lewis, Cost and Performance Baseline for Fossil Energy Plants Volume 1: Bituminous Coal and Natural Gas to Electricity, DOE/NETL (2013). Available from: http://www.netl.doe.gov/File%20Library/Research/Energy%20Analysis/OE/BitBase_FinRep_Rev2a-3_20130919_1.pdf (accessed 20/09/2014).

[146] C. Descamps, C. Bouallou, M. Kanniche, Efficiency of an Integrated Gasification Combined Cycle (IGCC) Power Plant including CO_2 removal, Energy 33 (2008) 874-881.

[147] F.V. Lopes, C.A. Grande, A.E. Rodrigues, Activated Carbon for Hydrogen Purification by Pressure Swing Adsorption: Multicomponent Breakthrough Curves and PSA Performance, Chem. Eng. Sci. 66 (2011) 303-317.

[148] M.D. Dolan, R. Donelson, N.C. Dave, Performance and Economics of a Pd-Based Planar WGS Membrane Reactor for Coal Gasification, Int. J. Hydrogen Energy, 35(20) (2010) 10994-11003.

[149] C.A. Scholes, K.H. Smith, S.E. Kentish, CO_2 Capture from Pre-Combustion processes—Strategies for Membrane Gas Separation, Int. J. Greenh. Gas Con., 4(5) (2010) 739-755.

[150] J.W. Dijkstra, J.A.Z. Pieterse, H. Li, Development of Membrane Reactor Technology for Power Production with Pre-Combustion CO_2 Capture, Energy Procedia, 4 (2011) 715-722.

[151] F. Mueller-Langer, E. Tzimas, M. Kaltschmitt, S. Peteves, Techno-economic assessment of hydrogen production processes for the hydrogen economy for the short and medium term, Int. J. Hydrogen Energy, 32 (2007) 3797-3810.

[152] G.Q. Lu, J.C. Diniz da Costa, M. Duke, S. Giessler, R. Socolow, R.H. Williams, T. Kreutz, Inorganic membranes for hydrogen production and purification: A critical review and perspective, J Colloid Interf. Sci. 314 (2007) 589-603

[153] R. Koc, N.K. Kazantzis, Y.H. Ma, Process Safety Aspects in Water-Gas-Shift (WGS) Membrane Reactors used for Pure Hydrogen Production, J. Loss Prev. Process Ind., 24 (6) (2011) 852-869.

[154] A.S. Augustine, I.P. Mardilovich, N.K. Kazantzis, Y.H. Ma, Durability of PSS-Supported Pd-Membranes Under Mixed Gas and Water-Gas Shift Conditions, J. Membr. Sci., 415-416 (2012) 213-220.

[155] F. Roa, J.D. Way, The Effect of Air Exposure on Palladium-Copper Composite Membranes, Appl. Surf. Sci, 240(1-4) (2005) 85-104.

[156] A.L. Mejdell, H. Klette, A. Ramachandran, Hydrogen Permeation of Thin, Free-Standing Pd/Ag 23% Membranes before and After Heat Treatment in Air. J. Membr. Sci., 307(1) (2008) 96-104.

[157] A.L. Mejdell, D. Chen, T.A. Peters, The Effect of Heat Treatment in Air on CO Inhibition of a ~3 μm Pd-Ag (23 wt.%) Membrane, J. Membr. Sci., 350(1-2) (2010) 371-377.

[158] T.F. Buss, The Effect of State Tax Incentives on Economic Growth and Firm Location Decisions: An Overview of the Literature, Economic Development Quarterly, 15(1) (2001) 90-105.

[159] M. Al-Juaied, A. Whitmore, Realistic Costs of Carbon Capture, Energy Technology Innovation Policy, Kennedy School of Government, Harvard University, Cambridge, MA.

[160] D. Patino-Echeverri, P. Fischbeck, E. Kriegler, Economic and Environmental Costs of Regulatory Uncertainty for Coal-Fired Power Plants, Environ. Sci. Technol. 2009, 43, 578-584.

[161] S. Benninga, Principles of Finance with Excel, Oxford University Press, New York & Oxford (2011).

[162] Gangwal, S.K., Portzer, J.W., Roberts, G.W., Kozup, S.C., 1998. Engineering evaluation of hot-gas desulfurization with sulfur recovery. Research Triangle Institute, Contract no. DE-AC21-94MC31258.

[163] Alptekin, G., Lind,J.,Amalfitano,R.,Copeland,R., 2003. Sorbents forMercuryRemoval from Coal-Derived Synthesis Gas. TDA Research, Inc, Wheat Ridge, CO

[164] Yeh, S., Rubin, E.S., 2007. A centurial history of technological change and learning curves for pulverized coal-fired utility boilers. Energy 32, 1996-2005.

[165] Rosenberg, W.G., Alpern, D.C., Walker, M.R., 2005. Deploying IGCC technology in this decade with 3 Party Covenant Financing: Volume I. Discussion Paper 2004-07. Belfer Center for Science and International Affairs, Kennedy School of Government, Harvard University, Cambridge, MA.